International School for Advanced Studies

Gutzwiller Approximation applied to inhomogeneous lattice models and solid state systems

Thesis submitted for the degree of
Doctor Philosophiæ

Candidate:

Giovanni Borghi

Supervisors:

Prof. Michele Fabrizio
and Prof. Erio Tosatti

Trieste, October 2011

"It is you who are unpoetical," replied the poet Syme. "If what you say of clerks is true, they can only be as prosaic as your poetry. The rare, strange thing is to hit the mark; the gross, obvious thing is to miss it. We feel it is epical when man with one wild arrow strikes a distant bird. Is it not also epical when man with one wild engine strikes a distant station? Chaos is dull; because in chaos the train might indeed go anywhere, to Baker Street or to Bagdad. But man is a magician, and his whole magic is in this, that he does say Victoria, and lo! it is Victoria. No, take your books of mere poetry and prose; let me read a time table, with tears of pride.

G.K. Chesterton (The Man Who Was Thursday)

Contents

Introduction

The search for the ground-state of a many-electron system has not ceased to be a challenge for theoretical condensed-matter and solid state physics, since the complexity of the exact solution increases exponentially with the number of particles, and, in most interesting cases, it is still not affordable by modern computers. This in spite of the relentless improvement of computational power that characterized the last thirty years.

The most promising tool for seeking the exact ground-state of many-body systems, Quantum Monte Carlo, suffers from the well-known sign problem, and can provide reliable results only for a limited class of models. Whenever there is need of investigating the electronic structure of large molecules, or crystalline systems, indispensable for understanding real materials, one has to resort to effective theories, and to find the most reliable approximations that correctly grasp the physical properties one aims to describe.

The simplest option is to bring the many-body problem back to a one-body one, by treating each particle as independent from the others, and modeling all interaction effects among particles at a mean-field level. This approximation, though often successful, fails to describe all physical phenomena that are driven by the effects of inter-particle entanglement. Whenever the effects, usually referred to as correlation effects, are determinant in the description of physical observables, one needs to engineer new way to re-introduce them into the effective theory.

Density Functional electronic structure calculations

One of the most popular methods used for electronic structure simulations is Density Functional Theory (DFT) within the Kohn-Sham framework [1, 2], which solves the many-electron problem by means of a system of auxiliary independent particles with the same density as actual electrons and moving in a fictitious external potential that accounts for the interaction effects in the real system. The solution of the Schrödinger equation for independent particles does not suffer from the exponential complexity of the correlated many-body problem, while the use of the density, instead of the wavefunction, as independent variable for the energy minimization made Kohn

Sham DFT extremely competitive, and soon even preferable in large scale simulations, to other theoretical tools of Quantum Chemistry such as the Hartree-Fock (HF) method [3].

In spite of its great successes, Kohn-Sham DFT has many weaknesses, which come from the fact that all the intricate quantum corrections to the classical electrostatic Hartree potential, divided into exchange and correlation effects, are included in the total energy only in an approximate way, through a fairly simple functional of the density.

The historically oldest and most simple approximation to the exchange and correlation energy is the Local Density Approximation (LDA) [2, 4–6], which gives the exact energy for a uniform electron gas. When applied to realistic crystalline systems, this approximation tends to underestimate band gaps and equilibrium lattice constants, while in the simulations of molecular systems and adsorption processes it shows a preference for higher coordination and shorter bond lengths [7, 8]. For the same reason, its performance in calculating dissociation properties of molecules is also unsatisfactory [9].

In general, LDA and its spin-resolved version Local Spin Density Approximation (LSDA), perform better in systems with slowly-varying density. On the contrary, the inability of these approximations in subtracting the electron self-interaction contained in the classical Hartree potential makes them less reliable in describing systems with strongly localized electrons. This limitation is particularly severe for $3d$ transition metal elements and compounds, where for geometrical reasons the Bloch functions with energies in the vicinity of the Fermi level keep most of the atomic character, and hence are not very spread in real space.

Many-body properties of transition metals and compounds

The strongly localized nature of electrons in transition metal compounds effectively enhances electron-electron interactions, to such an extent that in particular temperature and pressure conditions, electronic correlations, i.e. all effects that deviate from the independent-particle picture, can induce a transition from a metallic to an insulating phase. This correlation-driven metal-insulator transition, known as Mott transition [10, 11], makes some $3d$ metal compounds, as vanadium oxides, a natural laboratory for intriguing many-body physics.

With the discovery of high-temperature superconductivity [12] in cuprates, the importance of transition metal compounds increased even more, together with the theoretical efforts for a better understanding of their magnetic and conductive properties. Contrary to the Bardeen-Cooper-Schrieffer (BCS) superconductivity [13], which can be understood by means of mean-field independent-particle methods, high-

temperature superconductivity is described only through a correct inclusion of electronic correlations in the ground-state wavefunction, and appears often in materials which display in their phase diagram also a Mott insulating state.

Lattice models as the Hubbard model (HM) [14] were of great help in providing a fictitious environment where correlations can be accurately described by methods such as Quantum Monte Carlo (QMC) [15], Density Matrix Renormalization Group (DMRG) [16] and Dynamical Mean-Field Theory (DMFT) [17]. For the purpose of a quantitative understanding of experimental data, it was however of key importance to bring the expertise gained on lattice models over to realistic simulations of the solid state.

This was attempted for example through ad-hoc improvements of Density Functional Theory, with the inclusion of a local Hubbard correction in the Kohn-Sham Hamiltonian, solved either through static (LDA+U) [18, 19] or, more recently, dynamical (LDA+DMFT) [20] mean-field methods. A few years ago, also the Variational Quantum Monte Carlo (VQMC) approach [21, 22] was proved successful in reproducing electronic properties of atoms and simple molecules [23], and its development appears to be promising for more ambitious applications.

The Gutzwiller Variational Method

In this thesis we focus on a different approach, which is the Gutzwiller Variational Method (GVM). The GVM [24], proposed by Martin C. Gutzwiller in 1963, consists of introducing local many-body parameters to enlarge the variational freedom of a mean-field wavefunction such as a Slater determinant or BCS wavefunction, whose variational energy was previously optimized within an independent-particle framework. Its original formulation, with one variational parameter tuning the double occupation probability of each site of the single-band HM, is still exploited today in most VQMC calculations. Indeed the exact calculation of the expectation value of a lattice model Hamiltonian on the Gutzwiller variational wavefunction (GVW) can be computed in general only numerically.

An analytic approximation for these expectation values was suggested by the same Gutzwiller [25, 26], and later proved to become exact in the limit of infinite coordination lattices. This analytic approximation, widely adopted also in lattices of finite coordination, is known in literature as the Gutzwiller Approximation (GA). The GA can be understood as a further approximation to DMFT, a more refined tool for simulating strongly-correlated systems, which relies on an ansatz – the locality of the lattice self-energy – that again is strictly valid only in the limit of infinite lattice coordination [17].

The GA is not as accurate as DMFT. Nevertheless, it does provide qualitatively, and often quantitatively, correct descriptions of strongly correlated conducting materials that are insulators "in disguise" [27], i.e. materials whose thermodynamic, conduction and magnetic properties depend on correlations that are already present in their Mott insulating phase, and that continue to play an important role after their insulator-to-metal transition. The Resonating Valence Bond (RVB) picture, an intuition due to P.W. Anderson [28], describes this type of situation, and is an intriguing example of how high-T_c superconductivity can be partially explained through a Gutzwiller approach.

The advantage of the GA with respect to independent-particle methods such as HF is the possibility to describe the effects of electron-electron interaction on the band energy of a lattice system through an effective renormalization of the inter-site hopping. The hopping renormalization can be seen, in a Fermi liquid picture, as a renormalization à la Landau of the electronic band mass.

While the HF quasi-particles are electrons whose single-particle states have been renormalized by interactions, but whose effective mass and Fermi distribution remain unchanged with respect to the non-interacting case, the quasi-particles described by the GA are Landau quasi-particles with a reduced Fermi step and with enhanced mass, whose divergence signals the onset of many-body localization and of the metal-insulator transition. The transition to the insulating state does not require within GA any opening of a gap in the quasi-particle spectrum, which is instead a necessary condition to describe an insulator within the HF method.

Understanding surface sensitive ARPES spectra and studying correlation effects at interfaces and junctions

An experimental tool for the investigation of quasi-particle properties in strongly correlated materials displaying a Mott metal-insulator transition is Photoemission Spectroscopy (PES) [29], which is able to give access to the spectral function of a crystalline sample through the analysis of the electrons – also named photoelectrons – that are emitted after a photoelectric process has taken place below its surface. The finite mean-free path of electrons inside a crystal makes PES sensitive mainly to a sample surface properties. However, recent improvements of photoemission techniques provided photoelectrons with a larger probing depth [30–32], and introduced the possibility of sensing also the bulk spectral properties, and comparing them to the surface ones [33].

Stimulated by the recent progress in the photoemission spectroscopy on vanadium oxides, we apply the GVM to study the effects of a surface on the quasi-particle properties of a slab of a strongly correlated HM with layer-dependent Hubbard-U. For

this purpose we choose as variational wavefunction a Slater determinant renormalized by layer-dependent Gutzwiller projectors. In order to optimize the parameters of this wavefunction, we devise a two-step self-consistent method where the energy minimization with respect to Gutzwiller parameters is followed by a diagonalization of an effective single-particle Hamiltonian with renormalized hopping [34].

We find that, due to the lack of surface coordination, the quasi-particle band mass renormalization is always stronger near the surface, even when the Hubbard parameter U has the same value on all lattice sites. We further notice that that the difference between the Hubbard parameter U and its critical value U_c provides the system with a new length-scale, which determines the distance over which the larger surface quasi-particle mass decays to the bulk value.

Taking advantage from a known sum-rule for the spectral weight, we are able to provide an approximation to the layer-resolved spectral function of the Hubbard lattice, which shows from surface to bulk an increase of the peak due to quasi-particle low-energy excitations. The spectral weight of high-energy excitations not taking part in the conduction process, building the so-called Hubbard bands, is shown to be very weakly dependent on the layer distance from the surface, agreeing qualitatively with the recent photoemission data of Rodolakis *et al.* for a sample of vanadium sesquioxide [33].

Using the same theoretical approach based on the GA, we investigate the properties of an interface between strongly correlated metals with different bulk Hubbard parameters and between a metal and a Mott insulator [35]. We also address the behavior of quasi-particles crossing a metal-Mott insulator-metal junction. Our results are compared to simulations on similar interface and junction geometries performed with different theoretical tools, such as linearized-DMFT [36] and DMFT+NRG [37], in the light of which we discuss the possibility of quasi-particle tunneling across Mott insulating barriers.

While the first part of this thesis exploits a lattice model as a laboratory for reproducing the physics of strongly correlated materials, the second part is devoted to the discussion of a Gutzwiller-improved Density Functional Theory (DFT), and of its performance in the realistic description of the relevant physical properties of transition metals.

The Gutzwiller Density Functional: definition, implementation and a case study

A Gutzwiller density functional can be defined as an extension of the Local Density Approximation plus Hubbard-U (LDA+U) functional where the Hubbard energy and the kinetic energies are computed as the expectation value of Hubbard and kinetic

operator on a Gutzwiller projected Slater determinant. The expectation value can be computed analytically through a recent multi-band formulation of the GA [38]. This recipe gives more flexibility to the total energy minimization, providing the possibility of renormalizing the mass of the auxiliary Kohn-Sham particles, and therefore improving the results of conventional Local Density Approximation (LDA).

Within the Gutzwiller approach, the interaction Hamiltonian of LDA+U can be generalized to an interaction operator enforcing Hund's rules at the atomic level. The expectation values of all local many-body operators, such as the total spin and angular momentum, are accessible via the parameters of the GVW, and provide a new tool for discussing magnetic moment formation also in unpolarized calculations.

We choose to implement our version of Gutzwiller Density Functional (GDF) code by combining the Siesta electronic structure code [39], which we exploit to optimize total energy with respect to the Slater determinant, with a Levenberg-Marquardt algorithm implemented from scratch and used to optimize the GDF with respect to Gutzwiller parameters. The exchange-correlation potential of the GDF calculation is computed as a straightforward extension of LDA, so that we refer to our functional method as Local Density Approximation plus Gutzwiller Method (LDA+G).

We test the performance of LDA+G to compute the electronic structure of body-centered cubic iron, a system that can be described successfully even by calculations with a more standard density functional such as the Generalized Gradient Approximation (GGA), whose outcome can be compared with our data. The crystal field of bcc Iron splits the d-type orbitals into two different multiplets, doubly degenerate and triply degenerate at the Γ point respectively, corresponding to the e_g and t_{2g} irreducible representations of the cubic group.

In agreement with previous theoretical works [40–42], a recent Local Density Approximation plus Dynamical Mean-Field Theory (LDA+DMFT) study of paramagnetic Iron by Anisimov and coworkers [43] suggested that this metal may display an orbital selective localization of only the e_g multiplet, with the t_{2g} electrons remaining itinerant. This picture appears favorable to the development of double-exchange driven magnetism [44], a typically many-body phenomenon where the spin-polarization is accompanied by a gain of kinetic energy.

This kinetic gain distinguishes double exchange from Stoner magnetism [45], where the energy gain due to the emergence of magnetism is mainly of potential origin. Though our data for the band mass renormalization of e_g electrons does not show evidence for an orbital-selective full localization, a careful check of energy differences between polarized and unpolarized density functional calculations gives a hint that correlation effects may have a non-negligible role in the magnetism of Iron. While the GGA and LDA kinetic and electrostatic energy differences point to the prevalence of

Stoner magnetism, the LDA+G calculations suggest that a great fraction of it may be due to double-exchange.

When compared to simple LDA calculations, the LDA+G functional shows an improvement similar to the GGA functional in predicting a larger lattice parameter for both paramagnetic and ferromagnetic Iron, and a larger total magnetization and greater energy separation between up and down spin bands in the spin polarized phase.

On top of this, the possibility of accessing local magnetic moments already in the unpolarized phase makes the LDA+G functional able to distinguish between the enhancement of magnetic moment due to many-body localization, and the enhancement which is due to magnetic ordering, uncovered only in spin-polarized calculations. The fact that most of the local moment of ferromagnetic Iron is already present in its paramagnetic phase is another clue of the role of double-exchange, which predicts magnetic ordering to emerge from the alignment of large local moments increased by many-body localization.

Plan of the thesis

The plan of this thesis is as follows. Chapt. 1 is devoted to the explanation of the main theoretical tool of our work, namely the GVM and GA. After introducing their earliest formulation by Martin C. Gutzwiller, we discuss their effectiveness in describing the physics of strongly correlated conductors, emphasizing the improvements they bring in comparison with mean-field, independent-electron approximations such as HF, and their limitations with respect to more refined, though computationally more costly, methods like DMFT and VQMC.

We mention how the GA was initially exploited as an approximate tool for analytical calculation of expectation values on the GVW, and how later studies proved its exactness in the limit of infinite lattice coordination. After that, we discuss its more recent multi-band formulation which, together with the mixed-basis parametrization of Gutzwiller parameter matrix, is particularly important for combining the GVM with DFT.

In Chapt. 2 we present our results for the strongly correlated Hubbard lattice with broken translational invariance due to the presence of a surface (panel (a) in Fig. 1), a metal-metal or metal-insulator junction (panel (b)), or a "sandwich" of Mott insulator or strongly correlated metal between metallic leads (panel (c)). For all geometries, we show the layer dependence of the quasi-particle weight and provide approximate analytical fits for the data, together with a comparison with DMFT calculations on similar systems.
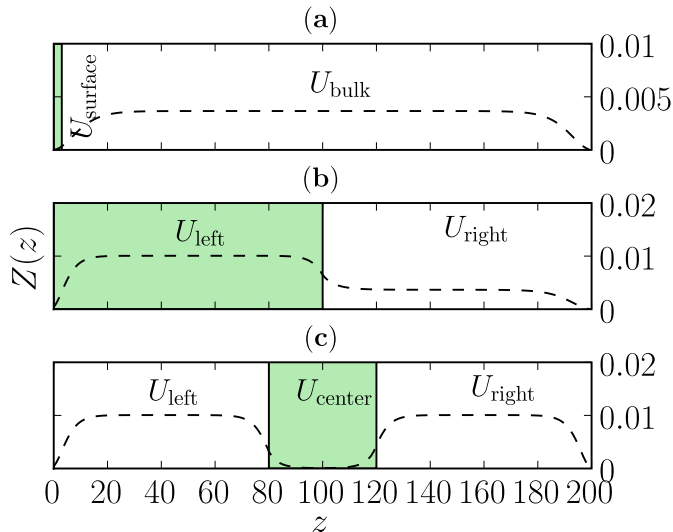
Figure 1: *The three types of layered geometry for the HM that we solved within GVM and GA in Chapt. 2.*

In Chapt. 3, we introduce the formalism of DFT, the Kohn-Sham self-consistent equations for the functional minimization and the LDA for exchange and correlation functionals. We further discuss the performance and limitations of LDA and present the LDA+U method as a way to correct the self-interaction error of LDA.

We explain the details of the GDF in Chapt. 4, and underline its similarities and differences with respect to the LDA+U functional. In the same chapter we present our data for paramagnetic and ferromagnetic bcc iron obtained through our implementation of LDA+G in the Siesta code. We show energy differences between spin-polarized and unpolarized Iron computed within LDA, GGA and LDA+G and with different basis sets. We compare the band structure, lattice parameters and magnetic moments (some sample data is shown in Table 1) obtained with these functionals, and discuss the implications of our results on the understanding of the origin of magnetism in transition metals.

In the appendices we list some important results that we believed too detailed or too marginal to be presented in the main body of the thesis. Appendix A is devoted to some proofs and detailed explanations related to the GVM. In Appendix B we include all details related to the calculations on the layered geometries of Chapt. 2.

In Appendix C we explain how to implement spin and orbital symmetries in the parametrization of the Gutzwiller projector, while in Appendix D we give the details of the minimization algorithm we implemented for optimizing the variational energy of the LDA+G calculation with respect to Gutzwiller parameters. Finally, Appendix E

	m	$2|S|$
LDA para		1.77
GGA para		
LDA ferro	2.02	2.96
GGA ferro	2.33	
LDA para(s)		1.77
LDA ferro(s)	2.066	2.61
LDA+G para		2.10
LDA+G ferro	2.35	2.90
LDA+G para(s)		2.47
LDA+G ferro(s)	2.44	3.04

Table 1: *Magnetic moment and magnetization of paramagnetic and ferromagnetic iron, in units of Bohr magnetons. The results were computed within single-ζ (label (s)) and double-ζ Siesta basis sets, and with LDA, GGA and LDA+G density functionals.*

contains various topics of DFT and LDA+U that are important for the understanding of the GDF we implemented and discussed in Chapt. 4.

Chapter 1

The Gutzwiller Variational Method

In this chapter we introduce the main theoretical tools exploited in our thesis, which are the Gutzwiller Variational Method (GVM) and the Gutzwiller Approximation (GA). Their aim is to improve a description of physical systems where each particle is treated independently from the others (as it happens for example in Hartree-Fock (HF) method), by accounting for the effects of local correlations between particles.

After discussing the limits of the independent-particle approaches, we introduce the GVM for fermions as initially formulated by Gutzwiller, and discuss its results for the single-band Hubbard model (HM) for different lattice dimensionalities. We explain its advantages and limitations in describing metal-insulator transitions due to interactions, and we compare its performance with that of Variational Quantum Monte Carlo (VQMC) methods using more sophisticated variational wavefunctions and of Dynamical Mean-Field Theory (DMFT). We end this chapter by expounding the recent multi-band formulation of Gutzwiller method, whose formalism is at the basis of all the results of this thesis.

1.1 Ground-state calculations in the independent- electron approximation

The many-fermion problem in solid state systems is as difficult in its solution as it is simple in its formulation. According to the Rayleigh-Ritz variational principle, finding the ground-state of a system of fermions consists of minimizing the expectation value of the Hamiltonian

$$E_{\rm GS} = \min_{\Psi}\langle\Psi|\hat{H}|\Psi\rangle = \langle\Psi_{\rm GS}|\hat{H}|\Psi_{\rm GS}\rangle \tag{1.1}$$

over all possible many-electron wavefunctions $|\Psi\rangle$ which are antisymmetric for particle exchange. For a N-fermion problem

$$\langle\boldsymbol{r}_1,\sigma_1;\boldsymbol{r}_2,\sigma_2;\ldots;\boldsymbol{r}_N\sigma_N|\Psi\rangle = \Psi(\boldsymbol{r}_1,\sigma_1;\boldsymbol{r}_2,\sigma_2;\ldots;\boldsymbol{r}_N\sigma_N)$$
$$= -\Psi(\boldsymbol{r}_2,\sigma_2;\boldsymbol{r}_1,\sigma_1;\ldots;\boldsymbol{r}_N\sigma_N)\,. \tag{1.2}$$

Whenever a many-electron Hamiltonian $\hat{H}$ can be written as the sum of single-electron Hamiltonians, the problem of finding its variational ground-state is greatly simplified. We will refer from now on to a Hamiltonian with this property as a Hamiltonian of independent or, we will use this term equivalently, non-interacting electrons. Any ground-state of an independent-electron Hamiltonian can be written as a the Slater determinant (or anti-symmetrized product) of single-electron orbitals.

$$\Psi_0(\boldsymbol{r}_1,\boldsymbol{r}_2,\ldots,\boldsymbol{r}_n) = \sum_{\{j\}}(-1)^{\{j\}}\phi_1(\boldsymbol{r}_{j_1})\phi_2(\boldsymbol{r}_{j_2})\ldots\phi_n(\boldsymbol{r}_{j_n})\,, \tag{1.3}$$

where $(-1)^{\{j\}}$ is equal to plus or minus one according to the parity of permutation $\{j\}$.

When minimizing the expectation value of the Hamiltonian of a system on all the Slater determinants with fixed number of particles that can be built from M single particle orbitals ϕ_α, one deals with M^2 degrees of freedom, which is the number of independent matrix elements of a unitary transformations within the orbital space. In fact, given the creation $\hat{c}^\dagger_\alpha$ and annihilation $\hat{c}_\alpha$ operators on the chosen original set of orbitals, obeying fermionic anticommutation relations

$$\{\hat{c}^\dagger_\alpha\hat{c}_\beta\} = \mathbb{1}\delta_{\alpha\beta}\,, \tag{1.4}$$

$$\{\hat{c}_\alpha\hat{c}_\beta\} = \{\hat{c}^\dagger_\alpha\hat{c}^\dagger_\beta\} = 0\,, \tag{1.5}$$

any independent electron state of N particles can be obtained from vacuum as

$$|\Psi_0\rangle = \prod\hat{d}^\dagger_{\alpha_1}\hat{d}^\dagger_{\alpha_2}\ldots\hat{d}^\dagger_{\alpha_N}|0\rangle\,, \tag{1.6}$$

where the creation operator $\hat{d}^\dagger_{\alpha_1} = U_{\alpha_1,\beta}\hat{c}^\dagger_\beta$ is linked to the original creation operators $\hat{c}^\dagger_\beta$ through a unitary transformation $U_{\alpha\beta}$.

The most general many-body wavefunction of N electrons is however built from linear combinations of more Slater determinants of the type (1.6). We will refer to a wavefunction that cannot be built by applying a single product of creation operators to the vacuum as a "correlated" wavefunction, as opposed to the "uncorrelated" Slater determinant.

Using the full space of uncorrelated and correlated wavefunctions as variational space means minimizing the expectation value of the Hamiltonian with respect to an exponential number of parameters. Searching for the exact ground-state of a system of interacting electrons is therefore an unfeasible task already when the number of particles N and orbitals M is quite small. The HF method overcomes this problem by minimizing also the expectation value of an interacting Hamiltonian on the class of Slater determinants,

$$E_{\mathrm{HF}} = \min_{|\Psi_0\rangle} \langle \Psi_0|\hat{H}|\Psi_0\rangle \,. \tag{1.7}$$

This means that every particle is treated as independent from the others. The effect of interaction on each particle is accounted for by an effective interaction potential which depends only on the average position of all other particles. The restriction of the variational space to the class of non-interacting wavefunctions implies that one can always find a residual energy $E_{\mathrm{c}} < 0$ such that

$$E_{\mathrm{HF}} + E_{\mathrm{c}} = E_{\mathrm{exact}} \,, \tag{1.8}$$

where the exact energy E_{exact} is given formally by Eq. (1.1), and involves a minimization of the variational energy over the whole many-body Hilbert space. The energy E_{c} is called correlation energy, since it contains all effects beyond the independent electron approximation, in particular those caused by the fluctuations of the interaction potential that have been disregarded by its mean-field approximation.

From the stationary condition for the HF energy we find an eigenvalue equation

$$\varepsilon_\eta \phi_\eta = \frac{\partial E_{\mathrm{HF}}}{\partial \phi_\eta} \,, \tag{1.9}$$

that can be solved to compute the single-particle eigenvectors ϕ_η and eigenvalues ε_η, which in the case of a crystal with discrete translational symmetry, build the single-particle energy bands $\varepsilon_{\boldsymbol{k}\alpha}$.

1.1.1 Failure of the independent-electron theory of conductivity

In an independent electron description of crystals, a material is predicted to be metallic if the density of states at the Fermi level is non vanishing ($\mathcal{D}(\varepsilon_{\mathrm{F}}) \neq 0$), while in

the case of $\mathcal{D}(\varepsilon_F) = 0$, the material is predicted to be insulating. For this definition to hold, translational invariance is crucial, since disorder effects like Anderson localization may spoil conductivity even in the case of $\mathcal{D}(\varepsilon_F) \neq 0$. In a system with translational invariance as a crystal, the density of states can be computed from a band calculation with the formula

$$\mathcal{D}(E) = \frac{1}{N_{\boldsymbol{k}}} \sum_{\alpha,\boldsymbol{k}} \delta(\varepsilon_{\alpha\boldsymbol{k}} - E) , \qquad (1.10)$$

where $N_{\boldsymbol{k}}$ is the number of $\boldsymbol{k}$-points in the first Brillouin Zone. From Eq. (1.10) it follows that the system is predicted to be insulating if ε_F lies between the top of the uppermost filled band and the bottom of the lowermost empty band. In which case there is usually a gap separating the two bands.

If spin symmetry is not broken, in order to have an insulating material, it is therefore necessary to have an even number of electrons per unit cell, because a full band can accomodate as many electrons with spin up as electrons with spin down. This condition is necessary, but not sufficient, since another requirement is that there is no energy overlap between valence and conduction bands.

While the insulating behavior of some materials can be accounted for without even including the effect of electron-electron interactions on their band structure, others are such that a nonzero $\mathcal{D}(\varepsilon_F)$ is found at the non-interacting level, but the band renormalization caused by the HF mean-field potential is sufficient to open a gap. When the material has an odd number of electrons per unit cell, the opening of a gap in the single-particle spectrum is possible only through the breaking of some spin symmetry or translational symmetry, which can lift the degeneracy of some bands and enable them to separate in energy.

The limits of the HF method become evident when we try to explain materials whose insulating phase is not accompanied by any spin or translational symmetry breaking, and where therefore the conductivity is suppressed as a result of the sole electronic correlations. One of the oldest-known compounds exhibiting such a puzzling insulating phase is Cobalt Oxide (CoO) [46]. Its zero temperature ground-state is antiferromagnetic, but at sufficiently high temperature the antiferromagnetic order sustaining its magnetic supercell vanishes, so that the chemical unit cell contains an odd number of electrons. The independent electron theory would therefore predict this system to be conducting. However, in reality this is not the case, and the disappearance of the magnetic order as temperature raises is not accompanied by any transition from insulator to metal.

1.2   The Gutzwiller projector

The Gutzwiller method is based, in its most general formulation, on a wavefunction $|\Psi_{\mathrm{G}}\rangle$ that can be obtained from a wavefunction of non-interacting particles by the application of independent local projectors acting on separate lattice sites $\boldsymbol{R}$. For our purposes this independent-particle wavefunction will always be a Slater determinant $|\Psi_0\rangle$ of single-electron orbitals, though in Sect. 1.5 we show how the Gutzwiller projector can be also applied to a Bardeen-Cooper-Schrieffer (BCS) wavefunction. The expression for Ψ_{G} is

$$\Psi_{\mathrm{G}} = \hat{\mathcal{P}}|\Psi_0\rangle = \prod_{\boldsymbol{R}} \hat{\mathcal{P}}_{\boldsymbol{R}}|\Psi_0\rangle \,. \tag{1.11}$$

While the Slater determinant must be constructed from the single-particle eigenfunctions of an independent electron calculation such as HF, which can be linear combinations of either plane waves or local orbitals like Gaussians or Wannier functions, the local projectors are defined on the basis of many-body configurations on a single lattice site.

Once a local single-particle basis set has been defined, with N_l local spin-orbitals, $\hat{\mathcal{P}}_R$ will be a $M \times M$ hermitian matrix, with $M = 2^{N_l}$ being the size of the local many-body space built of electronic configurations on the local single-particle basis.

Martin C. Gutzwiller introduced this method in 1963 [24] with the aim of better describing correlations between electrons of opposite spin in transition metals. As a minimal realization of the conduction band of a transition metal he considered an effective tight-binding model with one Wannier function per lattice site, with hopping strength t between nearest-neighbors ($\langle \boldsymbol{R}, \boldsymbol{R}'\rangle$), and with an on-site repulsion of strength U to mimic the short-range nature of the Coulomb interaction on d-type bands

$$\hat{H}_{\mathrm{HM}} = -t \sum_{\langle \boldsymbol{R}, \boldsymbol{R}'\rangle\sigma} \hat{c}^{\dagger}_{\sigma\boldsymbol{R}}\hat{c}_{\sigma\boldsymbol{R}'} + U \sum_{\boldsymbol{R}} \hat{n}_{\uparrow\boldsymbol{R}}\hat{n}_{\downarrow\boldsymbol{R}} \,. \tag{1.12}$$

His next suggestion was to consider, on every lattice site of the crystal, a local projector of the type:

$$\hat{\mathcal{P}}_{\boldsymbol{R}}(\eta) = \hat{\mathbb{1}} - (1 - \eta)\,\hat{n}_{\uparrow\boldsymbol{R}}\hat{n}_{\downarrow\boldsymbol{R}} \,, \tag{1.13}$$

where $\hat{n}_{\uparrow\boldsymbol{R}}\hat{n}_{\downarrow\boldsymbol{R}}$ is the double occupation operator of either electrons or holes at lattice site $\boldsymbol{R}$. Written in the subspace of many-body configurations on the site, the projector

becomes the following matrix[1]:

$$
\begin{array}{c}
| \, 0 \, \rangle \\
| \uparrow \rangle \\
| \downarrow \rangle \\
| \uparrow \downarrow \rangle
\end{array}
\begin{pmatrix}
1 & 0 & 0 & 0 \\
0 & 1 & 0 & 0 \\
0 & 0 & 1 & 0 \\
0 & 0 & 0 & \eta
\end{pmatrix},
\tag{1.14}
$$

which shows that the parameter η is tuning the probability that two electrons of opposite spins are dwelling on the same site. For every system where the short-range effects of the Coulomb repulsion are dominant, this parameter is crucial for the minimization of the energy.

The action of the projector can be seen, from another point of view, as a suppression of Hamiltonian matrix elements between Slater determinants which have a finite fraction of doubly occupied sites. In the limit of infinite U, one expects these matrix elements to give no contribution to the ground-state energy of the system.

The simple model showed in Eq. (1.12), known as the Hubbard model [14] is to the problem of electron correlations as the Ising model is to the problem of spin-spin interactions: it is the simplest possible model displaying many "real world" features. It is, however, much more difficult to analyze qualitatively than the Ising model. While its one-dimensional realization has been exactly solved by Bethe ansatz [47], the ground-states of its two-dimensional and three-dimensional realizations can only be approximated variationally.

The Gutzwiller variational wavefunction (GVW) with Gutzwiller parameter matrix defined as in Eq. (1.13) and with as Slater determinant $|\Psi_0\rangle$ the Fermi sea of non-interacting electrons ($U = 0$) was considered to be a sensible ansatz for variational calculations beyond HF in the HM. It has indeed the quality of providing not only an exact solution for $U = 0$ – when also the HF method is exact – but also for $U = +\infty$, where an independent-particle approach fails. In spite of the simplicity of these two solutions, obtained for $\eta = 1$ and $\eta = 0$ respectively, there is no general way of computing the expectation value $\langle \Psi_\mathrm{G} | \hat{H}_\mathrm{HM} | \Psi_\mathrm{G} \rangle$ analytically for general $0 < \eta < 1$ without approximations. In the next section we will present the most popular one, whose more recent multi-band formulation will be exploited throughout this thesis.

---

[1]The term "projector" is used improperly, since $\hat{\mathcal{P}}_{\boldsymbol{R}}^2$ is in general different than $\hat{\mathcal{P}}_{\boldsymbol{R}}$ when $\eta > 0$. In accord with the literature, we will continue using this term throughout the thesis, remembering that it should not be taken literally and that $\hat{\mathcal{P}}_{\boldsymbol{R}}$ can be chosen as a general hermitian matrix.

1.3   The Gutzwiller approximation

Immediately after the introduction of his variational wavefunction [25, 26], Martin C. Gutzwiller provided an approximate analytical expression for the expectation value of the Hubbard Hamiltonian on the projected Fermi sea, with projector defined in Eq. (1.13). His result can be found by counting the number of many-body configurations with N_{D} doubly occupied sites out of L sites, given the total number of particles N, and the number of spin up $N_\uparrow$ and spin down $N_\downarrow$ electrons on the lattice. The analytical value for the energy follows from supposing the many-body configurations at different lattice sites to be independent from one another.

For a translationally invariant HM with spin rotational symmetry and at half-filling ($N_\downarrow = N_\uparrow = L/2$), one finds that the expectation value of the double occupation operator in the limit $L \to \infty$ has the simple expression

$$\langle \Psi_{\mathrm{G}} | \hat{n}_{\uparrow \boldsymbol{R}} \hat{n}_{\downarrow \boldsymbol{R}} | \Psi_{\mathrm{G}} \rangle = D(\eta) = \frac{\eta}{2(1+\eta)} \,, \tag{1.15}$$

while the expectation value of a hopping operator $\hat{c}_{\sigma \boldsymbol{R}}^\dagger \hat{c}_{\sigma \boldsymbol{R}'}$ (with $\boldsymbol{R} \neq \boldsymbol{R}'$), on the GVW is renormalized with respect to its value computed on the Fermi by a factor $Z(\eta)$ independent of $\boldsymbol{R}$ and $\boldsymbol{R}'$, so that

$$\langle \Psi_{\mathrm{G}} | \hat{c}_{\sigma \boldsymbol{R}}^\dagger \hat{c}_{\sigma \boldsymbol{R}'} | \Psi_{\mathrm{G}} \rangle = Z(\eta) \langle \Psi_0 | \hat{c}_{\sigma \boldsymbol{R}}^\dagger \hat{c}_{\sigma \boldsymbol{R}'} | \Psi_0 \rangle \,, \tag{1.16}$$

with

$$Z(\eta) = \frac{4\eta}{(1+\eta)^2} \,. \tag{1.17}$$

The energy per site of the HM computed within the GA reads therefore

$$\frac{1}{L} \langle \Psi_{\mathrm{G}} | \hat{H}_{\mathrm{HM}} | \Psi_{\mathrm{G}} \rangle \approx \varepsilon_{\mathrm{GA}}(\eta) = 2Z(\eta) \epsilon_{\mathrm{kin}} + U D(\eta) \,, \tag{1.18}$$

where ϵ_{kin} is the average kinetic energy per particle per spin of the unprojected wavefunction

$$\epsilon_{\mathrm{kin}} = -\frac{t}{2L} \langle \Psi_0 | \sum_{\{\boldsymbol{R},\boldsymbol{R}'\}\sigma} \hat{c}_{\sigma \boldsymbol{R}}^\dagger \hat{c}_{\sigma \boldsymbol{R}'} | \Psi_0 \rangle \,. \tag{1.19}$$

In Appendix A.1 we report, for this special case of the Half-filled paramagnetic HM, a "thermodynamic argument" which is equivalent to the counting argument explained by Gutzwiller and reframed by Vollhardt [26, 48], and through which we can retrieve equations from (1.15) to (1.18).

In a Landau Fermi liquid picture, $Z(\eta)$ equals both the effective mass renormalization m/m^* of the Landau quasi-particle [49] and the discontinuity at the Fermi surface of the quasi-particle occupation number (see Appendix A.2). A HF approach to the HM is not able to directly access these two quantities, which can be recovered only through a linear response calculation of correlation energy starting from the HF ground-state [50]. Results similar to Eq. (1.15), (1.17) and (1.18) can be found away from half-filling, and will be presented after the multi-band generalization of GA, discussed in section 1.6.

1.3.1 The Brinkman Rice transition

We have already mentioned how the GVW provides the exact ground-state of the HM in the limit $U \to \infty$. In the case of half-filling, the correct value of the variational parameter is $\eta = 0$, so that the double occupation probability of the infinite-U system is completely suppressed. The GA result for the mass renormalization parameter à la Landau $Z(\eta)$ and for the double occupation $D(\eta)$ consistently predicts these two quantities to vanish in the infinite-U HM, describing a system with infinite quasi-particle mass and therefore fully localized electrons.

Brinkman and Rice [51] discussed how the GA predicts, for the half-filled HM, a phase with $Z(\eta) = 0$ – and therefore infinite quasi-particle mass – already for a finite value of U. We can see this by noticing that the value of η which minimizes $\varepsilon_{\mathrm{GA}}(\eta)$ is

$$
\bar{\eta} = \begin{cases} \dfrac{1 - U/U_{\mathrm{c}}}{1 + U/U_{\mathrm{c}}} \,, & U < U_{\mathrm{c}} \\ 0 \,, & U \geq U_{\mathrm{c}} \end{cases}
\tag{1.20}
$$

where $U_{\mathrm{c}} = 16|\epsilon_{\mathrm{kin}}|$. An expression in terms of U and U_{c} can be found also for the double occupation probability and the hopping renormalization, both becoming zero for $U = U_{\mathrm{c}}$

$$
D(U) = \begin{cases} \dfrac{1}{4}\left(1 - \dfrac{U}{U_{\mathrm{c}}}\right) \,, & U < U_{\mathrm{c}} \\ 0 \,, & U \geq U_{\mathrm{c}} \end{cases} \,,
\tag{1.21}
$$

$$
Z(U) = \begin{cases} 1 - \left(\dfrac{U}{U_{\mathrm{c}}}\right)^2 \,, & U < U_{\mathrm{c}} \\ 0 \,, & U \geq U_{\mathrm{c}} \end{cases} \,.
\tag{1.22}
$$

By looking at Eq. (1.18), we can find the GA prediction for the total energy of the Hubbard model

$$
\bar{\varepsilon}_{\mathrm{GA}}(U) = -2|\epsilon_{\mathrm{kin}}|\left(1 - \dfrac{U}{U_{\mathrm{c}}}\right)^2 \theta(U - U_{\mathrm{c}}) \,,
\tag{1.23}
$$

which also becomes identically zero for $U > U_c$.

The reason for the vanishing $Z(U)$ as U approaches U_c depends on the fact that the complete suppression of doubly occupied configurations prevents any hopping of particles between sites. The vanishing hopping matrix element is the symptom of a transition to an insulating phase where every electron is localized on a single site.

For $U \approx U_c$, and $U < U_c$, the GA describes therefore a metal-insulator transition, which was named Brinkman-Rice transition after its discoverers. As an order parameter for the metallic side of the transition one can choose either η or the double occupation probability. In both cases the transition is of second order, with a discontinuous second derivative of the energy with respect to the order parameter.

It can be shown that the Brinkman-Rice transition is also accompanied by the disappearance of the jump $\mathcal{Z}$ in the quasi-particle distribution function at $|\boldsymbol{k}| = k_F$, an event that normally signals the transition from a Fermi liquid to a non Fermi liquid state. The HF method does not allow any renormalization of the quasi-particle distribution, which remains always equal to the Fermi-Dirac distribution, and, as we mentioned in Sect. 1.1.1, it cannot account for any metal-insulator transition in a system with an odd number of electrons per unit cell unless it is accompanied by the breaking of spin or translational symmetry that enables the opening of a gap. The Brinkman-Rice transition does not lead to any broken symmetry state, and can be considered therefore the simplest example of critical phenomenon beyond the reach of independent-particle approaches.

1.3.2 Correlation energy and magnetic susceptibility within the Gutzwiller Approximation

Remaining on the metallic side of the Brinkman-Rice transition, where a non-trivial expression for the energy is at hand, we can compute the correlation energy per site included within GA from Eq. (1.8), setting $E_{\text{exact}}/L \approx \varepsilon_{\text{GA}}$ and inserting the HF energy of the paramagnetic Half-filled Hubbard model

$$E_{\text{HF}}/L = 2\epsilon_{\text{kin}} + \frac{U}{4} \,, \tag{1.24}$$

and we find the result

$$E_c/L = -\frac{U^2}{128|\epsilon_{\text{kin}}|} \,, \tag{1.25}$$

which is an approximate expression for the interaction energy of the HM up to second-order in U.

It is now worth mentioning the main point that makes the Brinkman-Rice correlated metal interesting beyond its description of the paramagnetic HM. One effect

of the vanishing double occupation probability in the GVW is the enhancement of spin fluctuations. This can be seen by looking at the variance σ_M of the local spin magnetization σ_M, which equals

$$
\begin{aligned}
\sigma_M &= \langle \Psi_{\mathrm{G}} | (\hat{M}_{z,j})^2 | \Psi_{\mathrm{G}} \rangle - \langle \Psi_{\mathrm{G}} | \hat{M}_{z,j} | \Psi_{\mathrm{G}} \rangle^2 = \\
&= \langle \Psi_{\mathrm{G}} | (\hat{n}_{i\uparrow} - \hat{n}_{i\downarrow})^2 | \Psi_{\mathrm{G}} \rangle = 1 - 2D = \frac{1}{2} \left(1 + \frac{U}{U_{\mathrm{c}}} \right) .
\end{aligned} \tag{1.26}
$$

Contrary to the HF result, where it is always equal to $1/2$, the GA result for σ_M increases linearly with U for $U < U_{\mathrm{c}}$. This suggests that correlations have a non trivial effect on the response of the system to spin perturbations.

When Brinkman and Rice computed the inverse spin susceptibility of the metallic phase within GA, they found the following expression

$$
\frac{1}{\chi_{\mathrm{s}}} = \frac{1 - (U/U_{\mathrm{c}})^2}{\mathcal{D}_0(\varepsilon_{\mathrm{F}})} \left\{ 1 - \mathcal{D}_0(\varepsilon_{\mathrm{F}}) U \left[\frac{1 + U/(2U_{\mathrm{c}})}{(1 + U/U_{\mathrm{c}})^2} \right] \right\} , \tag{1.27}
$$

where $\mathcal{D}_0(\varepsilon_{\mathrm{F}})$ is the density of states at the Fermi energy of the uncorrelated Fermi sea. Eq. (1.27) shows that the spin susceptibility of the system is enhanced by a factor $1/Z = m^*/m$. This implies that, since the density of states $\mathcal{D}(\varepsilon_{\mathrm{F}})$ of the correlated system is also proportional to the mass m^*, the enhancement of both quantities does not affect their ratio

$$
\frac{\mathcal{D}(\varepsilon_{\mathrm{F}})}{\chi_{\mathrm{s}}} \approx \mathrm{const} . \tag{1.28}
$$

The Stoner theory of magnetism [45], based on the HF description of the HM, predicts a linear response susceptibility enhancement which depends on exchange rather than correlation effects, with enhancement factor

$$
\frac{1}{\chi_{\mathrm{s}}} \propto 1 - \mathcal{D}_0(\varepsilon_{\mathrm{F}}) U , \tag{1.29}
$$

and an instability towards a ferromagnetic state for $U \propto 1/\mathcal{D}_0(\varepsilon_{\mathrm{F}})$. Within the same theory [52], the linear response mass enhancement factor[2] results proportional to the logarithm of the right-hand side of Eq. (1.29), with the result that

$$
\frac{\mathcal{D}(\varepsilon_{\mathrm{F}})}{\chi_{\mathrm{s}}} \to 0 , \tag{1.30}
$$

while the paramagnet to ferromagnet transition is approached.

---

[2]Since the Stoner theory is a linear response theory, its prediction for the mass enhancement can be computed from Random Phase Approximation [50].

$$|\epsilon_{\text{kin}}| = \begin{cases} \frac{2t}{\pi} & ,1D \\ \frac{8t}{\pi^2} & ,2D \\ t & ,3D \end{cases} ; \qquad U_{\text{c}} \approx \begin{cases} 10.20t & ,1D \\ 12.96t & ,2D \\ 16t & ,3D \end{cases} .$$

Table 1.1: *Values of average hopping energy per site per spin, and critical U for half-filled cubic lattices in 1, 2 and 3 dimensions.*

The result of Eq. (1.28) derived by Brinkman and Rice is in agreement with the measurements of the spin susceptibility and thermodynamic density of states [53] of vanadium sesquioxide (V_2O_3), which predict a comparable enhancement of the two quantities.

In spite of its simplicity, the theory of Brinkman and Rice ruled out the Stoner paramagnetic instability as an explanation for the susceptibility enhancement, and suggested that correlations should be given a major role in describing both the magnetic and transport properties of the metallic phase of a class of transition-metal oxides in the vicinity of the metal-insulator transition.

1.3.3 The Gutzwiller Approximation and the limit of infinite lattice coordination

The nature of the GA is such that the Brinkman Rice metal-insulator transition is found for every type of lattice, regardless of the dimensionality. Only the value of U_{c} changes, as a result of the changing of ϵ_{kin} with lattice geometry and dimensionality (see Table 1.1). This independence of the Brinkman-Rice transition on lattice and dimensionality features must be due to the neglect of the correlation between many-body configurations at different lattice sites. Such correlation is partly built in the GVW, but is completely discarded in the counting argument of Gutzwiller.

Metzner and Vollhardt devised an η expansion of expectation values of local and hopping operators on the GVW, with which they could access the exact value of the Gutzwiller variational energy (GVE), beyond the GA. The expansion for the energy of the one dimensional HM can be summed up analytically [54], and its minimization with respect to η provides the following large-U results for $D(U)$ and the jump in the
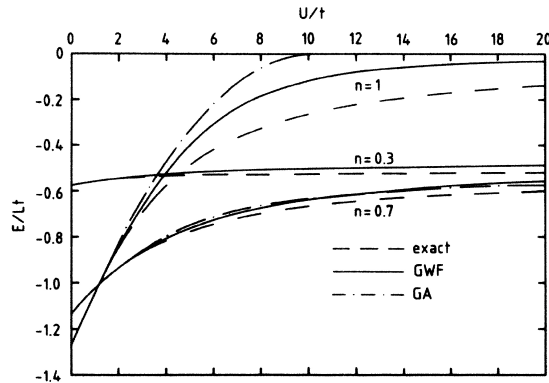
Figure 1.1: *Ground-state energy per particle of the one-dimensional HM, computed with GVM and GA, and Bethe-ansatz [47] for different values of filling n. From reference [55].* .

quasi-particle distribution $\mathcal{Z}(U)$

$$D(U) \approx \frac{4|\epsilon_{\text{kin}}|^2}{U^2} \left[\ln\left(\frac{U}{2|\epsilon_{\text{kin}}|}\right)\right]^{-1} , \tag{1.31}$$

$$\mathcal{Z}(U) \approx 8\frac{|\epsilon_{\text{kin}}|}{U} \left[\ln\left(\frac{U}{2|\epsilon_{\text{kin}}|}\right)\right]^{-1} , \tag{1.32}$$

and for the energy per particle

$$\varepsilon_{\text{Gw}}^{(\text{d}=1)}(U) = \frac{\langle\Psi_{\text{G}}|\hat{H}|\Psi_{\text{G}}\rangle}{L} \approx -\left(\frac{4}{\pi}\right)^2 \frac{t^2}{U} \left[\ln\left(\frac{U}{2|\epsilon_{\text{kin}}|}\right)\right] . \tag{1.33}$$

The above equations show that, while the variational energy remains finite for arbitrary U, $\mathcal{Z}(U)$ does not vanish for any finite U, as a Mott transition would require. This proves that the GVW is not able to describe a metal-insulator transition in one dimension. By means of the same η expansion for the energy of a cubic lattice of dimensionality d, the same conclusion was drawn for any $d < \infty$.

The Brinkman Rice transition for the half-filled lattice is recovered in the infinite-dimensional limit, where the η expansion of the GVE leads to the results of the GA with an appropriate scaling of hopping coefficient t [56]. The result of Metzner and Vollhardt [55] proves that the GA is an exact way of computing expectation values on the GVW for lattices of infinite coordination, or, an equivalent statement when dealing with hyper-cubic lattices, for lattices of infinite dimensionality.

For every finite lattice coordination, the GA grossly fails to approximate the GVE for $U > U_{\text{c}}$ in the half-filled HM, where it wrongly predicts a zero-energy phase. This is shown in Fig. 1.1 in the case of one dimension. In the same figure we can see how

for fillings $n \neq 0.5$ and for half filling when $U \ll U_c$ the GA provides reasonable approximations to the GVE. The agreement between the exact GVE and the GA result increases very rapidly with increasing lattice dimensionality, and while being perfect for $d = \infty$, it is already very good for $d = 3$ [56]. For general d, half filling and $U < U_c$, we can give a reasonable upper bound for the U below which the GA performs well, by requiring

$$\varepsilon_{\text{GA}}(U) \lesssim \varepsilon_{\text{Gw}}^{(d)}(U_c) \, , \qquad (1.34)$$

where $\varepsilon_{\text{Gw}}^{(d)}(U_c)$ is the exact GVE for dimensionality d.

The mismatch between the result of GA and the exact calculations with GVW in finite dimensionality can be traced back to the fact that the GA is unable to account for any off-site renormalization of the exchange hole (the charge depletion around a particle due to the Pauli principle) caused by interactions, since it treats only local correlations beyond mean-field. The range of the exchange hole can be shown to decrease with increasing dimensionality, and to become strictly on-site for $d = \infty$, which is the reason why in this limit the GA result for the GVE becomes exact.

It is important to stress that the optimized GVW is far from being the exact ground-state for the system under consideration. The GVE provides only an approximation to the exact ground-state energy of the HM, both in the case of finite and infinite dimensionality.

In the case of infinite dimensionality we have seen how the description of the Mott insulating phase of the half-filled HM provided by the GA (which in this case gives exactly the GVE) is trivial. In Sect. 1.3.4 we will show that the GA picture can be improved by DMFT, which provides the exact properties of the many-body insulating state in infinite-coordination lattices.

When it comes to finite coordination lattices, an improvement over the GVW can be obtained with more complex variational wavefunctions, optimized through VQMC. In Sect. 1.4 we show how extending the GVW to account for long-range correlations enables to recover a non-trivial paramagnetic metal-insulator transition also for lattices of finite coordination.

1.3.4 The Gutzwiller Approximation from the spectral point of view

To understand better the reason for the inability of the GA to describe the Mott-insulating phase of the paramagnetic HM, it is useful to look at the way it describes the spectral function of an interacting system. The results presented in this section are valid for an electron liquid with translational and rotational invariance. It is however straightforward to extend them to a crystalline system by considering $\boldsymbol{k}$ as the quasi-momentum label inside the first Brillouin zone, and by meaning with

$|\boldsymbol{k}| = k_{\mathrm{F}}$ the fact that $\boldsymbol{k}$ is a vector of the (not necessarily spherical) Fermi surface. It is known that the spectral function of a system of non-interacting particles with translational invariance is a simple delta-function

$$A_0(\boldsymbol{k}, \hbar\omega) = \delta[\omega - \varepsilon_{\boldsymbol{k}}/\hbar] \tag{1.35}$$

where $\varepsilon_{\boldsymbol{k}}$ is the non-interacting single-particle energy.

If interactions are switched on to their physical value adiabatically, so that $\boldsymbol{k}$ can be still used as approximate quantum number, the spectral function of the interacting system can be written in terms of the retarded self-energy $\Sigma(\boldsymbol{k}, \hbar\omega)$ as

$$A(\boldsymbol{k}, \hbar\omega) = -\frac{\hbar}{\pi} \frac{\Im m \Sigma(\boldsymbol{k}, \hbar\omega)}{[\hbar\omega - \varepsilon_{\boldsymbol{k}} - \Re e \Sigma(\boldsymbol{k}, \hbar\omega)] + [\Im m \Sigma(\boldsymbol{k}, \hbar\omega)]^2} . \tag{1.36}$$

In spite of the fact that for most systems of interest the exact expression for $\Sigma(\boldsymbol{k}, \hbar\omega)$ is unknown, any approximation to the spectral function Eq. (1.36) has to be bound to fulfill the sum-rule

$$\int A(\boldsymbol{k}, \hbar\omega) \, d\omega = 1 . \tag{1.37}$$

The spectral function $A(\boldsymbol{k}, \hbar\omega)$ is the probability distribution of a momentum eigenstate in the frequency space. When the interactions are absent, every eigenstate of momentum is also an eigenstate of the Hamiltonian, and its spectral weight is concentrated at a frequency $\omega = \varepsilon_{\boldsymbol{k}}$. When the system is interacting, the above spectral weight is transferred to a variety of coherent and incoherent modes, and spread over a wide range of frequencies.

The definition of normal Fermi liquid is that there exists a Fermi surface in $\boldsymbol{k}$ space such that the probability distribution in frequency of momentum states with wavevector on this surface is a sharp peak even in the presence of interactions. Close to this surface, the width of the peak should be much smaller than the distance between the peak frequency and the chemical potential. This is equivalent to require that

$$|\Im m \Sigma(|\boldsymbol{k}| \approx k_{\mathrm{F}}, \tilde{\varepsilon}_{\boldsymbol{k}})| \ll \tilde{\varepsilon}_{\boldsymbol{k}} - \mu , \tag{1.38}$$

where $\tilde{\varepsilon}_{\boldsymbol{k}} = \varepsilon_{\boldsymbol{k}} + \Re e \Sigma(\boldsymbol{k}, \varepsilon_{\boldsymbol{k}})$ is the quasi-particle energy renormalized by interactions.

In other words, the excitations of a Landau Fermi liquid in the vicinity of the Fermi surface are long-lived coherent excitations. Long-lived because they have a very small frequency spread, and coherent because their peak corresponds to a mode with definite $\boldsymbol{k}$. We can approximate the spectral weight due to the quasi-particle with a Lorentzian distribution

$$A_{\mathrm{qp}}(\boldsymbol{k}, \hbar\omega) \approx \frac{\mathcal{Z}_{\boldsymbol{k}}}{\pi} \frac{1/(2\tau_{\boldsymbol{k}})}{(\omega - \tilde{\varepsilon}_{\boldsymbol{k}}/\hbar)^2 + [1/(2\tau_{\boldsymbol{k}})]^2} , \tag{1.39}$$

with a peak of strength $\mathcal{Z}_{\boldsymbol{k}}$ (that we call quasi-particle weight) and finite lifetime (diverging for $|\boldsymbol{k}| \to k_{\mathrm{F}}$) $\tau_{\boldsymbol{k}}$ depending on the self-energy through

$$\frac{\hbar}{2\tau_{\boldsymbol{k}}} = \mathcal{Z}_{\boldsymbol{k}} |\Im m \Sigma(\boldsymbol{k}, \tilde{\varepsilon}_{\boldsymbol{k}})| \tag{1.40}$$

$$\mathcal{Z}_{\boldsymbol{k}} = \left(1 - \frac{1}{\hbar} \frac{\partial}{\partial \omega} \Re e \Sigma(\boldsymbol{k}, \hbar\omega) \Big|_{\hbar\omega = \tilde{\varepsilon}_{\boldsymbol{k}}} \right) . \tag{1.41}$$

Eq. (1.38) tells us that the approximation Eq. (1.39) is valid only for a small range of frequencies ω close to the chemical potential. The value of $\mathcal{Z}_{\boldsymbol{k}}$ for an interacting system is lower than 1, since the sum-rule (1.37) is fulfilled also thanks to the contribution of all incoherent structureless modes that arise due to interactions, and that we can include in a function $A_{\mathrm{incoh}}(\boldsymbol{k}, \hbar\omega)$, so that the following decomposition holds for the spectral function

$$A(\boldsymbol{k}, \hbar\omega) = A_{\mathrm{qp}}(\boldsymbol{k}, \hbar\omega) + A_{\mathrm{incoh}}(\boldsymbol{k}, \hbar\omega) . \tag{1.42}$$

Within the GA, the incoherent part of the spectral function is not taken into account. The same Lorentzian peak of *Eq.* (1.39) is recovered for the quasi-particle, but with always an infinite lifetime $\tau_{\boldsymbol{k}} = +\infty$ and with a $\boldsymbol{k}$-independent strength $Z = \mathcal{Z}_{k_{\mathrm{F}}}$. The infinite quasi-particle lifetime comes from the fact that the GA makes use of a purely real self-energy, equal to

$$\Sigma_{\mathrm{GA}}(\boldsymbol{k}, \hbar\omega) = \left(\frac{Z-1}{Z} \right) \hbar\omega - \frac{U}{2Z} . \tag{1.43}$$

The GA describes successfully the Mott transition on the metallic side because it correctly portrays the suppression of the quasi-particle peak. It however fails on the insulating side since, as soon as U becomes larger than U_{c}, the quasi-particle peak disappears, and the sum-rule Eq. (1.37) is fulfilled only by virtue of the incoherent excitations included in $A_{\mathrm{incoh}}(\boldsymbol{k}, \hbar\omega)$ that the GA is completely unable to describe.

Dynamical Mean-Field theory: accounting for the full spectral weight of the system

The advent of DMFT [17] enabled a more accurate description of the HM, with an approximate spectral function that fulfills the sum-rule Eq. (1.37) for all values of the Hubbard parameter U. This happens because DMFT provides an approximation to the the self-energy which is less naïve than Eq. (1.43), and relies on the only assumption of locality

$$\Sigma(\boldsymbol{k}, \omega) \approx \Sigma(\omega) . \tag{1.44}$$

With the above approximation one finds again that the HM undergoes a Mott transition independently of dimensionality and lattice type, and whose onset is signaled by the complete suppression of the quasi-particle peak in the spectral function. However, the high-energy excitations caused by electron-electron interactions and absent in the quasi-particle approximation are also taken into account, both on the metallic side, where they coexist with the quasi-particle peak, and on the insulating side, where they fully account for the sum-rule (1.37).

The DMFT self-energy of a HM is computed from the solution of an auxiliary impurity model, describing a single-site with Hubbard interactions and coupled to an effective bath, self-consistently determined to mimic the local properties of the lattice model. The impurity-model Hamiltonian reads (setting $\hat{c}_\sigma^\dagger \hat{c}_\sigma = \hat{n}_\sigma$)

$$\hat{H} = \sum_{\kappa\sigma} \epsilon_{\kappa\sigma} \hat{b}_{\kappa\sigma}^\dagger \hat{b}_{\kappa\sigma} + \sum_{\kappa\sigma} \left(V_{\kappa\sigma} \hat{c}_\sigma^\dagger \hat{b}_{\kappa\sigma} + V_{\kappa\sigma}^* \hat{b}_{\kappa\sigma}^\dagger \hat{c}_\sigma \right) + U \hat{n}_\uparrow \hat{n}_\downarrow - \mu \sum_\sigma \hat{n}_\sigma \,, \qquad (1.45)$$

where the couplings $V_{\kappa\sigma}$ between impurity and bath and the energy levels $\epsilon_{\kappa\sigma}$ of the bath can be used to build the hybridization function

$$\Delta_\sigma(\omega) = \sum_\kappa \frac{|V_{\kappa\sigma}|^2}{\hbar\omega - \epsilon_\kappa + i\eta} \,. \qquad (1.46)$$

In the absence of interactions ($U = 0$), the Green's function of the Hamiltonian (1.45) is simply the non-interacting Green's function

$$\mathcal{G}_{0\sigma}(\omega) = [\hbar\omega + \mu - \Delta_\sigma(\omega)]^{-1} \,. \qquad (1.47)$$

In the presence of a finite U, instead, the self-energy of the system can be found from the relation

$$\Sigma_\sigma(\omega) = \mathcal{G}_{0\sigma}^{-1}(\omega) - G_\sigma^{-1}(\omega) \,, \qquad (1.48)$$

where G is the interacting Green's function of the impurity model, computed by means of a suitable impurity-solver like Quantum Monte Carlo, exact diagonalization, or even GVM.

Once the self-energy of the impurity-model $\Sigma_\sigma(\omega)$ is known, it is set equal to the actual local self-energy of the HM, and can be used to build its approximate (exact in the limit of infinite lattice coordination) local Green's function $G_\sigma^{(l)}(\omega)$ through an integration over the density of states $\mathcal{D}_0$ of the non-interacting system

$$G_\sigma^{(l)}(\omega) = \int d\varepsilon \frac{\mathcal{D}_0(\varepsilon)}{\hbar\omega - \varepsilon + \mu - \Sigma_\sigma(\omega)} \,. \qquad (1.49)$$

The above expression enters, together with the self-energy, in the definition of the new hybridization function $\Delta_\sigma(\hbar\omega)$, which is

$$\Delta_\sigma(\omega) = \hbar\omega + \mu - \Sigma_\sigma(\omega) + \left[G_\sigma^{(l)}(\omega)\right]^{-1} . \tag{1.50}$$

The new parameters $V_{\kappa\sigma}$ and $\epsilon_{\kappa\sigma}$ are found by inverting Eq. (1.46), so that a new Hamiltonian (1.45) can be set up to close the self-consistent cycle.

The convergence of cycle $\Delta \to G \to G^{(l)} \to \Delta$ provides the dynamical mean-field solution of the HM. From the converged self-energy $\Sigma_\sigma(\omega)$ it is possible to compute the full spectral function $A(\omega)$ of the impurity, which features, both on the metallic and insulating sides, two broad bands of high-energy excitations that do not take part in the conduction process.

The so called Hubbard bands, shown on the spectral function plots of Fig. 1.2, belong to the incoherent part of the spectral function, and contain excitations with a finite value of double-occupation probability.
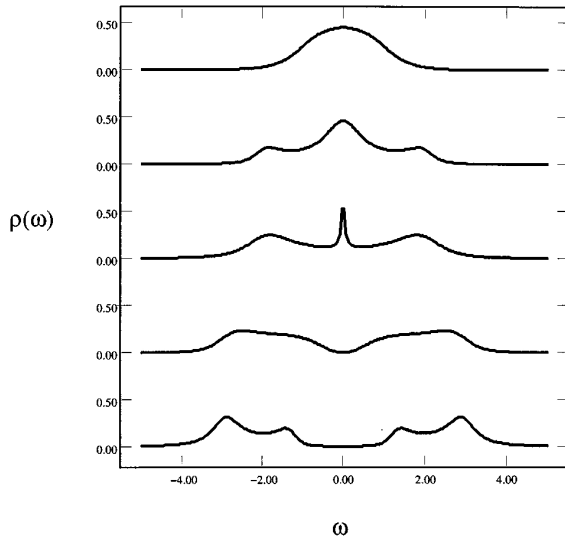
Figure 1.2: *Plots of the DMFT spectral function $A(\omega)$ for the HM. The value of U is increasing from top to bottom. Only the top three plots refer to the metallic phase, where there is a finite spectral weight for $\omega = 0$. The Hubbard bands, whose spectral weight cannot be accounted for by GA, are clearly visible in the last three plots. The last two plots refer to the insulating phase, for which the GA predicts $A(\omega) = 0$ everywhere. Adapted from reference [17].*

Both GA and DMFT make use of a spectral function with pure frequency dependence. This has the consequence that for both theories, on the metallic side of the transition, the weight of the quasi-particle peak $\mathcal{Z}_{\boldsymbol{k}}$ for $|\boldsymbol{k}| = k_{\mathrm{F}}$ (we refer to it as $\mathcal{Z}$), which can be proved to be equal to the jump in the quasi-particle distribution at k_{F}, can be identified also with the quasi-particle mass renormalization m/m^*, by virtue of the following formula of Landau Fermi liquid theory [50] [3] ($k = |\boldsymbol{k}|$)

$$\frac{m}{m^*} = \mathcal{Z}_{k_{\mathrm{F}}} \left(1 + \frac{m}{\hbar^2 k_{\mathrm{F}}}\frac{\partial}{\partial k}\Re e\Sigma(k,\mu)\Big|_{k=k_{\mathrm{F}}}\right) . \tag{1.51}$$

---

[3]This formula, valid for a spherical Fermi surface, can be extended for a liquid with a non-spherical Fermi surface, for which it will provide the renormalization of the mass tensor.

1.4 Variational wavefunctions describing the Mott transition in lattices of finite coordination

In Sect. 1.3.3 we mentioned the absence of a Mott transition from paramagnetic metal to paramagnetic insulator on the HM of finite dimensionality, when described with the GVM. It is now worth asking what other ingredients must be present in a variational wavefunction in order to make it suitable for computing the ground-state properties of a finite-dimensional system across this type of transition.

Whenever the value of the Hubbard U is large, but not infinite, both exact results for the expectation values of the double occupation operator $\hat{n}_\uparrow \hat{n}_\downarrow$ (as shown in Sect. 1.3.3) and of the hopping operator $\hat{c}_{i\sigma}^\dagger \hat{c}_{j\sigma}$ computed on the GVW are finite. This is not an unphysical result, since a finite hopping matrix element and double occupation are necessary for the energy to have a non-trivial expression in terms of the variational parameter η.

What prevents the GVW from describing an insulator is the non-vanishing value (1.32) of the jump in the quasi-particle distribution function, which for finite coordination lattices is different from the renormalization of the hopping matrix element. In the exact ground-state of a Mott insulator the former is expected to become zero even when the latter is finite. It is natural to expect off-site correlations to have an essential role in determining this behavior.

Kaplan *et al.* pointed out [57] that the transition to the insulating phase might be connected to a non-local phenomenon which is already present in the metallic phase of the HM and becomes more important near the Mott transition, which is the decrease of the average distance between doubly occupied (doublon) and empty (holon) sites with the increase of the Hubbard-U. This effect is due to the fact that a doublon cannot disappear through a single hopping process driven by the kinetic part of the Hubbard Hamiltonian, unless it has a holon as nearest-neighbor. For large U the lifetime of a doublon on the ground-state wavefunction is expected to be small, and this requires a holon to be close to it, in order to make the annihilation process more likely.

It was shown [58] that extending the Gutzwiller projector with the inclusion of nearest-neighbor or next-nearest-neighbor parameters accounting for short-range correlations is not sufficient to describe the holon-doublon binding, and therefore the Mott transition. The description of the Mott metal-insulator transition in the half-filled HM became possible only through the inclusion in the variational wavefunction

of a Jastrow factor [59] of the type ($\hat{n}_{\boldsymbol{R}} = \hat{n}_{\uparrow\boldsymbol{R}} + \hat{n}_{\downarrow\boldsymbol{R}}$)

$$\prod_{\boldsymbol{RR'}} \mathcal{J}_{\boldsymbol{RR'}} = \exp\left[\frac{1}{2}\sum_{\boldsymbol{RR'}} v_{\boldsymbol{RR'}}(\hat{n}_{\boldsymbol{R}}\,\hat{n}_{\boldsymbol{R'}})\right] , \qquad (1.52)$$

which, containing a sum over all lattice vectors $\boldsymbol{R}$ and $\boldsymbol{R'}$, ensures that correlations of arbitrary long range are taken into account.

1.5 Gutzwiller Variational Method and RVB wavefunctions

Among the successes of the Gutzwiller projective wavefunction, it is worth mentioning its representation of the Resonating Valence Bond (RVB) state, which was first introduced by Anderson [60] in 1973 and later proposed as an explanation of the properties of a class of oxide superconductors, among which La_2CuO_4 [28].

The superconducting phase of these compounds arises upon doping the stoichiometric phase that is an antiferromagnetic Mott insulator. In the insulator, each Cu ion has one hole in the d-shell. The large Coulomb repulsion and the Cu-O charge transfer gap prevent the holes from moving coherently, which leads to localized spin-1/2 moments. These latter are coupled among each other by an antiferromagnetic super-exchange across the filled oxygen p-orbitals, so that an anti-ferromagnetic quantum Heisenberg model describes the low energy physics:

$$\hat{H}_{\text{exch}} = J \sum_{\langle \boldsymbol{R},\boldsymbol{R'}\rangle} \hat{S}_{\boldsymbol{R}} \cdot \hat{S}_{\boldsymbol{R'}} , \qquad (1.53)$$

Classically, the ground-state of the antiferromagnetic Heisenberg model is a Néel state, with antiparallel neighboring spins. Quantum fluctuations are known to reduce the classical order parameter, the greater the lower the dimensionality. In fact, in one-dimension, the quantum Heisenberg model is not magnetically ordered and is in a sort of spin-liquid phase with gapless spin-waves, without any spin-symmetry breaking.

Anderson imagined that in the two-dimensional Cu-O planes (the cuprates, how high-T_c materials are universally known, are layered ceramics) quantum fluctuations were still quite substantial so that the actual ground state was Néel ordered, but very close in energy to a so-called Resonating Valence Bond (RVB) state. The RVB state is a spin-singlet wavefunction where pairs of spins are coupled into singlets in all possible ways, and different singlet coverings resonate among each other.

If singlet-pairs long distance apart are allowed, the wavefunction tends asymptotically to a Néel ordered state. If the singlet pairs extend up to a maximum distance,

e.g. just to neighboring sites – what is denoted as short-range RVB – the wavefunction is not anymore magnetically ordered, yet its energy is quite close to the actual ground state, which is indeed antiferromagnetically ordered.

Anderson's idea was that, once doping has melted the antiferromagnetic Mott insulator, the true long-range order is lost, but there remains still a substantial short-range antiferromagnetic order that can be well described by a short-range RVB wavefunction with inclusion of holes. The variational wavefunction that Anderson proposed for the RVB state is

$$|\Psi_{\text{RVB}}\rangle = \hat{\mathcal{P}}_{\text{N}}\hat{\mathcal{P}}_d \prod_{\boldsymbol{k}} \left[\frac{1}{\sqrt{1+a_{\boldsymbol{k}}^2}} + \frac{a_{\boldsymbol{k}}}{\sqrt{1+a_{\boldsymbol{k}}^2}}\hat{c}_{\boldsymbol{k},\uparrow}^\dagger \hat{c}_{-\boldsymbol{k},\downarrow} \right] |0\rangle. \tag{1.54}$$

One recognizes the uncorrelated wavefunction to be of BCS-type, the symmetry of the order parameter being controlled by the function $a_{\boldsymbol{k}}$. If $a_{\boldsymbol{k}} = a_{-\boldsymbol{k}}$ and $a_{k_x,k_y} = -a_{k_y,k_x}$, the pairing is in the d-wave singlet channel, the correct symmetry for cuprates. The Gutzwiller operator $\hat{\mathcal{P}}_d$ is actually a full projector that excludes all double occupancies. Finally, the operator $\hat{\mathcal{P}}_{\text{N}}$ projects the wavefunction, which alone would not be number-preserving, onto the manifold with fixed electron number N.

At half-filling the wavefunction describes an insulator and, depending on the spatial range of the pair-wavefunction, the Fourier transform of $a_{\boldsymbol{k}}$, it can also describe a Néel ordered phase, as aforementioned.

As soon as one dopes the insulating system described by the RVB state Eq. (1.54), removing the constraint of half-filling, the additional carriers build a superconducting pairing, which is already implicit in the BCS nature of the insulating wavefunction, and which is driven by the same parameter J as the antiferromagnetic pairing of the insulator. In spite of the more complex issues concerning high-temperature superconductivity which are rising in recent years [61], Anderson's Gutzwiller BCS-RVB wavefunction has remained a widely used ansatz for numerical simulations [62].

1.6 The Gutzwiller Approximation for multiband systems

The success of the GA for describing strongly correlated single-band models encouraged its application to more complex systems, where the local Gutzwiller projector depends on a great number of many-body variational parameters.

Bünemann, Gebhard and collaborators [38, 63, 64] developed a rigorous formulation of the GA for multiband models. With the works of Fabrizio [65] and Lanatà *et al.* [66], this formulation was further elucidated and extended with the suggestion of practical parametrizations of the Gutzwiller parameter matrix suitable for numerical calculations.

We now briefly expound the state of the art of the GA, by giving the recipe for computing expectation values of general operators on the multi-band GVW. We will show how the multi-band Gutzwiller formalism, where the GA is found from a perturbative expansion of the Gutzwiller projector, leads to the same results of the counting argument of references [26, 48] when applied to the single-band model.

1.6.1 Expectation values in the limit of infinite lattice coordination

The expectation value of a general local operator $\hat{O}_{\boldsymbol{R}}$ on the GVW $|\Psi_{\mathrm{G}}\rangle = \hat{\mathcal{P}}|\Psi_0\rangle$ is

$$\langle\Psi_0|\hat{\mathcal{P}}^\dagger\hat{O}_{\boldsymbol{R}}\hat{\mathcal{P}}|\Psi_0\rangle\,, \tag{1.55}$$

where $\hat{\mathcal{P}}$ is defined in Eq. (1.11) as

$$\hat{\mathcal{P}} = \prod_{\boldsymbol{R}}\hat{\mathcal{P}}_{\boldsymbol{R}}\,. \tag{1.56}$$

Bünemann and collaborators realized that the expression Eq. (1.55) reduces, on infinite-coordination lattices, to the simpler form

$$\langle\Psi_0|\hat{\mathcal{P}}^\dagger\hat{O}_{\boldsymbol{R}}\hat{\mathcal{P}}|\Psi_0\rangle \rightarrow \langle\Psi_0|\hat{\mathcal{P}}_{\boldsymbol{R}}^\dagger\hat{O}_{\boldsymbol{R}}\hat{\mathcal{P}}_{\boldsymbol{R}}|\Psi_0\rangle\,, \tag{1.57}$$

provided that the two following constraints (known as Gutzwiller constraints) are imposed on the Gutzwiller wavefunction

$$\langle\Psi_0|\hat{\mathcal{P}}_{\boldsymbol{R}}^\dagger\hat{\mathcal{P}}_{\boldsymbol{R}}|\Psi_0\rangle = 1 \tag{1.58}$$

$$\langle\Psi_0|\hat{\mathcal{P}}_{\boldsymbol{R}}^\dagger\hat{\mathcal{P}}_{\boldsymbol{R}}\hat{n}_{\boldsymbol{R},\alpha\beta}|\Psi_0\rangle = \langle\Psi_0|\hat{n}_{\boldsymbol{R},\alpha\beta}|\Psi_0\rangle\,, \tag{1.59}$$

where $\hat{n}_{\boldsymbol{R},\alpha\beta} = \hat{c}_{\boldsymbol{R}\alpha}^\dagger\hat{c}_{\boldsymbol{R}\beta}$ is the local single-particle density matrix operator on site $\boldsymbol{R}$. Imposing constraints (1.58) and (1.59) for local quantities causes also the expectation value of a quadratic off-site operator $\hat{c}_{\boldsymbol{R}\alpha}^\dagger\hat{c}_{\boldsymbol{R}'\beta}$ to become equal to

$$\langle\Psi_0|\hat{\mathcal{P}}^\dagger\hat{c}_{\boldsymbol{R}\alpha}^\dagger\hat{c}_{\boldsymbol{R}'\beta}\hat{\mathcal{P}}|\Psi_0\rangle \rightarrow \langle\Psi_0|\hat{\mathcal{P}}_{\boldsymbol{R}}^\dagger\hat{c}_{\boldsymbol{R}\alpha}^\dagger\hat{\mathcal{P}}_{\boldsymbol{R}}\hat{\mathcal{P}}_{\boldsymbol{R}'}^\dagger\hat{c}_{\boldsymbol{R}'\beta}\hat{\mathcal{P}}_{\boldsymbol{R}'}|\Psi_0\rangle \tag{1.60}$$

on an infinite-coordination lattice.

By expanding the above expectation value in Wick products, we see that it can be rewritten as

$$\langle\Psi_0|\hat{\mathcal{P}}_{\boldsymbol{R}}^\dagger\hat{c}_{\boldsymbol{R}\alpha}^\dagger\hat{\mathcal{P}}_{\boldsymbol{R}}\hat{\mathcal{P}}_{\boldsymbol{R}'}^\dagger\hat{c}_{\boldsymbol{R}'\beta}\hat{\mathcal{P}}_{\boldsymbol{R}'}|\Psi_0\rangle = \sum_{\gamma\delta}R_{\alpha\gamma}\langle\Psi_0|\hat{c}_{\boldsymbol{R}\gamma}^\dagger\hat{c}_{\boldsymbol{R}'\delta}|\Psi_0\rangle R_{\delta\beta}^\dagger\,, \tag{1.61}$$

where the parameters $R_{\alpha\beta}$ are computed from the equality

$$\langle\Psi_0|\hat{\mathcal{P}}_{\boldsymbol{R}}^\dagger\hat{c}_{\boldsymbol{R}\alpha}^\dagger\hat{\mathcal{P}}_{\boldsymbol{R}}\hat{c}_{\boldsymbol{R}\beta}|\Psi_0\rangle = \sum_{\gamma}R_{\alpha\gamma}^\dagger\langle\Psi_0|\hat{c}_{\boldsymbol{R}\gamma}^\dagger\hat{c}_{\boldsymbol{R}\beta}|\Psi_0\rangle\,. \tag{1.62}$$

Eq. (1.61) shows that, when appearing in the calculation of expectation values of off-site quadratic operators, every creation operator is effectively renormalized to

$$\hat{c}_{\boldsymbol{R}\alpha} \rightarrow \hat{\mathcal{P}}^{\dagger}\hat{c}_{\boldsymbol{R}\alpha}\hat{\mathcal{P}} = \sum_{\gamma} R^{\dagger}_{\gamma\alpha}\hat{c}_{\boldsymbol{R}\gamma}\,. \qquad (1.63)$$

The role of constraints Eq. (1.58) and (1.59) in determining expectation values in the limit of infinite lattice coordination can be understood as follows. Since a projector $\hat{\mathcal{P}}_{\boldsymbol{R}}$ at lattice site $\boldsymbol{R}$ commutes with projectors and operators at different lattice sites, the expectation value (1.55) can be written as

$$\langle\Psi_0|\hat{\mathcal{P}}^{\dagger}\hat{O}_{\boldsymbol{R}}\hat{\mathcal{P}}|\Psi_0\rangle = \langle\Psi_0|\hat{\mathcal{P}}^{\dagger}_{\boldsymbol{R}}\hat{O}_{\boldsymbol{R}}\hat{\mathcal{P}}_{\boldsymbol{R}}\left(\prod_{\boldsymbol{R}'\neq\boldsymbol{R}}\hat{\mathcal{P}}^{\dagger}_{\boldsymbol{R}'}\hat{\mathcal{P}}_{\boldsymbol{R}'}\right)|\Psi_0\rangle\,. \qquad (1.64)$$

The last term in brackets in Eq. (1.64) may be considered as an "interaction propagator" and expanded in multi-particle operators around the identity, devising a perturbative scheme for the calculation of expectation values on the GVW.

It can be proven that any term in the perturbative expansion where more than two fermionic lines come out of $\hat{\mathcal{P}}^{\dagger}_{\boldsymbol{R}'}\hat{\mathcal{P}}_{\boldsymbol{R}'}$ vanishes on an infinite-coordination lattice [38], so that only terms with zero or two fermionic lines are left. Enforcing Gutzwiller constraints causes also the contribution of terms where exactly two fermionic lines come out of the propagator to vanish, so that Eq. (1.64) becomes exactly equal to Eq. (1.57) in infinite dimensions.

To see how terms with two Fermionic lines disappear, it is enough to remark that the Wick decoupling of the left-hand side of (1.59) can be written as the sum of a disconnected term plus a connected term

$$\langle\Psi_0|\hat{\mathcal{P}}^{\dagger}_{\boldsymbol{R}'}\hat{\mathcal{P}}_{\boldsymbol{R}'}\hat{n}_{\alpha\beta,\boldsymbol{R}'}|\Psi_0\rangle = \langle\Psi_0|\hat{\mathcal{P}}^{\dagger}_{\boldsymbol{R}'}\hat{\mathcal{P}}_{\boldsymbol{R}'}|\Psi_0\rangle\langle\Psi_0|\hat{n}_{\alpha\beta,\boldsymbol{R}}|\Psi_0\rangle + \langle\Psi_0|\text{conn.}|\Psi_0\rangle\,. \qquad (1.65)$$

Due to the first Gutzwiller constraint Eq. (1.58), the disconnected term is sufficient to satisfy the equality established in Eq. (1.59), and therefore all connected terms where two fermionic lines come out of $\hat{\mathcal{P}}^{\dagger}_{\boldsymbol{R}'}\hat{\mathcal{P}}_{\boldsymbol{R}'}$ are bound to vanish (see Appendix A.4). This remains true when $\hat{\mathcal{P}}^{\dagger}_{\boldsymbol{R}'}\hat{\mathcal{P}}_{\boldsymbol{R}'}$ is averaged with multi-particle operators on different sites, like the operator $\hat{\mathcal{P}}^{\dagger}_{\boldsymbol{R}}\hat{O}_{\boldsymbol{R}}\hat{\mathcal{P}}_{\boldsymbol{R}}$ in Eq. (1.64).

As a result, only the zeroth-order term of the expansion of the operator in brackets in (1.64) is not discarded, and provides the expectation value of $\hat{O}_{\boldsymbol{R}}$ on the GVW for a lattice of infinite coordination. The same argument is valid also in order to prove the result of Eq. (1.60) for the renormalization of quadratic off-site operators.

1.6.2 The mixed-basis representation

With the introduction of Gutzwiller constraints, we are able to simplify the calculation of expectation values of local operators by considering in Eq. (1.55) only the

contribution of the projector on the same site. A general multi-band local projector $\hat{\mathcal{P}}_{\boldsymbol{R}}$ can be parametrized as

$$\hat{\mathcal{P}}_{\boldsymbol{R}} = \sum_{\Gamma\kappa} \Lambda_{\Gamma\kappa,\boldsymbol{R}} |\Gamma, \boldsymbol{R}\rangle\langle \kappa, \boldsymbol{R}| \,, \tag{1.66}$$

where Γ and κ label the different many-body states. From now on, in order to simplify the notation of this section, we will leave out the index $\boldsymbol{R}$ and we will refer to the local projector with the symbol $\hat{\mathcal{P}}$. The most intuitive many-body basis on which to write this projector can be built once a set of local single-particle spin-orbitals $\phi_{\alpha\sigma}$ is given. We will call this set, which may be for example the basis set provided by an electronic structure code, the original single-particle basis (OSB), and absorb from now on the spin index σ in the spin-orbital label α.

From the orbitals ϕ_{α} we can construct all possible local multi-particle Slater determinants, as many as 2^{2M}, where $2M$ is the total number of orbitals (the factor 2 accounts for spin degeneracy). We will refer to this basis of Slater determinants as the basis of electronic configurations (BC) on original orbitals. This is a local Fock basis that can be obtained by filling the zero-particle state $|0\rangle$ through the application of all combinations of creation operators $\hat{c}_{\alpha}^{\dagger}$ obeying fermionic anticommutation relations.

However, the definition of Eq. (1.66) allows for a mixed basis representation of $\hat{\mathcal{P}}_{\boldsymbol{R}}$, where, while the index Γ runs on the configurations on the original basis, the index κ runs over the configurations on a different single-particle basis, i.e. a Fock basis built by filling the vacuum with operators $\hat{d}_{\alpha}^{\dagger}$ creating fermions on another set ψ_a of spin-orbitals.

We can choose as ψ_a the "natural orbitals", i.e. the basis orbitals which diagonalize the local single-particle uncorrelated density matrix $n_{\alpha\beta}^{(0)} = \langle\Psi_0|\hat{c}_{\alpha}^{\dagger}\hat{c}_{\beta}|\Psi_0\rangle$, so that

$$n_{ab}^{(0)} = \langle\Psi_0|\hat{d}_a^{\dagger}\hat{d}_b|\Psi_0\rangle = n_a^{(0)}\delta_{ab} = U_{a\alpha}^{\dagger}n_{\alpha\beta}^{(0)}U_{\beta b} \,. \tag{1.67}$$

From now on we will refer to the local single-particle basis ψ_a as natural single-particle basis (NSB), and to $n_a^{(0)}$ as local "natural density matrix".

It is now convenient to introduce the local uncorrelated many-body density matrix $\hat{P}_0$, which is such that, for every local operator $\hat{O}$,

$$\langle\Psi_0|\hat{O}|\Psi_0\rangle = \text{Tr}\{\hat{P}_0\hat{O}\} \,. \tag{1.68}$$

When written in the BC on the natural orbitals, also the many-body uncorrelated density matrix is diagonal, with the explicit form [4]

$$P_{0\kappa\kappa'} = \langle\,\Psi_0\,||\kappa'\,\rangle\langle\,\kappa\,||\Psi_0\,\rangle = \delta_{\kappa\kappa'}P_{0\kappa} \tag{1.69}$$

$$P_{0\kappa} = \prod_{a\in\kappa}(n_a^{(0)})\prod_{b\notin\kappa}(1-n_b^{(0)})\,, \tag{1.70}$$

where $|\kappa'\,\rangle\langle\,\kappa|$ is a projector on local configurations. The factor $n_a^{(0)}$ appears on the right-hand side of Eq. (1.70) only if orbital ψ_a is full in configuration κ, while $1-n_b^{(0)}$ appears if ψ_b is empty.

From Eq. (1.69) it is clear that the operator $\hat{P}_0$ is positive-definite, and as a consequence we can define its square root $\sqrt{\hat{P}_0}$ with matrix elements $\sqrt{P_{0\kappa}}\delta_{\kappa\kappa'}$, and such that for any local operator $\hat{O}$

$$\langle\Psi_0|\hat{O}|\Psi_0\rangle = \mathrm{Tr}\{\sqrt{\hat{P}_0}\hat{O}\sqrt{\hat{P}_0}\}\,, \tag{1.71}$$

and in particular

$$\langle\Psi_0|\hat{\mathcal{P}}^\dagger\hat{\mathcal{P}}|\Psi_0\rangle = \mathrm{Tr}\{\sqrt{\hat{P}_0}\hat{\mathcal{P}}^\dagger\hat{\mathcal{P}}\sqrt{\hat{P}_0}\} = \mathrm{Tr}\{\hat{\Phi}^\dagger\hat{\Phi}\ \}\,, \tag{1.72}$$

where the auxiliary operator $\hat{\Phi}$ has matrix elements between configurations Γ and κ equal to

$$\Phi_{\Gamma\kappa} = \Lambda_{\Gamma\kappa}\sqrt{P_{0\kappa}}\,. \tag{1.73}$$

This operator enables us to rewrite Gutzwiller constraints no longer as an expectation value, but rather as a trace, namely (setting $\hat{d}_a^\dagger\hat{d}_b = \hat{n}_{ab}$)

$$\mathrm{Tr}\{\hat{\Phi}^\dagger\hat{\Phi}\ \} = \mathrm{Tr}\{\hat{P}_0\} = 1\,, \tag{1.74}$$

$$\mathrm{Tr}\{\hat{\Phi}\ \hat{n}_{ab}\hat{\Phi}^\dagger\} = \mathrm{Tr}\{\hat{P}_0\hat{n}_{ab}\} = n_a^{(0)}\delta_{ab}\,. \tag{1.75}$$

In the same way we can compute the expectation value of a local projected operator as

$$\langle\Psi_0|\hat{\mathcal{P}}^\dagger\hat{O}\hat{\mathcal{P}}|\Psi_0\rangle = \mathrm{Tr}\{\hat{\Phi}^\dagger\hat{O}\hat{\Phi}\ \}\,, \tag{1.76}$$

and the value of the hopping renormalization matrices $R_{\alpha\beta}$ from

$$R_{\alpha b}^\dagger = \frac{\mathrm{Tr}\{\hat{\Phi}^\dagger\hat{c}_\alpha^\dagger\hat{\Phi}\ \hat{d}_b\}}{\sqrt{n_b^{(0)}(1-n_b^{(0)})}}\,, \tag{1.77}$$

---

[4]The expression for P_0 in terms of $n^{(0)}a$ is obtained if we suppose the

where now $R_{\alpha b}^{\dagger}$ transforms original basis creation (annihilation) operators to renormalized natural basis creation (annihilation) operators as

$$\hat{c}_{\boldsymbol{R}\alpha} \to \hat{\mathcal{P}}^{\dagger} \hat{c}_{\boldsymbol{R}\alpha} \hat{\mathcal{P}} = \sum_{b} R_{b\alpha}^{\dagger} \hat{d}_{\boldsymbol{R}b}, \tag{1.78}$$

$$\hat{c}_{\boldsymbol{R}\alpha}^{\dagger} \to \hat{\mathcal{P}}^{\dagger} \hat{c}_{\boldsymbol{R}\alpha}^{\dagger} \hat{\mathcal{P}} = \sum_{b} R_{\alpha b} \hat{d}_{\boldsymbol{R}b}^{\dagger}. \tag{1.79}$$

The explicit derivation of Eq. (1.77), Eq. (1.74) and Eq. (1.75) can be found in a the work of Lanatà *et al.* [66] and in Appendix A.5. In Appendix A.3 we prove that the diagonal elements of $R_{\alpha\alpha}$ are lower or equal than one, which means that, at least for diagonal $R_{\alpha\beta}$, the effect of hopping renormalization is that of increasing the value of the kinetic energy, the squares $Z_{\alpha} = |R_{\alpha\alpha}|^2$ acting, as in the single-band case, as enhancement factors for the band mass.

It is important to stress that the uncorrelated local density matrix on natural orbitals

$$n_a^{(0)} \delta_{ab} = \mathrm{Tr}\{\hat{\Phi} \ \hat{n}_{ab} \hat{\Phi}^{\dagger}\}$$

and the Gutzwiller-renormalized local density matrix

$$n_{\alpha\beta} = \mathrm{Tr}\{\hat{\Phi}^{\dagger} \hat{n}_{\alpha\beta} \hat{\Phi} \}$$

are in general not the same matrix, since the above definitions differ from the position of $\hat{\Phi}^{\dagger}$ and $\hat{\Phi}$ with respect to the operator $\hat{n}_{\alpha\beta}$ in the trace. Not only each matrix is written in a different single-particle basis – the NSB and the OSB respectively – but even in the cases in which the two bases coincide, they are not equal unless the operator $\hat{\Phi}$ commutes with the density-matrix operator $\hat{n}_{ab}$. When $\hat{\Phi}$ is a number-conserving operator, as the one we will use throughout this thesis, we can only say that the trace of both density matrices is the same.

The great advantage that comes from the use of the mixed basis and of the trace representation of expectation values, is that this representation makes the knowledge of the natural orbitals ψ_a superfluous. While in a variational calculation the OSB is fixed once and for all, the NSB depends in general on the parameters of the variational wavefunction, and should be computed, if needed, at every variational optimization step from the diagonalization (1.67) of $n_{\alpha\beta}^{(0)}$.

The use of Φ as matrix of variational parameters is such that the many-body unitary change $\hat{\mathcal{U}}_{\Gamma\kappa}$ from configurations on the original basis to configurations on the natural basis is included in the mixed-basis projector $\Lambda_{\Gamma\kappa}$ in Eq. (1.73). As a result, the same matrix representation of Fock operators $\hat{c}_a^{\dagger}$ and $\hat{c}_b$ on the original basis can be used for creating and annihilating particles on the natural basis, provided that their matrix elements are being "sandwiched" between a bra and a ket representing a many-body

state in the natural Fock space, indeed, omitting the lattice vector $\boldsymbol{R}$,

$$\langle \Gamma | \hat{c}_\alpha^\dagger | \Gamma' \rangle = (-1)^{\mathcal{N}_{\Gamma' < \alpha}} \delta_{\Gamma' + \{\alpha\}, \Gamma} \tag{1.80}$$

$$\langle \kappa | \hat{d}_a^\dagger | \kappa' \rangle = (-1)^{\mathcal{N}_{\kappa' < a}} \delta_{\kappa' + \{a\}, \kappa}, \tag{1.81}$$

where $\delta_{\Gamma + \{\alpha\}, \Gamma'}$ is equal to one when the configuration Γ differs from Γ' only by one more particle in orbital α, and where $\mathcal{N}_{\Gamma' < \alpha}$ counts the number of particles in Γ' with orbital index smaller than α.

The matrix representations of Eq. (1.80) and Eq. (1.81) are valid for all creation operators written in their own Fock basis. We can use Eq. (1.81) in traces whenever the operators $\hat{d}$ and $\hat{d}^\dagger$ are multiplied on the left by the operator $\hat{\Phi}$, and on the right by $\hat{\Phi}^\dagger$, which is exactly the case for Eq. (1.75) and Eq. (1.77).

The matrix $\Phi_{\Gamma\kappa}$ defined in Eq. (1.73) and the subsequent equations, Eqs. (1.74) and (1.75), constitute a formalism that can be applied for a lattice model with an arbitrary number of bands. The expectation value of whatever Hamiltonian on the GVW reduces to a function

$$\langle \Psi_G | \hat{H} | \Psi_G \rangle \underset{\text{GA}}{\approx} \mathcal{E}(\Psi_0, \hat{\Phi}) \tag{1.82}$$

of the Slater determinant and $\hat{\Phi}$, subject to the normalization constraint $\langle \Psi_0 | \Psi_0 \rangle = 1$ and the Gutzwiller constraints.

The number of free parameters contained in $\Phi_{\Gamma\kappa}$ is expected to scale as $(2^{2M})^2$, but the symmetries of the system can make this number much smaller, as we will show in Chapt. 4 for our calculations on iron. In particular, imposing particle-number conservation and spin and orbital rotational symmetries, i.e. by requiring the commutation rules

$$\left[\hat{\Phi}, \hat{N} \right] = 0 \tag{1.83}$$

$$\left[\hat{\Phi}, \hat{S}_{x,y,z} \right] = 0 \tag{1.84}$$

$$\left[\hat{\Phi}, \hat{L}_{x,y,z} \right] = 0, \tag{1.85}$$

one can reduce the parameters of a 5-band model from around one million to a few thousands.

1.6.3 An application to the single-band paramagnetic Hubbard model

In this section we give the simplest example of the use of the formalism introduced in Sect. 1.6.1 and Sect. 1.6.2, by applying it to the single-band paramagnetic HM away from half-filling. The paramagnetic HM is particle-conserving and spin-rotationally

invariant. By requiring commutation rules Eq. (1.83) and (1.84), we find that the most general $\Phi_{\Gamma\Gamma'}$ is diagonal in the basis of spin configurations of the single local orbital of the model, and depends on three different parameters.

$$\Phi_{\Gamma\Gamma'} = \delta_{\Gamma\Gamma'}\Phi_\Gamma = \begin{pmatrix} \Phi_0 & 0 & 0 & 0 \\ 0 & \Phi_1 & 0 & 0 \\ 0 & 0 & \Phi_1 & 0 \\ 0 & 0 & 0 & \Phi_2 \end{pmatrix} \begin{array}{l} |\,0\,\rangle \\ |\,\uparrow\,\rangle \\ |\,\downarrow\,\rangle \\ |\,\uparrow\downarrow\,\rangle \end{array} \,. \tag{1.86}$$

In the single-band HM with spin rotational symmetry the NSB coincides therefore with the two local spin-orbitals $\phi_\uparrow$ and $\phi_\downarrow$, both having equal filling n. The Gutzwiller constraints Eq. (1.74) and (1.75) imply therefore that

$$|\Phi_0|^2 + 2|\Phi_1|^2 + |\Phi_2|^2 = 1 \tag{1.87}$$

$$2|\Phi_2|^2 + 2|\Phi_1|^2 = 2n \,, \tag{1.88}$$

which result in $|\Phi_0|^2 = |\Phi_2|^2 + 1 - 2n$ and $|\Phi_1|^2 = n - |\Phi_2|^2$.

All parameters Φ_j can therefore be written as functions of n and Φ_2. The square of the latter provides the expectation value of the double occupation probability, through

$$\mathrm{Tr}\{\hat{\Phi}^\dagger \hat{n}_\uparrow \hat{n}_\downarrow \hat{\Phi} \} = |\Phi_2|^2 \,, \tag{1.89}$$

while hopping renormalization operator R can be written in terms of n and Φ_2 as

$$R = \frac{\Phi_1^*\Phi_2 + \Phi_0^*\Phi_1}{\sqrt{n(1-n)}} =$$
$$= \sqrt{n - |\Phi_2|^2}\frac{\Phi_2 + \sqrt{|\Phi_2|^2 + 1 - 2n}\sqrt{n - |\Phi_2|^2}}{\sqrt{n(1-n)}} \,, \tag{1.90}$$

so that, using a hermitian $\hat{\Phi}$, the final variational energy has the form (ϵ_{kin} was defined in Eq. (1.19))

$$\varepsilon_{\mathrm{GA}} = -|\epsilon_{\mathrm{kin}}|\frac{2\Phi_1^2(\Phi_2 + \Phi_0)^2}{n(1-n)} + U|\Phi_2|^2 = \tag{1.91}$$

$$= -|\epsilon_{\mathrm{kin}}|\frac{2(|\Phi_2|^2 - n)(\Phi_2 + \sqrt{|\Phi_2|^2 + 1 - 2n})^2}{n(1-n)} + U|\Phi_2|^2 \,. \tag{1.92}$$

When $n = 1/2$, the minimization of the above energy gives the same result as Eq. (1.23). A plot of the energy and Z as a function of U is shown in Fig. 1.3 both for half-filling and for $n = 0.49$. The Brinkman-Rice transition disappears immediately as $n \neq 0.5$, showing that the energy per site is very sensitive to filling when U is large.
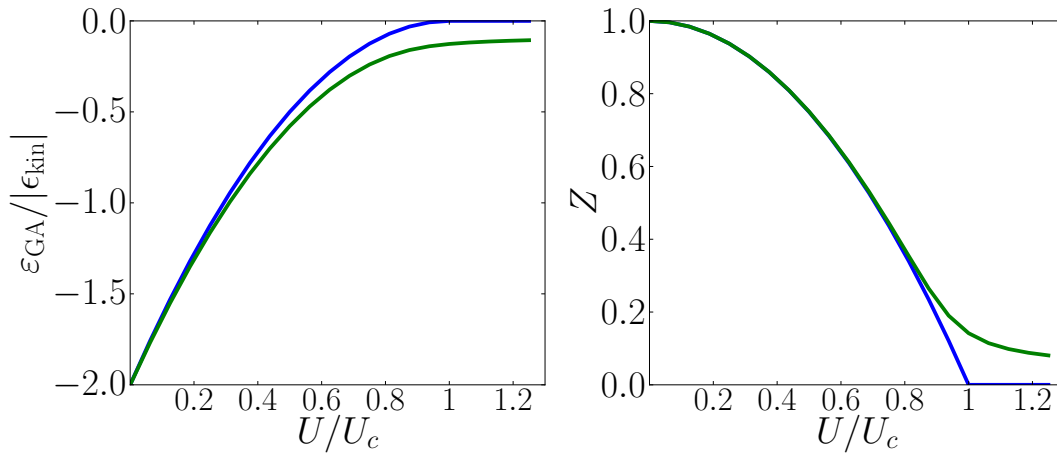
Figure 1.3: *Left panel, GA results for the energy per site $\varepsilon_{\mathrm{GA}}$ in units of $|\epsilon_{\mathrm{kin}}|$. The energy is plotted as a function of U/U_c, for fillings $n = 0.49$ (green line) and $n = 0.5$ (blue line). In the three-dimensional half-filled single-band HM on a cubic lattice $|\epsilon_{\mathrm{kin}}| = t$. The right panel shows a plot of the U dependence of the quasi-particle mass renormalization Z for the same two fillings.*

1.7   Final remarks

We can sum up the discussion of this chapter with some important remarks regarding the reliability of GA and GVW for describing the strongly correlated HM and the Mott transition.

We saw how the GVW improves the HF description of the HM by accounting for the suppression of the double occupation probability that is driven by the electron-electron interaction parameter U. The GVW cannot be used to describe systems with finite dimensionality that are expected to display a metal-insulator transition with no spin or translational symmetry breaking; a more refined variational wavefunction including a Jastrow factor is necessary for the purpose.

For a lattice of infinite coordination, the exact treatment of the GVW corresponds to the GA, which correctly predicts a metal-insulator transition for a finite value U_{c} of the interaction parameter U. The infinite-dimensional limit can be used as an approximation for systems of finite, not too low ($d > 2$) dimensionality. In particular, the GA can be applied to study the metallic phase of realistic three dimensional systems with Hubbard-type interactions in the vicinity of a Mott transition. The electronic correlations leading to the transition play an important role in the metallic phase, and their effect in determining quasi-particle mass renormalization and spin susceptibility can be correctly accounted for by the GA.

A drawback of the GA is that it describes a paramagnetic Mott insulator very poorly, for reasons that we elucidated in Sect. 1.3.4 and that depend on the inability of the GA to account for the incoherent many-body excitations of a strongly correlated system. A correct description of the many-body insulator in the limit of infinite lattice dimensionality can be retrieved within DMFT.

The multiband formulation of the GA explained in this chapter will be useful in Chapt. 4, where we will take advantage from the effectiveness of the GA in accounting for electronic localization and magnetic moment formation and we will apply its formalism to electronic structure calculations in the solid state.
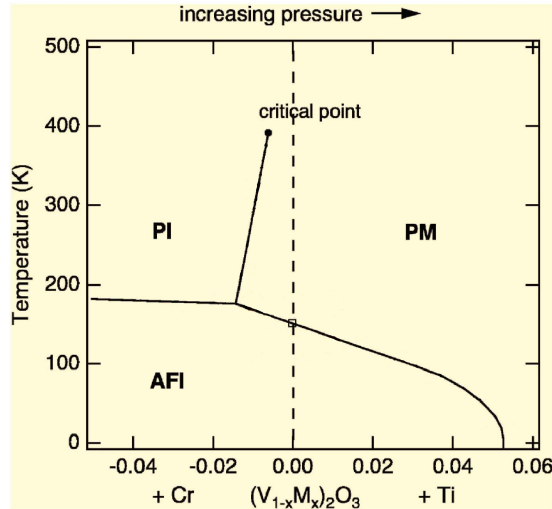
Chapter 2

Interfaces and junctions between metals and Mott insulators

In this chapter we address the problem of describing the quasi-particle properties of strongly correlated systems with broken translational invariance. We will discuss how a metallic crystal close to its metal-insulator transition can display surface quasi-particle properties different from those in the bulk. The stronger correlation between particles near the surface, where the kinetic energy is suppressed due to the reduced coordination, causes the surface layers to become worse conductors than the bulk.

The motivation of the work of Sect. 2.2 is the better understanding of the photoemission spectra of transition metal oxides. We will draw inspiration in particular from the recent data of Rodolakis *et al.* in vanadium sesquioxide (V_2O_3) [33]. This material displays a phase diagram (shown in Fig. 2.1) with both a paramagnetic metallic and paramagnetic insulating phase. The phase boundary between the two can be crossed by either increasing doping or temperature, and the paramagnetic metal-insulator transition can be simulated, at least qualitatively, as a Brinkman-Rice transition on the HM.

We will mimic the photoemission sample by a layered HM with two surfaces and layer-dependent Hubbard parameter U, and solve this model within GVM and GA. In Sect. 2.3 we will exploit the same model to study various types of interfaces between lattices with different values of U, larger or smaller than the critical value U_c for the Brinkman Rice transition. Using the same numerical technique developed in Sect. 2.2, we will address the intriguing problem of the tunneling of quasi-particles into a Mott insulator.

Figure 2.1: *Phase diagram of vanadium sesquioxide. The experiments mentioned in this chapter were performed for the paramagnetic metal (PM), close to the transition (showed by the vertical solid boundary line) to the paramagnetic insulating (PI) phase. The other region of the phase diagram refers to the antiferromagnetic insulating (AFI) phase. The photoemission data of Rodolakis et al. are obtained from different temperatures (200, 300 and 400 K) along the dashed line. Adapted from reference [32].*

2.1 Photoemission spectroscopy of strongly correlated systems

Photoemission Spectroscopy (PES) [29] is a technique based on the photoelectric effect, which was developed in the second half of the last century along with the technology of ultra-high vacuum and the physics of surfaces. Its experimental setup consists in a sincrotron light emitter providing the necessary photon beam, and of a properly aligned crystalline sample.

When the photons of the beam have a sufficiently high energy, their scattering with the electrons of the sample can provide the latter with a sufficient energy to escape from the crystal. The electrons are then collected by a detector analyzing their kinetic energy E_{kin} and, in Angle-Resolved Photoemission Spectroscopy (ARPES), also the outgoing angle θ. By knowing the crystal work-function it is possible to use these two values to compute the electron energy E_B and crystalline momentum $\hbar\mathbf{k}_\parallel$ parallel to the surface of the sample

$$E_{\mathrm{kin}} = \hbar\omega_{\mathrm{ph}} - W - |E_B^{(\mathbf{k})}|, \tag{2.1}$$
$$\hbar\mathbf{k}_\parallel = \sqrt{2mE_{\mathrm{kin}}}\sin\theta. \tag{2.2}$$

If $\hat{H}_{\text{e}-\text{ph}}$ is the Hamiltonian ruling the photoelectric process, the connection between photoemission intensity and spectral function can be recovered from the Fermi golden rule for the transition probability between a N-electron bound state $|\Psi_i^N\rangle$ and a state $|\Psi_f^N\rangle$ with $N-1$ bound electrons plus one free electron

$$P_{fi} = \frac{2\pi}{\hbar}|\langle\Psi_f^N|\hat{H}_{\text{e}-\text{ph}}|\Psi_i^N\rangle|^2\delta(E_f^N - E_i^N - \hbar\omega_{\text{ph}}),\qquad(2.3)$$

where $E_i^N = E_i^{N-1} - E_B^{\mathbf{k}}$ and $E_f^N = E_f^{N-1} + E_{\text{kin}}$ are the initial and final energy of the N-particle system, and where $E_B^{\mathbf{k}}$ is the binding energy of the photoelectron of kinetic energy E_{kin} and crystal momentum $\mathbf{k}$. The transition probability in Eq. (2.3) can be reframed as

$$P_{fi} = \sum_{f,i}|M_{f,i}^{\boldsymbol{k}}|^2\sum_m A_-(\boldsymbol{k}, \hbar\omega_{\text{ph}} - E_{\text{kin}}),\qquad(2.4)$$

in terms of the matrix element $|M_{f,i}^{\boldsymbol{k}}|^2$, which is a single-particle property, and the spectral function $A_-(\boldsymbol{k}, \hbar\omega)$

$$A_-(\boldsymbol{k},\omega) \;=\; \sum_n|\langle\phi_n^{(N-1)}|\hat{c}_{\boldsymbol{k}}|\phi_0^{(N)}\rangle|^2\delta(\omega - \xi_{n0}),\qquad(2.5)$$

which measures the total strength of all excitations of energy $\omega = \xi_{n0}$ removing one particle of momentum $\boldsymbol{k}$ from the system, and which is connected to the full spectral function $A(\boldsymbol{k}, \hbar\omega)$ discussed in Sect. 1.3.4 through

$$A(\boldsymbol{k},\omega) \;=\; A_-(\boldsymbol{k},\omega) + A_+(\boldsymbol{k},\omega),\qquad(2.6)$$

$$A_+(\boldsymbol{k},\omega) \;=\; \sum_n|\langle\phi_n^{(N+1)}|\hat{c}_{\boldsymbol{k}}^\dagger|\phi_0^{(N)}\rangle|^2\delta(\omega - \xi_{n0}).\qquad(2.7)$$

where $A_+(\boldsymbol{k},\omega)$ is related to an inverse-photoemission process, and sums up the spectral weight of all excitations adding one particle to the system. At zero temperature, $A_-(\boldsymbol{k},\omega)$ carries spectral contributions only for $\omega < 0$, while $A_+(\boldsymbol{k},\omega)$ is nonzero only for $\omega > 0$.

There are a few complications in obtaining experimental data for $A_-(\boldsymbol{k},\omega)$ in three-dimensional samples, which arise from the fact that the extracted photoelectrons have to cross the crystal surface. First, the Fermi golden rule Eq. (2.3) has to be supplied with an extra multiplicative factor that describes the transition probability of electrons through the surface. Second, when a bulk electron is excited, one also needs to remember that its journey to the surface is subject to a finite mean free path, which causes the final signal to be decreased by an amount depending on the depth at which the photoelectric process has occurred. Third, the orthogonal component of the crystal momentum $\boldsymbol{k}_\perp$ is not conserved through the crossing of the crystal surface, so that only a $\boldsymbol{k}_\parallel$-resolved spectral function is directly accessible.

Expecially this last limitation makes ARPES less predictive for 3d samples, and unable to have the access to their full band structure. Fortunately, this is not a major problem for the validation of DMFT predictions on strongly correlated materials. A DMFT simulation provides indeed only the $\boldsymbol{k}$-integrated spectral function $A(\omega)$, which can be compared with simple non-angle-resolved PES spectra.

We have seen in Sect. 1.3.4 how the DMFT-predicted spectral function for strongly correlated materials near their Mott metal-insulator transition features a sharp quasi-particle peak for $\omega \approx 0$ and two broad Hubbard bands for higher frequency. Early photoemission experiments [67–70] for metallic Chromium-doped vanadium sesquioxide $(V_{1-x}Cr_x)_2O_3$ near its metal-insulator transition, failed to reveal the sharp quasi-particle peak predicted by DMFT. The electronic spectrum was simply dominated by the lower Mott-Hubbard band with barely a hint of metallic weight at the Fermi energy.

A similar puzzle was actually reported much earlier in f-electron materials [71], and was soon ascribed to large surface effects in the presence of strong correlations [72]; the same conclusion was reached by the more recent photoemission experiments of other authors [73–79].

Only by using an higher frequency photon beam ($\hbar\nu$ of the order of 300 eV), it was eventually possible to observe in V_2O_3 a prominent quasi-particle peak coexisting with the incoherent Mott-Hubbard bands [30–32]. This was due to the fact that the photon beam could excite photoelectrons of larger energy and longer mean-free path, and thus able to travel all the way out of the crystal even when originated deep into the bulk. It was soon clear that the quasi-particle peak was caused by bulk electrons, and the question was risen about what could be the cause of the apparent absence of quasi-particles nearer to the surface.

The quasi-particle suppression in surface-sensitive probes was initially attributed [30] to surface-modified Hamiltonian parameters with a reduced atomic coordination. This can push the surface closer to the Mott transition than the underlying bulk, due to the lack of kinetic energy of surface electrons. The effects of larger electronic correlations at the surface have been later discussed by several authors through *ad-hoc* formulations of DMFT [36, 80, 81]. In their works there is general agreement on the fact that even if all Hamiltonian parameters were to remain identically the same up to the outermost atomic layer, the surface quasi-particle properties might still be intrinsically different [36].

More recently, the low-energy photon, bulk-sensitive ARPES measurements by Rodolakis *et al.* [33], showed that the coherent part of the spectral function of V_2O_3 reacts to the presence of the surface differently from the incoherent electronic

states over a length scale which is larger than the surface region as normally defined in surface science, and that can reach the value of tens of Angstroms.

This remark raises a more fundamental question. A metal does not possess any intrinsic length-scale at long distances other than the Fermi wavelength, thus an imperfection like a surface can only induce at large depth a power-law decaying disturbance such as that associated with Friedel's oscillations. Since one does not expect Luttinger's theorem to break down, even in a strongly correlated metal these oscillations should be controlled by the same Fermi wavelength as in the absence of interaction, irrespectively of the proximity of the Mott transition.

However, a strongly correlated metal does possess an intrinsic energy scale, the parametric distance of the Hamiltonian from the Mott transition, where that distance could be associated with a length scale. The surface as a perturbation should alter the quasi-particle properties within a depth corresponding to that length, a bulk property increasing near the Mott transition, unlike the Fermi wavelength that remains constant. In this respect, it is not *a priori* clear whether the recovery of bulk quasi-particle spectral properties with increasing depth should be strictly power-law with an oscillatory Friedel-type behavior, a picture compatible with the common view of a metal as an inherently critical state of matter, or whether it should be exponential, as one would expect by regarding the Mott transition as any other critical phenomena where power laws emerge only at criticality.

We find here in the simple half-filled HM that the quasi-particle spectral weight below the surface is actually recovered exponentially inside the bulk with a length-scale that depends only on the bulk properties and diverges approaching the continuous Mott transition.

2.2 Modeling the photoemission sample: a Hubbard slab with two surfaces

We model the crystalline sample for photoemission with a half-filled cubic lattice with nearest-neighbor hopping t, and electron-electron interactions included through a Hubbard term with Hubbard U resolved in the site index $\boldsymbol{R}$

$$H = -t \sum_{\{\boldsymbol{R}\boldsymbol{R}'\}\sigma} \hat{c}^{\dagger}_{\boldsymbol{R}\sigma} \hat{c}_{\boldsymbol{R}'\sigma} + H.c. + \sum_{\boldsymbol{R}} U_{\boldsymbol{R}}\, \hat{n}_{\boldsymbol{R}\uparrow} \hat{n}_{\boldsymbol{R}\downarrow}\,. \tag{2.8}$$

Conventionally, the Mott transition of the half-filled HM is studied restricting to the paramagnetic sector of the Hilbert space [17, 51, 82] so as to avoid spurious effects due to magnetism. We assume the cubic lattice of spacing a to have periodic boundary
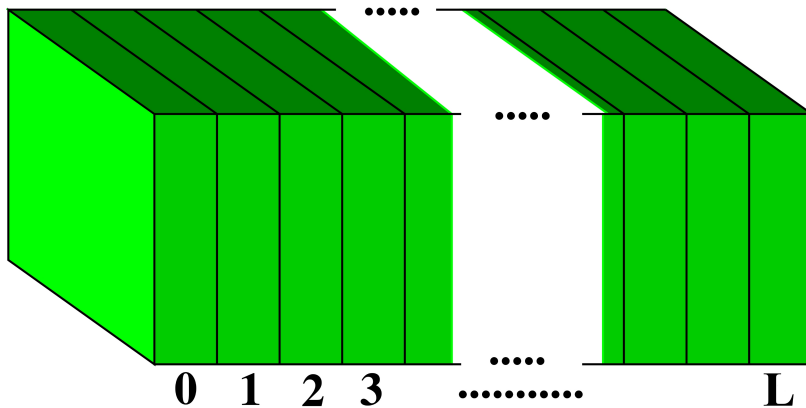
Figure 2.2: *Pictorial representation of the layered HM used to mimic the photoemission sample. The layers are labeled from 1 to L. Periodic boundary conditions are set within each layer.*

conditions in x and y directions and open boundary conditions in the z direction, in an L-layer slab geometry with two surfaces at $z = 0$ and $z = L\,a$ (see Fig. 2.2).

We choose a z-dependent Hubbard electron-electron interaction parameter $U_{\boldsymbol{R}} = U_{z=\boldsymbol{R}_\perp}$ equal to U everywhere except at the top surface layer ($z = 0$), where it takes a generally higher value $U_{\mathrm{s}} > U$. In this way we can compare effects at the ideal lower surface ($z = L\,a$), where $U_{La} = U$, with the more correlated upper surface ($z = 0$).

Following the Gutzwiller ansatz, we study Eq. (2.8) by means of the variational wavefunction

$$|\Psi\rangle = \prod_{\boldsymbol{R}} \mathcal{P}_{\boldsymbol{R}} |\Psi_0\rangle, \tag{2.9}$$

where $|\Psi_0\rangle$ is a paramagnetic Slater determinant. The parametrization of the projector must keep into account the spin rotational invariance of the system and the particle-hole symmetry arising from the bipartite character of the cubic lattice, and which implies the following equality between Fock operators

$$c^{\dagger}_{\boldsymbol{R}\sigma} \to \sigma\,(-1)^R\,c_{\boldsymbol{R}-\sigma}. \tag{2.10}$$

For a half-filled system, particle-hole symmetry causes every site to be occupied on average by exactly one electron, so that $\langle\Psi_0|\hat{n}_{\boldsymbol{R}\uparrow} + \hat{n}_{\boldsymbol{R}\downarrow}|\Psi_0\rangle = 1$. The equivalence of spin up and spin down electrons results in the identity

$$\langle\Psi_0|\hat{n}_{\boldsymbol{R}\uparrow}|\Psi_0\rangle = \langle\Psi_0|\hat{n}_{\boldsymbol{R}\downarrow}|\Psi_0\rangle = 1/2. \tag{2.11}$$

Following the formalism of Sect. 1.6.2 in the mixed-basis representation, we find that the most general z-dependent operator $\hat{\Phi}\,(z)$ compatible with symmetries is a

diagonal matrix in the space of electronic configurations, and its matrix elements $\Phi_{\Gamma\kappa}(z) = \Phi_\Gamma(z)\delta_{\Gamma\kappa}$ at every site are equal to the ones presented in Eq. (1.86) for the homogeneous case, with the simplification that, for each z, $\Phi_2(z) = \Phi_0(z)$.

Imposing the two Gutzwiller constraints 1.74 and 1.75 gives the further condition $\Phi_1^2(z) = \sqrt{1/2 - \Phi_2^2(z)}$. The expectation value of Eq. (2.8) is equal to (remembering that $z = \boldsymbol{R}_\perp$ and $z' = \boldsymbol{R}'_\perp$)

$$
\begin{aligned}
E = \frac{\langle\Psi|H|\Psi\rangle}{\langle\Psi|\Psi\rangle} = \sum_{\boldsymbol{R}} U_{\boldsymbol{R}}\, \Phi_2^2(z) \\
- t \sum_{<\boldsymbol{R}\boldsymbol{R}'>\sigma} R(z)\,R(z')\,\langle\Psi_0|c_{\boldsymbol{R}\sigma}^\dagger c_{\boldsymbol{R}'\sigma}^\dagger + H.c.|\Psi_0\rangle\,,
\end{aligned}
\tag{2.12}
$$

where the quasi-particle hopping renormalization factors $R(z)$ depend on $\Phi_2(z)$ through

$$
R(z) = 4\Phi_2(z)\sqrt{1/2 - \Phi_2^2(z)}\,.
\tag{2.13}
$$

We chose to invert this equation and to express $\Phi_2(z)$ as function of $R(z)$, which become the actual variational parameters together with the Slater determinant $|\Psi_0\rangle$. In order to minimize E in Eq. (2.12) we assume that the Slater determinant $|\Psi_0\rangle$ is built with single-particle wavefunctions that, because of the slab geometry, have the general expression $\phi_{\epsilon\boldsymbol{k}_{||}}(\boldsymbol{R}) = \sqrt{1/A}\,e^{i\boldsymbol{k}_{||}\cdot\boldsymbol{R}}\,\phi_{\epsilon\boldsymbol{k}_{||}}(z)$, where A is the number of sites per layer and $\boldsymbol{k}_{||}$ the momentum in the x-y plane.

The stationary value of E with respect to variations of $\phi_{\epsilon\boldsymbol{k}_{||}}(z)$ and $R(z)$ corresponds to the coupled equations

$$
\varepsilon\,\phi_{\epsilon\boldsymbol{k}_{||}}(z) = R(z)^2\,\epsilon_{\boldsymbol{k}_{||}}\,\phi_{\epsilon\boldsymbol{k}_{||}}(z) - t\,R(z)\sum_{p=\pm} R(z+p\,a)\,\phi_{\epsilon\boldsymbol{k}_{||}}(z+p\,a),
\tag{2.14}
$$

$$
\begin{aligned}
R(z) = \frac{4\sqrt{1-R(z)^2}}{U(z)A}\sum_{\epsilon\,\boldsymbol{k}_{||}}^{occupied}\Bigg[&-2\,R(z)\,\epsilon_{\boldsymbol{k}_{||}}\,\phi_{\epsilon\boldsymbol{k}_{||}}(z)^2 + \\
&+ t\,\phi_{\epsilon\boldsymbol{k}_{||}}(z)\sum_{p=\pm} R(z+p\,a)\,\phi_{\epsilon\boldsymbol{k}_{||}}(z+p\,a)\Bigg]\,,
\end{aligned}
\tag{2.15}
$$

where $\epsilon_{\boldsymbol{k}_{||}} = -2t\,(\cos k_x a + \cos k_y a)$ and the sum in Eq. (2.15) runs over all pairs of $(\epsilon, \boldsymbol{k}_{||})$ that are occupied in the Slater determinant $|\Psi_0\rangle$.

The first equation has the form of a Schrœdinger equation that the single-particle wavefunctions $\phi_{\epsilon\boldsymbol{k}_{||}}(z)$ must satisfy, depending parametrically on $R(z)$. The second equation has been intentionally cast in the form of a map

$$
R_{j+1}(z) = F\left[R_j(z), R_j(z+a), R_j(z-a)\right]
$$
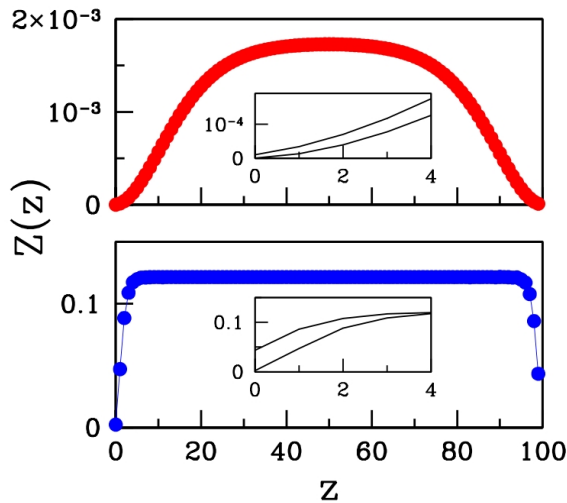
Figure 2.3: *The quasi-particle weight $Z(z) = R^2(z)$ as function of the coordinate z perpendicular to the surface (in units of the lattice spacing) for a 100-layer slab. The interaction parameter at $z = 0$ is $U_s = 20t$, while the bulk U is $15.98t$ in the upper panel and $15t$ in the lower one (while $U_c = 16$). The insets show the behavior of Z close to the two surfaces; the highest curve corresponding to the surface with bulk-like interactions, the other to $U_s = 20t$.*

whose fixed point we have verified to coincide with the actual solution of Eq. (2.15) in the parameter region of interest.

We can solve Eq. (2.14) and Eq. (2.15) through a two-step procedure. We first solve the Schrœdinger equation at fixed $R_j(z)$; next we find the new $R_{j+1}(z)$ using the old $R_j(z)$ and the newly determined wavefunctions $\phi_{\epsilon \boldsymbol{k}_{||}}(z)$. With the new $R_{j+1}(z)$, we repeat the above steps and iterate until convergence. Because of the large number of variational parameters, this iterative scheme is much more efficient than a direct minimization the energy E in Eq. (2.12).

In the case of z-independent Gutzwiller parameters, the solution of Eq. (2.14) and (2.15) goes back to the Brinkman-Rice result for the half-filled paramagnetic homogeneous HM. Looking at Table 1.1, we take the value $U_c = 16t$ for the Brinkman-Rice transition in the homogeneous cubic lattice as a reference value for our inhomogeneous calculation, and we study the behavior of the quasi-particle weight $Z(z)$ as a function of z for $U_{\text{bulk}} \lessapprox U_c$.

In Fig. 2.3 we plot $Z(z) = R^2(z)$ (the total spectral weight carried by quasi-particles), calculated as function of z (in units of the lattice spacing a) for $U_s = 20t$, for two different bulk values $15t$ and $15.98t$ of U below the critical Mott-transition value. Coming from the bulk, the quasi-particle weight $Z(z)$ decreases monotonically on approaching both surfaces, where it attains much smaller values than in bulk. As expected, the more correlated surface has a smaller quasi-particle weight, $Z(0) < Z(L)$. Note however that as long as the slab interior (the "bulk") remains metallic, the surface quasi-particle weight never vanishes no matter how large U_s[36]. Mathematically, this follows from Eq. (2.15), which is not satisfied by choosing $R(0) = 0$ while $R(z > 0) \neq 0$. Physically, some metallic character can always tunnel from the interior to the surface, as long as the bulk is metallic.
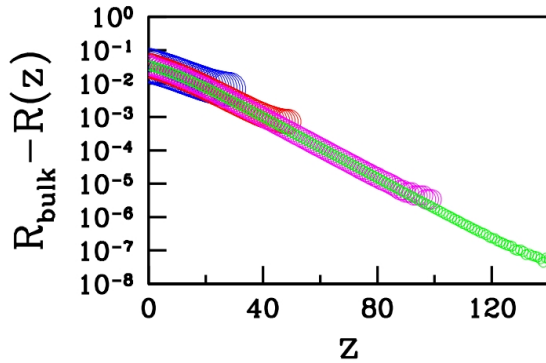
Figure 2.4: *Log scale plot of $R_{bulk} - R(z)$ versus z for $U = 15.99$, $U_s = 20t$ and for different thicknesses of the slab $L = 60, 100, 200, 400$.*

The quasi-particle weight approaches the surface with upward curvature when U is closest to U_c (see upper panel in Fig. 2.3) whereas the behavior is linear well below U_c, as found earlier within linearized DMFT [36]. We note that an upward curvature is in better accord with photoemission spectra of Rodolakis *et al.* on V_2O_3 [83]. The curvature becomes more manifest if the number of surface layers where $U_s > U$ is increased, as shown in Fig. 2.5.

Next, we analyze the dependence of $R(z)$ at large distance $1 \ll z \ll L/2$ below the surface. As Fig. 2.4 shows, we find no trace of a power law, and R is best fit by an exponential

$$R(z) = R_{bulk} + \left(R_{surf} - R_{bulk} \right) e^{-z/\xi}, \qquad (2.16)$$

where R_{bulk} is the bulk value (a function of U only) and $R_{surf} < R_{bulk}$. R_{surf} now depends on both U and on U_s, and vanishes only when R_{bulk} does at $U > U_c$. A detailed study by varying U and U_s shows that the surface "dead layer" thickness ξ depends only on bulk properties and diverges at the Mott transition as

$$\xi \sim (U_c - U_{bulk})^{-\nu}. \qquad (2.17)$$

Numerically we find $\nu = 0.53 \pm 0.3 \simeq 0.5$, a typical mean-field exponent [37]. The same conclusion can actually be drawn by analyzing Eqs. (2.14) and (2.15) deep inside the bulk. We note that the precise behavior at the outermost surface layers would in a real system depend on details, such as lack of electron-hole symmetry and/or surface dipoles, not included in our model.

Layer-resolved spectral function

In order to have a better connection with photoemission data, we compute a quantity that is naturally related to a bulk-sensitive photoemission experiment, which is the spectral function resolved in the layer index z of the crystal. If we indicate by $\boldsymbol{R}_\perp$
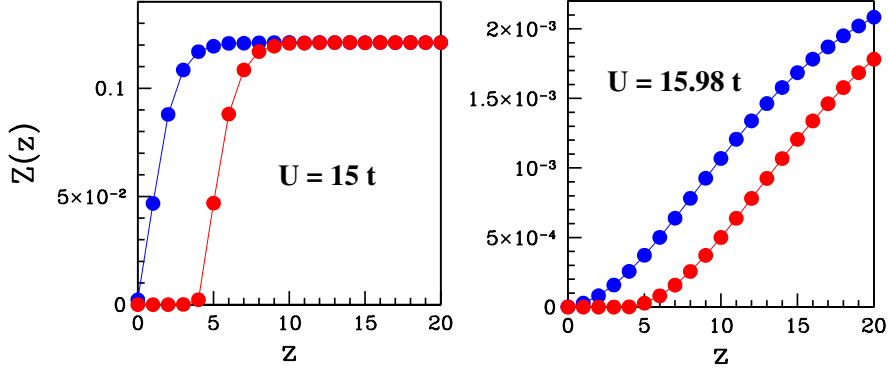
Figure 2.5: *Quasi-particle weight dependence on the distance z from the surface for two different bulk U values and for two cases: one where only the first layer has $U_s = 20\ t > U$ (upper curve in each panel), the other where five surface layers have $U_s = 20\ t$.*

the component of the lattice vector perpendicular to the crystal surface, this spectral function has the following definition.

$$A_-(z,\omega) = \frac{1}{A} \sum_{\boldsymbol{R}(\boldsymbol{R}_\perp = z)} \sum_n |\langle \phi_n^{(N-1)} | \hat{c}_{\boldsymbol{R}} | \phi_0^{(N)} \rangle|^2 \delta(\omega - \xi_{n0})\,. \qquad (2.18)$$

where $\hat{c}_{\boldsymbol{R}}$ is the creation operator on the lattice site $\boldsymbol{R}$. The above function measures the strength of the quasi-particle peak and Hubbard bands at every depth z below the crystal surface, and can therefore be compared, at least qualitatively, to the bulk-sensitive photoemission data of Mo [32] and Rodolakis *et al.* [33] for a paramagnetic metallic slab of vanadium sesquioxide near the transition to a paramagnetic insulator.

Exactly as the $\boldsymbol{k}$-resolved spectral function, $A_-(z,\omega)$ can be divided in two contributions. One, $A_-^{(\mathrm{qp})}(z,\omega)$, due to the coherent quasi-particle excitations, and the other, $A_-^{(\mathrm{Hub})}(z,\omega)$, due to the incoherent Hubbard bands. The second is not directly accessible through the GA, but can be retrieved by requiring that the sum of the coherent and incoherent spectral functions fulfills the sum-rule

$$\int A_-(z,\omega)d\omega = \int A_-^{(\mathrm{qp})}(z,\omega)d\omega + \int A_-^{(\mathrm{Hub})}(z,\omega)d\omega = n(z)\,, \qquad (2.19)$$

where $n(z)$ is the filling of layer z, which in our model is always equal to $1/2$ due to particle-hole symmetry. The coherent spectral function has the following expression

$$A_-^{(\mathrm{qp})}(z,\omega) = \frac{Z(z)}{A} \sum_{\boldsymbol{R}(\boldsymbol{R}_\perp = z)} \sum_n |\langle \Psi_{n,\mathrm{qp}} | \hat{c}_{\boldsymbol{R}} | \Psi_{0,\mathrm{qp}} \rangle|^2 \delta(\omega - \varepsilon_{n,\mathrm{qp}})\,, \qquad (2.20)$$

where $\Psi_{0,qp}$ is the ground-state Slater determinant built from the single-particle eigenstates that are solution of the coupled equations (2.14) and (2.15), while $\Psi_{n,qp}$ spans, from different n, all excited states with one particle removed from an eigenstate with energy $\varepsilon_{n,qp}$ and with a finite overlap with layer z.

If $U_{z\eta}^{\boldsymbol{k}_{\parallel}}$ is the unitary transformation diagonalizing the kernel of Eq. (2.14) with eigenvalues $\varepsilon_{\boldsymbol{k}_{\parallel},\eta}$ and occupations $f(\boldsymbol{k}_{\parallel},\eta)$, $A_{-}^{(qp)}(z,\omega)$ can be rewritten as

$$A_{-}^{(qp)}(z,\omega) = \frac{Z(z)}{A} \sum_{\boldsymbol{k}_{\parallel},\eta} f(\boldsymbol{k}_{\parallel},\eta) |U_{z\eta}^{\boldsymbol{k}_{\parallel}}|^2 \delta(\omega - \varepsilon_{\boldsymbol{k}_{\parallel},\eta}) \,. \qquad (2.21)$$

A good candidate for the incoherent spectral function, fulfilling the sum-rule (2.19) is the function

$$A_{-}^{(\mathrm{Hub})}(z,\omega) = \frac{1 - Z(z)}{A} \sum_{\boldsymbol{k}_{\parallel},\eta} f(\boldsymbol{k}_{\parallel},\eta) |\tilde{U}_{z\eta}^{\boldsymbol{k}_{\parallel}}|^2 \delta(\omega - \tilde{\varepsilon}_{\boldsymbol{k}_{\parallel}.\eta} - \Delta) \,. \qquad (2.22)$$

In the above expression, the wavefunction $\Psi_{0,\mathrm{Hub}}$ is a fictitious Slater determinant for the Hubbard bands. It can be built from the single-particle orbitals that are solutions of (2.14), where the double occupation and hopping renormalizations are computed from a Gutzwiller projector $(\hat{\mathbb{1}} - \hat{\mathcal{P}}(z))$ which is "orthogonal" to the quasi-particle projectors $\hat{\mathcal{P}}(z)$ minimizing the system ground-state energy.

It can be proved that the squared hopping renormalization factors resulting from this modified projector are equal to $1 - Z(z)$, while the fictitious double occupation of Hubbard bands is $\tilde{D} \approx (1 - Z)/4$. The eigen-energies $\tilde{\varepsilon}_{\boldsymbol{k}_{\parallel}.\eta}$ and unitary transformations $\tilde{U}_{z\eta}^{\boldsymbol{k}_{\parallel}}$ can be computed from the diagonalization of the modified Eq. (2.14), while the value of Δ is the difference between the average energy per site of Hubbard excitations and quasi-particles.

In spite of the fact that Eq. (2.22) is just a rough guess of the incoherent contribution to the spectral function, our predictions for $A_{-}(z,\omega)$, plotted in Fig. 2.7, show the clear difference in surface-sensitivity between the quasi-particle peak and the Hubbard bands which is evident also from the photoemission data of Fig. 2.8. Rodolakis *et al.* noted that the region of $\boldsymbol{k}$ space along the ΓZ line of the Brillouin zone of vanadium sesquioxide provides the largest contribution to the spectral weight of the system. The photoelectrons excited from this region are emitted around a direction normal to the (001) crystallographic plane of V_2O_3, so that the probing depth is maximized when the crystal is cleaved along that plane.

When instead the cleaving is along the (102) surface, the photoelectrons emitted normally to this surface provide a much smaller probing depth, as is pictorially shown in Fig. 2.6. As shown in Fig. 2.8, the incoherent part of spectrum is not subject to significant modifications with the change in cleaving plane, which instead greatly affects the strength of the quasi-particle peak.
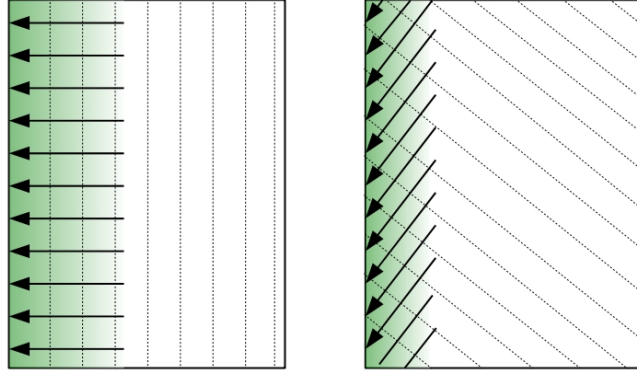
Figure 2.6: *Pictorial representation of the change in probing depth that occurs when the crystal of vanadium sesquioxide is cleaved along a different lattice plane. Above left, the (100) plane is perpendicular to the photoemission direction of the photoelectrons providing the most intense signal, while on the right the (102) cleaving is shown, with the wavevector of emitted photoelectrons forming an angle of 58.2° with the crystal surface. Only the properties of photoelectrons excited within the green shaded region can be probed.*
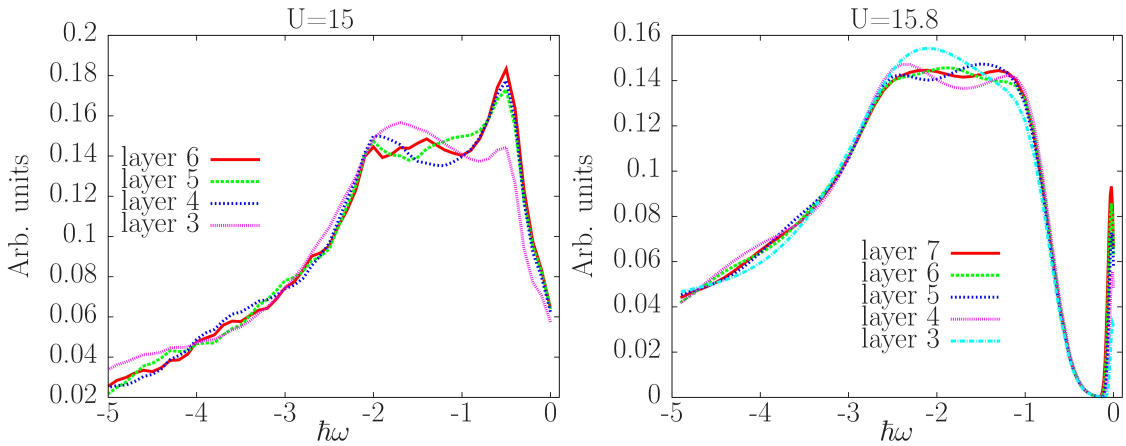
Figure 2.7: *GA result for $A_-(z, \omega)$ for the first few layers beneath the lattice surface, with a contribution of the Hubbard bands included through Eq. (2.22). For both panels, we used a slab of 200 layers, with a value of U equal for all layers. The left panel, where $U < U_c = 16t$, shows a more pronounced quasi-particle peak whose spectral weight saturates to the bulk value already after three layers. On the right panel, where $U \lessapprox U_c$, the healing length of the quasi-particle is larger than seven layers.*
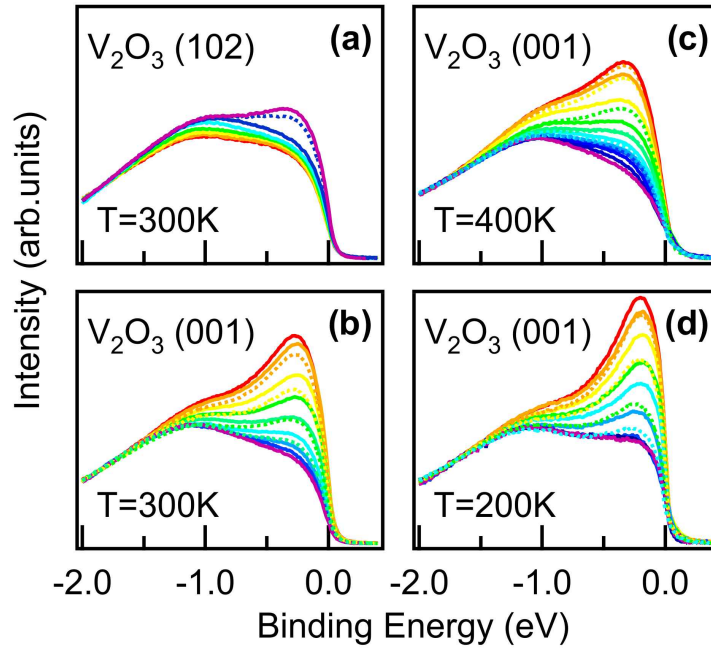
Figure 2.8: *Plot of photoemission intensity for a sample of vanadium sesquioxide cleaved along the (102) (panel a), and the (100) plane (panels b,c,d) and different temperatures. The colors correspond to different photoemission angles, from normal (red) to grazing (violet). The angle of $58.2°$ between the (102) and the (100) directions causes the probing depth in panel a to be diminished by an amount $58.2° \approx 1/2$ with respect to the one in panel b, so that the red curve shows the bulk quasi-particle peak only in the second case. The angle resolution around the direction normal to the surface is a further tool for varying the probing depth of detected photoelectrons. From reference [33].*
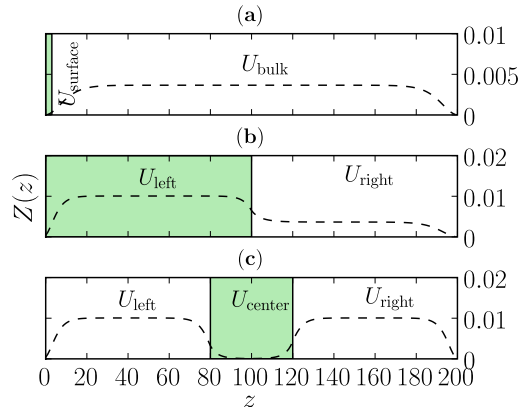
Figure 2.9: *The three different inhomogeneities studied in this paper: (a) free surface geometry, already discussed in Sect. 2.2 (b) junction between metals with different strength of correlation, (c) Mott (or strongly correlated metallic) slab sandwiched between metallic leads (sandwich geometry). The values for U in all the three cases shown are: (a) $U_{\mathrm{surface}} = 20t$, $U_{\mathrm{bulk}} = 15.9712t$; (b) $U_{\mathrm{left}} = 15.9198t$, $U_{\mathrm{right}} = 15.9712t$; (c) $U_{\mathrm{left}} = U_{\mathrm{right}} = 15.9198t$, $U_{\mathrm{center}} = 16.0288t$ (which is the case of a Mott central slab). In panel (c) the region with electron-electron interaction $U = U_{\mathrm{center}}$ is indicated by the green-shaded area.*

2.3 Investigation of other metal-insulator interfaces and junctions

Motivated by the qualitative success of the GA in depicting effects of strong correlations at the surface between a metal and vacuum, we applied the method elucidated in the previous section to different types of model interfaces that might be relevant for experiments: the junction between two different correlated metals and the tunneling between two metallic leads through a strongly correlated, possibly Mott insulating, region.

Although both cases were in fact previously studied by DMFT [37, 84, 85], the results were interpreted in contrasting ways. While Helmes *et al.* [37] concluded that the Mott insulator is impenetrable to the electrons coming from the metallic leads, Zenia *et al.* [85] drew the opposite conclusion that a conducting channel always opens up inside the insulator at sufficiently low temperature.

The present study, which is certainly less accurate than DMFT but can deal with much larger sizes, will also serve to clarify this issue. In particular, the large sizes allow us to address the asymptotic behavior and to identify the magnitude and interface role of the critical length associated with the bulk Mott transition.
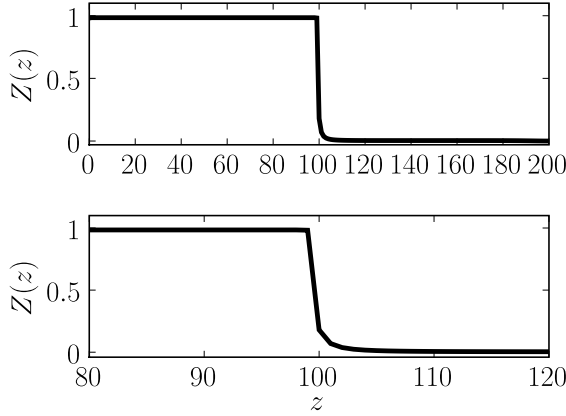
Figure 2.10: *Spatial dependence of $Z(z)$ for $U_{\text{left}} = 2t$ and $U_{\text{right}} = 15.9712t$. The lower panel shows the same data as the upper one but closer to the interface.*
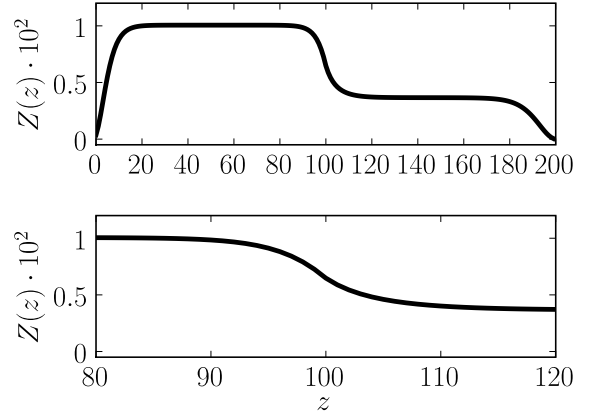
Figure 2.11: *Same as in Fig. 2.10, for $U_{\text{left}} = 15.9198t$ and $U_{\text{right}} = 15.9712t$.*

2.3.1 Geometry (b): Weakly correlated metal-strongly correlated metal interface

The junction between a metal and a Mott insulator or a strongly correlated metal was studied recently by Helmes, Costi and Rosch [37], who used the numerical renormalization group as a DMFT impurity solver. With our simpler method we can address a broader class of interfaces, including the general case of a correlated metal-correlated metal junction, with different values of electron-electron interaction in the left (U_{left}) and right (U_{right}) leads.

The system we consider, shown on Fig. 2.9(b), is made of two blocks of 100 layers each, with the junction center situated at $z = L/2$. Figs. 2.10 and 2.11 show the z dependence of the quasi-particle weight for fixed $U_{\text{right}} \simeq U_{\text{c}}$ and two different values of $U_{\text{left}} < U_{\text{right}}$. Even if $U(z)$ is changed stepwise from left to right, we find that the closer U_{left} is to U_{c}, the smoother the function $Z(z)$ for $z < L/2$.

On the right side of the junction, after a characteristic length ξ_{right}, the quasi-particle weight Z reaches exponentially its bulk value. We find for $z > L/2$ that the layer dependence of $R(z)$ is well represented by the form[1]

$$R(z) = R_{\text{right}} + (R_{\text{left}} - R_{\text{right}})\, e^{-(z-L/2)/\xi_{right}}. \tag{2.23}$$

The dependence of ξ_{right} on U_{right} is again given by Eq. (2.17), i.e

$$\xi_{\text{right}} \propto (U_{\text{c}} - U_{\text{right}})^{-\nu}\,, \tag{2.24}$$

---

[1]For a better fit see Eq. (B.13) with the minus sign.
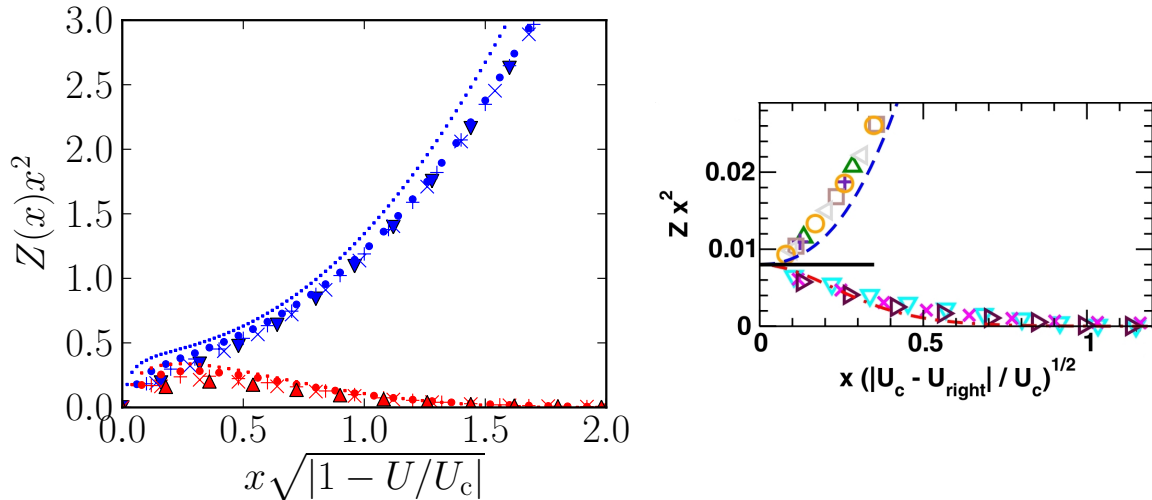
Figure 2.12: *Above left, plot of $Z(x)\,x^2$ versus the renormalized coordinate $x\,\sqrt{|1-U/U_c|}$ for $U < U_c$ (upper blue curves: $U = 15.7939t$ triangles, $U = 15.8424t$ crosses, $U = 15.9198t$ pluses, $U = 15.9712t$ points, $U = 15.9968$ tiny dots) and $U > U_c$ (lower red curves: $U = 16.2571t$ triangles, $U = 16.2035t$ crosses, $U = 16.1148t$ pluses, $U = 16.0511t$ points, $U = 16.0128$ tiny dots). This figure can be compared with the inset of Fig. 3 in reference [37], showed on the right, and displaying the same scaled results for various values of $U \gtrless U_c$, obtained with DMFT with a NRG impurity solver.*

with $\nu \approx 0.5$. By symmetry, the same holds in the left side too, upon interchanging the subscripts right and left.

Our results for weak U_{left} and $U_{\text{right}} \simeq U_c$ can be directly compared with those of Helmes *et al.* [37], who proposed that a strongly correlated slab (our right lead with $U_{\text{right}} \simeq U_c$), in contact with a non-interacting metal (our left lead), has a quasiparticle weight $Z(x)$ that, close to criticality, displays the scaling behavior

$$x^2\,Z(x) \simeq C\,f\left(x\left|\frac{U - U_c}{U_c}\right|^{1/2}\right), \tag{2.25}$$

where $f(0) = 1$ and x is the distance from the interface, translated in our notation $x = z - L/2$ and $U = U_{\text{right}}$. The prefactor $C \simeq 0.008$ and the asymptotic behavior $f(\zeta \to \infty) = 0.15\zeta^2$ of the scaling function were extracted by a DMFT calculation with a 40-layer correlated slab in contact with a 20-layer wide, almost uncorrelated metal [37].

In Fig. 2.12 we show the quantity $x^2\,Z(x)$ extracted by our Gutzwiller technique and plotted versus $x\,|1 - U/U_c|^{1/2}$ for different U's across the Mott transition value. The results are qualitatively similar to those of Ref. [37], but differs in two aspects.

First of all we find that $f(\zeta)$ defined in Eq. (2.25) shows a plateau only when

$$z_* \ll x \ll \left|1 - \frac{U}{U_{\rm c}}\right|^{-1/2}, \qquad (2.26)$$

where an approximate expression for the offset value z_* is given in Appendix B.2 (see Eqs. (B.14) and (B.27)). For $x \ll z_*$, $f(\zeta) \sim \zeta^2$ so that $Z(x)$ approaches its surface value at the interface. In our data the crossover between the two different regimes is clearly visible, unlike Ref. [37].

More importantly, the coefficient $C \simeq 0.08$ found by Helmes *et al.* [37] is almost two orders of magnitude smaller than ours, which is numerically around $\simeq 0.4$ [2]. In the same appendix we also show that, within the linearized DMFT approach introduced by Potthoff and Nolting [36] one would extract yet another value of the coefficient $C = 9/11 \sim 0.82$, of the same order as ours, and again larger than that found by Helmes *et al.* [37].

This disagreement is not just quantitative. Mainly because of the smallness of the prefactor, Helmes and coworkers [37] concluded that the strongly correlated slab with $U \simeq U_{\rm c}$ hence $Z_{\rm bulk} = Z(x \to \infty) \ll 1$ is very weakly affected by the proximity of the good metal, a conclusion later questioned by Zenia *et al.* [85], who however considered a different geometry.

Our results, as well as those that could be obtained by linearized DMFT, do not allow such drastic conclusion. Yet, since straight DMFT should be more reliable than either linearized DMFT or our Gutzwiller approach, it is likely that our $Z(x)$ is strongly overestimated and that Helmes *et al.*'s conclusions are basically correct. It seems worth investigating further this important question with full DMFT calculations on wider slabs.

2.3.2 Geometry (c): Correlated metal-Mott insulator (Strongly correlated metal)-correlated metal double junction

In this section we consider geometry (c) of figure 2.9, in which a strongly correlated slab of d layers is sandwiched between two weakly correlated metal leads, a setup already studied by DMFT [84, 85].

In Figs. 2.13, 2.14 and 2.15 we show the layer dependence of the quasi-particle weight for different values of the interaction parameters, the Hubbard U in the leads, $U_{\rm right} = U_{\rm left} < U_{\rm c}$, and in the central slab, $U_{\rm center} \overset{>}{\sim} U_{\rm c}$, and slab thickness d. From those results one can draw the following conclusions:

---

[2]The approximate analytical expressions discussed in Appendix B give a slightly larger value of 2/3, see Eqs. (B.19) and (B.30).
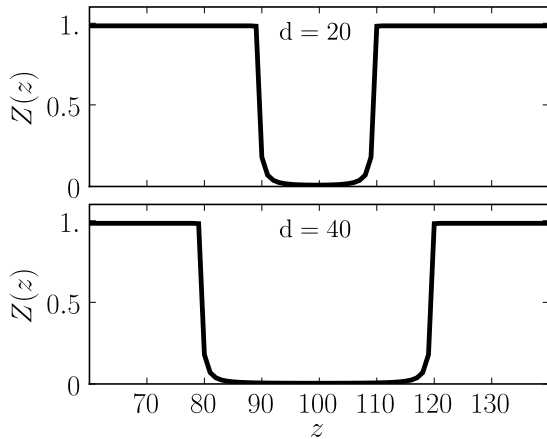
Figure 2.13: *Spatial dependence of $Z(z)$ for $U_{\text{left}} = U_{\text{right}} = 2t$ and $U_{\text{center}} = 15.9712t$. The upper panel refers to a central region of $d = 20$ layers, while the lower panel to $d = 40$*
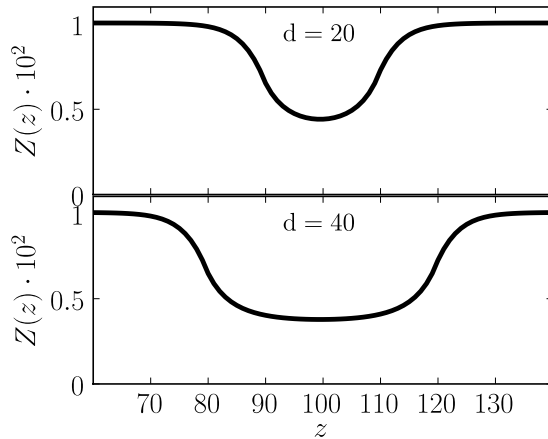
Figure 2.14: *Same as in Fig. 2.13, for $U_{\text{left}} = U_{\text{right}} = 15.9198t$ and $U_{\text{center}} = 15.9712t$.*

- For any finite thickness d, the quasi-particle weight in the central slab never vanishes, as better revealed in Figs. 2.16 and 2.17, even for $U_{\text{center}} > U_{\text{c}}$, fed as it is by the evanescent metallic quasi-particle strength from the metallic leads. This result agrees perfectly with recent DMFT calculations [85].

- For $U_{\text{center}} > U_{\text{c}}$, see Fig. 2.15, the minimum value Z_{min} in the central region decreases when d increases;

- The behavior of $Z(z)$ across the interface is smoother and smoother the closer and closer $U_{\text{right}} = U_{\text{left}}$ are to U_{center}.

Looking more in detail at Figs. 2.14, 2.15 and at the log-scale plots in Fig. 2.16 and 2.17, we can identify the characteristic differences between a Mott insulating slab and a strongly correlated metallic slab, when sandwiched between metallic leads. In a strongly correlated metallic slab, the central quasi-particle weight ultimately settles to the self-standing value it would have in a homogeneous system with $U = U_{\text{center}} < U_{\text{c}}$.

This value is independent of the junction width and of lead correlations. On the contrary, the quasi-particle weight inside the insulating slab is completely borrowed from the leads, and strongly depends therefore on their separation and correlation. What depends strictly on the central slab interaction $U_{\text{center}} > U_{\text{c}}$ is the quasi-particle decay length ξ_{center} from the lead to the center of the slab, which increases for increasing slab correlation according to the law $(U_{\text{center}} - U_{\text{c}})^{-\nu}$, with $\nu \approx 0.5$, a value that matches perfectly that found in section 2.2.

Figure 2.15: *Same as in Fig. 2.13, for $U_{\text{left}} = U_{\text{right}} = 15.9198t$ and $U_{\text{center}} = 16.0288t$.*

These considerations suggest that, if we look at the problem from a transport point of view, we are confronted with two completely different mechanisms. In a strongly correlated metallic central slab, ξ_{center} has the role of a screening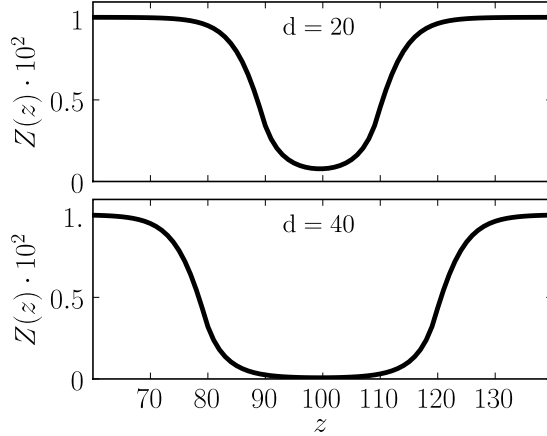 length, exactly the same role of ξ_{right} in section 2.3.1. If instead the central slab is insulating, the meaning of ξ_{center} becomes completely different, and it now becomes a tunneling length. No local quasi-particle peak would survive in a homogeneous Mott insulator: the residual quasi-particle peak that we find inside the central slab is therefore the evanescent lead electron wavefunction that tunnels into the slab.

A special case occurs exactly at criticality when $U_{\text{center}} \approx U_{\text{c}}$, where neither of the previous two pictures is valid. The crossover from the two opposite exponential decays describing either screening or tunneling is characterized by the absence of any characteristic length, which results in a power law variation of the quasi-particle strength upon the slab width d

$$ Z_{\min}(d) \sim \frac{1}{d^2} + O\left(\frac{1}{d^3}\right) , \qquad (2.27) $$

pictorially represented by the plots in Fig. 2.18. A simple analytical justification of the critical $1/d^2$ behavior is provided in Appendix B. We find that the $1/d^2$ behavior is, within our accuracy, independent of the specific properties of the metallic leads, while its prefactor, as well as the sub-leading terms in Eq. (2.27) do depend on them, as it can be understood by looking at Fig. 2.19.
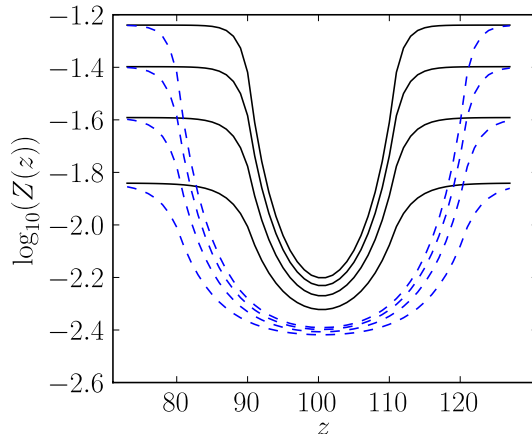
Figure 2.16: *Logarithm of the quasi-particle weight Z as a function of layer index z for a 20-sites wide (solid line) and 40-sites wide (dashed line) strongly correlated metallic slab ($U = 15.9712t < U_c$) sandwiched between two weakly correlated metal leads (with $U = 15.88438t$, $15.79388t$, $15.67674t$, $15.53236t$.). The entire system is 200-sites wide; the interfaces between the leads and the slab are at $z = 80$ and $z = 120$ for the 40-sites wide slab and $z = 90$ and $z = 110$ for the 20-sites wide slab. The figure shows that for increasing slab width the quasi-particle weight goes to a value that is independent of lead correlation.*

2.4 Final remarks

In this chapter we discussed how the spatial inhomogeneity of interfaces affects the physics of a strongly correlated electron system. To address this problem, we extended the conventional GA technique to account for inhomogeneous Hamiltonian parameters.

Moreover, to efficiently cope with the larger number of variational parameters in comparison with the homogeneous case, we derived iterative equations fully equivalent to the saddle point equations that identify the optimal variational solution, similarly to what is commonly done within unrestricted HF or *ab-initio* Local Density Approximation (LDA) calculations. These iterative equations can be solved without much effort for very large system sizes; an advantage with respect to more rigorous approaches, like e.g. DMFT calculations, which are numerically feasible only for small systems.

We applied the method to various interface geometries in three dimensions; specifically the interface of a strongly correlated metal with the vacuum, the interface between two differently correlated metals and the junction between two weakly correlated metals sandwiched by a strongly correlated slab. All these geometries had
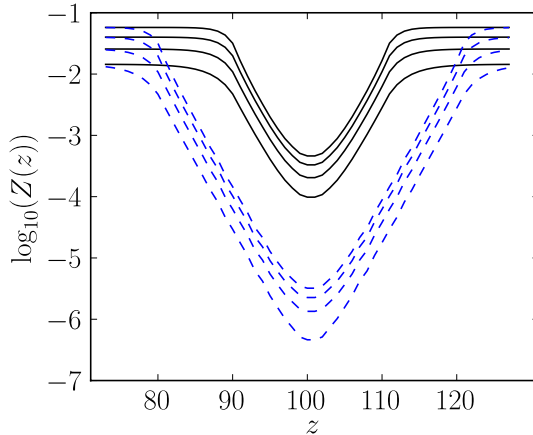
Figure 2.17: *Same as in Fig. 2.16, but the central layers have now $U = 16.1148 > U_c$. In this case the quasi-particle weight at the center of the junction is strongly dependent both on barrier width and on the strength of electron correlation in the leads. The central layer remains metallic for arbitrary values of $U > U_c$, but its quasi-particle weight decreases exponentially with the slab width.*

been already studied by DMFT [36, 37, 80, 81, 84–87], which allowed us to directly compare our results with more rigorous ones, thus providing a test on the quality of our approximation, which is then applied to much larger sizes.

Our main result is that the effects of an interface decay exponentially in the interior of a strongly correlated system on a very long length-scale proportional to the correlation length of the incipient Mott transition, a bulk property independent upon the details of the interface. [34] In particular, at the surface of a strongly correlated metal we find a significant suppression of the metallic properties, e.g. of the quasi-particle weight, which persists at a large depth controlled by the Mott transition correlation length. This results in the appearance of a "dead layer" [34], due to effective correlations being larger on the surface than in the bulk, which is consistent with photoemission experiments [83].

Conversely, metallic features from a metal lead penetrate inside a Mott insulator within a depth that, once again, diverges on approaching the Mott transition. As a consequence, a conducting channel always exists inside a Mott insulating slab contacted to two metallic leads, in agreement with recent DMFT analyses [85], implying a finite conductance at zero bias and temperature that decays fast on increasing both external parameters on an energy scale exponentially small in the length of the slab in units of the Mott transition correlation length.

The method that we have developed is very simple and flexible, so it can in principle be applied to a variety of realistic situations of current interest, not only for studying
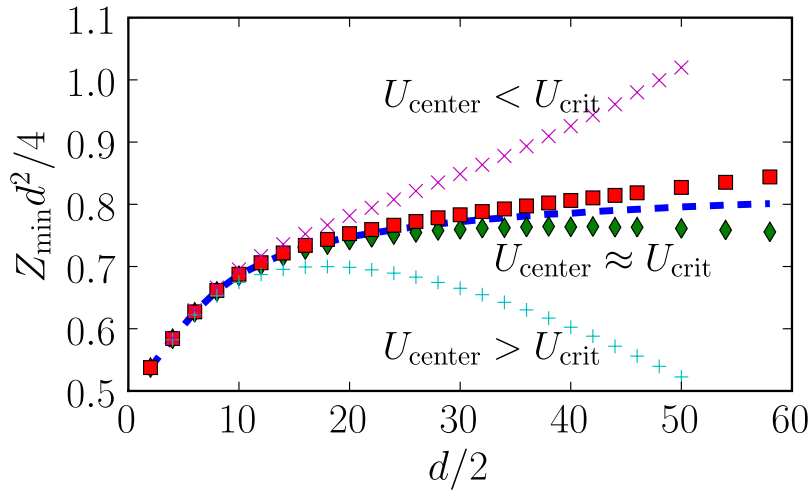
Figure 2.18: *Numerical results for $Z_{\min}d^2/4$ and $U_{\text{center}} = 15.999t$ (crosses), $16t$ (squares), $16.0002t$ (dashed line), $16.0004t$ (diamonds), $16.002t$ (pluses) for the sandwich geometry with $U_{\text{left}} = U_{\text{right}} = 2t$. The constant value approached for $U = 16.0002t \approx U_{\text{c}}$ and large junction width should be compared to the one we find in Eq. (B.57).*

interfaces but also for more general inhomogeneities, as those arising by impurities or other defects, and can easily incorporate additional features like magnetism, which we have disregarded throughout this work.
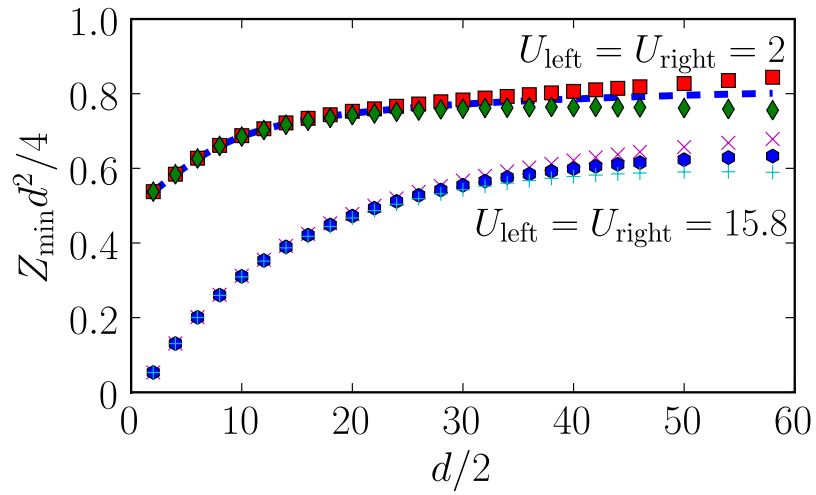
Figure 2.19: *Numerical results for $Z_{\min}d^2/4$ for $U_{\text{left}} = U_{\text{right}} = 2t$ [$U_{\text{center}} = 16t$ (squares), 16.0002t (dashed line), 16.0004t (diamonds)], and for $U_{\text{left}} = U_{\text{right}} = 15.8t$ [$U_{\text{center}} = 16.0002t$ (crosses), 16.0004t (hexagons), 16.0006t (pluses)]. The stronger lead correlation in the lower curves pushes the plateau of the function $Z_{\min}d^2/4$ towards larger values of d.*

Chapter 3

Basic concepts of Density Functional Theory

This chapter is devoted to the introduction to Density Functional Theory (DFT) as a tool for electronic structure simulations in crystals and molecules. We start by defining the density functional both through Legendre-transformation and constrained search, and by providing its parametrization in terms of the wavefunction of an auxiliary system of non-interacting particles and a scheme for its self-consistent minimization. We discuss the various terms composing the density functional of interacting electrons, and the most widely used approximations for its exchange and correlation part. The topics of this chapter are preparatory for the definition of the Gutzwiller Density Functional in Chapt. 4.

3.1 The electronic Hamiltonian for crystalline and molecular systems

The Hamiltonian for the electronic degrees of freedom of an interacting electron system in an external electrostatic potential can be written as the sum of three operators

$$\hat{H} = \hat{T} + \hat{V}_{\text{ee}} + \hat{V}_{\text{ext}} \, . \tag{3.1}$$

The first two operators, the kinetic operator $\hat{T}$ and the electron-electron interaction operator $\hat{V}_{\text{ee}}$ are independent of the system of interest, and can be written in first-quantized form as

$$\hat{T} = -\frac{\hbar^2}{2m} \sum_{i=1}^{N} \hat{\nabla}_i^2 \, , \tag{3.2}$$

$$\hat{V}_{\text{ee}} = \frac{1}{2} \sum_{i \neq j} \frac{e^2}{|\hat{\boldsymbol{r}}_i - \hat{\boldsymbol{r}}_j|} \, . \tag{3.3}$$

All differences between one fermionic system and another are included in the external potential, which is caused by the positive ions of the molecule or crystal of interest, treated as fixed within the Born-Oppenheimer approximation [88]. The explicit form for $\hat{V}_{\text{ext}}$ is

$$\hat{V}_{\text{ext}} = \int V(\boldsymbol{r}) \hat{n}(\boldsymbol{r}) d\boldsymbol{r} \, , \tag{3.4}$$

where $\hat{n}(\boldsymbol{r}) = \sum_{i=1}^{N} \delta(\boldsymbol{r} - \hat{\boldsymbol{r}}_i)$ is the density operator, whose expectation value on the fermionic wavefunction $|\Psi\rangle$ of the ground-state yields the electronic density of the system

$$n_\Psi(\boldsymbol{r}) = \langle \Psi | \hat{n}(\boldsymbol{r}) | \Psi \rangle = N \sum_{\sigma_i \dots \sigma_N} \int d\boldsymbol{r}_1 \dots d\boldsymbol{r}_N |\Psi(\boldsymbol{r}, \sigma_1; \boldsymbol{r}_2 \sigma_2; \dots; \boldsymbol{r}_N \sigma_N)|^2 \, . \tag{3.5}$$

3.2 Density Functional from Legendre transformation

From Eq. (3.1) and Eq. (3.4) it is clear that, in spite of the enormous number of many-body wavefunctions that compose the Hilbert space where the minimization Eq. (1.1) is performed, and in spite of the fact that the real-space representation of the ground-state wavefunction depends on N electronic coordinates, the ground-state energy of the system is a functional of a simple local scalar function of the coordinate $\boldsymbol{r}$, which is the external potential.

If we indicate with Ψ_{GS} the wavefunction minimizing the expectation value of the Hamiltonian,

$$E_{\text{GS}}[V_{\text{ext}}] = \langle \Psi_{\text{GS}}|\hat{T} + \hat{V}_{\text{ee}}|\Psi_{\text{GS}}\rangle + \int V_{\text{ext}}(\boldsymbol{r})n_{\Psi_{\text{GS}}}(\boldsymbol{r})d\boldsymbol{r}\,. \tag{3.6}$$

The functional $E_{\text{GS}}[V_{\text{ext}}]$ is also differentiable, by virtue of the Hellman-Feynman theorem it follows that

$$\frac{\delta E_{\text{GS}}[V_{\text{ext}}(\boldsymbol{r})]}{\delta V_{\text{ext}}(\boldsymbol{r})} = n_{\Psi_{\text{GS}}}(\boldsymbol{r})\,. \tag{3.7}$$

Combining Eq. (3.6) and Eq. (3.7) we see that the energy functional provides also a map between external potentials and ground-state densities. Hohenberg and Kohn [1] proved that this map is invertible, which means that any non-negative function $n(\boldsymbol{r})$ determines up to an additive constant the external potential that generates it as its ground-state density.

Their result enables us to define the Hohenberg-Kohn functional F_{HK} from the Legendre transformation of $E_{\text{GS}}[V_{\text{ext}}(\boldsymbol{r})]$

$$F_{\text{HK}}[n(\boldsymbol{r})] = E_{\text{GS}}[V_{\text{ext}}(\boldsymbol{r})] - \int \frac{\delta E_{\text{GS}}[V_{\text{ext}}(\boldsymbol{r})]}{\delta V_{\text{ext}}(\boldsymbol{r})}V_{\text{ext}}(\boldsymbol{r})d\boldsymbol{r} =$$
$$= E_{\text{GS}}\{V_{\text{ext}}[n(\boldsymbol{r})]\} - \int n(\boldsymbol{r})V_{\text{ext}}(\boldsymbol{r})d\boldsymbol{r}\,, \tag{3.8}$$

which depends no longer on the external potential $V_{\text{ext}}(\boldsymbol{r})$, but only on the density $n(\boldsymbol{r})$.

By adding the Hohenberg-Kohn functional and the external potential contribution to the ground-state energy, we are able to write E_{GS} as the minimum of a density functional

$$E_{\text{GS}}[n(\boldsymbol{r})] = \min_{n(\boldsymbol{r})} \mathcal{F}[n(\boldsymbol{r})]\,, \tag{3.9}$$

$$\mathcal{F}[n(\boldsymbol{r})] = \left\{ F_{\text{HK}}[n(\boldsymbol{r})] + \int V_{\text{ext}}(\boldsymbol{r})n(\boldsymbol{r}) \right\}\,. \tag{3.10}$$

If we restrict to density variations preserving the number of particles ($\int n(\boldsymbol{r})d\boldsymbol{r} = N$) and add the reasonable – though apparently to date unproven – assumption that the Hohenberg-Kohn functional is differentiable at constant particle density, its density derivative provides the inverse map from density to potentials. When computed for $n(\boldsymbol{r})$ equal to the ground-state density $n_{\text{GS}}(\boldsymbol{r}) = n_{\Psi_{\text{GS}}}(\boldsymbol{r})$, it is equivalent the stationary condition for the ground-state energy

$$\left.\frac{\delta F_{\text{HK}}[n(\boldsymbol{r})]}{\delta n(\boldsymbol{r})}\right|_{n(\boldsymbol{r})=n_{\text{GS}}(\boldsymbol{r})} = V_{\text{ext}}(\boldsymbol{r})\,. \tag{3.11}$$

An important remark about the proof of the Hohenberg and Kohn theorem is that the one-to-one correspondence between densities and potentials, up to an additive constant, is only valid for densities that are *pure state v-representable* (also referred to simply as *v-representable*), i.e. that can be computed from the ground-state wavefunction of an interacting Hamiltonian in some local external potential.

It is possible to find examples [50] of simple densities that do not have this property, and that can arise only from an ensemble of degenerate ground-states of a Hamiltonian with a suitable local potential. This property, called *ensemble v-representability*, is rigorously granted only for densities on a lattice [89], while is itself an assumption for continuous systems.

3.2.1 Kohn-Sham decomposition of the Hohenberg-Kohn functional

The consequence of the Hohenberg-Kohn definition of the Density Functional is that the knowledge of the universal functional $F_{\mathrm{HK}}[n(\boldsymbol{r})]$ would imply in principle the possibility of finding the ground-state density of any electronic system in a local external potential, which in turn would mean the knowledge of the electronic structure of all molecules and crystals.

Unfortunately, and not surprisingly in view of the astonishing generality of the previous statement compared to the complexity of the many body problem, the exact knowledge of $F_{\mathrm{HK}}[n(\boldsymbol{r})]$ is not affordable for most relevant physical systems. The formal definition provided by Eq. (3.30) is in most cases inapplicable, and in any case equivalent to using the Rayleigh-Ritz variational principle Eq. (1.1) directly for the computation of the ground-state energy.

In their original work Hohenberg and Kohn decomposed $F_{\mathrm{HK}}[n(\boldsymbol{r})]$ as a sum of the classical Hartree electron-electron interaction functional $E_{\mathrm{H}}[n(\boldsymbol{r})]$ plus a term $G[n(\boldsymbol{r})]$ including kinetic energy and all quantum corrections to the interaction

$$F_{\mathrm{HK}}[n(\boldsymbol{r})] = E_{\mathrm{H}}[n(\boldsymbol{r})] + G[n(\boldsymbol{r})]\,, \tag{3.12}$$

where

$$E_{\mathrm{H}}[n(\boldsymbol{r})] = \int \frac{n(\boldsymbol{r})n(\boldsymbol{r}')}{|\boldsymbol{r} - \boldsymbol{r}'|} d\boldsymbol{r} d\boldsymbol{r}'\,, \tag{3.13}$$

and where $G[n(\boldsymbol{r})]$ was approximated by the Thomas-Fermi expression valid for slowly-varying densities.

A parametrization of the Hohenberg and Kohn functional providing more physical insight than Eq. (3.12) was found by Kohn and Sham. Following their work we can further decompose the functional $G[n(\boldsymbol{r})]$ into a kinetic contribution $T_s[n(\boldsymbol{r})]$ and an exchange and correlation contribution $E_{\mathrm{xc}}[n(\boldsymbol{r})]$. The kinetic functional can be

defined from constrained-search as

$$T_s[n(\boldsymbol{r})] = \min_{\Psi \to n(\boldsymbol{r})} \langle \Psi | \hat{T} | \Psi \rangle \,. \tag{3.14}$$

Being the kinetic operator $\hat{T}$ a sum of single-particle operators, the wavefunction yielding the minimum expectation value at fixed density in Eq. (3.14) must be a Slater determinant. The exchange-correlation functional is simply defined as the difference

$$E_{\mathrm{xc}}[n(\boldsymbol{r})] = F_{\mathrm{HK}}[n(\boldsymbol{r})] - T_s[n(\boldsymbol{r})] - E_{\mathrm{H}}[n(\boldsymbol{r})] \,, \tag{3.15}$$

an expression which is of little help for practical calculations.

A reasonable approximation to $E_{\mathrm{xc}}[n(\boldsymbol{r})]$ comes from the knowledge of the physical properties of the uniform electron gas. The widely known Local Density Approximation to the exchange-correlation functional, prescribes to compute the latter as the integral over volume of an energy-density which is equal, at every point $\boldsymbol{r}$ in space, to the exchange-correlation energy-density $n(\boldsymbol{r})\epsilon_{\mathrm{xc}}^{(\mathrm{eg})}[n(\boldsymbol{r})]$ of a uniform electron gas of density $n^{(\mathrm{eg})} = n(\boldsymbol{r})$.

$$E_{\mathrm{xc}}[n(\boldsymbol{r})] \approx \int n(\boldsymbol{r})\epsilon_{\mathrm{xc}}^{(\mathrm{eg})}[n(\boldsymbol{r})]d\boldsymbol{r} \,. \tag{3.16}$$

The value of $\epsilon_{\mathrm{xc}}^{(\mathrm{eg})}[n(\boldsymbol{r})]$ was parametrized from the Diffusion Quantum Monte Carlo data of Ceperley and Alder [6] and from the analytical high-density expansion of Gell-Mann and Brückner [4].

In spite of neglecting the dependence of exchange and correlation energy from density fluctuations in space, LDA reveals to be a good approximation also for a variety of physical systems where the density is not slowly-varying.

The whole Kohn-Sham decomposition of the Density Functional reads finally

$$\mathcal{F}[n(\boldsymbol{r})] = T_s[n(\boldsymbol{r})] + E_{\mathrm{H}}[n(\boldsymbol{r})] + E_{\mathrm{xc}}[n(\boldsymbol{r})] + \int V_{\mathrm{ext}}(\boldsymbol{r})n(\boldsymbol{r})d\boldsymbol{r} \,. \tag{3.17}$$

The introduction of the kinetic term $T_s[n(\boldsymbol{r})]$ suggests that the minimization of the functional Eq. (3.17) for interacting electrons can be performed by considering an auxiliary system of non-interacting fermions, of which $T_s[n(\boldsymbol{r})]$ is the universal Hohenberg-Kohn functional.

The Density Functional for non-interacting particles

$$\mathcal{F}_{\mathrm{KS}}[n(\boldsymbol{r})] = T_s[n(\boldsymbol{r})] + \int V_{\mathrm{KS}}(\boldsymbol{r})n(\boldsymbol{r})d\boldsymbol{r} \,, \tag{3.18}$$

involves also an external potential $V_{\mathrm{KS}}(\boldsymbol{r})$ which we assume can be chosen so that the minimum of $\mathcal{F}_{\mathrm{KS}}[n(\boldsymbol{r})]$ is achieved for a density equal to the ground-state density $n_{\mathrm{GS}}(\boldsymbol{r})$ of the functional $\mathcal{F}[(\boldsymbol{r})]$ for interacting electrons.

When $n(\boldsymbol{r}) = n_{\mathrm{GS}}(\boldsymbol{r})$, $V_{\mathrm{KS}}(\boldsymbol{r})$ can be operatively defined by equating the right-hand sides of the two stationary conditions

$$\left.\frac{\delta T_s[n(\boldsymbol{r})]}{\delta n(\boldsymbol{r})}\right|_{n(\boldsymbol{r})=n_{\mathrm{GS}}(\boldsymbol{r})} = -V_{\mathrm{KS}}(\boldsymbol{r}) \tag{3.19}$$

$$\left.\frac{\delta T_s[n(\boldsymbol{r})]}{\delta n(\boldsymbol{r})}\right|_{n(\boldsymbol{r})=n_{\mathrm{GS}}(\boldsymbol{r})} = -V_{\mathrm{ext}}(\boldsymbol{r}) - \left.\frac{\delta\{E_{\mathrm{H}}[n(\boldsymbol{r})] + E_{\mathrm{xc}}[n(\boldsymbol{r})]\}}{\delta n(\boldsymbol{r})}\right|_{n(\boldsymbol{r})=n_{\mathrm{GS}}(\boldsymbol{r})}, \tag{3.20}$$

with the result

$$V_{\mathrm{KS}}[n(\boldsymbol{r})] = V_{\mathrm{ext}}(\boldsymbol{r}) + V_{\mathrm{H}}[n(\boldsymbol{r})] + V_{\mathrm{xc}}[n(\boldsymbol{r})]. \tag{3.21}$$

The knowledge of the Kohn-Sham potential enables us to minimize $\mathcal{F}_{\mathrm{KS}}[n(\boldsymbol{r})]$, given an initial density $n(\boldsymbol{r})$, by means of the following iterative procedure:

1. compute $V_{\mathrm{KS}}(\boldsymbol{r})$ corresponding to $n(\boldsymbol{r})$ from Eq. (3.21) and insert it into Eq. (3.18) in order to define the non-interacting Density Functional $\mathcal{F}_{\mathrm{KS}}[n(\boldsymbol{r})]$;

2. minimize $\mathcal{F}_{\mathrm{KS}}[n(\boldsymbol{r})]$ by diagonalizing the quadratic hamiltonian $\hat{T} + \hat{V}_{\mathrm{KS}}$ and by constructing the Slater determinant $|\Psi_0\rangle$ of the N lowest-energy single-particle states $\phi_{i\sigma}(\boldsymbol{r})$;

3. retrieve the minimizing density $n_{\mathrm{GS}}(\boldsymbol{r})$ through Eq. (3.5), which in the case of a Slater determinant is equivalent to

$$n(\boldsymbol{r}) = \sum_{i=1}^{N}\sum_{\sigma} |\phi_{i\sigma}(\boldsymbol{r})|^2 \, ; \tag{3.22}$$

4. feed $n(\boldsymbol{r})$ back into Eq. (3.21) and repeat the procedure until convergence.

The final ground-state energy of the system can be computed from the eigenvalues ε_η of the occupied single-particle orbitals of the auxiliary system[1]

$$E_{\mathrm{GS}} = \sum_{\eta=1}^{N}\varepsilon_\eta + E_{\mathrm{H}}[n_{\mathrm{GS}}(\boldsymbol{r})] + E_{\mathrm{xc}}[n_{\mathrm{GS}}(\boldsymbol{r})] - \int n_{\mathrm{GS}}(\boldsymbol{r})[V_{\mathrm{H}}(\boldsymbol{r}) + V_{\mathrm{xc}}(\boldsymbol{r})]d\boldsymbol{r} \, , \tag{3.23}$$

where the self-consistent potentials $V_{\mathrm{H}}(\boldsymbol{r})$ and $V_{\mathrm{xc}}(\boldsymbol{r})$ are computed at convergence.

---

[1]In density functional calculations one must add to E_{GS} also the electrostatic energy of the ions, which depends only on their position, while it is independent, within Born-Oppenheimer Approximation, from the electronic degrees of freedom.

The Kohn-Sham eigenvalues ε_η and eigenvectors do not have in general any particular physical meaning, since they refer to a fictitious system of particles which is linked to the real physical system only by having its same ground-state density. For a finite system, such as an atom or molecule, the eigenvalue of the highest-occupied Kohn-Sham eigenvector can be shown to be equal to minus the ionization energy, which governs the long-distance decay of the density profile.

We end this section by remarking two main requirements – silently taken for granted in most electronic structure calculations – that we need for the electronic systems under study in order to validate the self-consistent procedure above, and by discussing their range of validity.

Non-interacting v-representability

It is not always possible to find a local potential such that the Kohn-Sham functional Eq. (3.18) for non-interacting particles has the same minimizing density as the Density Functional Eq. (3.17). Every ground-state density $n_{\mathrm{GS}}(\boldsymbol{r})$ of the interacting problem that minimizes the non-interacting functional with a suitable $V_{\mathrm{KS}}(\boldsymbol{r})$, is said to be non-interacting v-representable.

Without non-interacting v-representability, which is a stronger condition than v-representability, the first step of the Kohn-Sham iterative minimization is meaningless. Unfortunately this property is not granted for every density and is in general taken as an assumption.

Even given this property, no-one expects the density dependence of $V_{\mathrm{KS}}(\boldsymbol{r})$ to be trivial, since it has to mimic all the effects of a non-local operator as the electron-electron interaction Hamiltonian. This is why the decomposition Eq. (3.21) is deceivingly simple, hiding in $V_{\mathrm{xc}}(\boldsymbol{r})$ all the enormous difficulties of defining an accurate Kohn-Sham potential.

Non-interacting N-representability

The third step of the iterative minimization requires that the ground-state density $n_{\mathrm{GS}}(\boldsymbol{r})$, which comes from the true N-particle ground-state wavefunction of the interacting system, should be generated also by a suitable Slater determinant of N particles.

This requirement, known as non-interacting N-representability, was proved to be fulfilled by every function $n(\boldsymbol{r})$ with the properties

$$n(\boldsymbol{r}) \geq 0 \tag{3.24}$$

$$\int n(\boldsymbol{r}) d\boldsymbol{r} = N \tag{3.25}$$

$$\int \frac{|\nabla n(\boldsymbol{r})|^2}{n(\boldsymbol{r})} d\boldsymbol{r} < \infty \,, \tag{3.26}$$

i.e for every non-negative $n(\boldsymbol{r})$ arising from a system of N particles and with a derivative satisfying a mild criterion of smoothness [90, 91]. The conditions (3.24) to (3.26) are expected to be true for all ground-state densities arising from reasonable external potentials.

3.2.2 Local Spin Density approximation

The most simple generalization of LDA, which is the Local Spin Density Approximation (LSDA), introduces two spin-dependent densities $n_\uparrow(\boldsymbol{r})$ and $n_\downarrow(\boldsymbol{r})$ as minimization variables for the density functional. The two spin densities enter the definition of the kinetic functional

$$T_s[n_\uparrow(\boldsymbol{r}), n_\downarrow(\boldsymbol{r})] = \min_{\Psi \to n_\uparrow(\boldsymbol{r}), n_\downarrow(\boldsymbol{r})} \langle \Psi | \hat{T} | \Psi \rangle; \,, \tag{3.27}$$

where the ground-state wavefunction of auxiliary non-interacting particles is explicitly allowed to be spin polarized.

Accordingly, the Local Density exchange-correlation functional is generalized to

$$E_{\mathrm{xc}}^{(\mathrm{LSDA})}[n_\uparrow(\boldsymbol{r}), n_\downarrow(\boldsymbol{r})] = \int n(\boldsymbol{r}) \epsilon_{\mathrm{xc}}^{(\mathrm{eg})}[n_\uparrow(\boldsymbol{r}), n_\downarrow(\boldsymbol{r})] d\boldsymbol{r} \,, \tag{3.28}$$

where $\epsilon_{\mathrm{xc}}^{(\mathrm{eg})}[n_\uparrow(\boldsymbol{r}), n_\downarrow(\boldsymbol{r})]$ is the exchange-correlation energy per particle of a uniformly polarized electron gas. From the functional derivatives of the above functional, added to the Hartree and external potential, one can compute the spin-resolved Kohn-Sham potentials $V_{\mathrm{KS}}^{(\uparrow)}(\boldsymbol{r})$ and $V_{\mathrm{KS}}^{(\downarrow)}(\boldsymbol{r})$.

Within this scheme, Density Functional Theory (DFT) can be generalized to electronic systems in an external space-dependent, axial magnetic field $B_{\mathrm{ext}}^{(z)}(\boldsymbol{r})$. In the absence of a magnetic field driving the magnetization, LSDA can account for the spontaneous breaking of spin-symmetry in ferromagnets and antiferromagnets. Even in paramagnetic systems, the introduction of spin densities can be helpful in providing more flexibility to the functional minimization, which is carried out in a wider functional space.

As a critique of LSDA, it is important to remember that the result of the Hohenberg and Kohn theorem cannot be applied as such to ground-state spin densities. This is due to the fact that one can in general choose couples of $V_{\text{ext}}^{(\uparrow)}$ and $V_{\text{ext}}^{(\downarrow)}$ differing by more than a constant shift that result in the same ground-state wavefunction.

Starting from the spin-resolved version of the stationary equations Eq. (3.11), Vignale [92] argued that the non-uniqueness of the external potentials yielding a particular set of spin densities implies that in general the spin-resolved Hohenberg-Kohn functional $F_{\text{HK}}[n_{\uparrow}(\boldsymbol{r}), n_{\downarrow}(\boldsymbol{r})]$ is a non-differentiable functional of spin-densities.

One, often underestimated, limitation of the smooth LSDA functional is of not being able to describe correctly physical observables for which this non-differentiability has a key role. One of these is the spin gap of half-metallic ferromagnets.

3.3 Density Functional Theory from constrained search

An alternative way of deriving the Hohenberg and Kohn functional was proposed independently by Levy [93, 94] and Lieb [95]. They converted the Rayleigh-Ritz variational principle for the wavefunction into a variational principle for the density through a constrained minimization at fixed density $n(\boldsymbol{r})$

$$E_{\text{GS}}[V_{\text{ext}}(\boldsymbol{r})] = \min_{n(\boldsymbol{r})} \left\{ \min_{\Psi \to n(\boldsymbol{r})} \langle \Psi | \hat{T} + \hat{V}_{\text{ee}} | \Psi \rangle + \int V_{\text{ext}}(\boldsymbol{r}) n(\boldsymbol{r}) \right\} . \tag{3.29}$$

By comparing Eq. (3.9) with Eq. (3.29), we can find the constrained-search definition of the Hohenberg-Kohn functional, i.e.

$$F_{\text{HK}}[n(\boldsymbol{r})] = \min_{\Psi \to n(\boldsymbol{r})} \langle \Psi | \hat{T} + \hat{V}_{\text{ee}} | \Psi \rangle , \tag{3.30}$$

which is, as expected, independent of the external potential V_{ext}. The stationary condition for the ground-state energy implies that the Hohenberg-Kohn functional is differentiable, and provides through Eq. (3.11) the map from density to external potential.

The whole Kohn-Sham decomposition of the density functional can be recovered in a constrained-search scheme. Namely, while the kinetic functional $T_s[n(\boldsymbol{r})]$ was already introduced through a density-constrained search in Eq. (3.14), the exchange and correlation functionals can be defined separately as

$$E_{\text{xc}}[n(\boldsymbol{r})] = E_{\text{x}}[n(\boldsymbol{r})] + E_{\text{c}}[n(\boldsymbol{r})] , \tag{3.31}$$

$$E_{\text{x}}[n(\boldsymbol{r})] = \langle \bar{\Psi}_0^{(n)} | \hat{T} + \hat{V}_{\text{ee}} | \bar{\Psi}_0^{(n)} \rangle - E_{\text{H}}[n(\boldsymbol{r})] , \tag{3.32}$$

$$E_{\text{c}}[n(\boldsymbol{r})] = \min_{\Psi \to n(\boldsymbol{r})} \langle \Psi | \hat{T} + \hat{V}_{\text{ee}} | \Psi \rangle - \langle \bar{\Psi}_0^{(n)} | \hat{T} + \hat{V}_{\text{ee}} | \bar{\Psi}_0^{(n)} \rangle , \tag{3.33}$$

where $|\bar{\Psi}_0^{(n)}\rangle$ is the (Slater determinant) minimizing the expectation value of $\hat{T}$ at fixed density $n(\boldsymbol{r})$.

Through the constrained search formulation of DFT, we can understand better the differences between DFT and HF electronic structure calculations.

The former is in principle an exact theory, provided the Hohenberg-Kohn functional (3.30) is known. The latter is always an approximate method, where correlation effects are never taken into account, and corresponds to an effective DFT whose Hohenberg-Kohn functional is defined as a constrained minimization in the space of Slater determinants only

$$F_{\text{HK}}^{(\text{HF})}[n(\boldsymbol{r})] = \min_{\Psi_0 \to n(\boldsymbol{r})} \langle \Psi_0 | \hat{T} + \hat{V}_{\text{ee}} | \Psi_0 \rangle \,. \tag{3.34}$$

Once the Slater determinant $|\bar{\Psi}_0^{(n)}\rangle$ minimizing the above expression has been found, one can plug it in the definition (3.32) and find the HF exchange functional, while the kinetic functional is equal to

$$T_{\text{HF}}[n(\boldsymbol{r})] = \langle \bar{\Psi}_0^{(n)} | \hat{T} | \bar{\Psi}_0^{(n)} \rangle \,, \tag{3.35}$$

where now $|\bar{\Psi}_0^{(n)}\rangle$ is the Slater determinant minimizing the expectation value of $\hat{T} + \hat{V}_{\text{ee}}$ [96], and not of $\hat{T}$ only, as in DFT, so that the inequality holds $T_s[n(\boldsymbol{r})] \leq T_{\text{HF}}[n(\boldsymbol{r})]$.

3.4 Going beyond LDA

The requirement of v-representability is that the Kohn-Sham potential should be local in space. This property does not necessarily mean that the value of V_{KS} at a point $\boldsymbol{r}$ cannot depend on the value of the density at a different point in space. The Hartree potential $V_{\text{H}}[n(\boldsymbol{r})]$, for example, depends on the values of $n(\boldsymbol{r})$ at every point in space, through the Coulomb integral

$$V_{\text{H}}(\boldsymbol{r}) = \int \frac{n(\boldsymbol{r}')}{|\boldsymbol{r} - \boldsymbol{r}'|} d\boldsymbol{r}' \,. \tag{3.36}$$

In general, also the value of the exchange-correlation potential $V_{\text{xc}}(\boldsymbol{r})$ is expected to depend on the values of the density at different points in order to account for all quantum interaction effects enclosed in the ground-state wavefunction (within HF, the exchange potential is not only a non-local functional of the density, but also a non-local potential itself).

In spite of this, LDA approximates it as a local functional of the *local density*, by assuming it coincides with the functional derivative of only the zeroth-order term of

the – formally exact – asymptotic gradient expansion

$$E_{\mathrm{xc}}[n(\boldsymbol{r})] = \int n(\boldsymbol{r})\epsilon_{\mathrm{xc}}^{(\mathrm{eg})}[n(\boldsymbol{r})]d\boldsymbol{r} + \int |\nabla n|^2 \varepsilon_{\mathrm{xc}}^{(2)}[n(\boldsymbol{r})]d\boldsymbol{r} + \ldots \qquad (3.37)$$

of the exchange-correlation energy.

In the simulation of the electronic structure of a crystal, keeping only the first term in Eq. (3.37) implies disregarding the effects of the lattice potential which squeezes the density around the nuclei, and treating the quantum effects at each point in space as those of an effective jellium model.

While this is reasonable for a metallic crystal where the density profile of conduction electrons is slowly varying, the same cannot be said for an interface between a metal and the vacuum, for a molecule, or for a single atom.

An advantage of the LDA exchange-correlation functional is that it is is locally able to account exactly for the global strength of the exchange-correlation hole, given by the sum-rule

$$\int [g_{\mathrm{xc}}(\boldsymbol{r}, \boldsymbol{r}') - 1]n(\boldsymbol{r})d\boldsymbol{r} = -1 \,, \qquad (3.38)$$

where $g(\boldsymbol{r}, \boldsymbol{r}')$ is the pair correlation function of a homogeneous electron gas of density $n(\boldsymbol{r}')$, with ground-state wavefunction $|\Psi_0^{(\mathrm{eg})}\rangle$

$$g_{\mathrm{xc}}(\boldsymbol{r}, \boldsymbol{r}') = \frac{1}{n^2(\boldsymbol{r}')}\langle \Psi_0^{(\mathrm{eg})}| \sum_{i \neq j} \delta(\boldsymbol{r} - \boldsymbol{r}_i)\delta(\boldsymbol{r}' - \boldsymbol{r}_j)|\Psi_0^{(\mathrm{eg})}\rangle \,, \qquad (3.39)$$

and corresponds to the probability of finding a particle in $\boldsymbol{r}'$ once we know that an electron is located at point $\boldsymbol{r}$.

Thanks to the property 3.38, LDA is able to provide reasonable results even for some systems where the density profile is not slowly varying. However, the LDA functional tends in general to underestimate both band gaps and equilibrium lattice constants in crystals, while in the simulations of adsorption processes it shows the preference for increased coordination and shorter bond lengths [7, 8]. A way to partially correct these flaws is to compute V_{xc} from higher-order terms of the gradient expansion (3.37).

Unfortunately, an uncritical inclusion of a few gradient corrections does improve the short-range part of V_{xc}, but results in an exchange-correlation hole that violates the sum-rule Eq. (3.38) for large $|\boldsymbol{r} - \boldsymbol{r}'|$, and may therefore perform worse than LDA in determining the total energy of systems in which the long-range part of the Coulomb potential dominates the interaction energy.

The well known Generalized Gradient Approximation (GGA) and its spin-resolved version σ-GGA are able to cure the spurious long-range part of the exchange-correlation

hole through a real-space cutoff procedure. Here we show the GGA expression for the exchange-only functional

$$E_{\mathrm{x}}[n(\boldsymbol{r})] = \int n(\boldsymbol{r})\epsilon_{\mathrm{x}}^{(\mathrm{eg})}[n(\boldsymbol{r})]f[s(\boldsymbol{r})]d\boldsymbol{r} \ , \tag{3.40}$$

which contains the LDA exchange energy per particle $\epsilon_{\mathrm{x}}^{(\mathrm{eg})} = -3/4e^2[3n(\boldsymbol{r})/\pi]^{1/3}$, and where the dependence on the gradient is included through $s(\boldsymbol{r}) \propto \nabla n(\boldsymbol{r})/n^{4/3}(\boldsymbol{r})$.

The choice of f determines the type of GGA, the most popular being that of Perdew and Wang [97] and Perdew, Burke and Ernzerhof [98], while, for $f[s(\boldsymbol{r})] = 1$, Eq. (3.40) recovers the LDA result.

3.4.1 Overcoming self-interaction

One severe flaw of the LDA functional and of its spin-resolved generalization LSDA which is not corrected within GGA, is that they contain spurious energy terms coming from the interaction of every Kohn-Sham quasi-particle with itself. This self-interaction energy is introduced by the classical Hartree functional $E_{\mathrm{H}}[n(\boldsymbol{r})]$ Eq. (3.13), and fails to be subtracted out by the approximate exchange-correlation functional.

Within the HF theory, this subtraction is exact, by virtue of the explicit orbital dependence of the Fock term. In fact, given a basis ϕ_α of single-particle spin-orbitals, the HF interaction energy reads

$$E_{\mathrm{int}}^{(\mathrm{HF})} = \langle\Psi_0|\hat{V}_{\mathrm{ee}}|\Psi_0\rangle = \sum_{\alpha\beta} f_\alpha f_\beta \Big[\int \frac{|\phi_\alpha(\boldsymbol{r})|^2|\phi_\beta(\boldsymbol{r}')|^2}{|\boldsymbol{r}-\boldsymbol{r}'|}d\boldsymbol{r}d\boldsymbol{r}'+$$
$$- \int \frac{\phi_\alpha^*(\boldsymbol{r})\phi_\alpha(\boldsymbol{r}')\phi_\beta^*(\boldsymbol{r}')\phi_\beta(\boldsymbol{r})}{|\boldsymbol{r}-\boldsymbol{r}'|}d\boldsymbol{r}d\boldsymbol{r}'\Big] , \tag{3.41}$$

and is such that no term with $\alpha = \beta$ gives contribution to the total energy of the system.

In order to solve the self-interaction problem of LDA, Perdew and Zunger [99] suggested the following correction to the LDA exchange-correlation functional

$$E_{\mathrm{xcSIC}}[n(\boldsymbol{r})] = E_{\mathrm{xc}}^{(\mathrm{LDA})}[n(\boldsymbol{r})] - \sum_{i\ \mathrm{occ.}} \big\{ E_{\mathrm{H}}[n_i(\boldsymbol{r})] + E_{\mathrm{xc}}^{(\mathrm{LDA})}[n_i(\boldsymbol{r})] \big\} \tag{3.42}$$

that makes use of the densities $n_i(\boldsymbol{r}) = f_i|\phi_i(\boldsymbol{r})|^2$ resolved on a set of orbitals ϕ_i of occupation f_i which can both be optimized in order to maximize the self-interaction removal.

The above Self-Interaction Correction (SIC) contribution to the total energy is larger for rapidly varying densities and strongly localized electrons, while it vanishes

in the jellium fully delocalized limit, where the LDA is already self-interaction free. While being always exact for a density arising from a single electron, the SIC subtraction is only approximately correct for a system of many electrons. Moreover, due to the optimization of the self-interaction removal, the minimization of the SIC functional cannot be straightforwardly included in a Kohn-Sham scheme.

The SIC functional was shown [100] to be very effective in predicting band gaps and magnetic moments of several transition metal oxides which are poorly described by LSDA.

In the following section we discuss another method that proved equally successful in removing self-interaction from the LSDA functional, which is the Local Density Approximation plus Hubbard-U (LDA+U) method. This method draws inspiration from the HM for strongly correlated electrons, and provides therefore more physical insight to electronic structure calculations of materials where the electron-electron interactions play an important role.

3.5   A local effective Hamiltonian: LDA+U

It can be argued that the self-interaction problem of LDA is connected to the fact that the LDA functional is not N-representable. It is in fact a known property of N-representable functionals to be self-interaction free [101]. The definition of N-representability for an approximate Hohenberg and Kohn functional $F'_{\mathrm{HK}}[n(\boldsymbol{r})]$, is that for each density $n(\boldsymbol{r})$ there exists a N-particle wavefunction $|\Psi\rangle$ yielding that density and such that

$$F'_{\mathrm{HK}}[n(\boldsymbol{r})] = \langle\Psi|\hat{T} + \hat{V}_{\mathrm{ee}}|\Psi\rangle \underset{\Psi \to n(\boldsymbol{r})}{}. \qquad (3.43)$$

This condition is satisfied by HF, as can be clearly undestood from Eq. (3.34). The same is not true for the LDA functional, whose exchange-correlation is implicitly computed at every point in space from a different wavefunction, each being the ground-state of an electron gas with a different number of particles.

A minimal way to improve LDA and LSDA can be therefore to re-introduce an explicit wavefunction dependence only in the part of interaction energy which is supposed to contain the largest self-interaction, as is the case for the interaction energy between localized electrons (see Appendix E.1).

For this purpose, Anisimov and coworkers [18] devised the LDA+U scheme (more precisely called Local Spin Density Approximation plus Hubbard-U (LSDA+U) in the case of spin-resolved calculations) by introducing a Hubbard-U interaction operator defined on selected sets of atomic orbitals of transition metals or transition metal

compounds (usually the d orbitals of the transition metal atom, labeled with magnetic quantum number m)

$$\hat{H}_{\text{Hub}} = \frac{U}{2} \sum_{mm',\sigma\sigma'} \hat{c}^\dagger_{m\sigma} \hat{c}^\dagger_{m'\sigma'} \hat{c}_{m'\sigma'} \hat{c}_{m\sigma} \,, \tag{3.44}$$

and reframed the Kohn-Sham functional as

$$\mathcal{F}[n(\boldsymbol{r})] = T_{i0}[n(\boldsymbol{r})] + E_{\text{H}}[n(\boldsymbol{r})] + E_{\text{xc}}[n(\boldsymbol{r})] - E_{\text{dc}}[n(\boldsymbol{r})] + \int d\boldsymbol{r}\, V_{\text{ext}}(\boldsymbol{r}) n(\boldsymbol{r}) \,, \tag{3.45}$$

where now the N-representable modified kinetic functional is defined as the minimum of the kinetic operator plus the Hubbard operator on the class of Slater determinants

$$T_{i0}[n(\boldsymbol{r})] = \min_{\Psi_0 \to n(\boldsymbol{r})} \langle \Psi_0 | \hat{T} + \hat{H}_{\text{Hub}} | \Psi_0 \rangle \,, \tag{3.46}$$

and where the double-counting energy $E_{\text{dc}}[n(\boldsymbol{r})]$ is a guess of the amount of Hubbard interaction energy already accounted for within LDA.

In the so called fully localized limit, better elucidated in Appendix E.3, the double-counting term is computed from the expectation value of Eq. (3.44) by neglecting fluctuations of the number operator $\hat{N}$ on d-orbitals around its expectation value $N = \langle \Psi_0 | \hat{N} | \Psi_0 \rangle$, with the result

$$E_{\text{dc}}[n(\boldsymbol{r})] = \frac{U}{2} N(N-1) \,. \tag{3.47}$$

Subtracting the $E_{\text{dc}}[n(\boldsymbol{r})]$ from the expectation value of $\hat{H}_{\text{Hub}}$ on the Slater determinant minimizing the right-hand side of Eq. (3.46), one finds that the total term added to the LDA energy functional can be written in terms of the density matrix on d-orbitals $\boldsymbol{n}$ (of matrix elements $n_{mm',\sigma\sigma'} = \langle \Psi_0 | \hat{n}_{mm',\sigma\sigma'} | \Psi_0 \rangle$) as

$$\Delta E_{\text{Hub}}[n(\boldsymbol{r})] = \frac{U}{2} \operatorname{Tr}\{\boldsymbol{n}(\mathbb{1} - \boldsymbol{n})\} \,. \tag{3.48}$$

The effect of the correction in Eq. (3.48) can be understood by thinking the localized d-orbitals as the single-particle states of an atomic impurity connected to a reservoir of electrons provided by the Bloch states of the crystal. For any fractional number of particles $(1-\lambda)N + \lambda(N+1)$ sitting on the impurity, the ground-state of the latter is a statistical mixture of states with exactly N and $N+1$ particles, and the impurity energy $E_{\text{loc}}[N+\lambda]$ is equal to the linear combination of the energies of the two integer-particle systems $(1-\lambda)E_{\text{loc}}[N] + \lambda E_{\text{loc}}[(N+1)]$.

The second derivative of the impurity energy with respect to λ is therefore expected to be zero for any $0 < \lambda < 1$. This is not the case within LDA and LSDA, where the value

$$S(N) = \frac{d^2 E_{\text{loc}}(N')}{dN'^2}\bigg|_{N'=(1-\lambda)N+\lambda(N+1)} \tag{3.49}$$
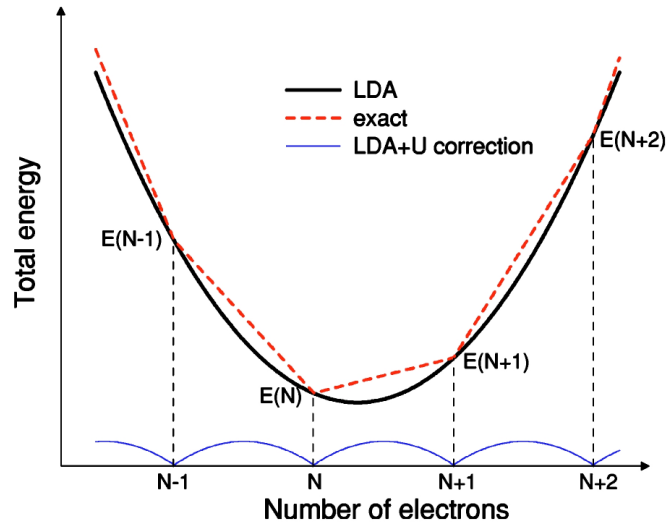
Figure 3.1: *Illustration of the mechanism with which LDA+U subtracts self-interaction from the LDA energy for any fractional occupation of the set of local orbitals. The zero second derivative of the local energy with respect to N means that the atomic ground state is a statistical mixture of states with different number of particles. Adapted from [102].*

can be considered as a measure of self-interaction on the impurity.

As shown in Fig. 3.1, the addition of $\Delta E_{\mathrm{Hub}}[n(\boldsymbol{r})]$ to E_{loc} is meant to correct the finite value of the double derivative, so that the LDA+U local energy $E_{\mathrm{loc}}(N) + \Delta E_{\mathrm{Hub}}(N)$ becomes piecewise linear in N for a suitable value of U.

Cococcioni and De Gironcoli [102] suggested a self-consistent approach for computing U from the condition $S(N) = 0$, making LDA+U a fully *ab-initio* method. From their calculations it becomes clear that the value of the Hubbard parameter can be fairly dependent on the environment surrounding the transition metal atom on which the Hubbard Hamiltonian 3.44 is defined.

This is due to the lattice-induced hybridization of the d-orbitals with the other atomic bands, which can result in a weaker or stronger d-electron localization according to the properties of the crystal under study. The choice of the radial function for the d-orbitals may also slightly influence the value of U in a minor fashion, the less the more localized the orbitals are.

3.6   Final remarks

The advantages of using DFT as a tool for electronic structure calculations come from the universality of the Hohenberg and Kohn functional, which is in principle the same for all Hamiltonians of electrons with Coulomb interactions, and from the use of a single-particle observable as the density as a minimizing variable for the energy of a many-body system.

Unfortunately, the exact form of the Hohenberg and Kohn functional is inaccessible, and has to be guessed by using physical insight and by making assumptions. Kohn and Sham suggested to decompose it into a kinetic and an interaction part, where the kinetic part is computed from a reference system of non-interacting electrons. The interaction part can be written as the sum of a classical (Hartree) term plus all quantum corrections, the exchange-correlation energy, which within Local Density Approximation are computed by integrating at every point in space the exchange-correlation energy density of a uniform electron gas with pointwise the same density as the physical system of interest.

The LDA exchange-correlation functional is unable to subtract from the Hartree energy the interaction of every electron with itself, bringing a bias into the calculation that needs to be corrected every time it jeopardizes correct physical predictions. The LDA+U functional subtracts self-interaction from a selected set of atomic orbitals by adding to the LDA functional the mean-field expectation value of a Hubbard interaction operator. This can improve the description of systems with strongly localized electrons as crystals of transition metals and transition metal compounds.

Whenever electrons are strongly localized, many-body effects beyond mean-field usually play an important role in determining relevant physical observables as spin susceptibility and magnetization. In the next chapter we will present the Gutzwiller Density Functional as an improvement of LDA+U where the Hubbard energy is computed beyond mean-field. This makes the investigation of a typically many-body phenomenon as double-exchange magnetism possible.

Chapter 4

Gutzwiller approach to Density Functional Theory

In this chapter we explain the advantages that a Gutzwiller-based DFT can bring to electronic structure simulations on the solid state. In the first section, Sect. 4.1 we point out some physical phenomena that conventional Density Functional approaches to realistic systems like LSDA and LSDA+U fail to describe correctly. One example is the dissociation of diatomic molecules, the other is magnetism driven by double-exchange. The Gutzwiller method is expected to provide a tool for dealing with both phenomena in a successful way. For this purpose, in Sect. 4.2 we define the Gutzwiller Density Functional, while in the following sections we show how it can be exploited to describe the electronic structure of a simple transition metal like body-centered cubic iron, where double-exchange is proved to have a relevant role in determining magnetic order.

4.1 Stoner Magnetism and Mott localization within LSDA and LDA+U

In Chapt. 3, we mentioned how LSDA fails, sometimes even grossly, to reproduce experimental band gaps and magnetic moments in transition metal oxides. The reason is that the local spin density functional suffers from spurious self-interaction effects that prevent electronic localization and magnetic moment formation on weakly dispersive orbitals.

For transition metal elements and compounds, these orbitals are Bloch functions built out of weakly hybridized atomic-like orbitals of d-type. The lack of hybridization is due to the particular arrangement of atoms in the lattice, and makes electron-electron interaction a relevant actor that is expected to further localize d-electrons and increase their band mass.

Removing self-interaction should be sufficient to correct the severe flaws of LSDA in transition metal compounds, a task that both the SIC and the LSDA+U schemes seem to perform efficiently. The reason why the removal of self-interaction favors localized states and local magnetic moments can be understood as follows.

If the electron-electron interaction on a local orbital is modeled with the Hubbard-U interaction operator, the energy gap of order U that opens between a singly and a doubly occupied local configuration in the absence of self-interaction gives the possibility for the half-filled state to lie well below the Fermi energy, where it does not take part in conduction processes.

Within LDA, the energy of a local orbital with fractional filling must lie at the Fermi level, where both its charge and spin configurations become subject to fluctuations which spoil localization and magnetic moment.

The only mechanism through which electronic localization can occur within the LSDA formalism is by explicitly breaking spin symmetry. The effect of the charge gap between singly and doubly occupied sites is now caused by the gap between atomic levels of majority and minority spin components, so that the former can have energies below the Fermi level and host localized electrons with a definite magnetic moment and a definite polarization. In this picture, the energy of a minority spin orbital lies above that of a majority spin orbital by an amount proportional to the coupling which drives spin polarization, which is in principle distinct from the pure Hubbard interaction U.

Gunnarsson [103] was the first to realize that the LSDA calculations on transition metals are mimicked by an effective Stoner model for the d-electrons, where the role of the Stoner interaction parameter in driving the spin polarization is played by the atomic Hund's rule exchange J, which has similar values for all $3d$ metals.

This actually means that magnetism can be stabilized in LSDA only in orbitally degenerate situations where the effective Hubbard-U is small enough to allow the inter-orbital exchange, driven by J, to overcome the effects of self-interaction. This is what happens in pure transition metals, where the large conduction bandwidth efficiently screens the Coulomb repulsion hence making the Hubbard U comparable to J, which instead remains practically unscreened. In these cases LSDA performs well.

In other cases, specifically transition metal oxides, screening is less efficient and U can be more than twice the value of J, which makes LSDA unable to reproduce a magnetic behavior that in reality occurs. It may even happen that the d-orbital degeneracy is lost completely and only a single d orbital lies around the Fermi energy. This is known to occur for instance in cuprates, where J is ineffective, and there is no way to stabilize magnetism within LSDA.

When these situations arise one is forced to resort to schemes beyond LDA that suffer less from self-interaction effects, as for instance LDA+U [18], which however has other drawbacks. For instance, within LDA+U one retrieves an effective Stoner model with Stoner parameter proportional to the Hubbard U. This model can correctly account for electron localization and magnetic moment formation, but cannot determine, being U pure charge repulsion, the temperature at which magnetism sets in, which is controlled by the smaller energy scale involved in magnetic ordering.

In the next two sections we will try and answer to the following questions: what features can a DFT based on a GVW add to an electronic structure simulation of a molecule or a crystal? In particular, can it add anything more to the description of transition metals, where the LSDA functional already gives satisfactory results?

The answer to these questions comes from the discussion of Sect. 1.3.1, where we understood how the Stoner approach to magnetic ordering is able to describe both mass and spin-susceptibility enhancement, but fails to account for the behavior of their ratio while approaching a phase transition.

The reason for this fact is that no enhancement of local spin moment can be described within a HF or LSDA calculation unless a global symmetry is broken, while the GVW can enhance local moments even irrespectively from any magnetic order. The Gutzwiller enables to differentiate between the mechanism of Mott localization and that of magnetic order, two phenomena that are distinct and controlled by different energy scales.

4.1.1 Localization mechanisms in the dissociation of H_2

The simplest example where to discuss the capabilities of the GVW compared to the performance of existing density functional methods is the dissociation of a hydrogen molecule. In the limit of infinite inter-atomic distance, the LDA energy of H_2 does not become twice the energy of a single hydrogen, as it should [9]. This well known result is due to the fact that the bonding orbital remains fully occupied for every lattice separation, so that inter-atomic fluctuations fail to be completely suppressed even at very large atomic distance, where we expect the wavefunction of each electron to localize on a single hydrogen at a time.

Within the LSDA formalism, the correct dissociation limit for the energy can be reached through the gradual alignment of the spin of the two electrons. The gain in exchange energy caused by spin polarization changes the ground-state from a doubly occupied bonding orbital to a state with bonding and anti-bonding orbitals occupied with one electron, corresponding to the single-determinant state

$$|\Psi_{0,\text{loc}}^{\text{LSDA}}\rangle = \frac{1}{\sqrt{2}} \left[\phi_A(1)\phi_B(2) - \phi_B(1)\phi_A(2) \right] \otimes \left[\chi_\uparrow(1)\chi_\uparrow(2) \right], \qquad (4.1)$$

where ϕ_A and ϕ_B are orbitals centered on atom A and atom B respectively, and where $\chi_\uparrow$ and $\chi_\downarrow$ are up and down spinors There is of course no physical reason why the magnetic moments of two hydrogen atoms separated by a large distance should be parallel to each other, and it is clear that the spontaneous magnetization of the system is just an artifact of LSDA. Moreover, the fact that the final spin state is a triplet implies that the ground-state Slater determinant is odd under inversion, while the exact ground-state should be inversion-symmetric.

Even if one searches for a solution where the two spins are anti-parallel, still inversion symmetry is lost, while spin rotational symmetry is not recovered because the anti-parallel spin configuration is not a singlet state. No qualitative improvement with respect to LSDA can be obtained within LSDA+U.

Within the multi-band formulation of the GA, it is instead possible to obtain the correct dissociation limit of the hydrogen molecule with a ground-state wavefunction for the dissociated state that does not break spin rotational or inversion symmetries. Different than $|\Psi_{0,\text{loc}}^{\text{LSDA}}\rangle$, this wavefunction is a multi-determinant state, with explicit form

$$|\Psi_{\text{loc}}^{\text{g,sing}}\rangle = \frac{1}{2} \left[\phi_A(1)\phi_B(2) + \phi_B(1)\phi_A(2) \right] \otimes \left[\chi_\uparrow(1)\chi_\downarrow(2) - \chi_\downarrow(1)\chi_\uparrow(2) \right]. \qquad (4.2)$$

Starting from the doubly occupied bonding orbital, which is the solution of the LDA calculation, one can apply a Gutzwiller projector $\hat{\mathcal{P}}$ defined on the inversion-symmetric, spin-singlet many-body configurations of two electrons. There are only two configurations of this type, namely

$$|\Psi_{0,\text{bond}}^{\text{g,sing}}\rangle = \frac{1}{\sqrt{2}} \left[\phi_b(1)\phi_b(2) \right] \otimes \left[\chi_\uparrow(1)\chi_\downarrow(2) - \chi_\downarrow(1)\chi_\uparrow(2) \right] \quad \sim \quad |\uparrow\rangle, \qquad (4.3)$$

$$|\Psi_{0,\text{antibond}}^{\text{g,sing}}\rangle = \frac{1}{\sqrt{2}} \left[\phi_a(1)\phi_a(2) \right] \otimes \left[\chi_\uparrow(1)\chi_\downarrow(2) - \chi_\downarrow(1)\chi_\uparrow(2) \right] \quad \sim \quad |\downarrow\rangle. \qquad (4.4)$$

One configuration has two electrons in the bonding orbital $\phi_b(1)$, while the other has two electrons in the anti-bonding orbital ϕ_a. The two configurations build a reduced

many-body space where they can be effectively treated as two pseudo-spinors $|\uparrow\rangle$ and $|\downarrow\rangle$.

If we use the representation in terms of the $\hat{\Phi}$ operators described in Sect. 1.6.2, we can show that in this reduced many-body space there is only one degree of freedom related to the Gutzwiller projector. The natural single-particle basis of this problem is that of the bonding and anti-bonding orbital, with the first being fully occupied on the Slater determinant. It follows that the natural density matrix $n_i^{(0)}\delta_{ij}$ has the form

$$n_i^{(0)} = \begin{cases} 1 & ; i = b \,(\text{bonding}) \\ 0 & ; i = a \,(\text{antibonding}) \end{cases}. \tag{4.5}$$

In the relevant many-body space we have

$$\hat{\Phi}^\dagger = \cos(\theta/2)\hat{\sigma}_+\hat{\sigma}_- + \sin(\theta/2)\hat{\sigma}_+\,, \tag{4.6}$$

where $\hat{\sigma}_+$ and $\hat{\sigma}_-$ are the spin raising and lowering operators in the pseudo-spinor basis. The operator $\hat{\Phi}^\dagger$ defined above correctly fulfills the first Gutzwiller constraint

$$\text{Tr}\{\hat{\Phi}^\dagger\hat{\Phi}\} = \cos^2(\theta/2) + \sin^2(\theta/2) = 1\,. \tag{4.7}$$

By virtue of the fact that the number operator on the bonding orbital $\hat{n}_{bb} = \hat{c}_b^\dagger\hat{c}_b$ (we omit the spin index which is irrelevant when matrix elements are computed between singlet states), restricted to our space of two many-body states, is a projector on $|\Psi_{0,\text{bond}}^{\text{g,sing}}\rangle$, while $\hat{n}_{aa}$ projects on $|\Psi_{0,\text{antibond}}^{\text{g,sing}}\rangle$, it easy to show that Φ fulfills also the second Gutzwiller constraint on the natural density matrix.

Using the fact that $\hat{n}_{bb} = \hat{\sigma}_+\hat{\sigma}_-$, and $\hat{n}_{aa} = \hat{\sigma}_-\hat{\sigma}_+$, we find

$$\text{Tr}\{\hat{\Phi}^\dagger\hat{\Phi}\,\hat{n}_{bb}\} = 1 = n_b^{(0)}\,, \tag{4.8}$$

$$\text{Tr}\{\hat{\Phi}^\dagger\hat{\Phi}\,\hat{n}_{aa}\} = 0 = n_a^{(0)}\,, \tag{4.9}$$

$$\text{Tr}\{\hat{\Phi}^\dagger\hat{\Phi}\,\hat{n}_{ab}\} = 0 = n_a^{(0)}\,, \tag{4.10}$$

where the last equality is due to the fact that $\hat{n}_{ab}$ has matrix elements only between states of different inversion symmetry, while $\hat{\Phi}^\dagger\hat{\Phi}$ has only matrix elements between states with the same inversion symmetry.

The value of the Gutzwiller-renormalized density matrix can be found from

$$\text{Tr}\{\hat{\Phi}^\dagger\hat{n}_{bb}\hat{\Phi}\} = \cos^2(\theta/2)\,, \tag{4.11}$$

$$\text{Tr}\{\hat{\Phi}^\dagger\hat{n}_{aa}\hat{\Phi}\} = \sin^2(\theta/2)\,, \tag{4.12}$$

$$\text{Tr}\{\hat{\Phi}^\dagger\hat{n}_{ab}\hat{\Phi}\} = 0\,, \tag{4.13}$$

so that $\theta = 0$ represents the bound state, while $\theta = \pi/2$ represents the fully dissociated state $|\Psi_{\text{loc}}^{\text{g,sing}}\rangle$. All values of θ between zero and $\pi/2$ interpolate between the two limits, and hence can describe the dissociation curve of H_2.

4.1.2 Exchange-driven and Correlation-driven magnetism

At the beginning of Sect. 4.1, we discussed how both LSDA and LSDA+U describe the effects of electron-electron interactions on magnetism through an effective Stoner theory. Stoner theory explains how an electron liquid can spontaneously develop a finite magnetization in order to lower its total energy. Such an energy lowering takes place through an increase in kinetic energy accompanied by a larger decrease in interaction energy.

We can see this by starting from the standard single-band HM with hopping energy leading to a non-interacting density of states $\mathcal{D}_0(\varepsilon)$, and by computing the mean-field total energy for a filling $n = (N_\uparrow + N_\downarrow)/L$ and spin imbalance $m = (N_\uparrow - N_\downarrow)/L$:

$$E(n, m) = \int_0^{\varepsilon_{F\uparrow}} \varepsilon \mathcal{D}(\varepsilon) + \int_0^{\varepsilon_{F\downarrow}} \varepsilon \mathcal{D}(\varepsilon) d\varepsilon + \frac{LU}{4}(n^2 - m^2)\,, \qquad (4.14)$$

where $\varepsilon_{F\uparrow}$ and $\varepsilon_{F\downarrow}$ are implicit functions of $N_\uparrow$ and $N_\downarrow$ through

$$\int_0^{\varepsilon_{F\uparrow(\downarrow)}} \mathcal{D}(\varepsilon) = N_{\uparrow(\downarrow)}\,. \qquad (4.15)$$

For a small imbalance $m = N_\uparrow - N_\downarrow$, we can expand the two integrals on the right-hand side of Eq. (4.14) around the value at $m = 0$, with the result

$$E(n, m) \approx E(n, m = 0) + \left(\frac{2}{\chi_P^{(0)}} - LU\right)\frac{m^2}{4}\,, \qquad (4.16)$$

where $\chi_P^{(0)}$ is the *positive* Pauli magnetic susceptibility of the non-interacting system, which is a measure of spin fluctuations.

The non-interacting static homogeneous susceptibility $\chi_P^{(0)}$ is twice the density of states $\mathcal{D}_0(\varepsilon_F)$, so that by taking the second derivative of $E(n, m)$ the Stoner susceptibility is recovered. The minus sign in front of the Hubbard-U in Eq. (4.16) indicates that the term favoring magnetism is the exchange part of the electron-electron interaction energy. From the same equation it is also clear how the polarized phase appears at the expense of the total kinetic energy, and is more favored the larger is the spin susceptibility of the system.

We would like to give another example of magnetism arising in systems of weakly compressible electrons, a type of magnetism that is driven by a physical mechanism completely different than direct exchange, which is double-exchange.

Spin polarization due to double-exchange can arise only in correlated systems with more than one band, and with a sufficiently strong Hund's first rule making local parallel spin configurations advantageous. The simplest way to model it is through a

two-band HM, with bands α and β, Hubbard-U and exchange J:

$$\hat{H} = \sum_{\gamma=\alpha,\beta} t_\gamma \sum_{\{i,j\}\sigma} \hat{c}^\dagger_{i\sigma\gamma}\hat{c}_{j\sigma\gamma} + U_\alpha \sum_i \hat{n}_{i\uparrow\alpha}\hat{n}_{i\downarrow\alpha} + U_\beta \sum_i \hat{n}_{i\uparrow\beta}\hat{n}_{i\downarrow\beta} - J \sum_i \hat{S}_i^2 , \quad (4.17)$$

where $\hat{S}_i^2$ is the square of the total spin operator at site i. We assume that the α band is half-filled, and that the whole system is more than quarter-filled.

If U_α is large enough with respect to the hopping t_α, the double occupancy of the α band is suppressed and the α electrons localize, giving rise to well-formed, unordered local moments. If the β electrons were localized as well, Hund's first rule would force parallel spins on each site, with no necessity for ordering among different sites.

If instead U_β is small enough compared to t_β to allow for sizable inter-site fluctuations, every β electron is itinerant, and the different sites through which it is delocalized are subject to an effective exchange potential tending to align the α spins to the underlying β magnetic moments.

It can be seen that when this happens, and the α band becomes fully polarized, the motion of the β electron is favored with respect to the unpolarized case, since no hopping process will violate Hund's first rule. This implies a kinetic energy gain of the ordered phase with respect to the disordered one. A pictorial explanation of the double-exchange mechanism is shown in Fig. 4.1. The phenomenon of double-exchange magnetism is peculiar since it happens only in cases where the itineracy and strong localization of electrons coexist. As in the case of Stoner magnetism, it is caused by strong local interactions. However, in this case localization and ordering, two phenomena treated on the same footing by the Stoner theory, are physically decoupled, with the Hubbard U driving the magnetic moment formation on the heavy fermion band, and the inter-band exchange J causing the magnetic ordering indirectly through hopping processes.

The transition metals and their compounds offer a natural laboratory where both localization and itineracy can survive. Double-exchange physics was shown to have an important role in the electronic structure of manganites [44]. In the following sections we show how a Gutzwiller-improved Density Functional can describe the role of double-exchange in determining the electronic structure of a simple transition metal as body-centered cubic iron.

4.2   The Gutzwiller density functional

Proceeding along the lines of chapter 3, we would like to introduce a functional which is devoid of self-interaction, as the LDA+U functional, and with the supplementary capability of accounting for an explicit renormalization of the electronic band mass.
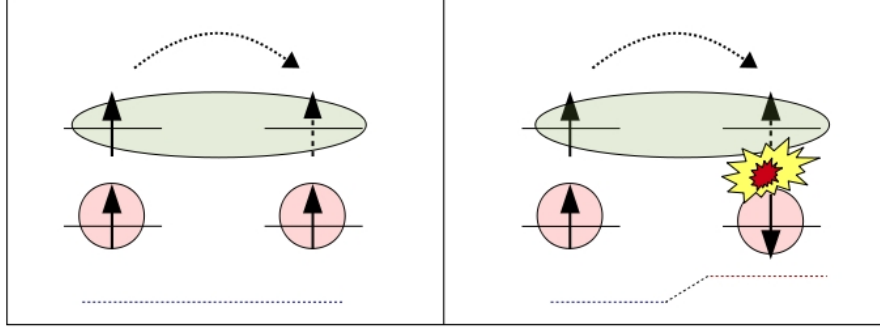
Figure 4.1: *Pictorial representation of the double-exchange mechanism. The red circles represent localized electrons, the green ellipse a delocalized electron hopping between two sites. The wavefunction of delocalized spins on the upper level creates an effective exchange coupling aligning clusters of localized moments on the lower level. The maximum kinetic gain is obtained when all moments are aligned, so that the motion of delocalized electrons is not penalized by Hund's rule potential barriers (pictured by the dashed line) due to anti-parallel local moments.*

This can be done by defining the new kinetic functional $T_{iG}[n(\boldsymbol{r})]$ as

$$T_{iG}[n(\boldsymbol{r})] = \min_{\Psi_G \to n(\boldsymbol{r})} \langle \Psi_G | \hat{T} + \hat{H}_{at} | \Psi_G \rangle \,, \tag{4.18}$$

where $\hat{H}_{at}$ is an atomic interaction Hamiltonian including the Hubbard-U term $\hat{H}_{Hub}$ and a Coulomb exchange locally enforcing Hund's rules. The above wavefunction $|\Psi_G\rangle$ spans all Gutzwiller-type wavefunctions with fixed $n(\boldsymbol{r})$, namely it is of the form

$$|\Psi_G\rangle = \hat{\mathcal{P}}|\Psi_0\rangle \,, \tag{4.19}$$

where $|\Psi_0\rangle$ is a Slater determinant.

Analogously to Eq. (3.45), we can write the density functional as

$$\mathcal{F}[n(\boldsymbol{r})] = T_{iG}[n(\boldsymbol{r})] + E_H[n(\boldsymbol{r})] + E_{xc}[n(\boldsymbol{r})] - E_{dc}[n(\boldsymbol{r})] + \int d\boldsymbol{r} \, V_{ext}(\boldsymbol{r})n(\boldsymbol{r}) \,. \tag{4.20}$$

Similarly to the LDA+U modified kinetic functional $T_{i0}[n(\boldsymbol{r})]$ in Eq. (3.46), which introduces an explicitly wavefunction-dependent mean-field interaction energy for independent particles, the Gutzwiller modified kinetic functional $T_{iG}[n(\boldsymbol{r})]$ contains an interaction energy for correlated particles, computed within the Gutzwiller framework. The constrained-search definition Eq. (4.18) of the Gutzwiller kinetic functional

implies the inequality

$$T_{i\mathrm{G}}[n(\boldsymbol{r})] \leq T_{i0}[n(\boldsymbol{r})] \,, \tag{4.21}$$

which is a result of the fact that the GVW has a larger variational freedom than a simple Slater determinant, or, from another point of view, that the Gutzwiller Density Functional (GDF) includes some correlations between quasi-particles already at the kinetic level. When the atomic interaction operator $\hat{H}_{\mathrm{at}}$ is set equal to zero, both $T_{i\mathrm{G}}[n(\boldsymbol{r})]$ and $T_{i0}[n(\boldsymbol{r})]$ functionals become equal to the Kohn-Sham kinetic functional (3.14).

If we define with $\bar{\Psi}_G^{(n)}$ the GVW minimizing the expectation value of $\hat{T} + \hat{H}_{\mathrm{at}}$ at fixed $n(\boldsymbol{r})$, and as $\bar{\Psi}_0^{(n)}$ the same wavefunction where the Gutzwiller projector has been set equal to identity, we can formally divide $E_{\mathrm{xc}}[n(\boldsymbol{r})]$ into three contributions

$$E_{\mathrm{xc}}[n(\boldsymbol{r})] = E_{\mathrm{x}}[n(\boldsymbol{r})] + E_{\mathrm{c}}^{(\mathrm{G})}[n(\boldsymbol{r})] + E_{\mathrm{c}}'[n(\boldsymbol{r})] \,, \tag{4.22}$$

where

$$E_{\mathrm{x}}[n(\boldsymbol{r})] = \langle \bar{\Psi}_0^{(n)} | \hat{V}_{\mathrm{ee}} | \bar{\Psi}_0^{(n)} \rangle - E_{\mathrm{H}}[n(\boldsymbol{r})] \,, \tag{4.23}$$

$$E_{\mathrm{c}}^{(\mathrm{G})}[n(\boldsymbol{r})] = \langle \bar{\Psi}_G^{(n)} | \hat{T} + \hat{V}_{\mathrm{ee}} | \bar{\Psi}_G^{(n)} \rangle - \langle \bar{\Psi}_0^{(n)} | \hat{T} + \hat{V}_{\mathrm{ee}} | \bar{\Psi}_0^{(n)} \rangle \,, \tag{4.24}$$

$$E_{\mathrm{c}}{}^*[n(\boldsymbol{r})] = \min_{\Psi \to n(\boldsymbol{r})} \langle \Psi | \hat{T} + \hat{V}_{\mathrm{ee}} | \Psi \rangle - \langle \bar{\Psi}_G^{(n)} | \hat{T} + \hat{V}_{\mathrm{ee}} | \bar{\Psi}_G^{(n)} \rangle \,. \tag{4.25}$$

The first contribution is the well known exchange functional, which within LDA has the simple form (E.5). Within LDA+U

$$E_{\mathrm{x}}[n(\boldsymbol{r})] = \langle \bar{\Psi}_0^{(n)} | \hat{H}_{\mathrm{at}} | \bar{\Psi}_0^{(n)} \rangle + \left(\langle \bar{\Psi}_0^{(n)} | \hat{V}_{\mathrm{ee}} - \hat{H}_{\mathrm{at}} | \bar{\Psi}_0^{(n)} \rangle - E_{\mathrm{H}}[n(\boldsymbol{r})] \right) \,, \tag{4.26}$$

i.e. $E_{\mathrm{x}}[n(\boldsymbol{r})]$ is partially parametrized as an explicitly wavefunction-dependent term, the expectation value of $\hat{H}_{\mathrm{at}}$ on the ground-state Slater determinant, plus a remainder (the term in brackets in Eq. (4.26)) that is approximated by the conventional LDA exchange functional minus the double-counting energy. The second contribution $E_{\mathrm{c}}^{(\mathrm{G})}[n(\boldsymbol{r})]$ embodies the improvement of the GDF over the LDA+U density functional. It can be again decomposed as

$$E_{\mathrm{c}}^{(\mathrm{G})}[n(\boldsymbol{r})] = \langle \bar{\Psi}_G^{(n)} | \hat{T} + \hat{H}_{\mathrm{at}} | \bar{\Psi}_G^{(n)} \rangle - \langle \bar{\Psi}_0^{(n)} | \hat{T} + \hat{H}_{\mathrm{at}} | \bar{\Psi}_0^{(n)} \rangle +$$
$$+ \left(\langle \bar{\Psi}_G^{(n)} | \hat{V}_{\mathrm{ee}} - \hat{H}_{\mathrm{at}} | \bar{\Psi}_G^{(n)} \rangle - \langle \bar{\Psi}_0^{(n)} | \hat{V}_{\mathrm{ee}} - \hat{H}_{\mathrm{at}} | \bar{\Psi}_0^{(n)} \rangle \right) \,, \tag{4.27}$$

with an explicitly wavefunction-dependent term plus a part (in brackets) that needs to be accounted for through a correlation functional of the LDA type. The term $E_{\mathrm{c}}^{(\mathrm{G})}[n(\boldsymbol{r})]$ of the GDF contains correlation effects beyond LDA both through the Gutzwiller renormalization of the local interaction $\hat{H}_{\mathrm{at}}$ and through the band-mass

renormalization, while the LDA+U functional can include part of these effects only indirectly by modifying the density profile so as to change the value of the LDA correlation functional. The functional $E_c^*[n(\boldsymbol{r})]$ in Eq. (4.25) is the part of correlation energy that is not included in the GVW, and should be added in as an LDA-like correlation functional in order to retrieve the approximate ground-state energy of the real system. We define

$$E_x'[n(\boldsymbol{r})] = E_{\text{dc}}[n(\boldsymbol{r})] + \left(\langle \bar{\Psi}_0^{(n)} | \hat{V}_{\text{ee}} - \hat{H}_{\text{at}} | \bar{\Psi}_0^{(n)} \rangle - E_{\text{H}}[n(\boldsymbol{r})] \right), \qquad (4.28)$$

$$E_c'[n(\boldsymbol{r})] = \left(\langle \bar{\Psi}_0^{(n)} | \hat{V}_{\text{ee}} - \hat{H}_{\text{at}} | \bar{\Psi}_0^{(n)} \rangle - E_{\text{H}}[n(\boldsymbol{r})] \right) + \qquad (4.29)$$

$$+ \left(\langle \bar{\Psi}_G^{(n)} | \hat{V}_{\text{ee}} - \hat{H}_{\text{at}} | \bar{\Psi}_G^{(n)} \rangle - \langle \bar{\Psi}_0^{(n)} | \hat{V}_{\text{ee}} - \hat{H}_{\text{at}} | \bar{\Psi}_0^{(n)} \rangle \right) + E_c^*[n(\boldsymbol{r})]. \qquad (4.30)$$

4.3 Gutzwiller density functional, an implementation and a case study

We decided to test the performance of the GDF by simulating the electronic structure of paramagnetic and ferromagnetic body-centered cubic iron, motivated by a recent Local Density Approximation plus Dynamical Mean-Field Theory (LDA+DMFT) study by Anisimov [43] and coworkers. The formalism of LDA+DMFT incorporates the DMFT self-consistent equations described in Sect. 1.3.4 into the realistic electronic structure calculation scheme provided by Kohn-Sham DFT [20]. The parameters of the DMFT impurity-model Hamiltonian are obtained from first-principles calculations, and the impurity Green's function can be afterwards used to compute a renormalized density (and therefore renormalized Kohn-Sham potential) via

$$-\frac{\hbar}{\pi} \Im m \int_{-\infty}^{\varepsilon_{\text{F}}} d\omega \, G(\boldsymbol{r}, \boldsymbol{r}, \omega), \qquad (4.31)$$

where $G(\boldsymbol{r}, \boldsymbol{r}, \omega)$ is obtained from the local lattice Green's function $G_{\mu\nu}^{(l)}$ (introduced in Eq. (1.49) for the single band case) as

$$G(\boldsymbol{r}, \boldsymbol{r}, \omega) = \sum_{\mu\nu, \boldsymbol{R}} G_{\mu\nu}^{(l)}(\omega) \phi_{\mu, \boldsymbol{R}}^*(\boldsymbol{r}) \phi_{\nu, \boldsymbol{R}}^*(\boldsymbol{r}). \qquad (4.32)$$

The LDA+DMFT equations are therefore a tool to investigate the effects of strong correlations in realistic solid state systems. In the case of a bcc crystal, the atomic d-type orbitals of an iron atom are split by the cubic crystal field into two multiplets, the doubly degenerate e_g and triply degenerate t_{2g} orbitals respectively, whose distinct orientations with respect to the lattice are shown in Fig. 4.2. The e_g orbitals are weakly hybridized and more localized, while the t_{2g} orbitals are more spread in space,
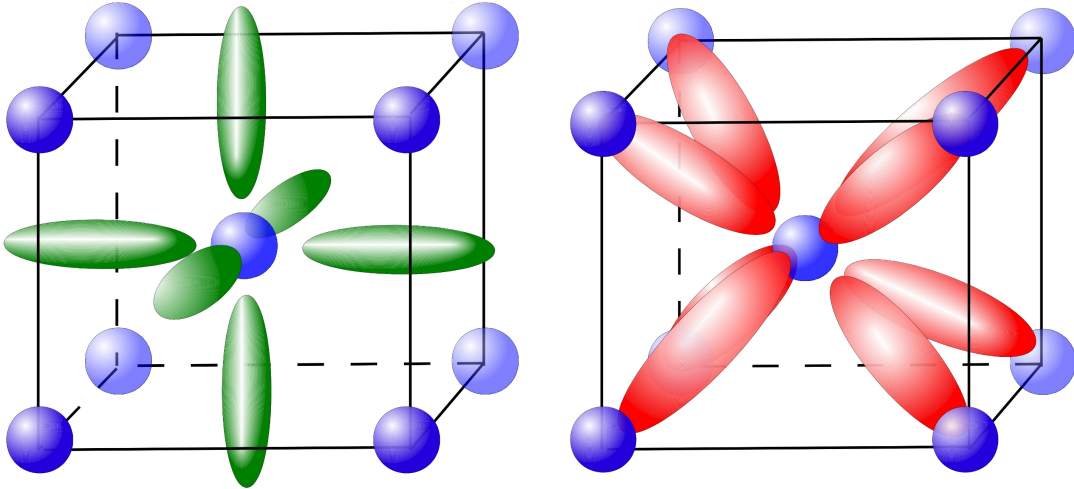
Figure 4.2: *Pictorial explanation of the lack of hybridization experienced by e_g orbitals compared to the t_{2g} orbitals. The square moduli of the wavefunctions of (green) e_g orbitals are larger towards the center of the bcc cell faces, while zero at the vertices, where the iron ions sit. On the contrary, the square moduli of the (red) t_{2g} wavefunctions are nonzero on the vertices, thus causing a stronger hybridization with orbitals at different lattice sites.*

and have a larger inter-site hopping matrix element. When part of the bcc crystal, the iron atom is in a configuration close to the $3d^7 \, 4s^1$, which is displayed in Fig. 4.3, and which is different than the one of the isolated atom, the $3d^6 \, 4s^2$.

In their work, the authors suggest that bcc iron might be an orbital-selective Mott insulator, where the weakly dispersive e_g-type electrons become fully localized due to interactions, while the conduction phenomena occur only within the t_{2g} manifold. This picture is in agreement with previous theoretical models [40–42], and is consistent with the conditions that lead to double-exchange magnetism, and that we elucidated in Sect. 4.1.2 (the e_g orbitals playing the role of the α orbital in that section).

We therefore exploit a Gutzwiller-renormalized LDA functional to try and grasp both the orbital selectivity of band mass renormalization in e_g and t_{2g} orbitals and to look for some clues of a double-exchange origin of the magnetism in iron.
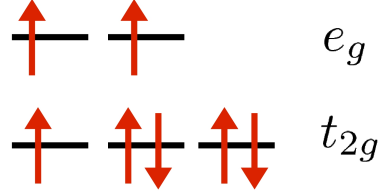
Figure 4.3: *In the picture above we show the e_g and t_{2g} configurations corresponding to the atomic $3d^7\ 4s^1$ configuration, which is the nearest one to the actual d configuration of an iron atom in a bcc lattice. The spin configuration shown above is already fulfilling Hund's first rule.*

Calculation of renormalized density

We start by introducing the density operator for a translational invariant system with one atom per unit cell

$$\hat{n}(\boldsymbol{r}) = \sum_{\alpha\beta,\boldsymbol{R}} \hat{n}_{\alpha\beta,\boldsymbol{R}} \phi^*_{\alpha,\boldsymbol{0}}(\boldsymbol{r})\phi_{\beta,\boldsymbol{R}}(\boldsymbol{r})\,, \tag{4.33}$$

where $\hat{n}_{\alpha\beta,\boldsymbol{R}} = \hat{c}^\dagger_{\alpha,\boldsymbol{0}}\hat{c}_{\beta,\boldsymbol{R}}$ is the density matrix operator written on a basis of atomic orthonormalized orbitals $\phi_{\alpha,\boldsymbol{R}}(\boldsymbol{r})$ centered on every lattice site $\boldsymbol{R}$.

From the expectation value of $\hat{n}(\boldsymbol{r})$ on the ground-state Slater determinant of the system we can compute the uncorrelated density $n^{(0)}(\boldsymbol{r})$

$$n^{(0)}(\boldsymbol{r}) = \sum_{\alpha\beta,\boldsymbol{R}} D^{(0)}_{\alpha\beta,\boldsymbol{R}} \phi^*_{\alpha,\boldsymbol{0}}(\boldsymbol{r})\phi_{\beta,\boldsymbol{R}}(\boldsymbol{r}) \tag{4.34}$$

in terms of the density matrix $D^{(0)}_{\alpha\beta,\boldsymbol{R}} = \langle\Psi_0|\hat{n}_{\alpha\beta,\boldsymbol{R}}|\Psi_0\rangle$. In similar way we can compute the renormalized density $n(\boldsymbol{r})$ as the expectation value of $\hat{n}(\boldsymbol{r})$ on the GVW

$$n(\boldsymbol{r}) = \sum_{\alpha\beta,\boldsymbol{R}} D_{\alpha\beta,\boldsymbol{R}} \phi^*_{\alpha,\boldsymbol{0}}(\boldsymbol{r})\phi_{\beta,\boldsymbol{R'}}(\boldsymbol{r})\,, \tag{4.35}$$

where now we made use of the correlated density matrix $D_{\alpha\beta,\boldsymbol{R}} = \langle\Psi_{\mathrm{G}}|\hat{n}_{\alpha\beta,\boldsymbol{R}}|\Psi_{\mathrm{G}}\rangle$. In the Siesta calculation we use as $\phi_{\alpha,\boldsymbol{R}}$, for every $\boldsymbol{R}$, a set of s, p and d-type orbitals, with the angular parts of p and d-orbitals being real spherical harmonics. These transform already as irreducible representations of the cubic group, a property that makes our local original basis $\phi_{\alpha,\boldsymbol{0}}$ also equal to the natural basis diagonalizing $D^{(0)}_{\alpha\beta,\boldsymbol{R}=0}$, and simplifies the calculations. In analogy with LDA+U, we make the site-independent Gutzwiller projector act in a non-trivial way only on the many-body space of d-orbital configurations, while we set it equal to identity on the remaining space [1].

---

[1] The full many-body space of the system can be written as a tensor product $\mathcal{C}_{\mathrm{d}} \otimes \mathcal{C}_{\mathrm{rem}}$ of the configuration space $\mathcal{C}_{\mathrm{d}}$ for d-orbitals, and $\mathcal{C}_{\mathrm{rem}}$ of the remaining orbitals. The Gutzwiller projection operator acts as $\hat{\mathcal{P}} \otimes \hat{\mathbb{1}}$

From now on, when there is the need of explicitly distinguishing between the "correlated" d-orbitals – subject to Gutzwiller projection – and the "uncorrelated" s and p-orbitals – which are left untouched –, we will use the Greek indices μ and ν for the former, and Latin indices i and j for the latter. From Eq. (1.76), Eq. (1.61) and Eq. (1.77) in Sect. 1.6.1 and 1.6.2, we can find the GA recipe for renormalizing the uncorrelated density matrix $D_{\alpha\beta,\boldsymbol{R}}^{(0)}$.

The symmetry properties of our original (and natural) single-particle basis ϕ_α and of the Gutzwiller parameter matrix $\hat{\Phi}$ for this system (we show the recipe for its parametrization in Appendix C) are such that the hopping renormalization matrix $R_{\mu\nu}$ is diagonal. The off-site density matrix on correlated orbitals is therefore renormalized according to

$$D_{\mu\nu,\boldsymbol{R}\neq\boldsymbol{0}} = R_{\mu\mu}D_{\mu\nu,\boldsymbol{R}\neq\boldsymbol{0}}^{(0)}R_{\nu\nu}\,, \tag{4.36}$$

while the on-site density matrix is computed from Gutzwiller parameters as

$$D_{\mu\nu,\boldsymbol{R}=\boldsymbol{0}} = \mathrm{Tr}\{\hat{\Phi}^\dagger \hat{n}_{\mu\nu,\boldsymbol{R}=\boldsymbol{0}}\hat{\Phi}\}\,. \tag{4.37}$$

The density matrix on uncorrelated orbitals has the same value when computed on the Slater determinant and on the GVW

$$D_{ij,\boldsymbol{R}\neq\boldsymbol{0}} = D_{ij,\boldsymbol{R}\neq\boldsymbol{0}}^{(0)}\,, \tag{4.38}$$

$$D_{ij,\boldsymbol{R}=\boldsymbol{0}} = D_{ij,\boldsymbol{R}=\boldsymbol{0}}^{(0)}\,, \tag{4.39}$$

while the density matrix terms coming from the hybridization – occurring only for $\boldsymbol{R}\neq 0$ – between correlated and uncorrelated orbitals changes according to

$$D_{\mu j,\boldsymbol{R}\neq\boldsymbol{0}} = R_{\mu\mu}D_{\mu j,\boldsymbol{R}\neq\boldsymbol{0}}^{(0)}\,. \tag{4.40}$$

Calculation of kinetic, external potential and atomic interaction energy

The modified functional $T_{\mathrm{iG}}[n(\boldsymbol{r})]$ can be divided in a purely kinetic term $T_{\mathrm{kG}}[n(\boldsymbol{r})] = \langle \Psi_{\mathrm{G}}|\hat{T}|\Psi_{\mathrm{G}}\rangle$ and atomic interaction term $E_{\mathrm{at}}[n(\boldsymbol{r})] = \langle \Psi_{\mathrm{G}}|\hat{H}_{\mathrm{at}}|\Psi_{\mathrm{G}}\rangle$.

Once the renormalized density $n(\boldsymbol{r})$ is known, the sum of external potential and kinetic energy is simply

$$T_{\mathrm{kG}}[n(\boldsymbol{r})] + \int n(\boldsymbol{r})V_{\mathrm{ext}}(\boldsymbol{r})d\boldsymbol{r} = \sum_{\alpha\beta,\boldsymbol{R}}(T_{\alpha\beta,\boldsymbol{R}} + V_{\alpha\beta,\boldsymbol{R}}^{(\mathrm{ext})})D_{\alpha\beta,\boldsymbol{R}}\,, \tag{4.41}$$

where

$$V_{\alpha\beta}^{(\mathrm{ext})} = \int \phi_{\alpha,\boldsymbol{0}}^*(\boldsymbol{r})V_{\mathrm{ext}}(\boldsymbol{r})\phi_{\beta,\boldsymbol{R}}(\boldsymbol{r})d\boldsymbol{r}\,, \tag{4.42}$$

$$T_{\alpha\beta} = -\frac{\hbar^2}{2m}\int \phi_{\alpha,\boldsymbol{0}}^*(\boldsymbol{r})[\nabla^2\phi_{\beta,\boldsymbol{R}}(\boldsymbol{r})]d\boldsymbol{r} \tag{4.43}$$

are two density-independent matrices, the only density dependence coming through $D_{\alpha\beta}$.

The atomic interaction Hamiltonian is entirely defined on correlated d-orbitals, and its expectation value on the GVW can be computed as indicated by Eq. (1.76)

$$E_{\mathrm{at}}[n(\boldsymbol{r})] = \mathrm{Tr}\{\hat{\Phi}^\dagger \hat{H}_{\mathrm{at}} \hat{\Phi}\} . \qquad (4.44)$$

Our $\hat{H}_{\mathrm{at}}$ is composed, apart from the Hubbard-U term $\hat{H}_{\mathrm{Hub}}$, by a Hund term $\hat{H}_{\mathrm{Hund}}$ with an inter-orbital exchange operator depending on the parameter J. Below we write their explicit form in terms of creation and annihilation operators on orbitals with definite magnetic quantum number m:

$$\hat{H}_{\mathrm{at}} = \hat{H}_{\mathrm{Hub}} + \hat{H}_{\mathrm{Hund}} \qquad (4.45)$$

$$\hat{H}_{\mathrm{Hub}} = \frac{U}{2} \sum_{mm',\sigma\sigma'} \hat{c}^\dagger_{m\sigma} \hat{c}^\dagger_{m'\sigma'} \hat{c}_{m'\sigma'} \hat{c}_{m\sigma} , \qquad (4.46)$$

$$\hat{H}_{\mathrm{Hund}} = \frac{J}{2} \sum_{m\neq m',\sigma\sigma'} \hat{c}^\dagger_{m\sigma} \hat{c}^\dagger_{m'\sigma'} \hat{c}_{m\sigma'} \hat{c}_{m'\sigma} . \qquad (4.47)$$

The dependence of $E_{\mathrm{at}}[n(\boldsymbol{r})]$ on the density $n(\boldsymbol{r})$ is implicit through the Gutzwiller constraints. We will discuss below on how to enforce them during the functional minimization.

For the double-counting energy E_{dc} we choose the expression in the fully-localized limit [104], supplemented with an additional mean-field term, which is important in enforcing the positivity of $E_{\mathrm{at}} - E_{\mathrm{dc}}$ with our definition of $\hat{H}_{\mathrm{Hund}}$ (see Appendix E.3 and Appendix E.4)

$$E_{\mathrm{dc}}[n^{(0)}(\boldsymbol{r})] = \frac{U}{2} N(N-1) - \frac{J}{2}\left[N_\uparrow(N_\uparrow-1) + N_\downarrow(N_\downarrow-1)\right] - \frac{J}{2l+1} N_\uparrow N_\downarrow . \qquad (4.48)$$

As in standard LDA+U, this double-counting energy is a function of the density $n^{(0)}(\boldsymbol{r})$ through the single-particle density matrix on local orbitals $n^{(0)}_{mm',\sigma}$, with $N = \sum_{m\sigma} n^{(0)}_{mm,\sigma}$, $N_\sigma = \sum_m n^{(0)}_{mm\sigma}$. The relationship between $n^{(0)}_{mm',\sigma}$ and the natural density matrix $n^{(0)}_a \delta_{ab}$ introduced in Sect. 1.6.2 is just a single-particle unitary transformation that does not affect the value of E_{dc} as far as s_z is a good quantum number. For this reason $E_{\mathrm{dc}}[n^{(0)}(\boldsymbol{r})]$ can be written as $E_{\mathrm{dc}}[n^{(0)}_a]$, i.e. as a function of the natural density matrix.

Choice of Hartree and exchange-correlation functional

We assume that the LDA exchange-correlation functional is a good approximation for the sum of the two functionals $E'_{\mathrm{xc}}[n(\boldsymbol{r})] = E'_{\mathrm{x}}[n(\boldsymbol{r})] + E'_{\mathrm{c}}[n(\boldsymbol{r})]$ defined in Eq. (4.29)

and Eq. (4.30), i.e.

$$E'_{\mathrm{xc}}[n(\boldsymbol{r})] = E^{(\mathrm{LDA})}_{\mathrm{xc}}[n(\boldsymbol{r})] = \int d\boldsymbol{r}\, n(\boldsymbol{r})\, \epsilon_{xc}[n(\boldsymbol{r})]\,, \tag{4.49}$$

For the feasibility of the GDF calculation we need to approximate $E^{(\mathrm{LDA})}_{\mathrm{xc}}[n(\boldsymbol{r})]$ with its first-order expansion around $n^{(0)}(\boldsymbol{r})$. Defining the quantity $\delta n(\boldsymbol{r}) = n(\boldsymbol{r}) - n^{(0)}(\boldsymbol{r})$, we have

$$E'_{\mathrm{xc}}[n(\boldsymbol{r})] \approx E^{(1)}_{\mathrm{xc}}\left[n(\boldsymbol{r}), n^{(0)}(\boldsymbol{r})\right] = \int d\boldsymbol{r}\, n^{(0)}(\boldsymbol{r}) \epsilon_{\mathrm{xc}}[n^{(0)}(\boldsymbol{r})] +$$
$$+ \int d\boldsymbol{r}\, v_{\mathrm{xc}}[n^{(0)}(\boldsymbol{r})]\delta n(\boldsymbol{r})\,, \tag{4.50}$$

where

$$v_{\mathrm{xc}}[n^{(0)}(\boldsymbol{r})] = \left.\frac{d(n\epsilon_{\mathrm{xc}}[n])}{dn}\right|_{n=n^{(0)}(\boldsymbol{r})}\,. \tag{4.51}$$

Similarly, we take a first-order expansion of the Hartree potential

$$E'_{\mathrm{H}}[n(\boldsymbol{r})] \approx E^{(1)}_{\mathrm{H}}\left[n^{(0)}(\boldsymbol{r}), n(\boldsymbol{r})\right] = \frac{e^2}{2} \int d\boldsymbol{r} d\boldsymbol{r}' \frac{n^{(0)}(\boldsymbol{r}) n^{(0)}(\boldsymbol{r}')}{|\boldsymbol{r}-\boldsymbol{r}'|} +$$
$$+ \int d\boldsymbol{r}\, \delta n(\boldsymbol{r})\, v_{\mathrm{H}}[n^{(0)}(\boldsymbol{r})]\,, \tag{4.52}$$

where

$$v_{\mathrm{H}}[n^{(0)}(\boldsymbol{r})] = \frac{e^2}{2} \int d\boldsymbol{r}' \frac{n(\boldsymbol{r}')}{|\boldsymbol{r}-\boldsymbol{r}'|}\,. \tag{4.53}$$

The term we are neglecting in Eq. (4.52) is

$$\Delta E_H\left[n^{(0)}(\boldsymbol{r}), n(\boldsymbol{r})\right] = \frac{e^2}{2} \int d\boldsymbol{r} d\boldsymbol{r}' \frac{\delta n(\boldsymbol{r})\, \delta n(\boldsymbol{r}')}{|\boldsymbol{r}-\boldsymbol{r}'|}\,, \tag{4.54}$$

and contains the electrostatic energy of the density fluctuations induced by the Gutzwiller projector. The above choice for the Hartree and exchange-correlation functionals has the great advantage that they depend on the Gutzwiller-renormalized density $n(\boldsymbol{r})$ only linearly. This enables to write the following decoupling

$$E^{(1)}_{\mathrm{H}}[n^{(0)}(\boldsymbol{r}), n(\boldsymbol{r})] = E^{(0)}_{\mathrm{H}}[n^{(0)}(\boldsymbol{r})] + \sum_{\alpha\beta,\boldsymbol{R}} V^{(\mathrm{H})}_{\alpha\beta,\boldsymbol{R}} D_{\alpha\beta,\boldsymbol{R}}\,, \tag{4.55}$$

$$E^{(1)}_{\mathrm{xc}}[n^{(0)}(\boldsymbol{r}), n(\boldsymbol{r})] = E^{(0)}_{\mathrm{xc}}[n^{(0)}(\boldsymbol{r})] + \sum_{\alpha\beta,\boldsymbol{R}} V^{(\mathrm{xc})}_{\alpha\beta,\boldsymbol{R}} D_{\alpha\beta,\boldsymbol{R}}\,, \tag{4.56}$$

where the first terms on the right-hand sides are functions of the uncorrelated density only

$$E_{\mathrm{H}}^{(0)}[n^{(0)}(\boldsymbol{r})] = -\frac{e^2}{2} \int d\boldsymbol{r} d\boldsymbol{r}' \frac{n^{(0)}(\boldsymbol{r})n^{(0)}(\boldsymbol{r}')}{|\boldsymbol{r}-\boldsymbol{r}'|} \,, \tag{4.57}$$

$$E_{\mathrm{xc}}^{(0)}[n^{(0)}(\boldsymbol{r})] = -\int d\boldsymbol{r} \, [n^{(0)}(\boldsymbol{r})]^2 \frac{d\epsilon_{\mathrm{xc}}[\xi(\boldsymbol{r})]}{d\xi(\boldsymbol{r})}\Big|_{\xi(\boldsymbol{r})=n^{(0)}(\boldsymbol{r})} \,, \tag{4.58}$$

while the second terms have a linear dependence on the Gutzwiller-renormalized density matrix analogous to the one displayed in Eq. (4.41), where the coefficients are the matrix elements of the two potentials

$$V_{\alpha\beta,\boldsymbol{R}}^{(\mathrm{H})}[n^{(0)}] = \int \phi_{\alpha,\boldsymbol{0}}^{*}(\boldsymbol{r})v_{\mathrm{H}}(\boldsymbol{r})\phi_{\beta,\boldsymbol{R}}(\boldsymbol{r})d\boldsymbol{r} \,, \tag{4.59}$$

$$V_{\alpha\beta,\boldsymbol{R}}^{(\mathrm{xc})}[n^{(0)}] = \int \phi_{\alpha,\boldsymbol{0}}^{*}(\boldsymbol{r})v_{\mathrm{xc}}(\boldsymbol{r})\phi_{\beta,\boldsymbol{R}}(\boldsymbol{r})d\boldsymbol{r} \,, \tag{4.60}$$

that depend self-consistently on $n^{(0)}(\boldsymbol{r})$. As shown in Appendix E.2, the first-order approximation for the exchange-correlation potential does not spoil the sum-rule for the exchange-correlation hole Eq. (3.38), which is one of the main strengths of LDA .

It is important to stress that, in spite of being explicitly defined as functions of two variables, $E_{\mathrm{H}}^{(1)}\left[n^{(0)}(\boldsymbol{r}), n(\boldsymbol{r})\right]$ and $E_{\mathrm{xc}}^{(1)}\left[n^{(0)}(\boldsymbol{r}), n(\boldsymbol{r})\right]$ can be thought as functionals of renormalized density $n(\boldsymbol{r})$ only. In fact, the uncorrelated density $n^{(0)}(\boldsymbol{r})$ is itself a functional of $n(\boldsymbol{r})$ via the constrained minimum condition

$$\min_{\hat{\mathcal{P}}|\Psi_0\rangle \to n(\boldsymbol{r})} \langle \Psi_0 | \hat{\mathcal{P}}^{\dagger} \hat{H} \hat{\mathcal{P}} | \Psi_0 \rangle \,, \tag{4.61}$$

which selects for every density $n(\boldsymbol{r})$ a minimizing projector $\hat{\mathcal{P}}$ and Slater determinant $|\Psi_0\rangle$, from which $n^{(0)}(\boldsymbol{r})$ can be recovered.

We will refer to our particular choice of GDF, with exchange-correlation terms explained in this section and with an atomic interaction Hamiltonian $\hat{H}_{\mathrm{at}}$ drawing inspiration from LDA+U, as the Local Density Approximation plus Gutzwiller Method (LDA+G). In the following sections we discuss its minimization and its performance when applied to bcc iron.

4.3.1 Three-step minimization of the LDA+G functional

The two densities $n(\boldsymbol{r})$ and $n^{(0)}(\boldsymbol{r})$ must be such that Gutzwiller constraints are fulfilled. When, as in body-centered cubic iron, $D_{\mu\nu,\boldsymbol{R}=0}^{(0)}$ is already diagonal with respect to the indices μ and ν of the Gutzwiller-correlated orbitals, the constraints on the density matrix can be written as

$$D^{(0)}_{\mu\nu,\boldsymbol{R}=0} = n^{(0)}_\mu \delta_{\mu\nu} \,, \tag{4.62}$$

$$\mathrm{Tr}\{\hat{\Phi}^\dagger\hat{\Phi}\ \hat{n}_{\mu\nu}\} = n^{(0)}_\mu \delta_{\mu\nu} \,, \tag{4.63}$$

where we introduced the local uncorrelated density matrix on natural orbitals $n^{(0)}_\mu \delta_{\mu\nu}$ as additional variable for the density functional. The above constraints can be enforced with Lagrange multipliers, together with the first Gutzwiller constraint

$$\mathrm{Tr}\{\hat{\Phi}^\dagger\hat{\Phi}\ \} = 1 \,. \tag{4.64}$$

Summing all the contributions defined in the previous paragraphs, we find that the functional we want to minimize has the form

$$
\begin{aligned}
\mathcal{F}[n(\boldsymbol{r}), n^{(0)}(\boldsymbol{r}), n^{(0)}_\mu] = \max_{\lambda_{\mu\nu}\lambda'_{\mu\nu}\lambda_0}\ & \mathcal{K}[n(\boldsymbol{r})] + E_{\mathrm{at}}[n(\boldsymbol{r})] - E_{\mathrm{dc}}[n^{(0)}_\mu] + \\
& + E^{(0)}_{\mathrm{H}}[n^{(0)}(\boldsymbol{r})] + E^{(0)}_{\mathrm{xc}}[n^{(0)}(\boldsymbol{r})] + \\
& - \lambda'_{\mu\nu}\left(D^{(0)}_{\mu\nu,\boldsymbol{R}=0} - n^{(0)}_\mu \delta_{\mu\nu}\right) - \lambda_{\mu\nu}\left(\mathrm{Tr}\{\hat{\Phi}^\dagger\hat{\Phi}\ \hat{n}_{\mu\nu}\} - n^{(0)}_\mu \delta_{\mu\nu}\right) \\
& - \lambda_0\left(\mathrm{Tr}\{\hat{\Phi}^\dagger\hat{\Phi}\ \} - 1\right) \,,
\end{aligned}
\tag{4.65}
$$

where the functional $\mathcal{K}[n(\boldsymbol{r})]$ contains all terms which depend on $n(\boldsymbol{r})$ linearly through the renormalized density matrix D, namely

$$\mathcal{K}(D) = \sum_{\alpha\beta,\boldsymbol{R}}\left\{T_{\alpha\beta,\boldsymbol{R}} + V^{(\mathrm{H})}_{\alpha\beta,\boldsymbol{R}} + V^{(\mathrm{xc})}_{\alpha\beta,\boldsymbol{R}} + V^{(\mathrm{ext})}_{\alpha\beta,\boldsymbol{R}}\right\} D_{\alpha\beta,\boldsymbol{R}} \,. \tag{4.66}$$

For every fixed value of $n^{(0)}_\mu \delta_{\mu\nu}$, we can optimize $\mathcal{F}[n(\boldsymbol{r}), n^{(0)}(\boldsymbol{r}), n^{(0)}_\mu]$ with respect to the two densities $n^{(0)}(\boldsymbol{r})$ and $n(\boldsymbol{r})$. In practice, by looking at equations (4.34, 4.35) and (4.36, 4.37) one can see that this is equivalent to a minimization with respect to the Slater determinant $|\Psi_0\rangle$ and the Gutzwiller parameters contained in the operator $\hat{\Phi}$. This minimization can be carried out in two separate steps:

1. a Siesta self-consistent calculation is performed in order to find the Slater determinant Ψ_0 that optimizes $\mathcal{F}[n(\boldsymbol{r}), n^{(0)}(\boldsymbol{r}), n^{(0)}_\mu]$ with respect to $n^{(0)}(\boldsymbol{r})$, enforcing the constraint (4.62) on $D^{(0)}_{\mu\nu}$ through an Augmented Lagrangian Method. The Gutzwiller parameters, and therefore the hopping renormalization parameters $R_{\mu\mu}$, are kept fixed throughout this optimization. The atomic energy $E_{\mathrm{at}}[n(\boldsymbol{r})]$ does not change, nor does the double-counting energy $E_{\mathrm{dc}}[n^{(0)}(\boldsymbol{r})]$, which is a function of $n^{(0)}(\boldsymbol{r})$ only through $n^{(0)}_a$. The self-consistent single-particle Kohn-Sham equations allowing the minimization with respect to $|\Psi_0\rangle$ are

$$(\mathcal{K}_{\alpha\beta,\boldsymbol{R}} + V^{(0)}_{\alpha\beta,\boldsymbol{R}} - \lambda'_{\alpha\beta})\psi_{\beta,\boldsymbol{R}} = \varepsilon\psi_{\alpha,\boldsymbol{0}} \,, \tag{4.67}$$

where

$$\mathcal{K}_{\alpha\beta,\boldsymbol{R}} = T_{\alpha\beta,\boldsymbol{R}} + V^{(\mathrm{H})}_{\alpha\beta,\boldsymbol{R}} + V^{(\mathrm{xc})}_{\alpha\beta,\boldsymbol{R}} + V^{(\mathrm{ext})}_{\alpha\beta,\boldsymbol{R}}, \tag{4.68}$$

$$V^{(0)}_{\alpha\beta,\boldsymbol{R}} = \int d\boldsymbol{r}\, \phi^*_{\alpha,\boldsymbol{0}}(\boldsymbol{r}) \left[\frac{\delta E^{(0)}_{\mathrm{H}}[n^{(0)}(\boldsymbol{r})]}{\delta n^{(0)}(\boldsymbol{r})} + \frac{\delta E^{(0)}_{\mathrm{xc}}[n^{(0)}(\boldsymbol{r})]}{\delta n^{(0)}(\boldsymbol{r})} \right] \phi_{\beta,\boldsymbol{R}}(\boldsymbol{r}). \tag{4.69}$$

2. a Lanczos-improved Levenberg-Marquardt (LM) algorithm (see Appendix D) optimizes $\mathcal{F}$ with respect to Gutzwiller parameters, enforcing the constraints (4.63) and (4.64). During this optimization, only the term $\mathcal{K}[n(\boldsymbol{r})]$ and the atomic energy $E_{\mathrm{at}}[n(\boldsymbol{r})]$ in Eq. (4.65) are modified. These two quantities, together with the terms enforcing constraints for Gutzwiller parameters, build a quartic functional of the matrices $\hat{\Phi}$, with explicit form (using Greek indices everywhere for simplicity)

$$\sum_{\alpha\beta} \left\{ \mathcal{K}_{\alpha\beta,\boldsymbol{R}=0} \operatorname{Tr}\{\hat{\Phi}^{\dagger}\hat{n}_{\alpha\beta}\hat{\Phi}\} + R_{\alpha\alpha}\tau_{\alpha\beta}R_{\beta\beta} \right\} + \operatorname{Tr}\{\hat{\Phi}^{\dagger}\hat{H}_{\mathrm{at}}\hat{\Phi}\} +$$

$$-\lambda_{\alpha\beta}\left(\operatorname{Tr}\{\hat{\Phi}^{\dagger}\hat{\Phi}\ \hat{n}_{\alpha\beta}\} - n^{(0)}_{\alpha}\delta_{\alpha\beta} \right) - \lambda_0 \left(\operatorname{Tr}\{\hat{\Phi}^{\dagger}\hat{\Phi}\} - 1 \right), \tag{4.70}$$

where $\tau_{\alpha\beta}$ is a hopping matrix computed from

$$\tau_{\alpha\beta} = \sum_{\boldsymbol{R}\neq 0,\alpha\beta} \mathcal{K}_{\alpha\beta,\boldsymbol{R}} D^{(0)}_{\alpha\beta,\boldsymbol{R}}, \tag{4.71}$$

and where $R_{\alpha\alpha}$ depends on $\hat{\Phi}$ through Eq. (1.77), in which the creation operator $\hat{d}_{\alpha}$ coincides with $\hat{c}_{\alpha,\boldsymbol{0}}$, since the NSB and OSB of our problem coincide. Namely (omitting the index $\boldsymbol{R} = 0$)

$$R^{\dagger}_{\alpha\alpha} = \frac{\operatorname{Tr}\{\hat{\Phi}^{\dagger}\hat{c}^{\dagger}_{\alpha}\hat{\Phi}\ \hat{c}_{\alpha}\}}{\sqrt{n^{(0)}_{\alpha}(1 - n^{(0)}_{\alpha})}}, \tag{4.72}$$

with α labeling e_g or t_{2g} states.

These two steps are repeated one after the other until self-consistency is achieved over both densities $n(\boldsymbol{r})$ and $n^{(0)}(\boldsymbol{r})$. Once converged, we are left with a total energy functional depending on the diagonal matrix elements $n^{(0)}_{\alpha}$, and that can be optimized with respect to them by steepest descent, so as to fulfill the stationary equations

$$\frac{\partial \mathcal{K}[n(\boldsymbol{r})]}{\partial n^{(0)}_{\alpha}} - \frac{\partial E_{\mathrm{dc}}[n^{(0)}(\boldsymbol{r})]}{\partial n^{(0)}_{\alpha}} + \lambda_{\alpha\alpha} + \lambda'_{\alpha\alpha} = 0. \tag{4.73}$$

The terms appearing in the above equations are the only ones depending on the local uncorrelated density matrix $n^{(0)}_{\alpha}$. The double-counting energy is a function of this density matrix only, while the functional $\mathcal{K}$, containing the renormalized density matrix $D_{\alpha\beta,\boldsymbol{R}}$, depends on $n^{(0)}_{\alpha}$ through the hopping renormalization parameters $R_{\alpha\alpha}$.

4.3.2 Siesta basis set

The Siesta LDA+G calculations we performed on bcc iron exploits a Siesta basis set of either 10 or 15 local Siesta orbitals, with a double-ζ [105] basis for s-orbitals, to which we add 3 p-like polarization orbitals, and either a single-ζ (5 orbitals) or double-ζ (10 orbitals) set of d-orbitals. All the GGA calculations we will show were performed with double-ζ d-orbitals, while the LDA or LDA+G calculations were done both with a double-ζ and a single-ζ set for d-orbitals; the latter type of calculation will be referred to with the extra label (s) in all the tables of Sect. 4.3.3.

In all LDA and LDA+G calculations we defined the local basis of original single-particle orbitals from the symmetric orthogonalization of the Siesta atomic orbitals. The local many-body space on which the Gutzwiller projector $\hat{\mathcal{P}}$ and operator $\hat{\Phi}$ are defined is the configuration space of these orbitals. The angular part of Siesta d-orbitals are the real spherical harmonics, which are irreducible representations of the cubic group. This ensures that the local single-particle density matrix $D^{(0)}_{ab,\boldsymbol{R}=0}$ is already diagonal. The Gutzwiller constraints on this matrix are imposed as in (4.62).

A complication arises in all the double-ζ calculations, where the Siesta basis set contains two d-orbitals with different radial functions for each spin and orbital quantum number m. In this case, $D^{(0)}_{\alpha\beta,\boldsymbol{R}=0}$ has couples of indices running over orbitals of identical spin and angular wavefunction. We decided to impose the second constraint (4.62) in this case as

$$\sum_{i\equiv\mu,j\equiv\nu} D^{(0)}_{ij,\boldsymbol{R}=0} = n^{(0)}_{\mu}\delta_{\mu\nu}\,, \tag{4.74}$$

where the indices μ and ν contain spin and angular quantum numbers only once, where i and j run over all the Siesta d-type orbitals. Nothing changes instead in the definition of the second constraint, Eq. (4.63).

In fact, even when the Slater determinant $|\Psi_0\rangle$ is built from a double-ζ basis, we defined the Gutzwiller projector $\hat{\mathcal{P}}$ on the configuration space of a single set of d-type orbitals. The radial function of this set will be the linear combination of the radial functions of the two d-type sets that optimizes the Siesta functional minimization.

An objection to this method in the double-ζ case may be that the atomic interaction Hamiltonian happens to be defined on the configuration space of a set of d-orbitals that is modified by the Siesta optimization, when it would seem more reasonable to define it on a fixed basis set. While the first-ζ radial function is of atomic type, as in LDA+U calculations, the second-ζ is more spread in space, since it has the function of better accounting for changes in the density shape around the positive ions of the lattice. A Hubbard Hamiltonian is traditionally defined on atomic-like orbitals, while in our double-ζ case the basis orbitals have the freedom of changing their localization during the energy optimization.

Taking these remarks into account, we still present the data we found for a double-ζ calculation along with the single-ζ results. The double basis set gives more flexibility to the Siesta optimization, and can provide more information for the discussion of the physical properties of iron arising from our simulations. It is of course clear that any comparison between different sets of data will be physically meaningful only when the calculations are made with the same type of basis set.

4.3.3 Results and discussion

The results we find for paramagnetic and ferromagnetic bcc iron by our implementation of LDA+G on the Siesta code are summarized in Fig. 4.4. There we plot the band structure for an unpolarized LDA+G calculation where we take the LDA value of the natural density matrix $n_a^{(0)}$, i.e. without the third step of the minimization procedure explained in Sect. 4.3.1.

Since the double-counting energy E_{dc} plays a role in determining the band structure only through the third optimization step, we do not worry about its explicit form, and introduce a quite general atomic interaction Hamiltonian

$$\hat{H}_{\mathrm{at}} = U/2\hat{N}(\hat{N} - \hat{\mathbb{1}}) - J|\hat{S}^2| - \kappa|\hat{L}^2|$$

with both first and second Hund's rules enforced by the parameter J and κ.

The value of $\kappa \approx 0.2$ eV can be estimated from the spectroscopic data of Corliss and Sugar [106], while an estimation of the correct value of J comes both from spectroscopy and from its expression in terms of Slater integrals F_2 and F_4 (see Appendix E.4), which we computed from the electronic structure program by Cowan [107] that yields a value in agreement with spectroscopic data. In the Table of Fig. 4.4 we also show the band mass renormalization factors Z_{e_g} and $Z_{t_{2g}}$ for different values of Hubbard parameters U.

Contrary to the claim of a full Mott localization of the e_g orbitals made by Anisimov and coworkers [43], we find only a minor localization of both e_g and t_{2g} orbitals, driven both by the Hubbard interaction U and by the Hund exchange J. The latter parameter has in fact a major role in the orbital-selectivity of the mass enhancement, as can be seen from Table 4.4.

The minor enhancement of e_g band mass with respect to the DMFT results may be connected to the fact that a sizable hybridization connects e_g orbitals on a site to s-orbitals on neighboring sites. Such a hybridization is ineffective close to the Γ point, where the e_g band remains quite flat, but is able to induce an appreciable dispersion in the rest of the Brillouin zone, especially close to the H point.

The local Gutzwiller projector can only provide a $\boldsymbol{k}$-independent renormalization Z, which is thus unable to distinguish between the flat dispersion around the Γ
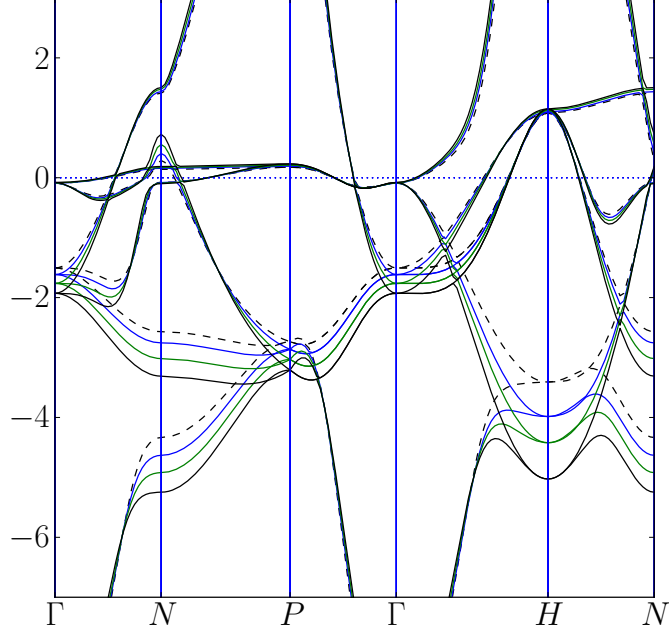
Figure 4.4: *Results for a Siesta LDA+G calculation on bcc iron with a double-ζ basis set for d-orbitals, without optimization of the natural density matrix $n_a^{(0)}$. The atomic interaction Hamiltonian we used is $\hat{H}_{\text{at}} = \hat{H}_{\text{Hub}} + \hat{H}_{\text{Hund}}$, with a slightly different Hund Hamiltonian than that presented in Eq. (4.47), including also Hund's second rule, $\hat{H}_{\text{Hund}} = -J|\hat{S}^2| - \kappa|\hat{L}^2|$. The value of κ is 0.2 eV and the value of J we used was always -1.2 eV, except for the rows marked with asterisk ($*$), for which $J = 0$ when $U = 0$, and $J = -2.2$ when $U = 10$. The band structure results corresponding to the last four rows of the table are plotted on the left upper panel, and show the effects of the band mass renormalization factors $Z_{e_g} = R_{e_g}^2$ and $Z_{t_{2g}} = R_{t_{2g}}^2$ on the bandwidth of d-type orbitals. The renormalization of total spin $|S|$ and of total angular momentum $|L|$ on d-orbitals are also shown, together with the variance of the number of d-electrons $\langle(\Delta N)^2\rangle = \langle\hat{N}^2\rangle - \langle\hat{N}\rangle^2$. The last line of the table shows how orbital selectivity is enhanced by an increase in Hund's exchange J.*

U (eV)	$\langle(\Delta N)^2\rangle$	$|S|$	$|L|$	Z_{e_g}	$Z_{t_{2g}}$
0*	2.30	0.89	3.22	1.	1.
2.5	1.37	1.00	3.27	0.94	0.96
5	1.10	1.03	3.29	0.90	0.93
10	0.82	1.04	3.31	0.82	0.87
10*	0.78	1.25	3.05	0.72	0.82

point, and e.g. the wider bandwidth in the H point. Somehow, Z can be regarded as an average of the quasi-particle residue on the whole Brillouin zone, which is a major limitation of the GA. Moreover, the hybridization with the weakly correlated s-orbitals prevents a full localization of e_g orbitals also for another reason. When a nonzero inter-orbital hopping is present between e_g and s orbitals, its Gutzwiller renormalization consists in multiplying it by a single R_{e_g} factor, since the s-orbitals are assumed to be non-correlated, see Eq. (4.40).

A condition for a – possibly orbital selective – Mott transition to occur is that the loss in kinetic energy E_{kin} due to hopping renormalization cannot be compensated by a gain in Hubbard energy E_{Hub}. In the single-band HM we saw that $R^2 \approx 1 - U/U_{\mathrm{c}} \approx D$ in the vicinity of the transition, so that $E_{\mathrm{kin}}/t \propto E_{\mathrm{Hub}}/U$, and for large enough U the compensation cannot occur. When, as in this case, a part of kinetic energy is renormalized with a single R, we have that $E_{\mathrm{kin}}/t \propto \sqrt{E_{\mathrm{Hub}}/U}$, so that the suppression of kinetic energy will never be large enough not to be compensated by a gain in E_{Hub}.

However, as pointed out in Chapt. 1, our main interest here is to understand if some features typical of a strongly correlated insulating state can have a role in determining the electronic structure of conducting iron. We therefore proceed to investigate the effects of spin polarization on kinetic, potential energy and mass renormalization of iron, trying to understand if its magnetic properties can be traced back, at least up to a certain amount, to a double-exchange mechanism.

In Tables 4.1 to 4.4 we list the data of the electronic structure of bcc iron with optimized $n_a^{(0)}$ and lattice parameters. The values of U and J used for these calculations are 2.5 eV and 1.2 eV respectively, both slightly larger than the values used by Anisimov and coworkers [43]. In the discussion that follows we will use the labels LDA and LDA+G for both non-spin-resolved and spin-resolved calculations, specifying when necessary if the system is unpolarized or polarized. We see from the second column of Table 4.1 that the optimization of $n_a^{(0)}$ in the LDA+G unpolarized case causes only small changes in the matrix elements of the natural density matrix with respect to the LDA result.

This suggests that such a value is mainly determined by electrostatic balance, which is well captured by LDA and does not require a better account of correlation effects. The Gutzwiller parameters do provide the wavefunction with more flexibility, but do not seem to give any important feedback on the natural density matrix.

This feedback becomes more important in the polarized case, where it contributes to an increase in total magnetization m. Furthermore, the renormalization of the Slater determinant has the additional important effect of increasing the lattice parameters, as can be seen by comparing the values in the second column of Table 4.2.

	Orb. dens.	QP mass renorm.
LDA para	0.606,0.685	1.,1.
LDA ferro	0.921,0.823,0.313,0.520	1.,1.,1.,1.
LDA para(s)	0.597,0.685	1.,1.
LDA ferro(s)	0.920,0.823,0.303,0.515	1.,1.,1.,1.
LDA+G para	0.607,0.685	0.977,0.986
LDA+G ferro	0.936,0.868,0.281,0.478	0.990,0.988,0.993,0.993
LDA+G para(s)	0.599,0.673	0.925,0.953
LDA+G ferro(s)	0.936,0.880,0.277 0.457	0.969,0.967,0.984,0.984

Table 4.1: *Orbital densities $n_a^{(0)}$ and quasi-particle mass renormalization parameters R_{aa}^2 for the different types of simulations performed, with $a = e_g, t_{2g}$ and $e_g \uparrow, t_{2g} \uparrow, e_g \downarrow , t_{2g} \downarrow$ for unpolarized and polarized calculations respectively. The labels of the first column are the explained in Table 4.2.*

In reality, the optimization of the lattice parameter suffers from the flaw that the Pulay force due to the atomic energy term $E_{at} - E_{dc}$ is not implemented in the code we used. Although its effect on the total forces should be checked in future calculations, we believe that it is small with respect to the effects of the Gutzwiller renormalization of the density through the parameters R_{aa}, which determines the increase of lattice parameter in the LDA+G calculation with respect to the simple LDA. Similarly to what one expects for LDA+U, the addition of a Hubbard and exchange term increases the magnetization of the polarized system, as well as its lattice constant, as can be seen in the second and third columns of Table 4.2.

Within our Gutzwiller approach we are also able to compute the local spin moment $|S|$ on d-type orbitals, from the expectation value of $\hat{S}^2$

$$S(S+1) = \text{Tr}\{\hat{\Phi}^\dagger \hat{S}^2 \hat{\Phi} \} \tag{4.75}$$

and calculate its percentage saturation, i.e. how much of the spin moment is aligned in the z-direction (fourth column of Table 4.2), thus contributing to the total magnetization m, which is instead computed from the Gutzwiller-renormalized density $n(\boldsymbol{r})$ as

$$m = \int d\boldsymbol{r} \, [n_\uparrow(\boldsymbol{r}) - n_\downarrow(\boldsymbol{r})] \; . \tag{4.76}$$

The percentage saturation increases from simple LDA to LDA+G calculations with the same basis set. In the case of double-ζ polarized calculations, the increase of total

	a_{lat} (Å)	m	m_d	$\langle \hat{S}^2 \rangle$ (2$|S|$) [%Sat.]
LDA para	2.73			1.68 (1.77)
GGA para	2.80			
LDA ferro	2.78	2.02	2.10	3.68 (2.96) [71%]
GGA ferro	2.87	2.33		
LDA para(s)	2.77			1.69 (1.77)
LDA ferro(s)	2.83	2.066	2.14	3.0 (2.61) [82%]
LDA+G para	2.75			2.16 (2.10)
LDA+G ferro	2.83	2.35	2.49	3.55 (2.90) [86%]
LDA+G para(s)	2.86			2.76 (2.47)
LDA+G ferro(s)	2.87	2.44	2.58	3.83 (3.04) [85%]
Exp.	2.87	2.22		

Table 4.2: *Results for optimized lattice parameter a_{lat}, total magnetization m, magnetization m_d on d-type orbitals, and total spin squared (magnetic moment in Bohr magnetons) [magnetic moment saturation] on d orbitals. The labels on the first column refer to unpolarized (para) and polarized (ferro) calculations, with single-ζ (label (s)), or double-ζ (no label (s)) basis set on d-orbitals, performed with GGA, LDA, or LDA+G. The magnetic moment saturation is the percentage of atomic magnetic moment $2|S|$ which contributes to the magnetization m_d. The last row shows the experimental values for lattice parameter and magnetization.*

magnetization from LDA to LDA+G is not accompanied by an equivalent increase in $|S|$, which means that in both case there exist local moments of similar magnitude but LDA+G is more capable to align them than LDA. In the case of single-ζ calculations, the increase of $|S|$ from LDA to LDA+G is instead significantly larger than the increase in magnetization, suggesting that the latter is mainly due to the larger local moment available in LDA+G.

At this point we think is worth discussing what physics lies beyond the difference between calculations that use a double or a single set of d-orbitals. As we mentioned, a double set gives more variational freedom to LDA hence should provide a better estimate of the ground-state energy. However, since the two types of d-orbitals have a different spread in real space, one should in principle treat them differently, each having its own U, hence its own renormalization factor.

Particularly, the more localized orbital must have a larger U thus a smaller Z. The weight of each orbital in the e_g Wannier function should be determined variationally, and we would expect that the more correlated the system the larger the weight of the localized d-orbital set with respect to the other. For convenience, we have treated the two orbital sets on equal footing, with the same U and Z. Because of this assumption, the Gutzwiller projector is less efficient when using the double set with respect to the single one.

For this reason, we tend to believe more in the physics uncovered by the single set calculation, although we have decided to present both results. In the future, we intend to improve the calculation by differentiating the two sets, as explained above, which we think will finally lead to the same physical scenario as in the single set with improved accuracy.

Therefore, let us concentrate for the moment on the single-ζ calculation and compare LDA with LDA+G. In the paramagnetic calculation, LDA+G predicts that a well established local moment exists on each lattice site even in the absence of net magnetization along z. A spin-resolved calculation provides all local moments with the possibility of becoming aligned, which indeed happens in iron since the ferromagnetic ground-state is energetically favored over the paramagnetic one. When magnetism is allowed, the magnetization due to d-type orbitals computed within LDA+G is roughly coincident, only slightly smaller than the moment that was available in the paramagnetic phase, as can be understood by comparing the magnetization and magnetic moments of unpolarized and polarized LDA+G calculations, shown on Table 4.2. On the contrary, the local moment obtained in paramagnetic single-ζ LDA is sensibly smaller than the magnetization found in the polarized LDA. Such a difference should have its counterpart in the balance of the various contributions to the total energy, which could provide further useful insights. In Table 4.3 we list the total energies

of the different density functional calculations we carried out, divided into atomic interaction, kinetic, electron-ion, Hartree and exchange-correlation.

The next table, Table 4.4, shows that the errors due to the first-order expansion in $n(\boldsymbol{r}) - n^{(0)}(\boldsymbol{r})$ of Hartree and exchange-correlation potentials – discussed in Sect. 4.3 – are very small, so that they are not expected to change our results in a significant way, even when we draw our conclusions from the calculation of energy differences.

Finally, in Table 4.5 we display the energy differences between couples of polarized and unpolarized calculations performed with the same functional and basis set. The last column of this table shows the percentage of local moment of the polarized calculation which was already present in the unpolarized calculation.

Focusing on the single-ζ calculations, on last two rows in Table 4.5, we note a quite surprising fact. While in LDA magnetism is accompanied by a loss of kinetic energy overwhelmed by a gain in electron-ion, Hartree and exchange energies, the opposite occurs in LDA+G. This is a clear sign that within LDA+G bcc iron is described as a correlated material, where magnetism sets in as an ordering of pre-existing moments which is driven by kinetic rather than potential energy.

A reason for the gain in kinetic energy is the fact that the quasi-particle weigths Z increase when a finite magnetization is allowed to appear, as can be seen in Table 4.1. This results is suggestive that the ferromagnetism of iron could actually be caused by a double-exchange mechanism, even though we could firmly establish it only by having a resolution in momentum space of the renormalization of quasiparticle weights.

In the double-ζ calculations the above features are less pronounced, as we could anticipate by the previous discussion; the kinetic energy now increases instead of decreasing upon allowing magnetism in LDA+G, although much less than in LDA.

A good assessment for the accuracy of this Gutzwiller approach is provided by the plots of band structures and density of states obtained within LDA , LDA+G and GGA, shown from Fig. 4.5 to Fig. 4.8. All GGA results are obtained with a double-ζ basis set, which is necessary in order to better describe the gradient changes in the density profile, a key ingredient in this density functional.

The spin-polarized GGA is generally considered as a reliable approach to transition metals, as it is able to provide a very good estimation of their lattice constants and magnetic moments. The Siesta GGA prediction for the iron lattice parameter is 2.87 Å, in good agreement with the experimental value, while its magnetic moment is slightly overestimated (2.33 vs. 2.22 Bohr magnetons). The polarized LDA+G band structure and density of states show a very good agreement with the GGA results, both when single-ζ and double-ζ basis set are used. In addition, LDA+G corrects the underestimation of lattice parameter which is a well known flaw of LDA, and increases the total magnetic moment from the under-estimated LDA value to an

	E_{tot}	$E_{\text{at}}{-}E_{\text{dc}}$	E_{kin}	E_{ie}	E_{H}	E_{xc}
LDA para	-780.599		764.261	-802.506	74.864	-385.988
LDA ferro	-780.920		766.959	-810.420	79.062	-386.640
GGA para	-781.625		765.108	-809.044	80.195	-389.121
GGA ferro	-782.235		769.901	-821.585	86.285	-390.533
LDA para(s)	-780.196		777.255	-821.272	80.940	-386.943
LDA ferro(s)	-780.567		777.947	-828.430	85.475	-387.308
LDA+G para	-777.202	2.752	766.440	-806.749	76.926	-385.943
LDA+G ferro	-777.831	2.707	767.115	-816.181	82.873	-386.095
LDA+G para(s)	-777.231	1.92	777.099	-830.914	87.494	-385.682
LDA+G ferro(s)	-777.499	2.35	774.182	-828.716	87.564	-386.117

Table 4.3: *Total energy for bcc iron computed with the different basis sets and functionals (see the caption of Table 4.2 for the explanation of labels), divided in atomic interaction contribution minus double-counting energy, kinetic energy, ion-electron interaction, Hartree and exchange-correlation energy.*

	ΔE_{H}	ΔE_{xc}
LDA+G para	0.0001	≈ 0
LDA+G ferro	0.0011	-0.0004
LDA+G para(s)	0.0083	-0.0012
LDA+G ferro(s)	0.0054	-0.0020

Table 4.4: *Estimated errors due to the approximate expressions (4.50) and (4.52) for the Hartree and exchange-correlation energies respectively, listed for the four types of simulation performed. The meaning of the labels on the first column is explained in the caption of Table 4.2. The quantities listed in the second and third columns are $\Delta E_{\text{H}} = E_{\text{H}}\left[n(\boldsymbol{r})\right] - E_{\text{H}}^{(1)}\left[n(\boldsymbol{r}), n^{(0)}(\boldsymbol{r})\right]$ and $\Delta E_{\text{xc}} = E_{\text{xc}}^{(\text{LDA})}\left[n(\boldsymbol{r})\right] - E_{\text{xc}}^{(1)}\left[n(\boldsymbol{r}), n^{(0)}(\boldsymbol{r})\right]$, in units of eV.*

|	δE_{tot}	$\delta(E_{\text{at}}-E_{\text{dc}})$	δE_{kin}	$\delta(E_{\text{ie}}+E_{\text{H}})$	δE_{xc}	δE_{ion}	$\%|S|$
LDA	-0.32		2.70	-3.72	-0.652	1.35	60%
GGA	-0.61		4.79	-6.45	-1.412	2.45	
LDA+G	-0.63	-0.04	0.68	-3.49	-0.15	2.48	72%
LDA(s)	-0.37		0.692	-2.623	-0.365	1.93	68%
LDA+G(s)	-0.27	0.43	-2.92	2.27	-0.44	0.38	90%

Table 4.5: *Energy differences between the spin-polarized and unpolarized ground-states, taken from Table 4.3, apart the seventh column, which shows the differences in ionic energies, which we did not list in Table 4.3. The last column shows the percentage of magnetic moment of the polarized system which is already accounted for by the unpolarized calculation. The LDA+G functional seems to limit the loss of kinetic energy and the gain in potential electrostatic energy of the electrons when the spin polarization along z is allowed. In the case of the single-ζ calculation the energy trends are even reversed, and spin polarization causes a decrease of kinetic energy and an increase in potential energy.*

over-estimated one, especially in the single-ζ case, where it becomes larger than the GGA result.

Comparing the unpolarized LDA+G single-ζ band structure and the unpolarized GGA band structure, we notice a slight disagreement, which may be connected to the use of a too large value of Hubbard parameter U. This is probably also the cause of the over-estimation of the total magnetization in the polarized case.

Therefore, even if the values of U and J we used for these calculations prove to be reasonable estimates of the Hubbard interaction and Hund's rules in iron, we believe that a finer tuning of these parameters will be necessary to achieve more quantitative results and discuss the advantages brought by GVM into the electronic structure calculations in transition metals.

Previous Quantum Espresso LDA+U calculations on iron [102] also pointed out the advantages of using an around-mean-limit instead of a fully-localized-limit expression for the double-counting energy. It is worth investigating the effects of this different double-counting in determining lattice constants, magnetic moments, and energy differences between polarized and unpolarized electronic structures.
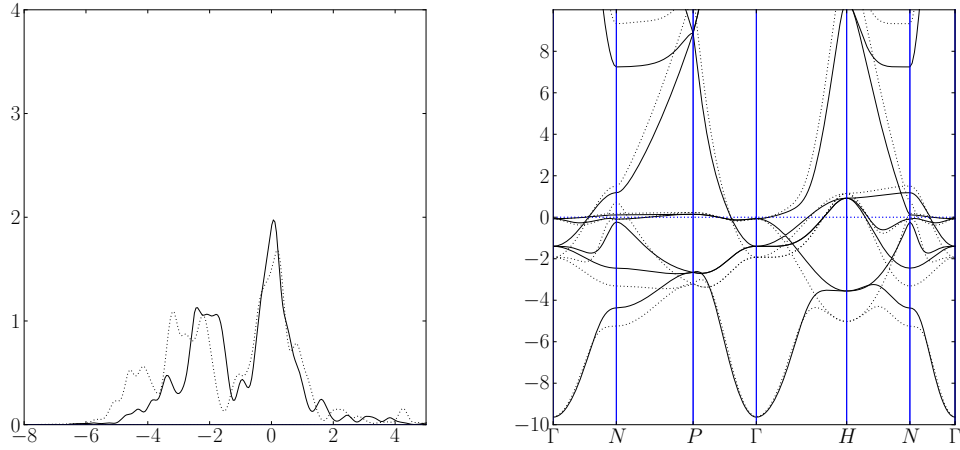
Figure 4.5: *Comparison of projected density of states and band structure between unpolarized single-ζ LDA+G (solid lines) and double-ζ LDA (dotted lines).*
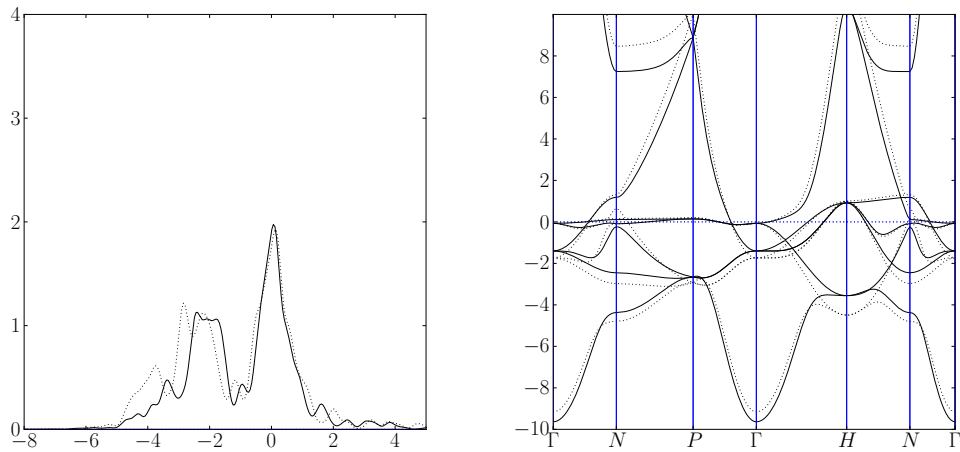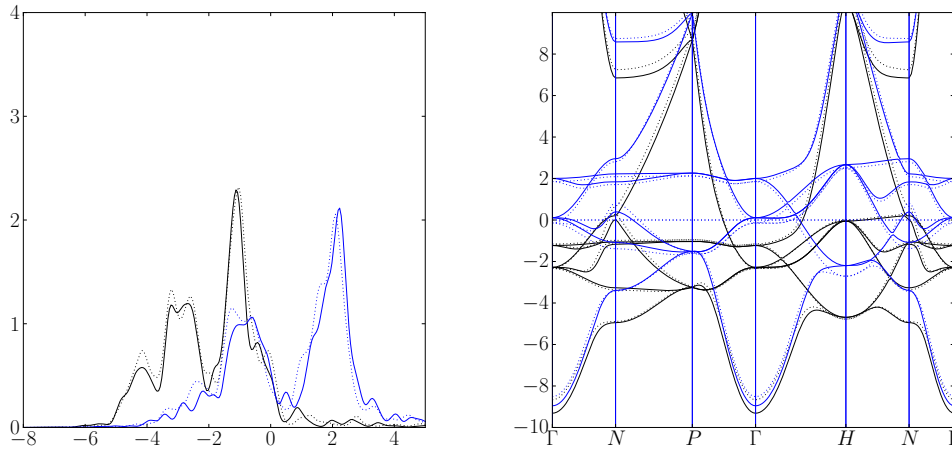

Figure 4.6: *Comparison of projected density of states and band structure between unpolarized single-ζ LDA+G (solid lines) and double-ζ GGA (dotted lines).*
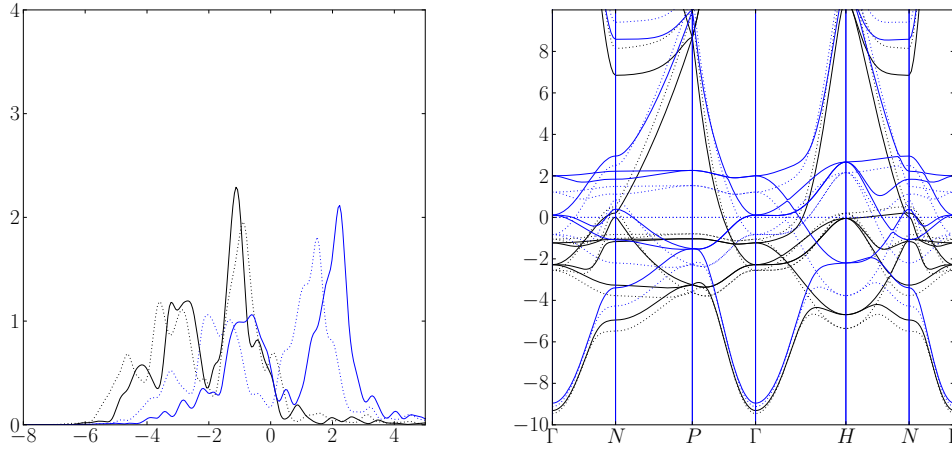
Figure 4.7: *Comparison of projected density of states and band structure between polarized single-ζ LDA+G (solid lines) and double-ζ LDA (dotted lines). The line colors blue and black refer to minority and majority spin component respectively.*

Figure 4.8: *Comparison of projected density of states and band structure between polarized single-ζ LDA+G (solid lines) and double-ζ GGA (dotted lines). The line colors blue and black refer to minority and majority spin component respectively.*

4.4 Final remarks

In this chapter integrated the formalism of Kohn-Sham DFT with that of GA, and applied the resulting LDA+G method to the calculation of the electronic structure of body-centered cubic iron. While we were not able to find a significant orbital-selective localization of electrons, as suggested by previous LDA+DMFT calculations [43], our results suggest that the magnetism of iron is, at least partially, driven by the double-exchange mechanism, which is a typically many-body phenomenon that cannot be described by conventional DFT.

The Gutzwiller approach enables to compute the magnetic-moment enhancement due to interactions already at the unpolarized LDA level, while the spin-polarized calculation provides the energy gain caused by magnetic ordering. The two phenomena, which are considered on the same footing within simple LDA, LSDA and LDA+U, appear correctly as distinct within LDA+G.

Our calculations of the electronic structure of iron through LDA+G implemented in the Siesta code can be perfected with the inclusion of two separate hopping renormalization factors on each e_g and t_{2g} multiplet of a double-ζ basis set, through which we will be able to better account for the effects of Hubbard-U and Hund's parameter J on electron localization. The estimation of lattice constants can be improved by a calculation of forces and stress including the Pulay force due to the expectation value of the atomic interaction Hamiltonian, while the prediction on the magnetic moment may be corrected through a better guess for the Hubbard-U and through the use of an AMF double-counting energy.

An application of the Gutzwiller method to realistic electronic structure calculations has been implemented by other authors in recent years. Bünemann, Weber and Gebhardt [108–110] implemented a non self-consistent Gutzwiller approach to electronic structure calculations, where a tight-binding model is set up from effective hopping parameters computed through a Kohn-Sham density functional calculation, and afterwards solved within the multi-band GA.

Fang and collaborators [111, 112] proposed a LDA+G approach where both density and Gutzwiller parameters are optimized self-consistently. To our knowledge, their method is in principle very similar to ours, with the difference that it does not include the possibility of using a projector with nonzero off-diagonal matrix elements, which is instead a natural feature of our mixed-basis parametrization with $\hat{\Phi}$ operators.

In spite of the great number of parameters contained in $\hat{\Phi}$, the Lanczos-enhanced LM algorithm we implemented for the minimization of the energy with respect to Gutzwiller parameters is stable and fast, and can be easily parallelized to deal with

more complex system as crystals having more than one atom per unit cell as transition metal compounds.

Conclusions and perspectives

Although the Gutzwiller Variational Method is not able to grasp the physics of the Mott transition on its insulating side, it is very effective when used to describe the properties of conducting materials that are "insulators in disguise", i.e. of strongly correlated metallic systems whose relevant physical observables are determined by the same many-body effects that drive the Mott transition to the insulating region of their phase diagram.

For finite lattice coordination, and for dimensionality larger than one, there is no exact method for computing the expectation value of a Hamiltonian on the Gutzwiller variational wavefunction (GVW) analytically, and one has to resort to the Gutzwiller Approximation (GA). The GA, which gives exact results for the variational energy in infinite-coordination lattices, reveals to be quite accurate already for three-dimensional systems.

When investigating the properties of single-band models, the GA can account correctly for the increased spin susceptibility due to the many-body localization of electrons, providing a reasonable explanation for magnetism where the Stoner theory appears to fail. Similar advantages characterize its multi-band formulation, which enables to describe the effects of inter-band correlations on magnetic moment formation and magnetic ordering.

The description of GVM and GA in Chapt. 1 is introductory to the results of Chapt. 2, where we proved the GA to be successfully applicable to lattice models with broken translational invariance. We showed that the GA leads to a good qualitative description of the decay of quasi-particle weight near interfaces between a strongly correlated metal and the vacuum, which can be applied to the understanding of Angle-Resolved Photoemission Spectroscopy (ARPES) spectra of realistic strongly correlated crystals as vanadium sesquioxide.

Within the same GA framework, we provided a characterization of quasi-particle properties across metal-insulator junctions that agrees in many aspects with the one obtained with more refined but computationally expensive methods such as DMFT+NRG [37, 113]. Our results were limited to half-filled cubic lattices with

no spin imbalance, but the GA was recently applied to a spin-polarized honeycomb lattice in order to investigate the magnetic properties of graphene ribbons [114].

After an introduction to Density Functional Theory in Chapt. 3, we devoted Chapt. 4 to discuss the application of the multi-band GA to realistic molecular and solid state systems, in synergy with DFT. As an extension of the LDA+U formalism, the Local Density Approximation plus Gutzwiller Method (LDA+G) method can correct the self-interaction error of Local Density Approximation (LDA), while at the same time allowing for a better description of correlations through the renormalization of the kinetic energy of the system.

We implemented our version of Local Density Approximation plus Gutzwiller Method method in the Siesta code, and showed its results for body-centered cubic paramagnetic and ferromagnetic iron, examining the role of electron-electron interactions in the magnetic moment formation and magnetic ordering.

The LDA+G functional can reproduce the GGA band structure of iron, while it is able to account for the enhancement of local magnetic moments also in unpolarized calculations, where the densities of spin up ($n_\uparrow(\boldsymbol{r})$) and spin down ($n_\downarrow(\boldsymbol{r})$) electrons coincide. The many-body driven increase in local moments, and the phenomenon of magnetic ordering, whose energy gain can be computed when the magnetization $m(\boldsymbol{r}) = n_\uparrow(\boldsymbol{r}) - n_\downarrow(\boldsymbol{r})$ is allowed to appear, are treated separately within LDA+G. In particular, magnetic ordering is shown to be accompanied by a kinetic energy gain which is typical of double-exchange magnetism.

The flexibility of the GVM as a zero-temperature, ground-state method for lattice models was recently extended to account for time-dependent correlations [115] in the single-band Hubbard model (HM), and is due for some further development in multi-band systems [116].

We believe that the LDA+G formalism can be implemented in the future in Car-Parrinello molecular dynamics codes, where the Gutzwiller parameters would act as many-body degrees of freedom to be optimized together with the electronic Slater determinant through damped dynamics. The major difficulty is the enforcement of Gutzwiller constraints, which are different than the simpler wavefunction orthogonality constraints imposed in molecular dynamics simulations. The integration of LDA+G and molecular dynamics can be the prelude to a time-dependent description of molecular and solid state systems.

Acknowledgements

I would like to thank my supervisors professors Michele Fabrizio and Erio Tosatti for wisely showing me the way through the forest of puzzled and intricate thoughts and ideas that my head is unfortunately so used to produce when nourished too well. And this enables me to thank the whole SISSA for the year of courses that were delivered by all professors, and which helped me being born into the world of numerical simulations. And still on the subject of nourishment, but on a more materialistic basis, I am glad to thank the SISSA cooks, for providing lunches whose quality greatly overtakes that of any canteen I have ever had the honour to attend.

Special thanks for useful advice and discussions related to the content of this thesis go to Nicola Lanatá, Gabriele Sclauzero, prof. Roger Fletcher, prof. Andrea Dal Corso, prof. Stefano de Gironcoli, Layla Martin-Samos, Ryan Requist, Matteo Cococcioni, prof. Nicola Manini, Alexander Smogunov. I thank Gabriele Sclauzero, Lorenzo Paulatto, Baris Malcioglu, Marco Giunta, Maurizio Zanello and Giuseppe Carleo for introducing me to the tips and tricks and traps of computational physics, and Davide Venturelli for following me at least for six months of my SISSA experience. I would like to thanks my master thesis supervisor Marco Polini, for providing me with the enthusiasm and experience that helped me so much during this PhD, and for encouraging my collaboration with his group in the first years of my stay in Trieste. My thankful thought goes also to the friends and collaborators of the group in Pisa, Prof. Reza Asgari, Dr. Andrea Tomadin, Dr. Saeed Abedinpour, Prof. A. MacDonald, Dr. Hongki Min.

I would like to thank my friends and long and short-term flatmates Lorenzo, Guido and Elisa for the welcoming, friendly and respectful environment I could feel at every moment of my stay in Trieste, so that I feel they have been like a second family to me. I thank them also for being so kind with providing me with very nicely cooked food, a favor that I was never able to return, due to my appalling cooking abilities, and due to the fact that I did not own an Allan Bay book. I also thank Lorenzo very much for giving me so many lifts, and for letting me use his old Renault so often in the first two years, and uncle Mario for giving me his nice purple japanese car for the last two years of my PhD.

I would like to thank my friends at SISSA, Davide Venturelli, Davide Rossini, Baris, Mike, Andrew, Gareth, Angus, Giuseppe, Pilar, Federica, Lorenzo, Gabriele, Marco, Serena, Janier, Juan, Nicola and all others. I thank my "local" friends Enrico, Giulio, Alberto, Emidio, with whom I shared numerous pizza dinners at pizzeria Marechiaro, always refreshed by a beer or quarter of white Friulano, and embossed by philosophical and theological discussions. A great encouragement to Enrico for the continuation of his journey.

My thanks goes then to my Modenese friends Andrea, Gianluca, Silvia and Carlo Alberto, who know me better than any other friend, to my Pisa friends Giacomino, Pozzo, Enrico, Dario, to my parents Angelo and Brunella, my quiet but unforgettably faithful grand-aunt Nella (no lady will ever beat her sense of humour, and I owe her more than she might have ever thought) my grand-aunt and uncle Elena and Renato, my grand-uncles Mario and Adelmo, and the blessed memories of "old pal" cat Napoleon and little cat Ginevra.

Of my family I thank specially my brother Paolo, who in these four years, as also in the past, went through the sunny days and tempests of life without the help of his older brother. I apologize to him for being such a (physically) "absent" brother, but swear that he has been always in my thoughts, and his silence and reservedness, his sensitivity and his sharp but humble intelligence have been more eloquent a music to my life than the words of any academic in the world.

Not few have been the moments of disappointment and dispair in these four years. I send a thanks back in time to Giovannino Guareschi and Gilbert Keith Chesterton, and all those who worked and work at the translation and understading of their works, that are being a source of strength and joy of living for many people. More than once the large feet of Don Camillo have encouraged my back not to sit down for too long, and his speaking crucifix has told me what's been always told, and makes our lives unfold.

I would like to dedicate this thesis to Martine Thompson, a wonderful girl who shared with me faith, many long phone calls, plane journeys, and lots of stressful and serene times of this last year, as well as deep discussions and hopes and misunderstandings and music and silence. I do not know how useful or successful this thesis will be, but whatever lies behind it, it's worth more than its appeerence, and this I dedicate to thee. Be it a source of decisiveness and strength in your own final PhD year, and for all its battles. Never give up!

I apologize to anyone who should have reached the end of this collection of paper sheets without finding any inspiration, or without understanding anything, or annoyed by my poor writing skills, I exhort them to read the appendix, or go to the beginning and start all over again, because something useful they will find, and

≪ *Loss and possession, death and life are one*
There falls no shadow where there shines no sun.≫ (H. Belloc)

Appendix A

Useful proofs and identities

This appendix contains some proofs and equations that help the understanding of the main ideas related to the Gutzwiller Variational Method (GVM) and expounded in Chapt. 1. We begin by proving the result of the Gutzwiller Approximation (GA) for the hopping renormalization and double occupation probability of the paramagnetic half-filled Hubbard model (HM). We next show how the hopping renormalization within GA is equal to the jump at k_{F} in the quasi-particle distribution function. In the subsequent sections we prove some of the results of the multi-band and mixed-basis formulation of the GA that are presented in Sect. 1.6.

A.1   The Gutzwiller Approximation via a thermodynamic argument

In this section we prove the GA result for the half-filled HM via a thermodynamic approach that is equivalent to the counting argument introduced by Gutzwiller [26] and better elucidated by Vollhardt [48].

If we suppose that the many-body configuration at a lattice site $\boldsymbol{R}$ is independent of the configurations on all other sites, we can consider every site as a subsystem of the global lattice, in thermodynamic equilibrium with the latter.

Tracing out the global density matrix of the system with respect to the degrees of freedom of all other sites, we are left with a 4×4 grand canonical density matrix whose entries can depend only on the parameters of the Gutzwiller projector and on

the average occupation of each site. The fermionic nature of the electrons is kept into account only at the local level, by restraining the occupation of the local orbital to be at most equal to 2.

The effect of the local Gutzwiller projector (1.13) is that of tuning the probability density of the "higher-energy" doubly occupied local configuration through an effective temperature depending on the parameter η. The double-occupation probability can be thought itself as an "entropy" which is minimum when the number of many-body configurations corresponding to the same local filling $1/2$ is minimum, i.e. when each site can be only singly occupied, while it is maximum when all many-body configurations of a site are equally populated.

From the probability densities predicted by the Gutzwiller variational wavefunction (GVW) for each configuration $|\Gamma_{\boldsymbol{R}}\rangle$,

$$W(\Gamma_{\boldsymbol{R}}) = \langle \Gamma_{\boldsymbol{R}} | \hat{\mathcal{P}}_{\boldsymbol{R}}^{\dagger} \hat{\mathcal{P}}_{\boldsymbol{R}} | \Gamma_{\boldsymbol{R}} \rangle \,, \tag{A.1}$$

we can build a grand-canonical partition function. Leaving out the index $\boldsymbol{R}$, we can easily see from Eq. (1.14) that $W(\Gamma) = \exp(-\beta D_\Gamma)$, where $\beta = -2\ln(\eta)$ and where D_Γ is the double occupation of configuration Γ, equal to 1 only for $\Gamma = |\uparrow\downarrow\rangle$ and zero in all other cases. The partition function can be written as

$$\mathcal{Z}(\beta, \mu) = \sum_{\Gamma} \exp(-\beta D_\Gamma) \exp(\mu N_\Gamma) \,, \tag{A.2}$$

where N_Γ is the number of electrons (0,1 or 2) of a configuration Γ. The configurations $|\uparrow\rangle$ and $|\downarrow\rangle$ are equivalent due to spin rotational symmetry.

Imposing the average number of particles per site to be equal to one, we find

$$\langle N \rangle = \frac{\sum_j N_\Gamma \exp(-\beta D_\Gamma + \mu N_\Gamma)}{\mathcal{Z}(\beta, \mu)} = \frac{2\exp(\mu) + 2\exp(2\mu - \beta)}{1 + 2\exp(\mu) + \exp(2\mu - \beta)} = 1 \,, \tag{A.3}$$

an equation which is true only for $\mu = \beta/2$. With this value of the chemical potential, we can compute the expectation value of the double occupation probability as

$$D = \frac{\sum_\Gamma D_\Gamma \exp(-\beta D_\Gamma + \mu N_\Gamma)}{\mathcal{Z}} = \frac{1}{2 + 2\exp(\beta/2)} = \frac{\eta}{2 + 2\eta} \,, \tag{A.4}$$

which is the GA result already introduced in Eq. (1.15).

In order to find the value of the hopping renormalization, we need to consider two sites, whose many-body configurations we suppose again independent of each other. The expectation value of the hopping operator $\hat{c}_{\uparrow,\boldsymbol{R}}^{\dagger} \hat{c}_{\uparrow,\boldsymbol{R}'}$ for an up spin between site $\boldsymbol{R}$ and $\boldsymbol{R}'$ can be computed from the amplitude

$$P(\boldsymbol{R}, \boldsymbol{R}') = \sum_{\Gamma_{\boldsymbol{R}} \Gamma_{\boldsymbol{R}'}' \Gamma_{\boldsymbol{R}}'' \Gamma_{\boldsymbol{R}'}'''} \langle \Gamma_{\boldsymbol{R}} \Gamma_{\boldsymbol{R}'}' | \hat{\mathcal{P}}_{\boldsymbol{R}'}^{\dagger} \hat{\mathcal{P}}_{\boldsymbol{R}}^{\dagger} \hat{c}_{\uparrow,\boldsymbol{R}}^{\dagger} \hat{c}_{\uparrow,\boldsymbol{R}'} \hat{\mathcal{P}}_{\boldsymbol{R}} \hat{\mathcal{P}}_{\boldsymbol{R}'} | \Gamma_{\boldsymbol{R}}'' \Gamma_{\boldsymbol{R}'}''' \rangle \,, \tag{A.5}$$

which, in the independent-site approximation, becomes

$$P(\boldsymbol{R}, \boldsymbol{R}') = \sum_{\Gamma_{\boldsymbol{R}} \Gamma'_{\boldsymbol{R}'} \Gamma''_{\boldsymbol{R}} \Gamma'''_{\boldsymbol{R}'}} \langle \Gamma_{\boldsymbol{R}} | \hat{\mathcal{P}}^\dagger_{\boldsymbol{R}} \hat{c}^\dagger_{\uparrow,\boldsymbol{R}} \hat{\mathcal{P}}_{\boldsymbol{R}} | \Gamma''_{\boldsymbol{R}} \rangle \langle \Gamma'_{\boldsymbol{R}'} | \hat{\mathcal{P}}^\dagger_{\boldsymbol{R}'} \hat{c}_{\uparrow,\boldsymbol{R}'} \hat{\mathcal{P}}_{\boldsymbol{R}'} | \Gamma'''_{\boldsymbol{R}'} \rangle = $$

$$\left(\sum_{\Gamma_{\boldsymbol{R}} \Gamma''_{\boldsymbol{R}}} \langle \Gamma_{\boldsymbol{R}} | \hat{\mathcal{P}}^\dagger_{\boldsymbol{R}} \hat{c}^\dagger_{\uparrow,\boldsymbol{R}} \hat{\mathcal{P}}_{\boldsymbol{R}} | \Gamma''_{\boldsymbol{R}} \rangle \right) \left(\sum_{\Gamma'_{\boldsymbol{R}'} \Gamma'''_{\boldsymbol{R}'}} \langle \Gamma'_{\boldsymbol{R}'} | \hat{\mathcal{P}}^\dagger_{\boldsymbol{R}'} \hat{c}_{\uparrow,\boldsymbol{R}'} \hat{\mathcal{P}}_{\boldsymbol{R}'} | \Gamma'''_{\boldsymbol{R}'} \rangle \right) . \qquad (A.6)$$

Using the Fock representation for creation and annihilation operators

$$[\hat{c}^\dagger_{\uparrow \boldsymbol{R}}]_{\Gamma \Gamma'} = \delta_{\Gamma,|\uparrow\rangle} \delta_{\Gamma',|0\rangle} + \delta_{\Gamma,|\downarrow\rangle} \delta_{\Gamma',|\uparrow\downarrow\rangle} , \qquad (A.7)$$

$$[\hat{c}_{\uparrow \boldsymbol{R}}]_{\Gamma \Gamma'} = [\hat{c}^\dagger_{\uparrow \boldsymbol{R}}]_{\Gamma' \Gamma} , \qquad (A.8)$$

one can easily see that each factor on the rightmost side of Eq. (A.6) is equal to $2 \exp(-\beta/2)/\mathcal{Z}$, so that

$$P(\Gamma_{\boldsymbol{R}} \Gamma'_{\boldsymbol{R}'} \to \Gamma''_{\boldsymbol{R}} \Gamma'''_{\boldsymbol{R}'}) = \frac{4 \exp(-\beta)}{\mathcal{Z}^2} = \frac{\eta^2}{(1+\eta)^2} . \qquad (A.9)$$

The hopping renormalization $Z(\eta)$ is the ratio between the above amplitude and the same amplitude in the absence of correlations, which can be found by setting $\eta = 1$ in the equation above. The final result for $Z(\eta)$ is therefore

$$Z(\eta) = \frac{4\eta^2}{(1+\eta)^2} , \qquad (A.10)$$

which proves the statement of Eq. (1.17).

A.2 Hopping renormalization and discontinuity in the quasi-particle distribution function

The Gutzwiller hopping renormalization Z can be shown to be equal to the jump $\mathcal{Z}$ in the quasi-particle distribution function. We prove this fact for the single-band half-filled paramagnetic HM. We use the notation $|\boldsymbol{k}| < k_{\mathrm{F}}$, $|\boldsymbol{k}| = k_{\mathrm{F}}$ and $|\boldsymbol{k}| > k_{\mathrm{F}}$ to mean that a wavevector $\boldsymbol{k}$ is inside, onto or outside the Fermi surface respectively.

In the non-interacting case, the quasi-particle distribution $n_{\boldsymbol{k}}$ at zero temperature is simply equal to a step function

$$n_{\boldsymbol{k}} = \langle \Psi_0 | \hat{c}^\dagger_{\boldsymbol{k}} \hat{c}_{\boldsymbol{k}} | \Psi_0 \rangle = \theta(|\boldsymbol{k}| < k_{\mathrm{F}}) . \qquad (A.11)$$

The above $n_{\boldsymbol{k}}$ can be written as the Fourier transform of the particle distribution in real space. For a translationally invariant system

$$n_{\boldsymbol{k}} = \sum_{\boldsymbol{R}} n_{\boldsymbol{R}} \exp(i\boldsymbol{k} \cdot \boldsymbol{R}) , \qquad (A.12)$$

where

$$n_{\boldsymbol{R}} = \langle \Psi_0 | \hat{c}_{\boldsymbol{R}}^\dagger \hat{c}_{\boldsymbol{R}'=0} | \Psi_0 \rangle \,. \tag{A.13}$$

In the presence of a nonzero Hubbard U, the GA recipe for the calculation of expectation values on the GVW provides the renormalized value for $n_{\boldsymbol{R}}$

$$\tilde{n}_{\boldsymbol{R}} = \begin{cases} \langle \Psi_0 | \hat{c}_{\boldsymbol{R}}^\dagger \hat{c}_{\boldsymbol{R}'=0} | \Psi_0 \rangle \,, & \boldsymbol{R} = 0 \\ Z(U) \langle \Psi_0 | \hat{c}_{\boldsymbol{R}}^\dagger \hat{c}_{\boldsymbol{R}'=0} | \Psi_0 \rangle \,, & \boldsymbol{R} \neq 0 \,, \end{cases} \tag{A.14}$$

where $Z(U)$ is given by Eq. (1.22).

Therefore, given a $\boldsymbol{k}$ with $|\boldsymbol{k}| = k_{\mathrm{F}}$ and a $\delta\boldsymbol{k}$ such that $|\boldsymbol{k} - \delta\boldsymbol{k}| < k_{\mathrm{F}}$ and $|\boldsymbol{k} + \delta\boldsymbol{k}| > k_{\mathrm{F}}$, we have

$$\mathcal{Z}(U) = \tilde{n}_{\boldsymbol{k}-\delta\boldsymbol{k}} - \tilde{n}_{\boldsymbol{k}+\delta\boldsymbol{k}} = 2iZ(U) \sum_{\boldsymbol{R}\neq 0} n_{\boldsymbol{R}} \exp(i\boldsymbol{k} \cdot \boldsymbol{R}) \sin(\delta\boldsymbol{k} \cdot \boldsymbol{R}) =$$

$$= Z(U) \left(n_{\boldsymbol{k}-\delta\boldsymbol{k}} - n_{\boldsymbol{k}+\delta\boldsymbol{k}} \right) = Z(U) \,, \tag{A.15}$$

where the last equality comes from the fact that the jump in the Fermi-Dirac distribution for the unprojected Fermi sea is exactly equal to 1.

A.3 Inequality for the quasi-particle renormalization factors R

In this section we prove that the absolute value of the diagonal hopping renormalization factor $|R_{\alpha\alpha}|$ computed within the multi-band Gutzwiller formalism is lower than or equal to 1. This shows, at least in the case of diagonal $R_{\alpha\beta}$, that the Gutzwiller projector always suppresses the hopping between different sites, and therefore always enhances the band mass. To begin with, we notice that, given two matrices A and B,

$$S(A, B) = \mathrm{Tr}\{A^\dagger B\} \tag{A.16}$$

is a positive-definite scalar product.

From the definition of $R_{\alpha\beta}^\dagger$ in Eq. (1.77), using for simplicity two Greek indices, we find

$$R_{\alpha\alpha}^* = \frac{\mathrm{Tr}\{\hat{\Phi}^\dagger \hat{c}_\alpha^\dagger \hat{\Phi}\, \hat{d}_\alpha\}}{\sqrt{n_\alpha^{(0)}(1 - n_\alpha^{(0)})}} \,, \tag{A.17}$$

where $n_\alpha^{(0)}$ is the diagonal element of the (uncorrelated) natural density matrix.

Since $\hat{d}_\alpha$ is sandwiched between a $\hat{\Phi}$ and a $\hat{\Phi}^\dagger$, its matrix representation is the same as $\hat{c}_\alpha$, so that we can formally write it exactly as the latter:

$$R_{\alpha\alpha}^* = \frac{\mathrm{Tr}\{\hat{\Phi}^\dagger \hat{c}_\alpha^\dagger \hat{\Phi}\, \hat{c}_\alpha\}}{\sqrt{n_\alpha^{(0)}(1 - n_\alpha^{(0)})}} \,. \tag{A.18}$$

Now we can use Eq. (A.16) to write the trace at the numerator of the previous equation as

$$\text{Tr}\{\hat{\Phi}^\dagger \hat{c}_\alpha^\dagger \hat{\Phi} \, \hat{c}_\alpha\} = S(\hat{c}_\alpha \hat{\Phi} \,, \hat{\Phi} \, \hat{c}_\alpha) \,. \qquad (A.19)$$

The Schwarz inequality can be applied to the scalar product on the right-hand side of Eq. (A.19), with the result

$$|S(\hat{c}_\alpha \hat{\Phi} \,, \hat{\Phi} \, \hat{c}_\alpha)| \leq \sqrt{S(\hat{c}_\alpha \hat{\Phi} \,, \hat{c}_\alpha \hat{\Phi})S(\hat{\Phi} \, \hat{c}_\alpha, \hat{\Phi} \, \hat{c}_\alpha)} = \sqrt{n_{\alpha\alpha}(1 - n_\alpha^{(0)})} \,, \qquad (A.20)$$

where n_α is the diagonal element of the (correlated) density matrix. The same trace can be rewritten as $S(\hat{\Phi}^\dagger \hat{c}_\alpha, \hat{c}_\alpha \hat{\Phi}^\dagger)$, and by applying the Schwarz inequality to this expression, we get

$$|S(\hat{\Phi}^\dagger \hat{c}_\alpha, \hat{c}_\alpha \hat{\Phi}^\dagger)| \leq \sqrt{S(\hat{\Phi}^\dagger \hat{c}_\alpha, \hat{\Phi}^\dagger \hat{c}_\alpha)S(\hat{c}_\alpha \hat{\Phi}^\dagger, \hat{c}_\alpha \hat{\Phi}^\dagger)} = \sqrt{n_\alpha^{(0)}(1 - n_{\alpha\alpha})} \,. \qquad (A.21)$$

Now we consider the two cases where $n_{\alpha\alpha} \leq n_\alpha^{(0)}$, and where $n_\alpha^{(0)} < n_{\alpha\alpha}$ (both values of the density matrix are bound to assume values between 0 and 1). In the first case, by using Eq. (A.20), we have

$$|\text{Tr}\{\hat{\Phi}^\dagger \hat{c}_\alpha^\dagger, \hat{\Phi} \, \hat{c}_\alpha\}| \leq \sqrt{n_{\alpha\alpha}(1 - n_\alpha^{(0)})} \leq \sqrt{n_\alpha^{(0)}(1 - n_\alpha^{(0)})} \,, \qquad (A.22)$$

while in the second case, by using Eq. (A.21), we find

$$|\text{Tr}\{\hat{\Phi}^\dagger \hat{c}_\alpha^\dagger, \hat{\Phi} \, \hat{c}_\alpha\}| \leq \sqrt{n_\alpha^{(0)}(1 - n_{\alpha\alpha})} < \sqrt{n_\alpha^{(0)}(1 - n_\alpha^{(0)})} \,, \qquad (A.23)$$

and in both cases, from Eq. (A.17), we conclude that $R_{\alpha\alpha} \leq 1$.

A.4 Expectation values in the limit of infinite lattice dimensionality

In this section, related to Sect. 1.6.1, we elucidate better the reason for the exactness of the expression (1.57) in the limit of infinite lattice dimensionality. We explain how all terms in the Wick expansion of the expectation value (1.64) where two fermionic lines are extracted from operators $\hat{\mathcal{P}}_{\boldsymbol{R}'}^\dagger \hat{\mathcal{P}}_{\boldsymbol{R}'}$ with $\boldsymbol{R}' \neq \boldsymbol{R}$, become equal to zero because of Gutzwiller constraints, while terms with four and more fermionic lines vanish in the limit of infinite lattice coordination.

Terms with two fermionic lines

The product $\hat{\mathcal{P}}_{\boldsymbol{R}}^{\dagger}\hat{\mathcal{P}}_{\boldsymbol{R}}$ of two number-preserving Gutzwiller projectors on the same site can be expanded as

$$\hat{\mathcal{P}}_{\boldsymbol{R}}^{\dagger}\hat{\mathcal{P}}_{\boldsymbol{R}} = \sum_{j\{\alpha\}\{\beta\}} \Theta_{j\{\alpha\}\{\beta\}}\hat{c}_{\alpha_1,\boldsymbol{R}}^{\dagger}\hat{c}_{\alpha_2,\boldsymbol{R}}^{\dagger}\cdots\hat{c}_{\alpha_j,\boldsymbol{R}}^{\dagger}\hat{c}_{\beta_1,\boldsymbol{R}}\hat{c}_{\beta_2,\boldsymbol{R}}\cdots\hat{c}_{\beta_j,\boldsymbol{R}}, \tag{A.24}$$

where each term in the sum contains exactly j creation and j annihilation operators, and where $\{\alpha\}$ and $\{\beta\}$ correspond to sets of indices labeling local single-particle orbitals.

We can rewrite the second Gutzwiller constraint Eq. (1.59) in the following way

$$\langle\Psi_0|\hat{\mathcal{P}}_{\boldsymbol{R}}^{\dagger}\hat{\mathcal{P}}_{\boldsymbol{R}}\hat{d}_{\gamma,\boldsymbol{R}}^{\dagger}\hat{d}_{\delta,\boldsymbol{R}}|\Psi_0\rangle = \langle\Psi_0|\hat{d}_{\gamma,\boldsymbol{R}}^{\dagger}\hat{d}_{\delta,\boldsymbol{R}}|\Psi_0\rangle. \tag{A.25}$$

Here the use of operators $\hat{d}_{\gamma,\boldsymbol{R}}^{\dagger}$ and $\hat{d}_{\delta,\boldsymbol{R}}$ in the definition of the density matrix instead of $\hat{c}_{\gamma,\boldsymbol{R}}^{\dagger}$ and $\hat{c}_{\delta,\boldsymbol{R}}$ is just a symbolic way to distinguish them from the creation and annihilation operators belonging to the definition of the two-projector product Eq. (A.24).

With this notation, we can see how the connected term in Eq. (1.65) looks like (using the short-hand notation $\langle\cdot\rangle = \langle\Psi_0|\cdot|\Psi_0\rangle$)

$$\langle\hat{\mathcal{P}}_{\boldsymbol{R}}^{\dagger}\hat{\mathcal{P}}_{\boldsymbol{R}}\hat{d}_{\gamma,\boldsymbol{R}}^{\dagger}\hat{d}_{\delta,\boldsymbol{R}}\rangle = \langle\hat{\mathcal{P}}_{\boldsymbol{R}}^{\dagger}\hat{\mathcal{P}}_{\boldsymbol{R}}\rangle\langle\hat{d}_{\gamma,\boldsymbol{R}}^{\dagger}\hat{d}_{\delta,\boldsymbol{R}}\rangle + \langle\text{conn.}\rangle \tag{A.26}$$

$$\langle\text{conn.}\rangle = \sum_{pq} \langle\hat{c}_{p,\boldsymbol{R}}^{\dagger}\hat{d}_{\delta,\boldsymbol{R}}\rangle\langle\hat{c}_{q,\boldsymbol{R}}\hat{d}_{\gamma,\boldsymbol{R}}^{\dagger}\rangle\langle\text{remainder}_{pq}\rangle. \tag{A.27}$$

The above remainder, labeled with indices p and q, is the operator

$$\text{remainder}_{pq} = \sum_{j\{\alpha\}\{\beta\}} \Theta_{j\{\alpha\}\{\beta\}}\delta(p\in\{\alpha\}, q\in\{\beta\})s(p\{\alpha\}, q\{\beta\})$$

$$\hat{c}_{\alpha_1,\boldsymbol{R}}^{\dagger}\hat{c}_{\alpha_2,\boldsymbol{R}}^{\dagger}\cdots\cancel{\hat{c}_{p,\boldsymbol{R}}^{\dagger}}\cdots\hat{c}_{\alpha_j,\boldsymbol{R}}^{\dagger}\hat{c}_{\beta_1,\boldsymbol{R}}\hat{c}_{\beta_2,\boldsymbol{R}}\cdots\cancel{\hat{c}_{q,\boldsymbol{R}}}\cdots\hat{c}_{\beta_j,\boldsymbol{R}}, \tag{A.28}$$

where $\delta(p\in\{\alpha\}, q\in\{\beta\})$ is one if indices p and q belong to sets $\{\alpha\}$ and $\{\beta\}$, and zero otherwise, while $s(p\{\alpha\}, q\{\beta\})$ accounts for the sign in the Wick decoupling. The dash on operators $\hat{c}_{p,\boldsymbol{R}}^{\dagger}$ and $\hat{c}_{q,\boldsymbol{R}}$ means that they have been removed from the above sum.

Since the right-hand side of Eq. (A.27) has to be zero for every γ and δ, and since $\langle\hat{c}_{p,\boldsymbol{R}}^{\dagger}\hat{d}_{\delta,\boldsymbol{R}}\rangle$ is a positive-definite matrix with indices p, δ (it is a single-particle density-matrix), one can conclude that the expectation value of the remainder has to be identically zero for every p and q.

This proves that even if we had operators $\hat{d}_{\delta,\boldsymbol{R}'}^{\dagger}$ and $\hat{d}_{\gamma,\boldsymbol{R}'}$ from a different site than the one where $\hat{\mathcal{P}}_{\boldsymbol{R}}^{\dagger}\hat{\mathcal{P}}_{\boldsymbol{R}}$ is defined, the connected term in Eq. (A.28) would still vanish. In short, the expectation value on the Slater determinant of every term which has two fermionic lines coming out of the operator $\hat{\mathcal{P}}_{\boldsymbol{R}}^{\dagger}\hat{\mathcal{P}}_{\boldsymbol{R}}$ is bound to vanish by virtue of Gutzwiller constraints.

Terms with four fermionic lines

In this paragraph we prove that all terms in the Wick decoupling (1.64) which connect two sites $\boldsymbol{R}$ and $\boldsymbol{R}'$ with four fermionic lines will vanish in the limit of infinite lattice dimensionality d.

Metzner and Vollhardt [56] remark that the only way to obtain a HM with a non-trivial kinetic energy in infinite dimensions is to rescale the hopping constant t as

$$t' = \frac{t}{\sqrt{d}}\,. \tag{A.29}$$

Summing the hopping matrix elements over all nearest-neighbors of a site $\boldsymbol{R}$, one gets

$$t' \sum_{\boldsymbol{R}',\langle\boldsymbol{R},\boldsymbol{R}'\rangle} \langle\Psi_0|\hat{c}^\dagger_{\boldsymbol{R}}\hat{c}_{\boldsymbol{R}'}|\Psi_0\rangle \propto dt'\langle\langle\Psi_0|\hat{c}^\dagger_{\boldsymbol{R}}\hat{c}_{\boldsymbol{R}'}|\Psi_0\rangle\rangle_{\boldsymbol{R}'} \propto \sqrt{d}\langle\langle\Psi_0|\hat{c}^\dagger_{\boldsymbol{R}}\hat{c}_{\boldsymbol{R}'}|\Psi_0\rangle\rangle_{\boldsymbol{R}'}\,, \tag{A.30}$$

where $\langle\langle\Psi_0|\hat{c}^\dagger_{\boldsymbol{R}}\hat{c}_{\boldsymbol{R}'}|\Psi_0\rangle\rangle_{\boldsymbol{R}'}$ is the average value of the hopping matrix element between nearest-neighbors $\boldsymbol{R}'$.

From the above equation one finds that, for large dimensionality d, the kinetic energy for site $\boldsymbol{R}$ is finite only for

$$\langle\langle\Psi_0|\hat{c}^\dagger_{\boldsymbol{R}}\hat{c}_{\boldsymbol{R}'}|\Psi_0\rangle\rangle_{\boldsymbol{R}'} \propto \frac{1}{\sqrt{d}}\,. \tag{A.31}$$

A connected term of the Wick decoupling of Eq. (1.64) where four fermionic lines join two sites $\boldsymbol{R}$ and $\boldsymbol{R}'$ consists of a product of four terms of the kind of Eq. (A.31), so that it behaves like $1/d^2$. Summing over all nearest-neighbors $\boldsymbol{R}'$, one finds a contribution of order $1/d$, which vanishes in the limit of infinite d.

It should be noted that the propagator in brackets in Eq. (1.64) contains a product over all sites $\boldsymbol{R}'$, not only the nearest-neighbors of $\boldsymbol{R}$. However, a scaling argument similar to the above one can be applied for next-nearest and further neighbors, since

$$\langle\langle\Psi_0|\hat{c}^\dagger_{\boldsymbol{R}}\hat{c}_{\boldsymbol{R}'}|\Psi_0\rangle\rangle_{\boldsymbol{R}'} \propto \frac{1}{d^{l/2}}\,, \tag{A.32}$$

where the average on the left-hand side is meant over all $\boldsymbol{R}'$ with a fixed metropolis distance l from $\boldsymbol{R}$. Each four-leg term for fixed $\boldsymbol{R}$ and $\boldsymbol{R}'$ behaves therefore as $1/d^{2l}$. The number n_l of sites with Metropolis distance l is, for large d, proportional to (the asymptotic result is exact for a cubic lattice)

$$n_l \approx \frac{(1 + 0.693147\, l\, d^l)}{l!}\,, \tag{A.33}$$

so that the sum over $\boldsymbol{R}'$ behaves like $1/d^l$, and vanishes for large d. It goes without saying that terms with a higher number of fermionic lines will vanish even faster for $d \to \infty$.

A.5 A proof of some equations of the mixed-basis Gutzwiller formalism

In this section we provide a brief derivation of Eq. (1.74), (1.75) and (1.77) in Sect. 1.6.2. From Eq. (1.62), we can pass to the mixed-basis representation, remembering that $R_{\alpha a}^\dagger$ transforms natural to original basis as well as renormalizing the hopping, and leaving out the index $\boldsymbol{R}$,

$$\langle \Psi_0 | \hat{\mathcal{P}}^\dagger \hat{c}_\alpha^\dagger \hat{\mathcal{P}} \hat{d}_b | \Psi_0 \rangle = \sum_a R_{\alpha a}^\dagger \langle \Psi_0 | \hat{d}_a^\dagger \hat{d}_b | \Psi_0 \rangle = R_{\alpha b}^\dagger n_b^{(0)} \,. \tag{A.34}$$

Using the recipe of Eq. (1.71), we can rewrite the above equation as

$$\mathrm{Tr}\{\sqrt{\hat{P}_0} \hat{\mathcal{P}}^\dagger \hat{c}_\alpha^\dagger \hat{\Phi} \ \hat{\mathcal{P}} \hat{d}_b \sqrt{\hat{P}_0}\} = R_{\alpha b}^\dagger n_b^{(0)} \,. \tag{A.35}$$

Exploiting the matrix representation of $\hat{P}_0$ in the basis of configurations on natural orbitals Eq. (1.70), we find that

$$\hat{d}_b \sqrt{\hat{P}_0} = \sqrt{\frac{n_b^{(0)}}{1 - n_b^{(0)}}} \sqrt{\hat{P}_0} \hat{d}_b \,, \tag{A.36}$$

so that Eq. (A.35) can be rewritten as

$$\frac{\mathrm{Tr}\{\sqrt{\hat{P}_0} \hat{\mathcal{P}}^\dagger \hat{c}_\alpha^\dagger \hat{\mathcal{P}} \sqrt{\hat{P}_0} \hat{d}_b\}}{\sqrt{n_b^{(0)}(1 - n_b^{(0)})}} = R_{\alpha b}^\dagger \,. \tag{A.37}$$

From Eq. (1.66) and (1.73), we can write $\hat{\Phi} = \hat{\mathcal{P}}\sqrt{\hat{P}_0}$, so that Eq. (A.34) becomes

$$\frac{\mathrm{Tr}\{\hat{\Phi}^\dagger \hat{c}_\alpha^\dagger \hat{\Phi} \ \hat{P}_0 \hat{d}_b\}}{\sqrt{n_b^{(0)}(1 - n_b^{(0)})}} = R_{\alpha b}^\dagger \,, \tag{A.38}$$

which is exactly Eq. (1.77).

Starting from Eq. (1.59) written in the natural basis

$$\langle \Psi_0 | \hat{\mathcal{P}}^\dagger \hat{\mathcal{P}} \hat{d}_a^\dagger \hat{d}_b | \Psi_0 \rangle = \langle \Psi_0 | \hat{d}_a^\dagger \hat{d}_b | \Psi_0 \rangle = n_a^{(0)} \delta_{ab} \,, \tag{A.39}$$

we can rewrite it remembering Eq. (1.71), so that

$$\mathrm{Tr}\{\sqrt{\hat{P}_0} \hat{\mathcal{P}}^\dagger \hat{\mathcal{P}} \hat{d}_a^\dagger \hat{d}_b \sqrt{\hat{P}_0}\} = \langle \Psi_0 | \hat{d}_a^\dagger \hat{d}_b | \Psi_0 \rangle = n_a^{(0)} \delta_{ab} \,. \tag{A.40}$$

We can now use the fact that

$$\hat{d}_b^\dagger \sqrt{\hat{P}_0} = \sqrt{\frac{1 - n_b^{(0)}}{n_b^{(0)}}} \sqrt{\hat{P}_0} \hat{d}_b^\dagger \,, \tag{A.41}$$

together with Eq. (A.36), and by inserting again the definition of $\hat{\Phi}$, we get

$$\sqrt{\frac{(1 - n_a^{(0)}) n_b^{(0)}}{n_a^{(0)} (1 - n_b^{(0)})}} \, \text{Tr}\{\hat{\Phi}^\dagger \hat{\Phi} \, \hat{d}_a^\dagger \hat{d}_b\} = \langle \Psi_0 | \hat{d}_a^\dagger \hat{d}_b | \Psi_0 \rangle = n_a^{(0)} \delta_{ab} \,. \tag{A.42}$$

Since only the term with $a = b$ is nonzero on the rightmost side of Eq. (A.42), provided that the pathological situation with $n_a^{(0)} = 0$ or $n_b^{(0)} = 0$ is avoided, we can safely divide the leftmost expression with $a \neq b$ by the square-root, so as to find

$$\text{Tr}\{\hat{\Phi}^\dagger \hat{\Phi} \, \hat{d}_a^\dagger \hat{d}_b\} = n_a^{(0)} \delta_{ab} \,, \tag{A.43}$$

which is the same expression as Eq. (1.75), with $\hat{n}_{ab} = \hat{d}_a^\dagger \hat{d}_b$. The result of Eq. (1.74) can be trivially proved with the same arguments as above.

Analytical expressions for quasi-particle weight in the layered Hubbard Model

In this appendix, entirely related to Chapt. 2, we show how to derive simple analytical expressions for the layer dependence of the quasi-particle residue $Z(z)$ in the half-filled HM with broken translational invariance near criticality, i.e. in the limit $U \to U_c$ for some of the Hubbard-Us involved in the calculation.

## B.1 Equations for the hopping renormalization R parameters near criticality

We assume a three dimensional slab geometry with constant hopping but inhomogeneous interaction $U(z)$ and with particle-hole symmetry. We define as $2\epsilon_{||}(z)$ and $2\epsilon_{\perp}(z-1/2)$ the average over the uncorrelated Slater determinant $|\Psi_0\rangle$ of the hopping energy per bond within layer z and between layers z and $z-1$, respectively.

With these definitions, the equation Eq. (2.15) can be written as

$$0 = 4\, R(z) \bigg(4\,\epsilon_{||}(z) + \epsilon_{\perp}(z - 1/2) + \epsilon_{\perp}(z + 1/2) \bigg) +$$

$$+ 2 \bigg(\epsilon_{\perp}(z - 1/2) + \epsilon_{\perp}(z + 1/2) \bigg) \bigg(R(z+1) + R(z-1) - 2R(z) \bigg) +$$

$$+ 2 \bigg(\epsilon_{\perp}(z + 1/2) - \epsilon_{\perp}(z - 1/2) \bigg) \bigg(R(z+1) - R(z-1) \bigg) + \frac{U(z)}{4} \frac{R(z)}{\sqrt{1 - R^2(z)}}.$$

$$\tag{B.1}$$

Near criticality, we expect that the layer dependence should appear as a dependence upon the scaling variable z/ξ, and, since $\xi \gg 1$, we are allowed to regard z/ξ as a continuous variable and expand Eq. (B.1) in the leading gradients.

Because of the breaking of translational invariance due to the interface, both $\epsilon_{||}(z)$ and $\epsilon_\perp(z-1/2)$ must acquire a Friedel-like z-dependence. However, as shown explicitly in Fig. B.1, $\epsilon_{||}(z)$ and $\epsilon_\perp(z-1/2)+\epsilon_\perp(z-1/2)$ vary appreciably only close to the interfaces, while $\epsilon_\perp(z-1/2)-\epsilon_\perp(z-1/2)$ is negligible. Indeed, we found that the amplitude of the Friedel's oscillations is strongly reduced near criticality, while the period stays invariant, so that it is legitimate to neglect the z dependence of $\epsilon_{||}(z)$ and $\epsilon_\perp(z\pm1/2)$ and use for them their large-z bulk values, $\epsilon_{||}$ and $\epsilon_\perp$. Noting that the
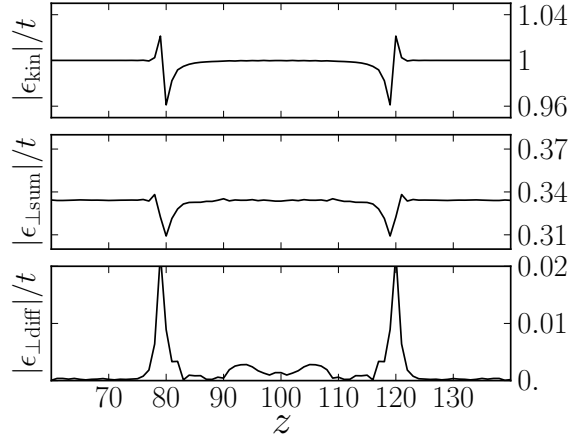
Figure B.1: *Upper panel, plot of $|\epsilon_{\mathrm{kin}}|/t$ for the sandwich geometry (c) in Fig. 2.9, with 40 central layers, $U_{\mathrm{left}} = U_{\mathrm{right}} = 2t$ and $U_{\mathrm{center}} = 15.9712t$. The value deviates by 2 to 4% from the value it would have in a homogeneous system (for which $|\epsilon_{\mathrm{kin}}| = t$). Middle panel, plot of $|\epsilon_{\perp\mathrm{sum}}| = \epsilon_\perp(z+1/2)+\epsilon_\perp(z-1/2)$. Lower panel, plot of $|\epsilon_{\perp\mathrm{diff}}| = \epsilon_\perp(z+1/2) - \epsilon_\perp(z-1/2)$*

average hopping energy per site per spin in the homogeneous case is $\epsilon_{\mathrm{kin}} = 4\epsilon_{||} + 2\epsilon_\perp$, we can write the above Eq. (B.1) in the continuous limit as

$$4\,R(z)\,\epsilon_{\mathrm{kin}} + \frac{U(z)}{4}\,\frac{R(z)}{\sqrt{1-R^2(z)}} + 4\epsilon_\perp\,\frac{\partial^2 R(z)}{\partial z^2} = 0\,, \tag{B.2}$$

and proceed to solve it for a region of space with a uniform value of $U \approx U_{\mathrm{c}}$.

Eq. (B.2) admits an integral of motion, namely

$$E = 2\epsilon_\perp \left(\frac{\partial R(z)}{\partial z}\right)^2 + 2\epsilon_{\mathrm{kin}} R^2(z)+$$

$$+ \frac{U}{4}\left(1 - \sqrt{1 - R^2(z)}\right)$$

$$\equiv 2\epsilon_\perp \left(\frac{\partial R(z)}{\partial z}\right)^2 + \mathcal{E}\left[R(z)\right], \tag{B.3}$$

where $\mathcal{E}\left[R(z)\right]$ is the Gutzwiller variational energy (GVE) for a homogeneous system calculated at fixed $R = R(z)$, i.e. without optimization.

The constant of motion E must be chosen to correspond to $\mathcal{E}[R(z_0)] = E[R_0]$, where z_0 is the layer coordinate at which we expect vanishing derivative. In a single interface, we expect that $R(z)$ will reach a constant value only asymptotically far from the interface, i.e. $z_0 \to \infty$, where R_0 becomes equal to its bulk value

$$R_0 = \sqrt{1 - u^2}, \tag{B.4}$$

and where $E[R_0]$ becomes equal to the optimized energy in a homogeneous system

$$E = E[R_0] = -\frac{U_{\mathrm{c}}}{8}\left(1 - u\right)^2 \theta(1 - u), \tag{B.5}$$

where $u = U/U_{\mathrm{c}}$ and $U_{\mathrm{c}} = -16\epsilon_{\mathrm{kin}}$.

In the case of a correlated slab sandwiched between two metal leads, we expect that $R(z)$ will reach a minimum somewhere at midway between the two interfaces. If the leads are identical, the minimum occurs right in the middle, so that R_0 becomes an unknown parameter that has to be fixed by imposing that the actual solution $R[z, R_0]$, which depends parametrically on R_0, has zero slope $\partial_z R[z, R_0] = 0$ when z is in the middle of the slab.

With the same definitions as above,

$$\mathcal{E}\left[R(z)\right] = -\frac{U_{\mathrm{c}}}{8} R^2(z) + \frac{U_{\mathrm{c}}}{4} u \left(1 - \sqrt{1 - R^2(z)}\right). \tag{B.6}$$

Since in a homogeneous cubic lattice $\epsilon_\perp = \epsilon_{\mathrm{kin}}/6 = -U_{\mathrm{c}}/96$, Eq. (B.3) can be rewritten as

$$\frac{1}{6}\left(\frac{\partial R(z)}{\partial z}\right)^2 = R_0^2 + 2u\left(1 - \sqrt{1 - R_0^2}\right)+$$

$$- R^2(z) + 2u\left(1 - \sqrt{1 - R^2(z)}\right), \tag{B.7}$$

where

$$R_0^2 + 2u\left(1 - \sqrt{1 - R_0^2}\right) = (1 - u)^2 \theta(1 - u) \tag{B.8}$$

in the case of a single interface. The prefactor 6 of the $(\partial R(z)/\partial z)^2$ comes from the homogeneous relation $\epsilon_{\text{kin}}/\epsilon_\perp = 6$. As we shall see, the numerical data can be better interpreted if $\epsilon_{\text{kin}}/\epsilon_\perp$ is considered as a free fitting parameter.

The differential equation Eq. (B.7) controls the z-dependence of $R(z > 0)$, hence of the quasi-particle residue $Z(z) = R^2(z)$, assuming that the interface affects only the boundary condition $R(z = 0) = R_{\text{surf}}$. Therefore, a surface less correlated than the bulk should be described by Eq. (B.7) with $R_{\text{surf}} > R_{\text{bulk}} = \sqrt{1 - u^2}\,\theta(1 - u)$, while the opposite case (as for instance the interface with the vacuum of section 2.2) should be obtained by setting $R_{\text{surf}} < R_{\text{bulk}}$.

We now consider separately the case of a single junction and of the double junction, with either metallic or insulating bulk. With "bulk" we refer to the region of space where we seek a solution near criticality, i.e. in the scaling regime where the continuum limit for Eq. (B.1) can be taken.

B.2   Single interface with metallic bulk

In the case of a single interface between a weakly and a strongly correlated metal, we solve Eq. (B.1) on the side of the strongly correlated metal by using Eq. (B.8) with $u \leq 1$. The differential equation Eq. (B.7) reads

$$\frac{1}{6}\left(\frac{\partial R(z)}{\partial z}\right)^2 = \left(\sqrt{1 - R^2(z)} - u\right)^2, \tag{B.9}$$

so that

$$\frac{\partial R(z)}{\partial z} = \sqrt{6}\left(\sqrt{1 - R^2(z)} - u\right), \tag{B.10}$$

with equivalent integral form

$$\int_{R_{\text{surf}}}^{R(z)} \frac{dR}{\sqrt{1 - R^2} - u} = \sqrt{6}\,z\,. \tag{B.11}$$

This integral equation can be solved exactly, leading to the implicit formula

$$\sqrt{6}\,z = \int_{\arcsin R_{\text{surf}}}^{\arcsin R(z)} \frac{\cos x\, dx}{\cos x - u} = \arcsin R(z) - \arcsin R_{\text{surf}}+$$

$$+ \frac{u}{\sqrt{1 - u^2}}\,\tanh^{-1}\left(\frac{R(z)\,R_{\text{bulk}}}{1 - \sqrt{(1 - R_{\text{bulk}}^2)(1 - R^2(z))}}\right) +$$

$$- \frac{u}{\sqrt{1 - u^2}}\,\tanh^{-1}\left(\frac{R_{\text{surf}}\,R_{\text{bulk}}}{1 - \sqrt{(1 - R_{\text{bulk}}^2)(1 - R_{\text{surf}}^2)}}\right). \tag{B.12}$$

Close to criticality, $u \simeq 1$, one can neglect the arcsines in the right-hand side of the first line of the above equation, and find the explicit expression

$$R(z) = \frac{R_{\text{bulk}} \sinh \zeta}{\cosh \zeta \pm \sqrt{1 - R_{\text{bulk}}^2}} \,, \tag{B.13}$$

where the plus sign refers to the case $R_{\text{surf}} < R_{\text{bulk}}$, and the minus sign to the opposite case, and where

$$\zeta = \sqrt{6\left(1 - u^2\right)}\, z + \tanh^{-1}\left(\frac{R_{\text{surf}}\, R_{\text{bulk}}}{1 - \sqrt{\left(1 - R_{\text{bulk}}^2\right)\left(1 - R_{\text{surf}}^2\right)}}\right) \equiv \sqrt{6}\, R_{\text{bulk}}\,\left(z + z_*\right). \tag{B.14}$$

The above solution provides a definition of the correlation length for $u \approx 1$

$$\xi = \frac{1}{\sqrt{6\left(1 - u^2\right)}} \simeq 0.289 \left(\frac{U_{\text{c}}}{U_{\text{c}} - U}\right)^{1/2}, \tag{B.15}$$

which is quite close to the Dynamical Mean-Field Theory value [37].

We note that, for $\zeta \gg 1$, Eq. (B.13) becomes

$$R(z \to \infty) \simeq R_{\text{bulk}}\left(1 \mp \sqrt{1 - R_{\text{bulk}}^2}\, \text{e}^{-\zeta}\right), \tag{B.16}$$

and therefore

$$Z(z) = R^2(z) \simeq Z_{\text{bulk}}\left(1 \mp 2\sqrt{1 - R_{\text{bulk}}^2}\, \text{e}^{-x/\xi}\right) \tag{B.17}$$

tends exponentially to its bulk value on a length scale ξ, from below or above according to $R_{\text{surf}} \gtrless R_{\text{bulk}}$, respectively.

Near criticality, i.e. $R_{\text{bulk}} = \sqrt{1 - u^2} \ll 1$, Eq. (B.13) becomes
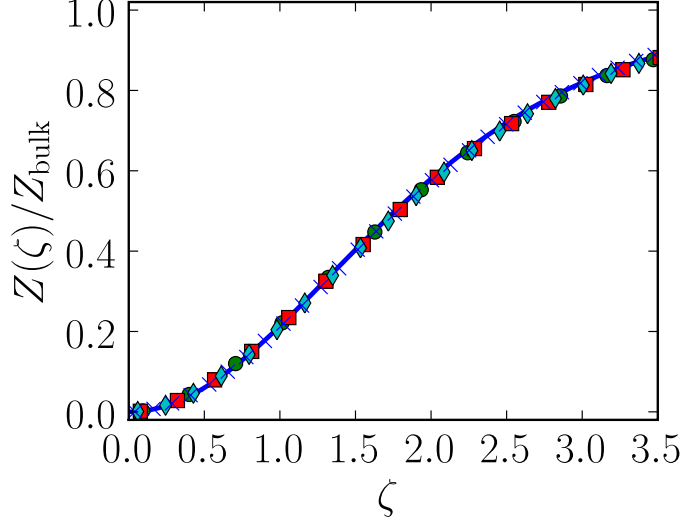
$$R(z) \simeq R_{\text{bulk}} \coth \frac{\zeta}{2}\,, \tag{B.18}$$

so that $Z(z)$ shows a simple scaling behavior [37]

$$(z + z_*)^2\, Z(z) = (z + z_*)^2\, R(z)^2 = \frac{4}{6}\left(\frac{1}{4}\zeta^2 \coth^2 \frac{\zeta}{2}\right) \equiv \frac{2}{3}\, f_{u<1}(\zeta)\,. \tag{B.19}$$

The scaling function $f_{u<1}(\zeta)$ that we find has the asymptotic behavior: $f_{u<1}(0) = 1$ and $f_{u<1}(\zeta \to \infty) \simeq \zeta^2/4$.

Another case of interest is that of the interface with vacuum discussed in section 2.2, which is equivalent to the interface between a Mott insulator and a strongly-correlated

Figure B.2: *Numerical results for $Z(z)$ in the surface geometry, with $U = 15.9872t$ (crosses), $15.9712t$ (diamonds), $15.9487t$ (squares), $15.9198t$ (circles). The solid curve is $\tanh^2(\zeta/2)$, i.e. $R^2(\zeta)$ as defined in Eq. (B.13) (with plus sign) and expanded to first order in $R_{\mathrm{bulk}} \ll 1$. In order to define ζ the same expansion has been carried out in Eq. (B.14), where we set the quantity $\epsilon_{\mathrm{kin}}/\epsilon_\perp$ equal to 9.427 instead of 6, in order to fit the numerical data.*

metal. Solving on the metallic side requires $R_{\mathrm{surf}} \ll 1$, so that from Eq. (B.14) it follows that

$$z_* \simeq \frac{R_{\mathrm{surf}}}{\sqrt{6}(1 - u)} \ll 1 \,. \tag{B.20}$$

Away from criticality and for $\zeta \ll 1$, which is allowed since $z_* \ll 1$, we find through Eq. (B.13) with the plus sign that

$$R(z) \simeq \sqrt{6} \, (1 - u) \, (z + z_*) \,, \tag{B.21}$$

so that

$$Z(z) \simeq 6 \, (1 - u)^2 \, (z + z_*)^2 \,, \tag{B.22}$$

showing that the quasi-particle residue approaches its surface value with a finite curvature.

In Fig. B.2 and Fig. B.3 we show the rescaled numerical data for an interface between a 200-layer-wide correlated metal slab and the vacuum and for a junction between a weakly correlated metal and a strongly correlated metal. It is easy to fit this data with the function $R^2(z)$ displayed in Eq. (B.14) by tuning just one parameter,

which, as discussed above, is the value of $\epsilon_{\text{kin}}/\epsilon_\perp$ (equal to 6 in the homogeneous problem). The fact that the ideal theoretical result, relying on homogeneous values for hopping and kinetic energy, fits the numerical data with just a single tunable parameter, is a pleasant feature.
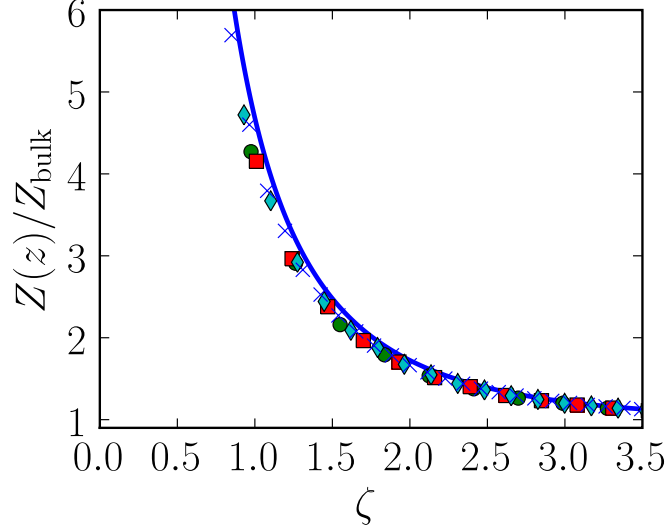
Figure B.3: *Numerical results for $Z(z)$ in the single junction geometry with metallic bulk, the position of the junction is chosen as the origin for the spatial coordinate, the metal on the left side is very weakly correlated ($U = 2t$); the values for U on the right side are the same of Fig. B.2. The solid curve is now the function $1/\tanh^2(\zeta/2)$, i.e. the second power of Eq. (B.13) (with minus sign) expanded to first order in R_{bulk}. As in Fig. B.2, the definition of ζ has been obtained from Eq. (B.14) by expanding to first order in R_{bulk}. The value of $\epsilon_{\text{kin}}/\epsilon_\perp$ that fits the data is now 8.254.*

B.3   Single interface with insulating bulk

In this case of an interface between a weakly correlated metal and a Mott insulator, we solve Eq. (B.1) on the insulating side, for which purpose we have to set $u \geq 1$ in Eq. (B.8). Eq. (B.7) now reads

$$\frac{1}{6}\left(\frac{\partial R(z)}{\partial z}\right)^2 = -R^2(z) + 2u\left(1 - \sqrt{1 - R^2(z)}\right), \qquad \text{(B.23)}$$

leading to

$$\int \frac{dR}{\sqrt{2u - R^2 - 2u\sqrt{1 - R^2}}} = -\sqrt{6}\int dz, \qquad \text{(B.24)}$$

where we have assumed that on the surface R_{surf} is finite, while R decays into the bulk, so that the derivative is negative.

The above integral equation can be solved with an implicit solution

$$-\sqrt{6\,(u-1)}\,z = 2\,\sqrt{u-1}\,\arcsin\left(\frac{\cos y(z)}{\sqrt{u}}\right) - 2\,\sqrt{u-1}\,\arcsin\left(\frac{\cos y_{\text{surf}}}{\sqrt{u}}\right)$$
$$- \tanh^{-1}\left(\frac{\sqrt{u-1}\,\cos y(z)}{\sqrt{u-\cos^2 y(z)}}\right) + \tanh^{-1}\left(\frac{\sqrt{u-1}\,\cos y_{\text{surf}}}{\sqrt{u-\cos^2 y_{\text{surf}}}}\right) , \quad \text{(B.25)}$$

where $R(z) = \sin 2y(z)$, $R_{\text{surf}} = \sin 2y_{\text{surf}}$.

As before the arcsines can be neglected near criticality, so that we can obtain the explicit solution

$$R^2(z) = 1 - \left(1 - \frac{2\,(u-1)}{u\cosh^2 \zeta - 1}\right)^2 , \quad \text{(B.26)}$$

with

$$\zeta = \sqrt{6\,(u-1)}\,z + \tanh^{-1}\left(\frac{\sqrt{u-1}\,\cos y_{\text{surf}}}{\sqrt{u-\cos^2 y_{\text{surf}}}}\right) \equiv \sqrt{6\,(u-1)}\,(z + z_*) . \quad \text{(B.27)}$$

In the case of an insulating bulk, the correlation length defined through Eq. (B.28) is therefore

$$\xi = \frac{1}{\sqrt{6\,(u-1)}} \simeq 0.408\left(\frac{U_{\text{c}}}{U - U_{\text{c}}}\right)^{1/2} , \quad \text{(B.28)}$$

with a different numerical prefactor, actually a $\sqrt{2}$ greater, with respect to the metallic bulk Eq. (B.15).

Near criticality, $u \gtrsim 1$,

$$R(z)^2 = Z(z) \simeq \frac{4\,(u-1)}{\sinh^2 \zeta} , \quad \text{(B.29)}$$

so that, as before,

$$(z + z_*)^2\,Z(z) = \frac{4}{6}\left(\frac{\zeta^2}{\sinh^2 \zeta}\right) \equiv \frac{2}{3}\,f_{u>1}(\zeta) , \quad \text{(B.30)}$$

has a scaling behavior with $f_{u>1}(0) = 1$ and

$$f_{u>1}(\zeta \to \infty) \simeq 4\zeta^2\,\mathrm{e}^{-2\zeta} . \quad \text{(B.31)}$$

B.4 Double junction

We model the double junction as a slab of length $2d$ in contact with two leads. In this case we need to use Eq. (B.7) with a R_0 that has to be fixed by imposing that the desired solution $R(z)$ becomes equal to R_0 at some z_0 within the slab. If we assume that both leads are less correlated than the slab, then $R(z)$ always decreases moving away from any of the two interfaces, and we can determine R_0 by imposing either of the two conditions:

$$\int_{R_{\mathrm{surf}}^<}^{R_0} \frac{dR}{\sqrt{R_0^2 + 2u\sqrt{1 - R_0^2} - R^2 - 2u\sqrt{1 - R^2}}} = -\sqrt{6}\, z_0, \tag{B.32}$$

$$\int_{R_0}^{R_{\mathrm{surf}}^>} \frac{dR}{\sqrt{R_0^2 + 2u\sqrt{1 - R_0^2} - R^2 - 2u\sqrt{1 - R^2}}} = \sqrt{6}\,(2d - z_0)\,, \tag{B.33}$$

where $R_{\mathrm{surf}}^<$ and $R_{\mathrm{surf}}^>$ are the values of $R(z)$ at the left and right surfaces, respectively. Taking the difference Eq. (B.33) minus Eq. (B.32) we find

$$\sqrt{6}\,2d = \left(\int_{R_0}^{R_{\mathrm{surf}}^>} + \int_{R_0}^{R_{\mathrm{surf}}^<} \right) \frac{dR}{\sqrt{R_0^2 + 2u\sqrt{1 - R_0^2} - R^2 - 2u\sqrt{1 - R^2}}}\,, \tag{B.34}$$

which has to be solved to find R_0 as function of the other parameters. Once R_0 is found, one can determine z_0.

In order to simplify the calculations, we will assume two identical leads, i.e. $R_{\mathrm{surf}}^< = R_{\mathrm{surf}}^> = R_{\mathrm{surf}}$, so that $z_0 = d$ and Eq. (B.34) becomes

$$\sqrt{6}\,d = \int_{R_0}^{R_{\mathrm{surf}}} \frac{dR}{\sqrt{R_0^2 + 2u\sqrt{1 - R_0^2} - R^2 - 2u\sqrt{1 - R^2}}}$$

$$= \frac{2}{\sqrt{(a - c)(b - p)}} \left[(c - b)\,\Pi\left(\phi, \frac{c - p}{b - p}, k \right) + b\,F(\phi, k) \right]\,, \tag{B.35}$$

with parameters $a > b > c > u \geq p$. The last expression can be derived easily after the change of variable $R = \sqrt{1 - x^2}$, and seemingly $R_0 = \sqrt{1 - x_0^2}$ and $R_{\mathrm{surf}} = \sqrt{1 - x_{\mathrm{surf}}^2}$. $\Pi(\phi, n, k)$ and $F(\phi, k)$ are elliptic integrals of third and first kind, respectively

$$F(\phi, k) = \int_0^\phi \frac{dx}{\sqrt{1 - k^2 \sin^2 x}}\,, \tag{B.36}$$

$$\Pi(\phi, n, k) = \int_0^\phi \frac{dx}{\left(1 - n \sin^2 x\right)\sqrt{1 - k^2 \sin^2 x}}\,, \tag{B.37}$$

and

$$\phi = \arcsin \sqrt{\frac{(b-p)(c-u)}{(c-p)(b-u)}} \, , \tag{B.38}$$

$$k = \sqrt{\frac{(a-b)(c-p)}{(a-c)(b-p)}} \, . \tag{B.39}$$

The various parameters are, when $2u - x_0 \geq 1$,

$$\begin{cases} a & = 2u - x_0 \, , \\ b & = 1 \, , \\ c & = x_0 \, , \\ p & = -1 \, , \\ u & = x_{\text{surf}} \, , \end{cases} \tag{B.40}$$

so that

$$\phi = \arcsin \sqrt{\frac{2\left(x_0 - x_{\text{surf}}\right)}{\left(x_0 + 1\right)\left(1 - x_{\text{surf}}\right)}} \, , \tag{B.41}$$

$$k = \sqrt{\frac{\left(2u - x_0 - 1\right)\left(x_0 + 1\right)}{4\left(u - x_0\right)}} \, . \tag{B.42}$$

On the contrary, if $2u - x_0 < 1$, then

$$\begin{cases} a & = 1 \, , \\ b & = 2u - x_0 \, , \\ c & = x_0 \, , \\ p & = -1 \, , \\ u & = x_{\text{surf}} \, , \end{cases} \tag{B.43}$$

hence

$$\phi = \arcsin \sqrt{\frac{(2u - x_0 + 1)(x_0 - x_{\text{surf}})}{(x_0 + 1)(2u - x_0 - x_{\text{surf}})}} \, , \tag{B.44}$$

$$k = \sqrt{\frac{(1 - 2u + x_0)(x_0 + 1)}{(1 - x_0)(2u - x_0 + 1)}} \, . \tag{B.45}$$

We rewrite

$$(c - b)\, \Pi\left(\phi, \frac{c - p}{b - p}, k\right) + b\, F(\phi, k) =$$

$$= \int_0^\phi dx \, \left(\frac{p(b - c) + b(c - p)\cos^2 x}{(b - c) + (c - p)\cos^2 x}\right) \frac{1}{\sqrt{1 - k^2 \sin^2 x}} \, , \tag{B.46}$$

and note that, at $x = \phi$

$$\frac{p(b-c) + b(c-p)\cos^2\phi}{(b-c) + (c-p)\cos^2\phi} = x_{\text{surf}} \geq 0. \tag{B.47}$$

and in addition that $b - c$ in both cases is very small.

Indeed, for $2u - x_0 > 1$, which corresponds to an insulating slab where $R_0 = \sqrt{1 - x_0^2} \to 0$ for large d, we have that $b - c = 1 - x_0 \ll 1$. In the opposite case of a weakly correlated slab, it is still true that $b - c = 2u - x_0 - x_0 \ll 1$ since $x_0 \to u$ for large d. Therefore, the quantity

$$\frac{p(b-c) + b(c-p)\cos^2 x}{(b-c) + (c-p)\cos^2 x} \tag{B.48}$$

is practically constant and equal to b everywhere but close to the extreme of integration, where it rapidly decays to x_{surf}. To leading order we can then write

$$(c-b)\,\Pi\left(\phi, \frac{c-p}{b-p}, k\right) + b\,F(\phi, k) \simeq b\,F(\phi, k)\,, \tag{B.49}$$

so that the equation to be solved becomes

$$\sqrt{6}\,d = \frac{2b}{\sqrt{(a-c)(b-p)}}\,F(\phi, k) =$$

$$= \frac{2b}{\sqrt{(a-c)(b-p)}}\left[K(k) - F\left(\arcsin\frac{\cos\phi}{\sqrt{1 - k^2\sin^2\phi}}, k\right)\right], \tag{B.50}$$

where $K(k) = F(\pi/2, k)$, and where the last expression is more convenient since $\phi \simeq \pi/2$. In order to find x_0 as function of the other parameters, we have to consider separately three different cases.

Insulating off-critical behavior: $u \gg 1$

In this case $2u - x_0 > 1$. We note that k as a function of u at fixed $x_0 \simeq 1$ is equal to

$$k^2 = \frac{x_0 + 1}{4} \simeq \frac{1}{2}\,, \tag{B.51}$$

for $u = 1$, and increases very rapidly to its asymptotic $u \gg 1$ value

$$k^2 = \frac{x_0 + 1}{2} \simeq 1\,. \tag{B.52}$$

Therefore Eq. (B.50) is, at leading order,

$$\sqrt{6}\,d = \frac{1}{\sqrt{u-1}}\,K\left(\sqrt{\frac{1 + x_0}{2}}\right) \simeq \frac{1}{2\sqrt{u-1}}\,\ln\frac{32}{1 - x_0}\,, \tag{B.53}$$

so that in this limit we have a value

$$Z_0 = R_0^2 \simeq 64\,e^{-\sqrt{24(u-1)}\,d} \tag{B.54}$$

which vanishes exponentially with the width of the slab.

Critical behavior: $u = 1$

In this case

$$k^2 = \frac{x_0 + 1}{4} \simeq \frac{1}{2},$$ (B.55)

hence at leading order Eq. (B.50) reads

$$\sqrt{6}\, d = \frac{1}{\sqrt{1 - x_0}} K\left(\frac{1}{\sqrt{2}}\right) = \frac{1}{4\sqrt{\pi}\,\sqrt{1 - x_0}} \left[\Gamma\left(\frac{1}{4}\right)\right]^2,$$ (B.56)

from which it follows that

$$Z_0 = R_0^2 = \frac{1}{48\pi} \left[\Gamma\left(\frac{1}{4}\right)\right]^4 \frac{1}{d^2} \simeq \frac{1.146}{d^2}.$$ (B.57)

Once again we find a critical behavior $d^2 Z_0 \simeq const.$, with a sizable constant 1.146.

Metallic off-critical behavior: $u \ll 1$

This is the case in which $2u - x_0 < 1$ and $x_0 \simeq u$, so that

$$1 - k^2 = \frac{4(u - x_0)}{(2u - x_1 + 1)(1 - x_0)} \simeq \frac{4(u - x_0)}{1 - u^2}.$$ (B.58)

Therefore Eq. (B.50) is

$$\sqrt{6}\, d \simeq \frac{u}{\sqrt{1 - u^2}} \ln \frac{16}{1 - k^2} = \frac{u}{\sqrt{1 - u^2}} \ln \frac{4(1 - u^2)}{u - x_0},$$ (B.59)

whose solution is

$$u - x_0 = 4(1 - u^2)\, \mathrm{e}^{-\sqrt{6}\,\sqrt{1 - u^2}\, d/u}.$$ (B.60)

Since $Z_{\mathrm{bulk}} = 1 - u^2$, it follows that

$$Z_0 \simeq Z_{\mathrm{bulk}} \left(1 + 8u\, \mathrm{e}^{-\sqrt{6}\,\sqrt{1 - u^2}\, d/u}\right).$$ (B.61)

B.5 Comparison with Dynamical Mean-Field Theory

Near the Mott transition, $U \simeq U_{\mathrm{c}}$, Potthoff and Nolting in Ref. [36] introduced a set of linearized DMFT recursive equations for the layer dependent quasi-particle

residue. Taking, as before, the continuous limit of their Eq. (37), with $q = 4$ $p = 1$ and $U_c = 6t\sqrt{6}$, one finds the following differential equation

$$\frac{1}{6} \frac{\partial^2 Z(z)}{\partial z^2} + 2\,Z(z)\,(1-u) - c\,Z(z)^2 = 0\,. \tag{B.62}$$

The numerical constant is estimated to be $c = 11/9$ [117]. The limiting behavior for $u \to 1$ is the solution of

$$\frac{1}{6} \frac{\partial^2 Z(z)}{\partial z^2} = c\,Z(z)^2\,, \tag{B.63}$$

namely

$$z^2\,Z(z) = \frac{1}{c} = \frac{9}{11} \simeq 0.82\,. \tag{B.64}$$

Let's consider instead our Eq. (B.2) that, divided by $4\epsilon_{\text{kin}} = -U_c/4$, can be written as

$$
\begin{aligned}
0 &= \frac{1}{6} \frac{\partial^2 R(z)}{\partial z^2} + R(z) - u\,\frac{R(z)}{\sqrt{1 - R(z)^2}} \\
&\simeq \frac{1}{6} \frac{\partial^2 R(z)}{\partial z^2} + (1-u)\,R(z) - \frac{1}{2}\,R(z)^3\,.
\end{aligned} \tag{B.65}
$$

At criticality, $u \to 1$, the solution

$$z^2\,R(z)^2 = z^2\,Z(z) = \frac{2}{3} \simeq 0.66\,, \tag{B.66}$$

is just the limiting value of Eqs. (B.30) and (B.19) for $\zeta = 0$. The numerical coefficient $2/3$ that we find is slightly smaller than the linearized DMFT one, $9/11$, but both are much bigger than the value extracted by straight DMFT calculations in Ref. [37], namely 0.008. Supposedly, straight DMFT is a better approximation than linearized DMFT, which in turn should be better than our Gutzwiller technique. It is therefore likely that our results overestimate the quasi-particle residue Z.

Building the symmetric Gutzwiller projector

Whenever we wish to define a Gutzwiller projector $\hat{\mathcal{P}}$, or generalized Gutzwiller projector $\hat{\Phi}$ in the mixed-basis formalism, we need to choose a local many-body basis for its matrix representation. The most intuitive basis for this purpose is the basis of electronic configurations (BC), or in other words the basis of single Slater determinants, built with occupied local single-particle spin-orbitals (in Sect. 1.6.2 we referred to these single-particle orbitals with the term original single-particle basis (OSB)). If represented on this basis of configurations, the number operator $\hat{N}$ and the z-component of the spin operator $\hat{S}_z$ are diagonal matrices.

When the angular part of the orbitals in the OSB is built from spherical harmonics, the BC diagonalizes also the z-projection $\hat{L}_z$ of total angular momentum. However, it does not diagonalize neither the square modulus of the total spin operator $\hat{S}^2$, nor that of the total angular momentum $\hat{L}^2$.

In sections C.1 and C.2 we explain the procedure we used to linearly combine the Slater determinants of the BC in order to build states labeled by the quantum numbers $\{N, S, S_z, L, L_z\}$. For this purpose, we need to perform a unitary transformation in the local many-body space, so as to switch from the BC what we will call the many-body symmetric basis (MSB) for full rotational symmetry, i.e. the basis diagonalizing the generators of the group of spin $(SU(2))$ and orbital rotations $(O(3))$.

In Sect. C.3 we show how to linearly transform the MSB in the case of full rotational symmetry to the MSB in the case of a lower symmetry as the cubic crystal symmetry. The last section, Sect. C.4, contains the recipe to build the Gutzwiller parameter

matrix $\hat{\Phi}$ that commutes with all the generators of the symmetry group of the given system.

C.1   Implementation of spin rotational symmetry

It is a known fact [118] that Young Tableaux can be used to combine $SU(2)$ states to form eigenstates of total spin operators $\hat{S}^2$ and $\hat{S}_z$. We use this knowledge to build the spin-symmetric many-body basis for our Gutzwiller calculations.

A single electronic configuration, i.e. a Slater determinant of local orbitals, can be built by specifying which orbitals are doubly occupied (we will pictorially represent them with the symbol ■), which are empty (□), and which are occupied by just a single up ↑ or down ↓ spin. Electronic configurations on M orbitals can therefore be thought as "words" that are M characters long, built with only four (□, ■, ↑, ↓) types of letters. Above and below left in Table C.1 are shown examples of these configurations.

Since both singly and doubly occupied sites are spin-singlets, only the ↑ and ↓ letters, carrying a spin of $1/2$, are of some importance for building eigenstates of total spin. The Young Tableaux provide us with the unitary transformation that diagonalizes $\hat{S}^2$ and $\hat{S}_z$ in the subspace of all configurations with the same number and position of singly occupied orbitals, and with the same ■ and □ symbols on the remaining ones.

C.1.1   Counting of spin states

The total number of configurations N_a with a singly occupied sites on M orbitals is equal to

$$N_a = \binom{M}{a} 2^{M-a} 2^a \,, \tag{C.1}$$

where the first factor counts the ways of choosing a singly occupied states, the second accounts for their degeneracy due to the –irrelevant for labeling the spin configuration – ■ and □ configurations, and the third counts the spin degrees of freedom of a set of a spins. The position of the singly occupied sites and the configuration of the remaining empty and doubly occupied sites will not be altered by the unitary transformation to the basis of eigenstates of $\hat{S}_z$ and $\hat{S}^2$.

We can therefore restrict our discussion to a set of a spins sitting on different spatial orbitals, without having to specify any information about their orbital quantum number. On this set, the total spin along z can have values between $a/2$ and $-a/2$.

$$|\square\,\square\,\square\,\square\,\square\,\rangle \qquad\qquad |\blacksquare\,\blacksquare\,\blacksquare\,\blacksquare\,\blacksquare\,\rangle$$

$$|\uparrow\downarrow\uparrow\uparrow\downarrow\rangle \qquad\qquad \frac{1}{\sqrt{2}}\big(|\uparrow\downarrow\,\square\,\square\,\blacksquare\,\rangle - |\downarrow\uparrow\,\square\,\square\,\blacksquare\,\rangle\big)$$

Table C.1: *Above and below left, examples of Slater determinants composing the BC of a set of 5 orbitals (as the atomic d-orbitals of a transition metal), 10 spin-orbitals. Above left, empty configuration; above right, full configuration. Below left, a Slater determinant belonging to the set of half-filled configurations. Below right, example of a singlet $S = 0$ configuration of four particles, which is found by unitary transforming the BC. The matrix elements of the unitary transformation that diagonalizes the operator $\hat{S}^2$ are the same between configurations that have the same position and number of squares, irrespective of their color.*

The states with exactly $S_z = -a/2 + N_\downarrow$ are

$$\binom{a}{N_\downarrow}, \tag{C.2}$$

if $N_\downarrow$ is the number of spin-down electrons in the set.

C.1.2   Young Tableau classification of a set of 5 spins

Given a set of 5 spins 1/2, we have exactly $2^5 = 32$ different spin states. The state with maximum S_z component ($S_z = 5/2$) can be built only from the totally symmetric Young Tableau

$$\boxed{\uparrow\,|\,\uparrow\,|\,\uparrow\,|\,\uparrow\,|\,\uparrow}, \tag{C.3}$$

which corresponds to $S = 5/2$. This particular state is a single Slater determinant, already belonging to the basis of spin configurations.

The application of the operator $\hat{S}_-$ provides us with the totally symmetric state

$$\boxed{\uparrow\,|\,\uparrow\,|\,\uparrow\,|\,\uparrow\,|\,\downarrow} \tag{C.4}$$

with $S = 5/2$ and $S_z = 3/2$. This state is a combination of 5 different Slater determinants. However, this is not the only state which can be built with $S_z = 3/2$. Four other ones can be built from a tableau of different shape

$$4 \times \begin{array}{|c|c|c|c|}\hline \uparrow & \uparrow & \uparrow & \uparrow \\\hline \downarrow \\\cline{1-1}\end{array}. \tag{C.5}$$

The number 4 tells that the above tableau refers to four states with the same symmetry. The tableau degeneracy number depends only on its shape, and not on the symbols that fill the boxes of the tableau. The tableau shape in Eq. (C.5) cannot be obtained for four electrons with the same spin because the elements along every column are antisymmetrized. It corresponds to the $S = 3/2$ and $S_z = 3/2$ spin state.

When the spin lowering operator is applied again to the tableaux (C.4) and (C.5), we find three different tableau shapes

$$\boxed{\uparrow|\uparrow|\uparrow|\downarrow|\downarrow},\ 4 \times \begin{array}{|c|c|c|c|}\hline \uparrow & \downarrow & \uparrow & \uparrow \\\hline \downarrow \\\cline{1-1}\end{array},\ 5 \times \begin{array}{|c|c|c|}\hline \uparrow & \uparrow & \uparrow \\\hline \downarrow & \downarrow \\\cline{1-2}\end{array} \tag{C.6}$$

which are spin states with $S = 2$, $S = 1$ and $S = 0$ respectively, and all with $S_z = 1/2$. The sum of all tableau degeneracies for states with $S_z = 1/2$ gives the result of Eq. (C.2) with $a = 5$ and $N_\downarrow = 2$. Just to give another example, we can mention the case of two spins ($a = 2$), where two possible tableaux represent states with $S_z = 0$, and they are the symmetric tableau

$$\boxed{\uparrow|\downarrow}, \tag{C.7}$$

for the triplet state, and the antisymmetric tableau

$$\begin{array}{|c|}\hline \uparrow \\\hline \downarrow \\\hline\end{array}, \tag{C.8}$$

for the singlet, also shown below right in Table C.1 for a 5-band model with two singly-occupied orbitals.

The tableau representations of states are symmetrizations/antisymmetrizations of sets of Slater determinants. In order for these representations to be used as a basis of orthonormal many-body states, they need both to be normalized and, in case they carry a degeneracy, orthogonalized within the space of all tableaux of the same shape and S_z quantum number. Once this has been done, they build the unitary transformation from the basis of spin configurations to the spin symmetric basis.

C.2 Implementation of space rotational symmetry

Thanks to Young Tableaux we are able to label states with the quantum numbers $\{N, S, S_z, L_z\}$. For each of these sets of quantum numbers, there are several states with different values of the square modulus $L(L + 1)$ of total angular momentum.

If the OSB of our Gutzwiller calculation is already built from single-particle eigenstates of $\hat{L}_z$ and $\hat{L}^2$, as for instance the $3d$ orbitals of a transition metal ($l = 2$), it is very easy to build the angular momentum raising operator explicitly

$$\hat{L}_+ = \sum_{m=-l}^{l-1} \sqrt{l(l+1) - m(m+1)}\, \hat{c}^\dagger_{m+1} \hat{c}_m \,. \tag{C.9}$$

From $\hat{L}^2 = \hat{L}_+\hat{L}_- + \hat{L}_z(\hat{L}_z - 1)$ we can build the operator $\hat{L}^2$, which will be block-diagonal in every subspace with fixed $\{N, S, S_z, L_z\}$. The diagonalization of every block gives the desired set of states, labeled by $\{N, S, S_z, L, L_z\}$. For large many-body spaces, as for instance the one built from d-electrons of a transition metal, another index θ might be needed, in order to distinguish between different states having the same set of quantum numbers listed above.

C.3   Implementation of crystal cubic symmetry

Provided that a set of many-body eigenstates of spin and angular momentum operators has been given, it is easy to break the rotational symmetry of the MSB in favor of some lower crystal symmetry when necessary. In this section we will treat, as an example, the case of cubic symmetry. What we need for this purpose are just the following:

1. the 3×3 matrix representation $G(g)_{ij}$ of the action of each element g of the cubic group on a three-dimensional vector $\boldsymbol{r}$,

2. the character table of the group, for the cubic group it is shown in Table C.2,

3. the $\boldsymbol{r}$-space representation in spherical coordinates of an external potential with the symmetry of the group; an example for a potential with cubic symmetry is

$$v[\hat{\boldsymbol{r}}(\theta, \phi)] = \cos(\theta)^4 + \frac{1}{4}[3 + \cos(4\phi)]\sin(\theta)^4, \qquad (C.10)$$

where $\hat{\boldsymbol{r}}$ is the radial unit vector.

	E	$8C_3$	$3C_2(C_4^2)$	$6C_2$	$6C_4$
A_1	1	1	1	1	1
A_2	1	1	1	-1	-1
E	2	-1	2	0	0
T_1	3	0	-1	-1	1
T_2	3	0	-1	1	-1

Table C.2: *Character table of the cubic group. The first row lists all the group classes along with the number of symmetry operations they contain. The following rows list the irreducible representations, and their character on each symmetry class. From reference [119].*

Once these three ingredients are at hand, we proceed as follows:

- for each set of spherical harmonics $Y_{L,m}(\theta, \phi)$ with given L, we compute (by means of the algorithm of Gimbutas *et al.* [120]) and diagonalize the matrix

$$C^{(L)}_{m,m'} = \int Y^*_{L,m}(\hat{\boldsymbol{r}}) v(\hat{\boldsymbol{r}}) Y_{L,m'}(\hat{\boldsymbol{r}}) \, d\Omega \, ; \qquad \text{(C.11)}$$

- for each set of spherical harmonics with given l and for each group element g, we calculate the matrix elements

$$M(g)^L_{m,m'} = \int Y^*_{L,m}(\hat{\boldsymbol{r}}) Y_{L,m'}(G(g)^{-1}\hat{\boldsymbol{r}}) \, d\Omega \, ; \qquad \text{(C.12)}$$

- for each eigenvalue ε of the matrix $C^{(L)}$, and for all eigenvectors $c^{\varepsilon, L, i}$ relative to this eigenvalue, we compute the character

$$\chi(\mathcal{C}, L, \varepsilon) = \sum_i \sum_j c^{\varepsilon, L, i}_j M(g \in \mathcal{C})^L_{jk} c^{\varepsilon, L, i}_k \qquad \text{(C.13)}$$

relative to the class $\mathcal{C}$. The value of the character enables us to assign the correct label of irreducible representation $\mathcal{I}$ to the eigenvectors $c^{\varepsilon, L, i}$.

The matrices $U^{(L)}_{ij} = c^{\varepsilon, L, i}_j$ are the unitary matrices we need to apply to every block of may-body basis states with a given value of L in order to switch from a basis labeled with $\{N, S, S_z, L, L_z\}$ to a basis indicated by $\{N, S, S_z, L, \mathcal{I}, \iota\}$[1], where ι labels the states within the same irreducible representation $\mathcal{I}$.

C.4 Building the most general Gutzwiller parameter matrix

In this section we show how to parametrize the matrix $\boldsymbol{\Phi}$ of Gutzwiller parameters in the case of full spin and orbital rotational symmetry. The procedure is similar in the case of cubic symmetry.

We can easily construct the most general Gutzwiller parameter matrix $\boldsymbol{\Phi}$ commuting with the operators $\hat{S}^2$, $\hat{L}^2$, $\hat{S}_{x,y,z}$ and $\hat{L}_{x,y,z}$ by the following procedure. Operatively,

1. we find the quantum numbers that uniquely identify the irreducible representation of the symmetry group, in this case spin and spatial rotations $SU(2) \times O(3)$. These quantum numbers are $\boldsymbol{\alpha} = \{N, S, L\}$. The same representation can appear multiple times, so we will add another quantum number θ to distinguish between equivalent representations. Each irreducible representation has

---

[1] The quantum number L is still used to label states since each irreducible representation of the cubic group comes from a definite representation of the rotation group $O(3)$. However, in the case of cubic symmetry L is no longer a conserved quantum number, and the ground-state of the Hamiltonian will not necessarily have a definite L.

a degeneracy $n_{\{\boldsymbol{\alpha},\theta\}} = L(L+1) \times S(S+1)$; we will distinguish between states that are a basis for the same irreducible representation $\{\boldsymbol{\alpha},\theta\} = \{N,S,L,\theta\}$ through the index $\iota = \iota(\boldsymbol{\alpha}\theta)$. In the case of spin and rotational symmetry ι lists all the eigenstates of $\hat{S}_z$ and $\hat{L}_z$ within the same S and L.

2. With the previous definitions, the matrix elements of $\boldsymbol{\Phi}$ are labeled

$$\Phi_{\boldsymbol{\alpha}\theta\iota,\boldsymbol{\beta}\theta'\iota'} = \delta_{\boldsymbol{\alpha}\boldsymbol{\beta}}\delta_{\iota\iota'}\phi^{\boldsymbol{\alpha}}_{\theta\theta'} \, , \tag{C.14}$$

where $\phi^{\boldsymbol{\alpha}}_{\theta\theta'}$ is a reduced matrix element. The labels $\boldsymbol{\alpha}\theta\iota$ and $\boldsymbol{\beta}\theta'\iota'$ identify univocally one state of the MSB, so that our parametrization of $\boldsymbol{\Phi}$ is complete.

The same recipe holds when the spatial symmetry is, for example, the crystal cubic symmetry. In this case $\boldsymbol{\alpha} = \{N,S,\mathcal{I}\}$.

The result expressed by Eq. (C.14) comes directly from Schur's lemma, which states that a matrix commuting all the matrices of an irreducible representation of a group $\mathcal{G}$ must be a multiple of identity. The matrix $\Phi_{\boldsymbol{\alpha}\theta\iota,\boldsymbol{\beta}\theta'\iota'}$ must be nonzero only for $\boldsymbol{\alpha} = \boldsymbol{\beta}$ since, if $\hat{G}$ is a generator of the group and $\varepsilon_{\boldsymbol{\alpha}}$ its eigenvalue with respect to any basis vector belonging to irreducible representation α, the commutation relations $[\hat{\boldsymbol{\Phi}}, \hat{G}] = 0$ imply that

$$\hat{G}\hat{\boldsymbol{\Phi}}\,|\boldsymbol{\alpha}\rangle = \hat{\boldsymbol{\Phi}}\,\hat{G}|\Psi_{\boldsymbol{\alpha}}\rangle = \varepsilon_{\boldsymbol{\alpha}}\hat{\boldsymbol{\Phi}}\,|\Psi_{\boldsymbol{\alpha}}\rangle \tag{C.15}$$

and that $\hat{\boldsymbol{\Phi}}\,|\boldsymbol{\alpha}\rangle$ must be a vector with the same quantum numbers $\boldsymbol{\alpha}$.

Again from the condition of zero commutator, we have that $\Phi_{\boldsymbol{\alpha}\theta\iota,\boldsymbol{\alpha}\theta'\iota'}$, seen as a matrix in the indices $\iota\iota'$ with fixed $\theta = \theta'$, must commute with all the matrices of irreducible representation $\boldsymbol{\alpha}$, and by Schur's lemma it must be a multiple of the identity matrix. For $\theta \neq \theta'$ the same statement does not hold, since the representations are distinct.

However, their equivalence implies that the matrices of the first are related to the matrices of the second through a unitary transformation. We can choose this transformation to be the identity, and this enables us to draw for $\theta \neq \theta'$ the same conclusions as for $\theta = \theta'$, so that $\Phi_{\boldsymbol{\alpha}\theta\iota,\boldsymbol{\alpha}\theta'\iota'}$ is diagonal in $\iota\iota'$ irrespectively of θ and θ'.

Minimization algorithm for Gutzwiller parameters

The minimization of the variational energy Eq. (4.65) with respect to the matrix elements of $\hat{\Phi}$ is performed by a Lanczos-enhanced sparse constrained Levenberg-Marquardt (LM) algorithm (the part of the energy functional depending only on Gutzwiller parameters is shown in Eq. (4.70)).

We expound the unconstrained LM algorithm [121] in the first section of this appendix, in the second section we discuss how to enforce general constraints on the minimization parameters and in the third and last section we explain how we implemented the algorithm for sparse matrices, and with a Lanczos approximation of the Hessian matrix.

D.1   The Levenberg-Marquardt algorithm

Given a generic functional $\mathcal{F}(\boldsymbol{\Phi})$, whose arguments are organized in a matrix $\boldsymbol{\Phi}$, a minimization step of this algorithm starts with expanding $\mathcal{F}(\boldsymbol{\Phi})$ up to second order around some point $\bar{\bar{\boldsymbol{\Phi}}}$ in parameter space, so as to work with the effective quadratic expression

$$
\mathcal{F}_2(\boldsymbol{\Phi}) = \mathcal{F}(\bar{\bar{\boldsymbol{\Phi}}}) + \sum_{\alpha\beta} \overbrace{\left.\frac{\partial \mathcal{F}(\boldsymbol{\Phi})}{\partial \Phi_{\alpha\beta}}\right|_{\boldsymbol{\Phi}=\bar{\bar{\boldsymbol{\Phi}}}}}^{g_{\alpha\beta}(\bar{\bar{\boldsymbol{\Phi}}})} \delta\Phi_{\alpha\beta} + \frac{1}{2}\delta\Phi^{\dagger}_{\alpha\beta} \overbrace{\left(\left.\frac{\partial^2 \mathcal{F}(\boldsymbol{\Phi})}{\partial \Phi_{\alpha\beta}\partial\Phi_{\gamma\delta}}\right|_{\boldsymbol{\Phi}=\bar{\bar{\boldsymbol{\Phi}}}}\right)}^{h_{\alpha\beta\gamma\delta}(\bar{\bar{\boldsymbol{\Phi}}})} \delta\Phi_{\gamma\delta}\,, \quad \text{(D.1)}
$$

where g and h are the gradient and Hessian of the functional $\mathcal{F}$ computed at point $\bar{\bar{\Phi}}$.

This second order approximation is used to find a direction in parameter space along which to carry out a line minimization. The required direction is the solution $\delta\Phi_j$ of the equation:

$$h_{ij}(\bar{\bar{\Phi}})\delta\Phi_j = -g_i(\bar{\bar{\Phi}})\,, \tag{D.2}$$

where for simplicity we indicated with i the couple of indices $\alpha\beta$, and with j the couple $\gamma\delta$.

In order for a solution of Eq. (D.2) to exist, we need the matrix h_{ij} to be invertible. A further requirement on the Hessian $\boldsymbol{h}$ is that it is positive-definite, so that the second order expansion Eq. (D.1) has itself a minimum. This is not always the case, since a non-quadratic functional like $\mathcal{F}$ can feature also saddle-points and maxima, and as long as the minimization is not completed the expansion point $\bar{\bar{\Phi}}$ may happen to be in the vicinity of these points.

Whenever $\boldsymbol{h}$ happens to be non-positive-definite, one can substitute it with the positive matrix

$$\boldsymbol{h}' = \boldsymbol{h} - \eta\mathbb{1}\,, \tag{D.3}$$

where η is larger than the smallest eigenvalue of $\boldsymbol{h}$, and then solve Eq. (D.2) by inverting $\boldsymbol{h}'$. After a direction $\delta\boldsymbol{\Phi}$ is found, a steepest descent minimization of the full functional $\mathcal{F}(\boldsymbol{\Phi})$ can be carried out along $\delta\boldsymbol{\Phi}$. The advantage of this procedure is that it converges in exactly one step for a quadratic $\mathcal{F}(\boldsymbol{\Phi})$. If the functional is quartic, as in the case of our work (see Eq. (4.70)), more than one step is needed, but usually just few ones are sufficient to get satisfactorily close to the required minimum $\boldsymbol{\Phi} = \boldsymbol{\Phi}_{\mathrm{min}}$.

D.2   Enforcing constraints

Constraints in the LM algorithm are enforced via both Lagrange multipliers and penalty functional. In our case all constraints are quadratic, so they can be expressed as

$$\mathcal{C}^{(a)}(\boldsymbol{\Phi}) = \Phi_j\Phi_i C_{ij}^{(a)} - \kappa^{(a)}\,. \tag{D.4}$$

The quantity that has to be added to the functional $\mathcal{F}$ in order to manage constraints is itself a quartic functional of $\boldsymbol{\Phi}$, with explicit form

$$\mathcal{L}(\boldsymbol{\Phi},\boldsymbol{\nu},\boldsymbol{\Upsilon}) = -\sum_a \nu_a\mathcal{C}^{(a)}(\boldsymbol{\Phi}) + \frac{\Upsilon_a}{2}\left[\mathcal{C}^{(a)}(\boldsymbol{\Phi})\right]^2\,. \tag{D.5}$$

After performing a minimization of $\mathcal{F}(\mathbf{\Phi}) + \mathcal{L}(\mathbf{\Phi}, \boldsymbol{\nu}, \boldsymbol{\Upsilon})$ at fixed $\boldsymbol{\nu}$ and $\boldsymbol{\Upsilon}$, it is necessary to update the Lagrange multipliers $\boldsymbol{\nu}$, and this can be done through the formula

$$\nu'_a = \nu_a - \sum \mathcal{M}_{ab}^{-1} \mathcal{C}^{(b)} \tag{D.6}$$

$$\mathcal{M}_{ab} = (\nabla \mathcal{C}^{(a)})_i^\dagger h_{ij}^{-1} (\nabla \mathcal{C}^{(a)})_j \,, \tag{D.7}$$

where $\boldsymbol{h}^{-1}$ is matrix inverse of either the Hessian $\boldsymbol{h}$ defined in Eq. (D.1) (if that is already positive-definite), or of the modified one $\boldsymbol{h}'$ of Eq. (D.3), and where

$$(\nabla \mathcal{C}^{(a)})_i = \frac{\partial \mathcal{C}^{(a)}}{\partial \Phi_i}\Big|_{\mathbf{\Phi}=\mathbf{\Phi}_{\min}}. \tag{D.8}$$

The advantage of using Lagrange multipliers together with penalty functionals is that the constraints can be fulfilled exactly even without the need of increasing the value Υ_a of each penalty up to very large values, which would jeopardize the efficiency of the unconstrained convergence. The value of Υ_a can be either kept constant, or moderately increased as $\mathcal{C}^{(a)}$ approaches zero, in order to speed up convergence.

D.3   LM algorithm with Lanczos approximation for the Hessian

Depending on the quantity of single-particle orbitals involved in the definition of the Gutzwiller parameter matrix, the number of parameters in the block-diagonal matrix $\Phi_{\alpha\beta}$ can be very large, which makes it computationally very expensive to solve Eq. (D.2), or to find the inverse of the Hessian for the multiplier updates in Eq. (D.6). It can be convenient to write the second order approximation Eq. (D.1) in a smaller parameter space, defined by taking several Lanczos steps through the positive-definite Hessian matrix $\boldsymbol{h}$ (or $\boldsymbol{h}'$).

Also the memory storage of the algorithm can take great advantage from this possibility, since the definition of the Lanczos basis does not have as a requirement the knowledge of the full matrix h_{ij}, but only the knowledge of products $h_{ij}\Phi_j$. Keeping in memory the full Hessian matrix is possible only for a small number of parameters, while it implies a considerable slow down of simulations in the case of a 5-band Gutzwiller projector like the one we need for dealing with transition metals.

Whenever we choose the starting Lanczos vector, we need to remember that finding an accurate solution for Eq. (D.2) requires this solution $\delta\Phi_j$ to have a nonzero component on the first vector of the Lanczos chain. We now give some reasons why a good starting vector is the gradient g_i itself. The first reason is that with this choice, a single Lanczos step is equivalent to solving the whole minimization problem with the steepest descent algorithm. The second reason is that the gradient has a nonzero

projection on $\delta\boldsymbol{\Phi}$, since by virtue of the positive-definiteness of $\boldsymbol{h}$ (or $\boldsymbol{h}'$)

$$\sum_{ij} \delta\Phi_i^* h_{ij} \delta\Phi_j > 0 \,, \tag{D.9}$$

but $\sum_j h_{ij}\delta\Phi_j = -g_i$, which means that

$$g_i^* \delta\Phi_i < 0 \,. \tag{D.10}$$

We can say more than this, namely that there is a nonzero component of $\delta\boldsymbol{\Phi}$ also on $\boldsymbol{hg}$, since

$$\sum_{ij} \delta\Phi_j^* h_{ij} g_i = -\sum_{ij}(g_i^* h_{ij}\delta\Phi_j)^* = -\sum_j g_j g_j^* < 0 \,. \tag{D.11}$$

Finally, there is a nonzero component of $\delta\boldsymbol{\Phi}$ also on $\boldsymbol{h^2 g}$, again due to the positive-definiteness of the Hessian

$$\sum_{ij} \delta\Phi_i^* (h^2)_{ij} g_j = \sum_{ij}(g_i^*(h^2)_{ij}\delta\Phi_j)^* = -\sum_i (g_i^* h_{ij} g_j)^* < 0 \,. \tag{D.12}$$

This means that three Lanczos steps will certainly improve a steepest descent problem. Any further step will further refine the approximation to the correct descent direction $\delta\boldsymbol{\Phi}$.

Various topics of Density Functional theory

In this appendix we discuss in more depth some concepts of Local Density Approximation plus Hubbard-U (LDA+U) and Local Density Approximation plus Gutzwiller Method (LDA+G) that are introduced in Chapt. 3 and Chapt. 4. We show in practice how Local Density Approximation (LDA) is unable to subtract the self-interaction from the Hartree energy of a single electron, and we prove how our first-order approximation for the exchange-correlation functional of LDA+G fulfills the sum-rule for the exchange-correlation hole. The last two sections are devoted to LDA+U and the definition of the atomic Hamiltonian $\hat{H}_{\mathrm{at}} = \hat{H}_{\mathrm{Hub}} + \hat{H}_{\mathrm{Hund}}$ that we exploit in Chapt. 4.

E.1   Self-interaction in the LDA functional

If we compute the self-interaction of a single-electron density with a Gaussian profile

$$n_a(\boldsymbol{r}) = \left(\frac{1}{2\pi a^2} \right)^{3/2} \exp\left(-\frac{r^2}{2a^2} \right) , \tag{E.1}$$

we find

$$\mathrm{SIC}_a = \frac{e^2}{2} \int d\boldsymbol{r} d\boldsymbol{\tau} \frac{n_a(\boldsymbol{r}) n_a(\boldsymbol{r} + \boldsymbol{\tau})}{\tau} = \frac{1}{\sqrt{\pi} a} \approx \frac{0.282}{a} , \tag{E.2}$$

where the energy unit is the Hartree (units of e^2/a_{Bohr}) when a is expressed in units of the Bohr radius a_{Bohr}. The previous result tells us that the narrower the density profile, the larger will be the self-interaction.

The exact self-interaction energy per particle corresponding to a Gaussian electron is a non-local function of the density $n_a(\boldsymbol{r})$

$$\text{SI}_a = \int d\boldsymbol{r}\, n_a(\boldsymbol{r})\epsilon^{(\text{SI})}[n_a](\boldsymbol{r}) \tag{E.3}$$

$$\epsilon^{(\text{SI})}[n_a](\boldsymbol{r}) = \frac{e^2}{2}\int d\boldsymbol{\tau}\,\frac{n_a(\boldsymbol{r}+\boldsymbol{\tau})}{\tau}\,. \tag{E.4}$$

This non-locality is absent from the LDA self-interaction, where $\epsilon^{(\text{SI})}[n_a](\boldsymbol{r})$ is computed from the local value of the density $n_a(\boldsymbol{r})$. Since a uniform electron gas has no other length scale than $1/V^{1/3}$, where V is the volume of the gas, the LDA exchange contribution to its self-interaction energy per particle for must scale as $[n_a(\boldsymbol{r})]^{1/3}$ (any logarithmic term is included in the correlation contribution to self-interaction); in fact, the LDA exchange kernel is equal to

$$\epsilon_{\text{x}}^{(\text{LDA})}[n(\boldsymbol{r})] = -\frac{3e^2}{4}\left(\frac{3}{\pi}\right)^{1/3}[n(\boldsymbol{r})]^{1/3}\,, \tag{E.5}$$

an expression which is known as Stoner-exchange. Changing the sign of the above expression, we find the LDA exchange-only approximation to the self-interaction kernel

$$\epsilon_{\text{x}}^{(\text{SI};\text{LDA})}[n_a(\boldsymbol{r})] = \frac{3e^2}{4}\left(\frac{3}{\pi}\right)^{1/3}[n_a(\boldsymbol{r})]^{1/3}\,. \tag{E.6}$$

When we compute the integral Eq. (E.3) with the above kernel, we find the value of the LDA self-interaction

$$\text{SI}_a^{(\text{LDA})} = \int d\boldsymbol{r}\, n_a(\boldsymbol{r})\epsilon_{\text{x}}^{(\text{SI};\text{LDA})}[n_a(\boldsymbol{r})] = \frac{9\left(\frac{3}{\pi}\right)^{5/6}}{32\sqrt{2}a} \approx \frac{0.191}{a}\,, \tag{E.7}$$

with the same units as Eq. (E.2). This shows that approximately 30% of the self-interaction energy of a Gaussian electron is not subtracted by the LDA exchange functional. For $a = a_{\text{Bohr}}$ the error is about 2.5 eV.

If we add the correlation to the self-interaction calculation, we will find that the LDA subtracts an excess of self-interaction for Gaussians with standard deviation larger than 4 Bohr radii [122], while for smaller Gaussians the exchange-only result remains approximately valid, and the total self-interaction error scales as $1/a$. The average distance between a $3d$ electron and the nucleus of atomic iron is less than half a Bohr radius, and similarly small result are found for all transition metals. In all crystals containing transition metal atoms with atomic-like d-type orbitals, the self-interaction error is therefore expected to be important.

E.2 First order approximation to the exchange-correlation functional

In this section we want to prove rigorously that the first order expansion 4.50 to the LDA exchange-correlation functional satisfies the exchange-hole sum-rule Eq. (3.38). To begin with, we remind that the exchange-correlation energy can be defined rigorously as

$$E_{\mathrm{xc}}[n] = \int d\boldsymbol{r}\, \epsilon_{\mathrm{xc}}[n](\boldsymbol{r})n(\boldsymbol{r})\,, \tag{E.8}$$

where the general expression for the exchange-correlation kernel $\epsilon_{\mathrm{xc}}[n](\boldsymbol{r})$ is provided by coupling-constant integration

$$\epsilon_{\mathrm{xc}}[n](\boldsymbol{r}) = -\frac{e^2}{2}\int d\boldsymbol{r}'\, \frac{n(\boldsymbol{r}')}{|\boldsymbol{r}-\boldsymbol{r}'|}\int_0^1 d\gamma\, h_{\mathrm{xc}}^{(\gamma)}[n](\boldsymbol{r},\boldsymbol{r}')\,. \tag{E.9}$$

The quantity $h_{\mathrm{xc}}^{(\gamma)}[n](\boldsymbol{r},\boldsymbol{r}') = 1 - g_{\mathrm{xc}}^{(\gamma)}[n](\boldsymbol{r},\boldsymbol{r}')$ is the probability density of finding a hole at point $\boldsymbol{r}'$ when a particle is in $\boldsymbol{r}$, and is computed for a system of density $n(\boldsymbol{r})$ where the electronic charge has been rescaled as $e' = e\sqrt{\gamma}$.

The electron-electron interaction operator of such a system results to be rescaled by γ, so that for $\gamma = 0$, $h_{\mathrm{xc}}^{(0)}[n](\boldsymbol{r},\boldsymbol{r}')$ is the hole probability density for a system of non-interacting electrons, while $h_{\mathrm{xc}}^{(1)}[n](\boldsymbol{r},\boldsymbol{r}')$ equals to the hole probability density of the real system. The sum-rule (3.38) is of course true when the value of $h_{\mathrm{xc}}^{(\gamma)}[n](\boldsymbol{r},\boldsymbol{r}')$ is computed, for every γ and $\boldsymbol{r}$, from a reference homogeneous system of equal coupling constant γ, and of uniform density equal to $n(\boldsymbol{r})$, i.e. when we choose to approximate the exchange and correlation functionals within LDA. In this case the Local Density ansatz requires that $\epsilon_{\mathrm{xc}}[n](\boldsymbol{r}) = \epsilon_{\mathrm{xc}}^{(\mathrm{eg})}[n(\boldsymbol{r})]$, and that in the definition of Eq. (E.9) $n(\boldsymbol{r}')$ is set everywhere equal to $n(\boldsymbol{r})$, so that we find the following expression for the energy kernel

$$\epsilon_{\mathrm{xc}}[n(\boldsymbol{r})] = -\frac{e^2}{2}\int d\boldsymbol{r}'\, \frac{n(\boldsymbol{r})}{|\boldsymbol{r}-\boldsymbol{r}'|}\int_0^1 d\gamma\, h_{\mathrm{xc}}^{(\gamma)}[n(\boldsymbol{r})](\boldsymbol{r},\boldsymbol{r}')\,, \tag{E.10}$$

where $h_{\mathrm{xc}}^{(\gamma)}[n(\boldsymbol{r})](\boldsymbol{r},\boldsymbol{r}')$ is the hole probability density in a system with constant density $n(\boldsymbol{r})$ and coupling constant γ. Since Eq. (3.38) is valid for any density, it is in particular valid for a convex combination of $n^{(0)}(\boldsymbol{r})$ and $n(\boldsymbol{r})$. Within LDA

$$\int d\boldsymbol{r}'\, h_{\mathrm{xc}}^{(\gamma)}\left[n_\lambda(\boldsymbol{r})\right](\boldsymbol{r},\boldsymbol{r}')n_\lambda(\boldsymbol{r}) = 1 \tag{E.11}$$

$$n_\lambda(\boldsymbol{r}) = n^{(0)}(\boldsymbol{r}) + \lambda\left[n(\boldsymbol{r}) - n^{(0)}(\boldsymbol{r})\right]\,, \tag{E.12}$$

where λ is a positive parameter smaller than 1. We can rewrite Eq. (E.11) by using well known theorems of calculus, and we find

$$
\lambda \int d\boldsymbol{r}' \left\{ h_{\mathrm{xc}}^{(\gamma)}[n_\lambda(\boldsymbol{r})](\boldsymbol{r},\boldsymbol{r}') + n_\lambda(\boldsymbol{r}) \frac{\partial h_{\mathrm{xc}}^{(\gamma)}[n(\boldsymbol{r})](\boldsymbol{r},\boldsymbol{r}')}{\partial n(\boldsymbol{r})}\bigg|_{n(\boldsymbol{r})=n_{\lambda'}(\boldsymbol{r})} \right\} \delta n(\boldsymbol{r}) =
$$
$$
= 1 - \int d\boldsymbol{r}' \, h_{\mathrm{xc}}^{(\gamma)}[n^{(0)}(\boldsymbol{r})](\boldsymbol{r},\boldsymbol{r}')n^{(0)}(\boldsymbol{r}) \,, \tag{E.13}
$$

where $\delta n(\boldsymbol{r}) = n(\boldsymbol{r}) - n^{(0)}(\boldsymbol{r})$, and $\lambda' \le \lambda$ is a suitable positive constant. The right-hand side of Eq. (E.13) is identically zero, due to the sum-rule for a density $n^{(0)}(\boldsymbol{r})$. The left-hand side must therefore be zero for every value of λ. Supposing that the integrand on the left-hand side is a well-behaved function, we can therefore say that the integral must be zero for every λ. For $\lambda = 0$ we have that λ' must be zero, and we find

$$
\int d\boldsymbol{r}' \left\{ h_{\mathrm{xc}}^{(\gamma)}[n^{(0)}](\boldsymbol{r},\boldsymbol{r}') + n^{(0)}(\boldsymbol{r}') \frac{\partial h_{\mathrm{xc}}^{(\gamma)}[n](\boldsymbol{r},\boldsymbol{r}')}{\partial n}\bigg|_{n=n^{(0)}} \right\} \delta n(\boldsymbol{r}) = 0 \,. \tag{E.14}
$$

The integrand of Eq. (E.14) is the same that appears in the definition of the difference between $E_{\mathrm{xc}}^{(1)}\left[n(\boldsymbol{r}),n^{(0)}(\boldsymbol{r})\right]$ in Eq. (4.50) and $E_{\mathrm{xc}}^{(\mathrm{LDA})}\left[n^{(0)}(\boldsymbol{r})\right]$, indeed

$$
E_{\mathrm{xc}}^{(1)}\left[n(\boldsymbol{r}),n^{(0)}(\boldsymbol{r})\right] - E_{\mathrm{xc}}^{(\mathrm{LDA})}\left[n^{(0)}(\boldsymbol{r})\right] =
$$
$$
= -\frac{e^2}{2} \int d\boldsymbol{r}' \frac{n^{(0)}(\boldsymbol{r})\delta n(\boldsymbol{r})}{|\boldsymbol{r}-\boldsymbol{r}'|} \int d\gamma \left\{ h_{\mathrm{xc}}^{(\gamma)}[n^{(0)}](\boldsymbol{r},\boldsymbol{r}') + n^{(0)}(\boldsymbol{r}) \frac{\partial h_{\mathrm{xc}}^{(\gamma)}[n](\boldsymbol{r},\boldsymbol{r}')}{\partial n}\bigg|_{n=n^{(0)}} \right\} \,. \tag{E.15}
$$

This is a proof that the additional term in $E_{\mathrm{xc}}^{(1)}\left[n(\boldsymbol{r}),n^{(0)}(\boldsymbol{r})\right]$ does not add any contribution to the sum-rule (3.38), which is fulfilled for $E_{\mathrm{xc}}^{(\mathrm{LDA})}\left[n^{(0)}(\boldsymbol{r})\right]$ and remains fulfilled for our choice of the exchange-correlation functional $E_{\mathrm{xc}}^{(1)}\left[n(\boldsymbol{r}),n^{(0)}(\boldsymbol{r})\right]$ in LDA+G.

E.3 LDA+U and double-counting terms

We want derive here the formula for LDA+U energy used by many authors, *in primis* Dudarev *et al* [123], and more recently Cococcioni and De Gironcoli [102], and presented in Sect. 3.5 of this thesis. The formula is:

$$
E_{\mathrm{LDA+U}} = \frac{U}{2} \, \mathrm{Tr}\{\boldsymbol{n}(\mathbb{1} - \boldsymbol{n})\} \,, \tag{E.16}
$$

where $\boldsymbol{n}$ is the single-particle density matrix on a selected set of orbitals (usually the d orbitals when dealing with transition metals), and includes double-counting.

In order to prove this result we firstly remind that the philosophy of LDA+U is to add to the density functional the expectation value on the Kohn-Sham Slater determinant of a Hubbard interaction term

$$E_{\text{Hub}} = \langle \Psi_0 | \hat{H}_{\text{Hub}} | \Psi_0 \rangle = \frac{U}{2} \langle \Psi_0 | \sum_{mm',\sigma\sigma'} \hat{c}^\dagger_{m\sigma} \hat{c}^\dagger_{m'\sigma'} \hat{c}_{m'\sigma'} \hat{c}_{m\sigma} | \Psi_0 \rangle . \qquad \text{(E.17)}$$

This expectation value will carry a Hartree contribution and a Fock contribution. Part of these contributions are already present in the LDA Hamiltonian, since the Hartree and Exchange-correlation functionals are able, though in an approximate way, to account for electron-electron interaction. We should therefore subtract from Eq. (E.17) the contribution to the Hubbard energy which has supposedly been already included through LDA.

There is no agreement on how this contribution should be subtracted from the density functional, so that more than one guess based on physical insight is available. Since within LDA the Kohn-Sham potential is a function of local density $n(\boldsymbol{r})$ with no dependence on spin and orbital quantum numbers, we suppose that the LDA functional is able to account only for those mean-field terms of the interaction that are independent of spin and angular momentum, and therefore likely to be of the form

$$\frac{U}{2} \left(\alpha \langle \hat{n} \rangle \langle \hat{n} \rangle + \beta \langle \hat{n} \rangle \right) . \qquad \text{(E.18)}$$

The two expressions for the double-counting energy that are most widely used in electronic structure calculations are both of the above type, and give the exact subtraction in two relevant limits, the around-mean-field (AMF), and the fully-localized (FLL) limit. In the next section we show how to recover both of them starting from Eq. (E.17).

E.3.1   The fully-localized limit

We begin by writing the Hubbard operator in Eq. (E.17) in a different way, using commutation rules of fermionic operators:

$$\hat{H}_{\text{Hub}} = -\frac{U}{2} \sum_{mm',\sigma\sigma'} [\hat{c}^\dagger_{m\sigma}(\mathbb{1}_{mm',\sigma\sigma'} - \hat{c}_{m\sigma}\hat{c}^\dagger_{m'\sigma'})\hat{c}_{m'\sigma'}] =$$

$$= \frac{U}{2} \sum_{mm',\sigma\sigma'} [-\mathbb{1}_{mm',\sigma\sigma'}\hat{c}^\dagger_{m\sigma}\hat{c}_{m'\sigma'} + \hat{c}^\dagger_{m\sigma}\hat{c}_{m\sigma}\hat{c}^\dagger_{m'\sigma'}\hat{c}_{m'\sigma'}] . \qquad \text{(E.19)}$$

In terms of the orbital occupation operators $\hat{n}_{m\sigma}$, the previous term becomes

$$\hat{H}_{\text{Hub}} = \frac{U}{2} \sum_{mm',\sigma\sigma'} [\hat{n}_{m\sigma}\hat{n}_{m'\sigma'} - \hat{n}_{m\sigma}\delta_{mm'\sigma\sigma'}] , \qquad \text{(E.20)}$$

and assume now that LDA can account for only the Hartree part of $\langle \Psi_0 | \hat{H}_{\text{Hub}} | \Psi_0 \rangle$ with the Hubbard operator in the form (E.20)[1], so that

$$\langle \Psi_0 | \hat{H}_{\text{Hub}} | \Psi_0 \rangle \underset{LDA}{\rightarrow} \frac{U}{2} \sum_{mm',\sigma\sigma'} [n_{m\sigma} n_{m'\sigma'} - n_{m\sigma} \delta_{mm',\sigma\sigma'}] = \frac{U}{2} N(N-1) = E_{\text{dc}},$$

(E.21)

where $n_{m\sigma} = \langle \hat{n}_{m\sigma} \rangle$ and $N = \sum_{m,\sigma} n_{m\sigma}$.

If instead we do a full HF decoupling of the expectation value of Eq. (E.19), we find (shortening the notation by writing $\langle \cdot \rangle$ instead of $\langle \Psi_0 | \cdot | \Psi_0 \rangle$)

$$E_{\text{Hub}} = \langle \hat{H}_{\text{Hub}} \rangle \underset{HF}{\rightarrow} \frac{U}{2} \langle \sum_{mm',\sigma\sigma'} [\hat{c}_{m\sigma}^\dagger \hat{c}_{m\sigma} \hat{c}_{m'\sigma'}^\dagger \hat{c}_{m'\sigma'} - \mathbb{1}_{mm',\sigma\sigma'} \hat{c}_{m\sigma}^\dagger \hat{c}_{m'\sigma'}] \rangle =$$

$$= \frac{U}{2} \sum_{mm',\sigma\sigma'} [\underbrace{\langle \hat{c}_{m\sigma}^\dagger \hat{c}_{m\sigma} \rangle \langle \hat{c}_{m'\sigma'}^\dagger \hat{c}_{m'\sigma'} \rangle}_{\text{Hartree}} + \underbrace{\langle \hat{c}_{m\sigma}^\dagger \hat{c}_{m'\sigma'} \rangle \langle \hat{c}_{m\sigma} \hat{c}_{m'\sigma'}^\dagger \rangle}_{\text{Fock}} - \langle \mathbb{1}_{mm',\sigma\sigma'} \hat{c}_{m\sigma}^\dagger \hat{c}_{m'\sigma'} \rangle] =$$

$$= \frac{U}{2} \sum_{mm',\sigma\sigma'} [\underbrace{n_{m\sigma} n_{m'\sigma'}}_{\text{Hartree}} + \delta_{\sigma\sigma'} \underbrace{n_{mm',\sigma} (\cancel{\delta_{mm',\sigma\sigma'}} - n_{m'm,\sigma})}_{\text{Fock}} - \cancel{\delta_{mm',\sigma\sigma'} n_{m\sigma}}],$$

(E.22)

where $n_{mm',\sigma} = \langle \hat{c}_{m\sigma}^\dagger \hat{c}_{m'\sigma} \rangle$, $n_{m,\sigma} = \langle \hat{c}_{m\sigma}^\dagger \hat{c}_{m\sigma} \rangle$, and where we omitted all spin-flip terms ($n_{mm',\sigma\neq\sigma'} = 0$), which are zero for an unpolarized or spin-polarized collinear calculation. Note how two terms of the Wick decoupling cancel already in Eq. (E.22).

Now we can subtract the LDA double-counting energy E_{dc} from the HF Hubbard energy E_U, with the result

$$E_{\text{LDA+U}} = E_{\text{Hub}} - E_{\text{dc}} = \frac{U}{2} \sum_{mm',\sigma\sigma'} (n_{m\sigma} \delta_{mm',\sigma\sigma'} - \delta_{\sigma\sigma'} n_{mm',\sigma} n_{m'm,\sigma}) =$$

$$= \frac{U}{2} \text{Tr}\{\boldsymbol{n}(\mathbb{1} - \boldsymbol{n})\}.$$

(E.23)

where $\boldsymbol{n}$ has matrix elements $n_{mm'\sigma\sigma'} \delta_{\sigma\sigma'}$. This is the formula used also by Cococcioni *et al.* [102].

E.3.2 The around-mean-field limit

In the around mean-field limit, the double-counting energy is computed directly as the Hartree part of the expectation value Eq. (E.17), without changing the form of $\hat{H}_{\text{Hub}}$,

$$\langle \Psi_0 | \hat{H}_{\text{Hub}} | \Psi_0 \rangle \underset{LDA}{\rightarrow} \frac{U}{2} \sum_{mm',\sigma\sigma'} [n_{m\sigma} n_{m'\sigma'}] = \frac{U}{2} N^2 = E_{\text{dc}}.$$

(E.24)

---

[1]Only if both Hartree and Fock contribution to the expectation value of $\hat{H}_{\text{Hub}}$ are taken into account, the result is independent of the way one writes $\hat{H}_{\text{Hub}}$.

Following this recipe, the LDA+U energy is simply the Fock term in Eq. (E.22)

$$E_{LDA+U} = -\frac{U}{2}\,\text{Tr}\{\boldsymbol{nn}\}\,. \tag{E.25}$$

Interpretation of FLL and AMF double-counting in terms of probability distributions

The around-mean-field expression for the double-counting energy is exact when the electron distribution on the local orbitals is Poissonian, i.e.

$$\sigma_{\hat{N}}^2 = \langle \hat{N}^2 \rangle - N^2 \underset{LDA}{=} N\,. \tag{E.26}$$

This would be true if the eigenstate of the electronic Hamiltonian were plane waves, and is approximately true when LDA describes electrons as itinerant rather than localized.

Instead, the double-counting energy in the fully-localized limit (E.21) is exact when the LDA particle distribution on the local orbitals has zero variance, i.e. when

$$\sigma_{\hat{N}}^2 = \langle \hat{N}^2 \rangle - N^2 \underset{LDA}{=} 0\,. \tag{E.27}$$

This is of course never true, since the local atomic orbitals used in LDA+U are not the single-particle basis of an isolated system, and their electrons can hop to neighboring sites and to other local orbitals that are not subject to the Hubbard interaction. In general, the correct recipe for double-counting energy is a mixture of the fully-localized and around-mean-field expressions.

E.4 Definitions for the Hubbard and Hund operators used in LDA+G

From Eq. (E.20) we see that the Hubbard Hamiltonian can be written in terms of the number operator on the local atomic orbitals as

$$\hat{H}_{\text{Hub}} = \frac{U}{2}\hat{N}(\hat{N} - \hat{\mathbb{1}})\,, \tag{E.28}$$

which is the result we used for the Hubbard Hamiltonian of our LDA+G functional in Sect. 4.3. The form we chose for the inter-orbital Hund exchange operator, defined in Eq. (4.47), can also be recast in terms of more familiar operators as the number and spin operators

$$\hat{H}_{\text{Hund}} = -J\left\{\hat{S}^2 + \frac{\hat{N}^2}{4} - \hat{N} + \sum_m \hat{n}_{m\uparrow}\hat{n}_{m\downarrow}\right\}\,. \tag{E.29}$$

The double-counting term that subtracts the LDA contribution to the Hund exchange in the fully-localized limit reads

$$E_{\mathrm{dc}}{}^{(FLL)} = -\frac{J}{2} \left[N_\uparrow(N_\uparrow - 1) + N_\downarrow(N_\downarrow - 1) \right] , \tag{E.30}$$

and can be obtained from the expectation value of the first three terms of Eq. (E.29) by supposing that within LDA $\langle \hat{N} \rangle = N_\uparrow + N_\downarrow$ and $\langle \hat{S}^2 \rangle = (N_\uparrow - N_\downarrow)^2/4$, i.e. that particle numbers $N_\uparrow$, $N_\downarrow$ and spin projection S_z do not fluctuate around their expectation values.

In order to account for the expectation value of the last term in Eq. (E.29), we supplement Eq. (E.30) with another mean-field term[2], so that our choice for the double-counting energy reads

$$E_{\mathrm{dc}} = -\frac{J}{2} \left[N_\uparrow(N_\uparrow - 1) + N_\downarrow(N_\downarrow - 1) \right] - \frac{J}{2l+1} N_\uparrow N_\downarrow . \tag{E.31}$$

Rotationally-invariant definitions for U and J (see [124]) can be found from an explicit calculation of matrix elements of the electron-electron interaction Hamiltonian between local atomic states of angular momentum azimuthal quantum number l (l=2 for d-orbitals), and magnetic quantum numbers m, m', m'' and m'''. This calculation relates them to the strength F_n of the multi-poles of order n of the Coulomb operator, also named Slater integrals. The value of Hubbard-U can be proved to be equal to the monopole integral F_0, through the expression

$$U = \frac{1}{(2l+1)^2} \sum_{m,m'} U_{m,m'} = F_0 , \tag{E.32}$$

where

$$U_{mm'} = \langle m, m' | V_{ee} | m, m' \rangle . \tag{E.33}$$

In the case of $l = 2$, J can be defined from the quadrupole (F_2) and octupole (F_4) Slater integrals by combining Eq. (E.32) with

$$U - J = \frac{1}{2l(2l+1)} \sum_{m,m'} [U_{m,m'} - J_{m,m'}] = F_0 - \frac{(F_2 + F_4)}{14} , \tag{E.34}$$

where

$$J_{mm'} = \langle m, m' | V_{ee} | m', m \rangle , \tag{E.35}$$

so that we find

$$J = \left(\frac{1}{2l(2l+1)} \sum_{m,m'} J_{m,m'} \right) - \frac{U}{2l} = \frac{F_2 + F_4}{14} . \tag{E.36}$$

---

[2]There is no FLL form for the double-counting term related to the last operator in Eq. (E.29). Being a sum of orbital-resolved double-occupation operators, we chose to treat it, within each orbital, with the around-mean-field recipe.

A way to compute the values of F_n is from HF calculations of atomic energy levels, implemented for instance in the code by Cowan [107].

List of Acronyms

Bibliography

[1] P. Hohenberg and W. Kohn, Phys. Rev. **136**, B864 (1964).

[2] W. Kohn and L. J. Sham, Phys. Rev. **140**, A1133 (1965).

[3] A. Szabo and N. S. Ostlund, Modern Quantum Chemistry (Macmillan Publishing Co., 1982).

[4] M. Gell-Mann and K. A. Brueckner, Phys. Rev. **106**, 364 (1957).

[5] J. P. Perdew and Y. Wang, Phys. Rev. B **45**, 13244 (1992).

[6] D. M. Ceperley and B. J. Alder, Phys. Rev. Lett. **45**, 566 (1980).

[7] L. Mitas, J. C. Grossman, I. Stich, and J. Tobik, Phys. Rev. Lett. **84**, 1479 (2000).

[8] P. J. Feibelman, B. Hammer, J. K. Nørskov, F. Wagner, M. Scheffler, R. Stumpf, R. Watwe, and J. Dumesic, The Journal of Physical Chemistry B **105**, 4018 (2001).

[9] M. Gruning, O. V. Gritsenko, and E. J. Baerends, Journal of Chemical Physics **118** (2003).

[10] N. F. Mott, Proceedings of the Physical Society A **62**, 416 (1949).

[11] N. F. Mott, Metal Insulator Transition (Taylor and Francis, London, 1990).

[12] J. G. Bednorz and K. A. Müller, Zeitschrift für Physik B Condensed Matter **64**, 189 (1986).

[13] J. Bardeen, L. N. Cooper, and J. R. Schrieffer, Phys. Rev. **106**, 162 (1957).

[14] J. Hubbard, Proceedings of the Royal Society of London **276**, 238 (1963).

[15] W. M. C. Foulkes, L. Mitas, R. J. Needs, and G. Rajagopal, Rev. Mod. Phys. **73**, 33 (2001).

[16] U. Schollwöck, Rev. Mod. Phys. **77**, 259 (2005).

[17] A. Georges, G. Kotliar, W. Krauth, and M. J. Rozenberg, Rev. Mod. Phys. **68**, 13 (1996).

[18] V. I. Anisimov, J. Zaanen, and O. K. Andersen, Phys. Rev. B **44**, 943 (1991).

[19] F. A. V. I. Anisimov and A. I. Lichtenstein, Journal of Physics: Condensed Matter **9**, 767 (1997).

[20] V. I. Anisimov, D. E. Kondakov, A. V. Kozhevnikov, I. A. Nekrasov, Z. V. Pchelkina, J. W. Allen, S.-K. Mo, H.-D. Kim, P. Metcalf, S. Suga, et al., Phys. Rev. B **71**, 125119 (2005).

[21] D. Ceperley, G. V. Chester, and M. H. Kalos, Phys. Rev. B **16**, 3081 (1977).

[22] S. Sorella, Physical Review B **71**, 241103 (2005).

[23] M. Marchi, S. Azadi, M. Casula, and S. Sorella, Journal of Chemical Physics **131**, 154116 (2009).

[24] M. C. Gutzwiller, Phys. Rev. Lett. **10**, 159 (1963).

[25] M. C. Gutzwiller, Phys. Rev. **134**, A923 (1964).

[26] M. C. Gutzwiller, Phys. Rev. **137**, A1726 (1965).

[27] P. Fazekas, Lecture Notes on Electron Correlation and Magnetism (World Scientific Publishing, Singapore, 1999).

[28] P. W. Anderson, Science **235**, 1196 (1987).

[29] A. Damascelli, Z. Hussain, and Z.-X. Shen, Rev. Mod. Phys. **75**, 473 (2003).

[30] S.-K. Mo, J. D. Denlinger, H.-D. Kim, J.-H. Park, J. W. Allen, A. Sekiyama, A. Yamasaki, K. Kadono, S. Suga, Y. Saitoh, et al., Phys. Rev. Lett. **90**, 186403 (2003).

[31] S.-K. Mo, H.-D. Kim, J. W. Allen, G.-H. Gweon, J. D. Denlinger, J.-H. Park, A. Sekiyama, A. Yamasaki, S. Suga, P. Metcalf, et al., Phys. Rev. Lett. **93**, 076404 (2004).

[32] S.-K. Mo, H.-D. Kim, J. D. Denlinger, J. W. Allen, J.-H. Park, A. Sekiyama, A. Yamasaki, S. Suga, Y. Saitoh, T. Muro, et al., Phys. Rev. B **74**, 165101 (2006).

[33] F. Rodolakis, B. Mansart, E. Papalazarou, S. Gorovikov, P. Vilmercati, L. Petaccia, A. Goldoni, J. P. Rueff, S. Lupi, P. Metcalf, et al., Phys. Rev. Lett. **102**, 066805 (2009).

[34] G. Borghi, M. Fabrizio, and E. Tosatti, Phys. Rev. Lett. **102**, 066806 (2009).

[35] G. Borghi, M. Fabrizio, and E. Tosatti, Phys. Rev. B **81**, 115134 (2010).

[36] M. Potthoff and W. Nolting, Phys. Rev. B **60**, 7834 (1999).

[37] R. W. Helmes, T. A. Costi, and A. Rosch, Phys. Rev. Lett. **101**, 066802 (2008).

[38] J. Bünemann, W. Weber, and F. Gebhard, Phys. Rev. B **57**, 6896 (1998).

[39] J. M. Soler, E. Artacho, J. D. Gale, A. García, J. Junquera, P. Ordejón, and D. Sánchez-Portal, Journal of Physics: Condensed Matter **14**, 2745 (2002).

[40] J. B. Goodenough, Phys. Rev. **120**, 67 (1960).

[41] M. B. Stearns, Physical Review B **8**, 4383 (1973).

[42] G. Stollhoff and P. Thalmeier, Zeitschrift für Physik B Condensed Matter **43**, 13 (1981).

[43] A. A. Katanin, A. I. Poteryaev, A. V. Efremov, A. O. Shorikov, S. L. Skornyakov, M. A. Korotin, and V. I. Anisimov, Phys. Rev. B **81**, 045117 (2010).

[44] P. G. de Gennes, Phys. Rev. **118**, 141 (1960).

[45] E. C. Stoner, Proceedings of the Royal Society A **165**, 372 (1938).

[46] K. Terakura, T. Oguchi, A. R. Williams, and J. Kübler, Phys. Rev. B **30**, 4734 (1984).

[47] E. H. Lieb and F. Y. Wu, Phys. Rev. Lett. **20**, 1445 (1968).

[48] D. Vollhardt, Reviews of Modern Physics **56**, 99 (1984).

[49] P. Nozières and D. Pines, The Theory of Quantum Liquids (Perseus Books, Cambridge, Massachussets, 1966).

[50] G. F. Giuliani and G. Vignale, Quantum Theory of the Electron Liquid (Cambridge University Press, 2005).

[51] W. F. Brinkman and T. M. Rice, Phys. Rev. B **2**, 4302 (1970).

[52] S. Doniach and S. Engelsberg, Phys. Rev. Lett. **17**, 750 (1966).

[53] D. B. McWhan, J. P. Remeika, J. P. Maita, H. Okinaka, K. Kosuge, and S. Kachi, Phys. Rev. B **7**, 326 (1973).

[54] W. Metzner and D. Vollhardt, Phys. Rev. Lett. **59**, 121 (1987).

[55] W. Metzner and D. Vollhardt, Phys. Rev. B **37**, 7382 (1988).

[56] W. Metzner and D. Vollhardt, Phys. Rev. Lett. **62**, 324 (1989).

[57] T. A. Kaplan, P. Horsch, and P. Fulde, Phys. Rev. Lett. **49**, 889 (1982).

[58] A. J. Millis and S. N. Coppersmith, Phys. Rev. B **43**, 13770 (1991).

[59] M. Capello, F. Becca, M. Fabrizio, S. Sorella, and E. Tosatti, Phys. Rev. Lett. **94**, 026406 (2005).

[60] P. W. Anderson, Materials Research Bulletin **8**, 153 (1973).

[61] T. M. Rice, Journal of Magnetism and Magnetic Materials **310**, 454 (2007).

[62] B. Edegger, Ph.D. thesis, Johann Wolfgang Goethe-Universität in Frankfurt am Main (2007).

[63] F. Gebhard, J. Phys.: Condens. Matter **9**, 7343 (1997).

[64] J. Bünemann, F. Gebhard, and R. Thul, Phys. Rev. B **67**, 075103 (2003).

[65] M. Fabrizio, Phys. Rev. B **76**, 165110 (2007).

[66] N. Lanatà, P. Barone, and M. Fabrizio, Phys. Rev. B **78**, 155127 (2008).

[67] G. A. Sawatzky and D. Post, Phys. Rev. B **20**, 1546 (1979).

[68] K. E. Smith and V. E. Henrich, Physical Review B **50**, 1382 (1994).

[69] S. Shin, Y. Tezuka, T. Kinoshita, T. Ishii, T. Kashiwakura, M. Takahashi, and Y. Suda, Journal of the Physical Society of Japan **64**, 1230 (1995).

[70] R. Zimmermann, R. Claessen, F. Reinert, P. Steiner, and S. Hüfner, Journal of Physics: Condensed Matter **10**, 5697 (1998).

[71] B. Johansson, Phys. Rev. B **19**, 6615 (1979).

[72] L. Z. Liu, J. W. Allen, O. Gunnarsson, N. E. Christensen, and O. K. Andersen, Phys. Rev. B **45**, 8934 (1992).

[73] A. Sekiyama, T. Iwasaki, K. Matsuda, Y. Saitoh, Y. Onuki, and S. Suga, Nature **403**, 396 (2000).

[74] K. Maiti, D. D. Sarma, M. J. Rozenberg, I. H. Inoue, H. Makino, O. Goto, M. Pedio, and R. Cimino, Europhys. Lett. **55**, 246 (2001).

[75] N. Kamakura, Y. Takata, T. Tokushima, Y. Harada, A. Chainani, K. Kobayashi, and S. Shin, Europhys. Lett. **67**, 240 (2004).

[76] R. Eguchi, T. Kiss, S. Tsuda, T. Shimojima, T. Mizokami, T. Yokoya, A. Chainani, S. Shin, I. H. Inoue, T. Togashi, et al., Physical Review Letters **96**, 076402 (2006).

[77] G. Panaccione, M. Altarelli, A. Fondacaro, A. Georges, S. Huotari, P. Lacovig, A. Lichtenstein, P. Metcalf, G. Monaco, F. Offi, et al., Phys. Rev. Lett. **97**, 116401 (2006).

[78] A. Sekiyama, H. Fujiwara, S. Imada, S. Suga, H. Eisaki, S. I. Uchida, K. Takegahara, H. Harima, Y. Saitoh, I. A. Nekrasov, et al., Phys. Rev. Lett. **93**, 156402 (2004).

[79] M. Yano, A. Sekiyama, H. Fujiwara, Y. Amano, S. Imada, T. Muro, M. Yabashi, K. Tamasaku, A. Higashiya, T. Ishikawa, et al., Physical Review B **77**, 035118 (2008).

[80] A. Liebsch, Phys. Rev. Lett. **90**, 096401 (2003).

[81] H. Ishida, D. Wortmann, and A. Liebsch, Phys. Rev. B **73**, 245421 (2006).

[82] D. B. McWhan, T. M. Rice, and J. P. Remeika, Phys. Rev. Lett. **23**, 1384 (1969).

[83] F. Rodolakis, B. Mansart, J. P. Rueff, P. Vilmercati, L. Petaccia, A. Goldoni, S. Lupi, P. Metcalf, and M. Marsi, Mott-hubbard transition in cr-doped V_2O_3 studied with low energy photoemission, unpublished (2008).

[84] J. K. Freericks, Phys. Rev. B **70**, 195342 (2004).

[85] H. Zenia, J. K. Freericks, H. R. Krishnamurthy, and T. Pruschke, arXiv:0809.4993 (2009).

[86] J. K. Freericks, V. Zlatić, and A. M. Shvaika, Phys. Rev. B **75**, 035133 (2007).

[87] S. Schwieger, M. Potthoff, and W. Nolting, Phys. Rev. B **67**, 165408 (2003).

[88] M. Born and J. Oppenheimer, Zur Quantentheorie der Molekeln **389**, 457 (1927).

[89] J. Chayes, L. Chayes, and M. Ruskai, Journal of Statistical Physics **38**, 497 (1985).

[90] T. L. Gilbert, Phys. Rev. B **12**, 2111 (1975).

[91] J. E. Harriman, Phys. Rev. A **24**, 680 (1981).

[92] K. Capelle and G. Vignale, Phys. Rev. Lett. **86**, 5546 (2001).

[93] M. Levy, Proc. Natl. Acad. Sci. USA **76**, 6062 (1979).

[94] M. Levy, Phys. Rev. A **26**, 1200 (1982).

[95] E. Lieb, Int. J. Quantum Chem. **24**, 243–77 (1983).

[96] A. Görling and M. Ernzerhof, Phys. Rev. A **51**, 4501 (1995).

[97] J. P. Perdew and W. Yue, Phys. Rev. B **33**, 8800 (1986).

[98] J. P. Perdew, K. Burke, and M. Ernzerhof, Phys. Rev. Lett. **77**, 3865 (1996).

[99] J. P. Perdew and A. Zunger, Phys. Rev. B **23**, 5048 (1981).

[100] A. Svane and O. Gunnarsson, Physical Review Letters **65**, 1148 (1990).

[101] P. Mori-Sánchez, A. J. Cohen, and W. Yang, Journal of Chemical Physics **125**, 201102 (2006).

[102] M. Cococcioni and S. de Gironcoli, Phys. Rev. B **71**, 035105 (2005).

[103] O. Gunnarsson, J. Phys. F: Met. Phys. (1976).

[104] A. G. Petukhov, I. I. Mazin, L. Chioncel, and A. I. Lichtenstein, Phys. Rev. B **67**, 153106 (2003).

[105] J. Junquera, O. Paz, D. Sánchez-Portal, and E. Artacho, Phys. Rev. B **64**, 235111 (2001).

[106] C. Corliss and J. Sugar, J. Phys. Chem. Ref. Data **11** (1982).

[107] R. D. Cowan, Theory of Atomic Structure and Spectra (University of California Press, 1981).

[108] W. Weber, J. Bünemann, and F. Gebhard, arXiv:010.7033v1 (2001).

[109] J. Bünemann, F. Gebhard, T. Ohm, S. Weiser, and W. Weber, in Frontiers in Magnetic Materials, edited by A. Narlikar (Springer, Berlin, 2005), pp. 117–151.

[110] J. Bünemann, F. Gebhard, T. Ohm, S. Weiser, and W. Weber, Phys. Rev. Lett. **101**, 236404 (2008).

[111] X. Deng, L. Wang, X. Dai, and Z. Fang, Phys. Rev. B **79**, 075114 (2009).

[112] G. Wang, Y. Qian, G. Xu, X. Dai, and Z. Fang, Physical Review Letters **104**, 047002 (2010).

[113] H. Zenia, J. K. Freericks, H. R. Krishnamurthy, and T. Pruschke, Physical Review Letters **103**, 116402 (2009).

[114] S. Ziraldo, Master's thesis, University of Trieste and SISSA (2009).

[115] M. Schiró and M. Fabrizio, Phys. Rev. Lett. **105**, 076401 (2010).

[116] E. v. Oelsen, G. Seibold, and J. Bünemann, Phys. Rev. Lett. **107**, 076402 (2011).

[117] R. Bulla and M. Potthoff, Euopean Physics Journal B **13**, 257 (2000).

[118] T. Inui, Y. Tanabe, and Y. Onodera, Group Theory and Its Applications in Physics (Springer, New York, 1996).

[119] M. Tinkham, Group Theory and Quantum Mechanics (Dover, 1964).

[120] Z. Gimbutas and L. Greengard, Journal of Computational Physics **228**, 5621 (2009).

[121] R. Fletcher, Practical Methods of Optimization (John Wiley & Sons, 1987).

[122] T. Körzdörfer, Journal of Chemical Physics **134**, 094111 (2011).

[123] S. L. Dudarev, G. A. Botton, S. Y. Savrasov, C. J. Humphreys, and A. P. Sutton, Phys. Rev. B **57**, 1505 (1998).

[124] A. I. Liechtenstein, V. I. Anisimov, and J. Zaanen, Phys. Rev. B **52**, R5467 (1995).